CRANFIELD UNIVERSITY

JOMBO GBANAIBOLOU

IMPROVED GAS TURBINE DIAGNOSTICS TOWARDS AN INTEGRATED PROGNOSTIC APPROACH WITH VIBRATION AND GAS PATH ANALYSIS

SCHOOL OF AEROSPACE, TRANSPORT AND MANUFACTURING

PhD in Aerospace

PhD

Academic Year: 2016 - 2017

Supervisor: Dr Suresh Sampath and Prof. Pericles Pilidis

January 2017

CRANFIELD UNIVERSITY

SCHOOL OF AEROSPACE, TRANSPORT AND MANUFACTURING
PhD in Aerospace

PhD

Academic Year 2016 - 2017

JOMBO GBANAIBOLOU

Improved Gas Turbine Diagnostics towards an Integrated Prognostic Approach with Vibration and Gas Path Analysis

Supervisor: Dr. Suresh Sampath and Prof. Pericles Pilidis

January 2017

This thesis is submitted in partial fulfilment of the requirements for the degree of PhD

ABSTRACT

The degradation of a gas turbine engine in operation is inevitable, leading to losses in performance and eventually reduction in engine availability.

Several methods like gas path analysis and vibration analysis have been developed to provide a means of identifying the onset of component degradation. Although both approaches have been applied individually with successes in identifying component faults; localizing complex faults and improving fault prediction confidence are some of the further benefits that can accrue from the integrated application of both techniques.

Although, the link between gas path component faults and rotating mechanical component faults have been reported by several investigators, yet, gas path fault diagnostics and mechanical fault diagnostics are still treated as separated toolsets for gas turbine engine health monitoring.

This research addresses this gap by laying a foundation for the integration of gas path analysis and vibration to monitor the effect of fouling in a gas turbine compressor.

Previous work on the effect of compressor fouling on the gas turbine operation has been on estimating its impact on the gas turbine's performance in terms of reduction in thermal efficiency and output power. Another methodology often used involves the determination of correlations to characterize the susceptibility and sensitivity of the gas turbine compressor to fouling.

Although the above mentioned approaches are useful in determining the impact of compressor fouling on the gas turbine performance, they are limited in the sense that they are not capable of being used to access the interaction between the aerodynamic and rotordynamic domain in a fouled gas turbine compressor.

In this work, a Greitzer-type compression system model is applied to predict the flow field dynamics of the fouled compressor. The Moore-Greitzer model is a lumped parameter model of a compressor operating between an inlet and exit

duct which discharges to a plenum with a throttle to control the flow through the compression system.

In a nutshell, the overall methodology applied in this work involves the interaction of four different models, which are: Moore-Greitzer compression system model, Al-Nahwi aerodynamic force model, 2D transfer matrix rotordynamic model and a gas turbine performance engine model.

The study carried out in this work shows that as the rate of fouling increases, typified by a decrease in compressor massflow, isentropic efficiency and pressure ratio, there is a corresponding increase in the vibration amplitude at the compressor rotor first fundamental frequency. Also demonstrated in this work, is the application of a Moore-Greitzer type compressor model for the prediction of the inception of unstable operation in a compressor due to fouling.

In modelling the interaction between the aerodynamic and rotordynamic domain in a fouled gas turbine compressor, linear simplifications have been adopted in the compression system model. A single term Fourier series has been used to approximate the resulting disturbed flow coefficient. This approximation is reasonable for weakly nonlinear systems such as compressor operating with either an incompressible inlet flow or low Mach number compressible inlet flow. To truly account for nonlinearity in the model, further recommendation for improvement includes using a second order or two-term Fourier series to approximate the disturbed flow coefficient. Further recommendation from this work include an extension of the rotordynamic analysis to include non-synchronous response of the rotor to an aerodynamic excitation and the application of the Greitzer type model for the prediction of the flow and pressure rise coefficient at the inlet of the compressor when fouled.

Keywords:

Moore-Greitzer Model, Compression System Modelling, Rotordynamics, Compressor Fouling, RotorMatch

ACKNOWLEDGEMENTS

I thank God for the wisdom, knowledge and motivation to follow through with this research.

To my parents Late Dr. & Mrs P. P. Jombo, thank you for the inspiration to never stop learning.

To Prof David Mba, thank you for planting the seed and passion I now have for rotating equipment condition monitoring and also recommending me to the department of power and propulsion for a departmental bursary.

To Prof. Pericles Pilidis and the Centre for Propulsion Engineering, thank you for the departmental bursary to cover my PhD tuition and also providing a research direction that I am passionate about.

To my supervisor Dr. Suresh Sampath, thank you for the outstanding guidance all through this research and also for instilling in me the need to breakdown problems to their fundamentals.

Special thanks to the Niger Delta Development Commission (NDDC) for the upkeep grant, it meant a lot to my family and I.

To the Winners family Milton Keynes, thank you for nourishing my family and me in God's word and also being a solid rock for my family and me.

To my son Tokoni Jamin Jombo, you truly are a blessing.

Finally, to my beloved Wife Enipene, words alone fail me in expressing my deepest gratitude for your many sacrifices and unwavering support all through this research.

TABLE OF CONTENTS

LIST OF FIGURES

LIST OF TABLES

NOMENCLATURE

a_s	Speed of sound
A	Resultant amplitude of the disturbed axial flow coefficient $\left(A = \sqrt{a^2 + b^2}\right)$
A_b	Beam cross-sectional area
A_c, A_T	Annulus flow area for compressor and throttle duct
A_{tu}, A_{pr}	Flow through areas for the turning and pressure forces
$(AR)_s, (AR)_b$	Stage and blade aspect ratio
a', b' (a'_n, b'_n)	Amplitudes of the first and nth harmonics in the Fourier series expression of the disturbed axial flow coefficient
a, b	Transformed amplitudes of the first harmonics in the Fourier series expression for the disturbed axial flow coefficient $(\mathrm{a} = a'/(2W)\,;\mathrm{b} = b'/(2W))$
b_{ij}	Elements of the overall rotor matrix
B	Greitzer B-parameter
$[B]$	Overall rotor matrix
C, c	Journal bearing clearance
C_p	Specific heat at constant pressure
C_x	Axial flow velocity
$C_{xx,}C_{yy,}$ $C_{xy,}C_{yx,}$	Bearing damping coefficients
D	Diameter
E	Modulus of elasticity
F(.)	Axisymmetric pressure rise characteristic for a single stage
$[F]_i$	Field matrix of the i-th shaft segment
$\bar{F}_{ae}$, F_{ae}	Dimensional and non-dimensional total aerodynamic force
$\bar{F}_x^{ae}, \bar{F}_y^{ae}$	X and Y component of the dimensional aerodynamic force
$\bar{F}_{pr}, F_{pr}$	Dimensional and non-dimensional pressure force respectively
$\bar{F}_{tu}, F_{tu}$	Dimensional and non-dimensional turning force respectively
$\bar{F}_{un}, F_{un}$	Dimensional and non-dimensional unsteady momentum force respectively
FP	Fouling parameter
g(.)	Disturbed axial flow coefficient component

$[g]_i$	Forcing function matrix
G	Shear modulus, geometric parameter
H, W	Parameters from curve fitting the compressor pressure rise characteristic
h(.)	Circumferential flow coefficient at the IGV entrance
h	Blade span
$H, H^{-1}, H^T, H^{\#}$	Influence matrix, fault coefficient matrix, transpose of H and pseudo inverse of H
I	Area moment of inertia
I_T	Transverse mass moment of inertia
I_P	Polar mass moment of inertia
K_G	IGV pressure recovery coefficient
K_i	Spring stiffness
$K_{xx,}K_{yy,}$ $K_{xy,}K_{yx,}$	Bearing stiffness coefficients
L_I, L_E	Inlet and exit duct length
L_i	Length of the i-th elastic shaft segment
l_I, l_E	Non-dimensional inlet and exit duct length ($l_I = L_I/R$, $l_E = L_E/R$)
l_c	Non-dimensional effective compressor & duct flow path length ($l_c = l_I + \mu + l_E$)
L_C, L_T	Dimensional effective length of compressor and throttle
l_z	Axial blade chord ($l_z = l\cos\gamma$)
l	Blade chord
L	Length of journal bearing
m	Exit duct approximation (m = 1 [short duct], m = 2 [long duct])
m_i	Mass of the point element at the i-th station
M	Bending moment
N	Number of blade row stages, time lag in revolution
P	Pressure, Transformed plenum pressure rise coefficient ($P = \Psi/H$)
$[P]_i$	Point matrix of the i-th point element
q, Q	Transformed flow and annulus averaged flow coefficient respectively ($q = \phi/(2W)$, $Q = \Phi/(2W)$)
R	Mean compressor wheel radius, radius of journal bearing

R_g	Residue function for the Galerkin method
r	Compressor pressure ratio
S	Pressure rise characteristic aspect ratio ($S = H/W$), Sommerfeld number, throttle parameter
$[S]_i^L, [S]_i^R$	State vector at the left and right side of a point element respectively at the i-th station
t	Time
T	Temperature
$\bar{u}$	Vector representing ambient and operating conditions
u_i	Unbalance at the i-th station
U	Compressor wheel speed at the mean radius
V	Shear force
V_p	Volume of the plenum
V_{un}	Volume for the unsteady momentum storage
$\bar{\mathrm{v}}_{xyz}$	Dimensional flow field velocity
v_{xyz}	Non-dimensional flow field velocity
$\hat{\mathrm{v}}_{XYZ}$	Average flow field velocity
$\dot{W}_a, \dot{W}_f, \dot{W}_T$	Compressor mass flow, fuel flow rate, turbine mass flow
$\bar{x}$	Component performance parameter vector
Y(.)	Velocity potential disturbance at the IGV inlet
y	Rotor deflection
$\bar{z}$	Measured engine parameter vector

Greek

α_F	Form factor i.e. circular sections $\alpha_F = 4/3$, rectangular sections $\alpha_F = 1.5$
ϵ_o	Journal bearing eccentricity ratio
α	Absolute flow angle
β	Relative flow angle
ξ	Non-dimensional time ($\xi = Ut/R$)
ρ	Density
ρ_p	Density of gas accumulating in the plenum
ϕ	Axial flow coefficient ($\phi = C_x/U$)

Φ, Φ_c	Annulus averaged axial flow coefficient through the compressor
Φ_T, Φ_{th}	Annulus averaged axial flow coefficient through the throttle or throttle characteristic
η	Axial co-ordinate in the Moore-Greitzer model
θ	Circumferential co-ordinate in the Moore-Greitzer model, rotor slope
ΔMF	Relative change in the massflow
ΔP	Stage pressure-rise
ΔPR	Relative change in pressure ratio
$\Delta\bar{x}$	Component parameter deviation vector
$\Delta\bar{z}$	Measured parameter deviation vector
τ	Coefficient of stage pressure rise lag or compressor flow relaxation time
$(\bar{\tau}_c)_i, (\tau_c)_i$	Dimensional and non-dimensional stage torque
$\tau_{c0}, \tau_{c1}, \tau_{c2}, \tau_{c3}$	Compressor torque characteristic coefficients
γ	Blade stagger angle
μ, λ	Inertia parameters
μ	Dynamic viscosity of lubricant in journal bearing
$\tilde{\phi}$	Velocity potential
$\tilde{\phi}'$	Velocity potential disturbance
$\bar{\phi}$	Relative change in the axial flow coefficient
$[\bar{\phi}]_{max}$	Maximum amplitude of the relative change in the axial flow coefficient
Ψ	Compressor total to static pressure rise coefficient
$\psi_c', \Psi_{c,ss}$	Axisymmetric compressor pressure-rise characteristic
ψ_c	Transformed compressor pressure rise characteristic $(\psi_c = \psi_c'/H)$
ψ_{c0}	Shut-off value of the compressor pressure rise characteristic (ψ_c')
ψ_{cf}	Fouling sensitivity coefficient
$\bar{\psi}_c^c, \bar{\psi}_c^{cs}, \bar{\psi}_c^c$	Cartesian expression of the averaged, sine and cosine moments of ψ_c
γ	Throttle coefficient, ratio of specific heat constants
Γ	Phase angle

η^*	Phase angle of the amplitudes of disturbed flow coefficients
$\eta_c, \eta_t, \eta_{comb}$	Compressor isentropic efficiency, turbine isentropic efficiency, combustion efficiency
ω, Ω	Shaft rotational speed
j	Complex number $(\sqrt{-1})$
χ	Aerodynamic-Rotordynamic coupling
λ_{tu}	Turning force scaling factor
λ_{pr}	Pressure force scaling factor
λ_{un}	Unsteady momentum storage

Suffixes

0	Entrance of inlet guide vane station
1	Compressor inlet station
E	Compressor exit station
S	Plenum station
T	Entrance of the inlet duct station
$[.]_\eta$	Derivative with respect to η
$[.]_\theta$	Derivative with respect to θ
$[.]_\xi$	Derivative with respect to ξ
$[.]_i^R, [.]_i^L$	Right or left parameter vector or matrix with regards to a particular i-th location
$[.]_y$	Acting along the y-axis
$[.]_x$	Acting along the x-axis

LIST OF ABBREVIATIONS

1D	One Dimension
1X	One times the nominal rotational speed or frequency
0.5X	0.5 times the nominal rotational speed or frequency
2D	Two Dimension
AR	Aspect Ratio
ASHRAE	American Society of Heating, Refrigerating and Air-Conditioning Engineers
CN, PCN	Corrected speed lines
CS	Control Surface
CV	Control Volume
CW	Compressor Work
DM	Diagnostic Method
EPA	Efficiency Particulate Air filter
ETA	Isentropic Efficiency
EW	Expansion Work
FP	Fouling Parameter
GE	General Electric
GPA	Gas Path Analysis
HEPA	High-Efficiency Particulate Air filter
HI	Heat Input
HOT	Higher Order Terms
IGV	Inlet Guide Vane
ISO	International Organization for Standardization
LHV	Lower Heating Value of fuel
LGPA	Linear Gas Path Analysis
MERV	Minimum Efficiency Reporting Value
NDMF	Non-Dimensional Mass Flow
NGPA	Non-linear Gas Path Analysis
OEM	Original Equipment Manufacturer
PR	Pressure Ratio
PS	Pressure Side (concave side of the blade)
SF	Scale Factor

SFC	Specific Fuel Consumption
SS	Suction Side (convex side of the blade)
SW	Specific Work
ULPA	Ultra-Low Penetration Air filter

LIST OF PUBLICATIONS

Conferences

- Jombo, G., Pilidis, P., Sampath, S. & Mba, D. (2015). "A Fatigue Life Assessment Methodology for Rolling-Element Bearing Under Irregular Loading". Proceedings of the Twelfth International Conference on Condition Monitoring and Machinery Failure Prevention Technologies, 9-11 June, 2015, Oxford, UK.

- Jombo, G., Sampath, S. & Gray, I. (2017). “Diagnostics of Gas Turbine Systems Using Gas Path Analysis and Rotordynamic Response Approach". Proceedings of the 23rd International Symposium on Air Breathing Engines (ISABE), 3-8 September, 2017, Manchester, UK.

Journals

- Jombo, G., Jiri, P., Sampath, S. & Mba, D. (2017). "Influence of Fouling on Compressor Dynamics: Experimental and Modeling Approach". ASME J. Eng. Gas Turbines Power. 140(3):032603-032603-7

1 INTRODUCTION

1.1 Background and Motivation

Gas turbine technology has drastically evolved during the past decades, with higher turbine entry temperature, 3D twisted compressor blade design, innovative approaches to reducing emissions such as the dry low NOx combustor technology, advanced cooling systems for components such as nozzles, blades and transition pieces, the use of advanced and exotic materials, etc. (Zachary, 2008). With these advances in technology, it is not surprising that the gas turbine has become the prime mover of choice for both power generation and mechanical drive applications.

However, these advances have resulted in increased complexities with regards managing engine availability and component life (Boyce and Latcovich, 2002; Meher-homji and Cullen, 1992).

In addition, the technological advances in the axial compressor design which include 3D twisted blades, results in a compressor with fewer and thinner blades with higher loading and clearances per stage; this compressor blade design, as compared with the NACA 65 compressor blade, leaves the compressor operating at a narrower surge margin, creating a challenge in managing the compressor's surge margin especially when degraded (Boyce, 2012).

Therefore, it becomes necessary for the gas turbine operator to be able to detect and correct damaging conditions quickly and efficiently.

From literature, several techniques for the condition monitoring of gas turbines are: gas path analysis, vibration analysis, oil analysis, optical pyrometry, combustor acoustics monitoring, exhaust gas debris monitoring, etc. (Boyce and Latcovich, 2002). The conventional approach when considering gas turbine condition monitoring is centred mostly on the independent application of each technique to diagnose a particular fault set. This research departs from this conventional approach by investigating the integration of different condition monitoring techniques for gas turbine condition monitoring.

Integrated condition monitoring in a nutshell involves the combined use of a variety of techniques such as gas path analysis, vibration analysis, oil analysis, optical pyrometry, combustor acoustics monitoring, exhaust gas debris monitoring, etc. to monitor any significant change in the gas turbine engine and operating parameters which is indicative of a developing fault, provides one of such means to address the issue of engine availability improvement and limiting component degradation (Boyce and Latcovich, 2002; Li, 2002; Meher-homji and Cullen, 1992) .

The benefits of integrating different condition monitoring techniques for gas turbine health monitoring would provide increased confidence in fault diagnosis and also help in localizing the root cause of complex fault conditions. Meher-Homji and Cullen (1992) reports three cases, the overhaul of an offshore gas turbine compressor train, industrial gas turbine exhibiting bearing sub-harmonic resonance and random vibration trips on a centrifugal turbocharger, where performance and vibration data where used to effectively diagnose and localize the faults. Meher-Homji and Focke (1985) investigated the use of vibration and performance monitoring for the reduction of gas turbine blading problems. Biliotti et al. (2015) looked at the use of vibration and performance monitoring to study the rotating stall behaviour of centrifugal compressors in order to improve their minimum stable flow limit.

Gas path analysis and vibration response analysis are two well established condition monitoring techniques for gas turbine system diagnostics; thus, this research would address their integration to monitor the effect of fouling in a gas turbine compressor.

Compressor fouling is typically a gas path component fault, involving the deposition of airborne particles or contaminants on the compressor blades, stators and annulus walls (Igie et al., 2014). Compressor fouling is estimated to account for 70% - 85% of the gas turbine performance degradation (Meher-Homji and Bromley, 2004).

Since gas path analysis address faults that are of aero-thermal origin and vibration diagnostics addresses faults that are of rotordynamic origin, to

effectively integrate both techniques to monitor the effect of fouling in the compressor, it becomes a question of understanding the interaction between the aerodynamic and rotordynamic domain in the compressor caused by fouling.

1.2 Previous Works

1.2.1 Aerodynamic and Rotordynamic Domain Interaction in Compressors

Alford (1965) studied the aerodynamic excitations in axial compressors and turbine caused by the variation of the circumferential pressure with displacement in labyrinth seals and also the variation in the circumferential pressure in axial compressors due to blade tip clearance asymmetry. Alford (1965) proposed two criteria which are the seal-deflection criteria and torque-deflection criteria, to ensure stable design of rotors.

Alford (1965) while working on labyrinth seals, proposed that the circumferential pressure distribution around the labyrinth seal annulus varied linearly with the radial displacement of the rotor in the labyrinth seal annulus. He extended this findings to axial compressors, and showed that a 1% increase in blade tip clearance results in a 1% reduction in compressor efficiency (Alford, 1965).

Alford (1965) also showed that the aerodynamic excitation or whirl producing force was due to the tangential component of aerodynamic force. To eliminate the aerodynamic excitation effects, Alford (1965) proposed providing sufficient stiffness to the rotor and bearings.

Weigl (1997) in his experiments on the active control of rotating stall and surge in a single transonic stage axial compressor, reported an interaction between the aerodynamic domain and rotordynamic domain in an axial compressor. He observed that, whenever the rotor rotational frequency coincided with the frequency of a rotating stall mode, it increased the energy content of the rotating stall as shown in Figure 1-2. He also observed, when comparing the power spectrum of the baseline healthy compressor in Figure 1-1 to the power spectrum of a compressor running on a deteriorated journal bearing in Figure 1-3, there

was a marked increase in the energy content at the frequency of the first stall mode in the deteriorated bearing compressor power spectrum.

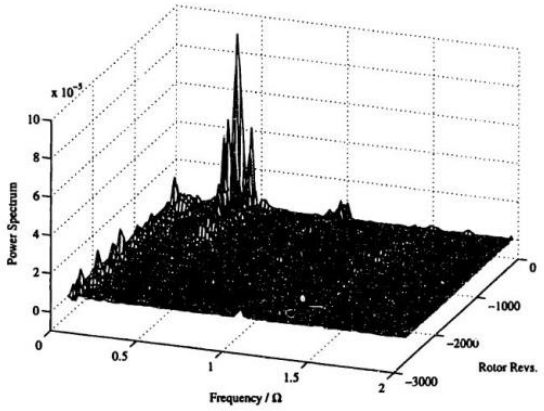

Figure 1-1 Stall power spectrum of Weigl baseline case (Source: Weigl, 1997)

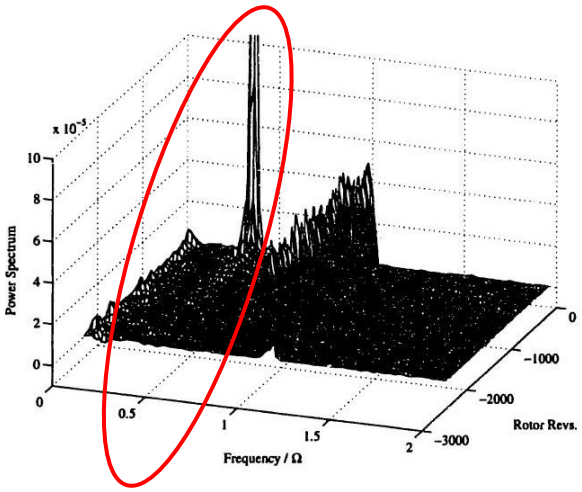

Figure 1-2 Stall power spectrum when rotor rotational frequency equals a rotating stall mode frequency (Source: Weigl, 1997)

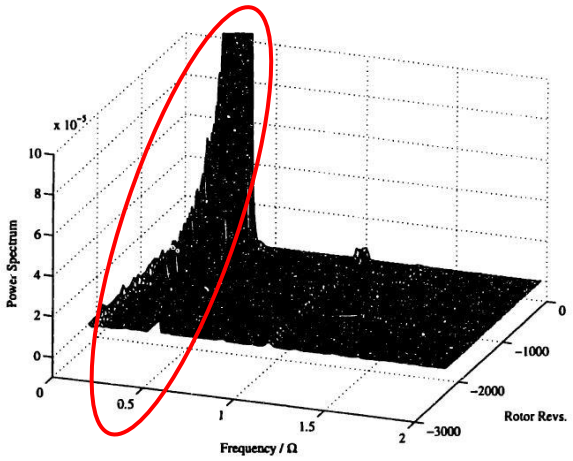

Figure 1-3 Stall power spectrum of compressor when running on deteriorated journal bearing (Source: Weigl, 1997)

Tryfonidis et al. (1995) in their work on the pre-stall behaviour of high speed compressors, observed a coupling between the aerodynamic and rotordynamic domain. They noted that the frequency of the first two stall mode was strongly related to the compressor rotational speed.

In their experiment, when the compressor was rotating at 70% of its nominal speed, the first two rotating stall mode where excited (0.5X and 1X) as shown in Figure 1-4; when the compressor was rotating at 100% of its nominal speed, only the second stall mode was excited (1X), also shown in Figure 1-4.

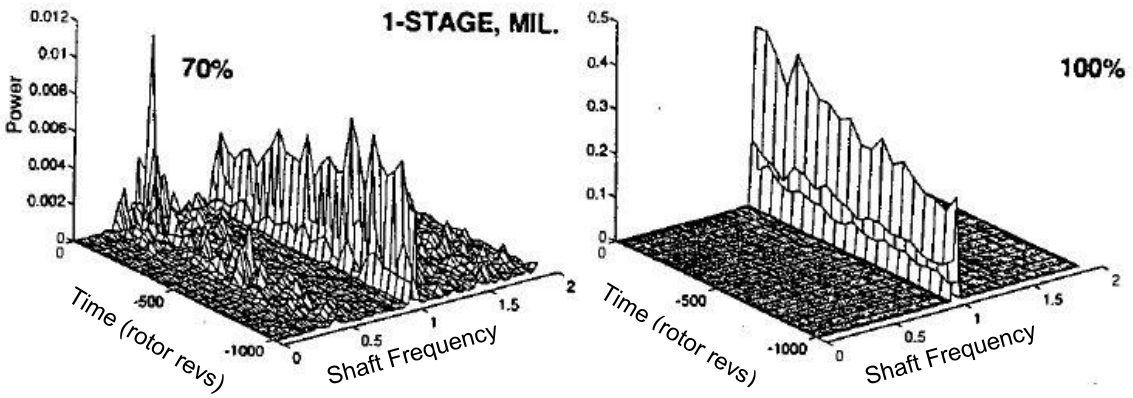

Figure 1-4 Influence of compressor rotating speed on the stall mode (Source: Tryfonidis et al., 1995)

1.2.1.1.1 Integrated Diagnostics of Mechanical and Performance Faults in Compressors

Loukis et al.(1991) investigated the possibility of detecting the presence of the following blade faults: rotor fouling, fouling of individual rotor blade, twisting of individual blade and staggering of rotor blade using an integrated approach involving unsteady pressure measurements, casing vibration, shaft displacement measurements and acoustic field measurements. They concluded that the data from the pressure, vibration and acoustic probes were more promising for diagnostic purposes. They went on to apply a differencing technique (i.e. amplitude difference of the logarithm of the spectra of the healthy engine and faulty engine) to the test data from each transducer, leading them to propose a spectra signature for each fault type. They further tested the use of acoustic imagining techniques such as acoustic power ceptrum, acoustic power spectrum and back propagation imaging to locate or localise the source of a fault type.

Mathioudakis and Tsalavaoutas (1995) experimented on the influence of mechanical alterations such as obstructions at the compressor inlet and diffuser passage, tip clearance variation and fouling on the performance of a centrifugal compressor. The intent of their research was to determine the correlation between these various faults and the compressor performance for use in compressor health diagnostics. Based on their experimental data, they proposed two approaches; the first technique involves analysing the changes in the coefficients of a second order polynomial equation representing the curve fit for the modified generalised compressor pressure rise characteristics for each fault. This approach is based on the fact that each mechanical fault modifies the baseline compressor pressure rise characteristic differently. Although this approach did not provide much insight in differentiating the different faults investigated, their second approach, the use of the diagnostic plane, proved more successful. The diagnostic plane which is a 2D plot of the variation in pressure rise coefficient against variation in the mass flow coefficient between a chosen operating point in the baseline compressor and the faulty compressor. From this analysis, they found out that for a particular compressor, each fault when plotted on the diagnostic plane has a distinctive slope, which could be used to identify

each fault. Also, they noted that the increase in the amplitude of each plot was indicative of worsening condition for that particular fault.

Mohammed and Mba (2015) investigate the effect of compressor fouling and labyrinth seal deterioration on the performance and vibration synchronous response of a centrifugal compressor. They modelled the effect of fouling as an unbalance and cross-coupled stiffness and the worn seal using a one-control-volume model by Childs (1993); they further validated their simulation model with field data. They showed that the forced response of the centrifugal compressor depended on three factors, which are: the amount of unbalance, the location of the unbalance and the amount of clearance on the labyrinth seal. They also recorded deterioration in the performance of the centrifugal compressor due to the effect of fouling of the impeller and wear on the labyrinth seal.

Kyriazis et al. (2006) have applied probabilistic neural network and Bayesian believe network to classify different types of blade faults in compressors from the integrated use of fault data from vibration, pressure and acoustic sensors.

Loukis et al. (1991), sequel to their work on determining the reduced characteristic fault signature for different types of compressor blade faults (Loukis et al., 1991), have applied Euclidean distance and normalized cross-correlation coefficient to the reduced characteristic fault signature to develop an automated diagnostic system for the integrated use of internal pressure, casing vibration and acoustic measurements to diagnose different compressor blade faults e.g. fouling, mistuned rotor blade fault and mistuned stator blade fault.

Aretakis and Mathioudakis (1998) have applied the statistical pattern recognition techniques of Euclidean distance, cross correlation coefficient and optimal directions to diagnose the following faults: inlet obstruction, tip clearance increase, fouling & diffuser passage obstruction in centrifugal compressors through the integration of fault data from vibration and acoustic sensors.

To summarise the state of the art of this research, the idea of an integrated condition monitoring approach for gas turbine has been the subject of the work of several investigators, such as: Loukis et al. (1991), Mathioudakis and

Tsalavaoutas (1995), Mohammed and Mba (2015), Kyriazis et al. (2006) and Aretakis and Mathioudakis (1998). They have all applied different approaches mostly based on statistical pattern recognition, machine learning and vibration response for the integrated diagnosis of different gas turbine faults.

As the previous works have been based solely on the determination of fault signature based on statistical analysis, vibration response or developing neural network models from the different faulty data sources, there is a gap in understanding of the underlying physical phenomena governing such interactions.

This work deviates from the previous approaches by adopting a first principle physic modelling methodology based on insights by the works of Alford (1965), Weigl (1997) and Tryfonidis et al. (1995) on the existence of a relationship between the aerodynamic and rotordynamic domain in a gas turbine compressor.

1.3 Approach

Previous works on the effect of compressor fouling on the gas turbine operation has been on estimating its impact on the gas turbine's performance in terms of reduction in thermal efficiency and output power.

Aker and Saravanamuttoo (1989) used a stage stacking compressor model with an assumption of a linear fouling degradation in the compressor to formulate an approach to estimate the performance deterioration of a gas turbine due to compressor fouling. Rodriguez et al. (2013) has further improved on the work by Aker and Saravanamuttoo (1989) by including the effect of stage temperature rise coefficient deterioration to the Aker model. Melino et al. (2010) and Yang and Xu (2014) have also applied the stage stacking compressor model to investigate the effect of compressor fouling on the gas turbine performance.

Another methodology used by other investigators to determine the effect of fouling on a gas turbine operation involves the development of correlations to characterizing the susceptibility and sensitivity of the gas turbine compressor to fouling.

Tarabin et al. (1998) developed a susceptibility index to characterize the performance deterioration of a compressor due to fouling based on the principle for the entrainment efficiency of a cylinder due to inertia deposition. Song et al. (2003) has improved on the work by Tarabin (1998) to better account for the flow conditions around an actual blade. Seddigh and Saravanamuttoo (1991) have developed a fouling index to access the susceptibility of a compressor to fouling.

Although the above mentioned approaches are useful in determining the impact of compressor fouling on the gas turbine performance, they are limited in the sense that they are not capable of being used to access the interaction between the aerodynamic and rotordynamic domain in a fouled gas turbine compressor.

In this work, a Greitzer-type compression system model is applied to predict the flow field dynamics of the fouled compressor.

Greitzer (1976) first developed a nonlinear lumped parameter model for axial compressors capable of predicting the compressor dynamics during a surge cycle. Hansen et al. (1981) further proved that this model is also applicable to centrifugal compressor. Further improvements to the model by Moore and Greitzer (1986) have resulted in the model being capable of describing the operation of a compressor in surge and rotating stall and also possible coupling between the two instabilities. Fink et al. (1992) have added rotor dynamic effect to the Greitzer model to account for rotor speed variations. Macdougal and Elder (1983) have also expanded the Greitzer model by introducing the effect of a compressible inlet flow. Spakovszky (2000b) has further developed the model into a two-dimensional, compressible flow model suitable for centrifugal and axial compressors.

In this work, the Moore-Greitzer (1986) model variant is adopted as neither the effect of rotor speed variation or compressible inlet flow is considered in this work.

Figure 1-5 summarises the methodology applied in this work.

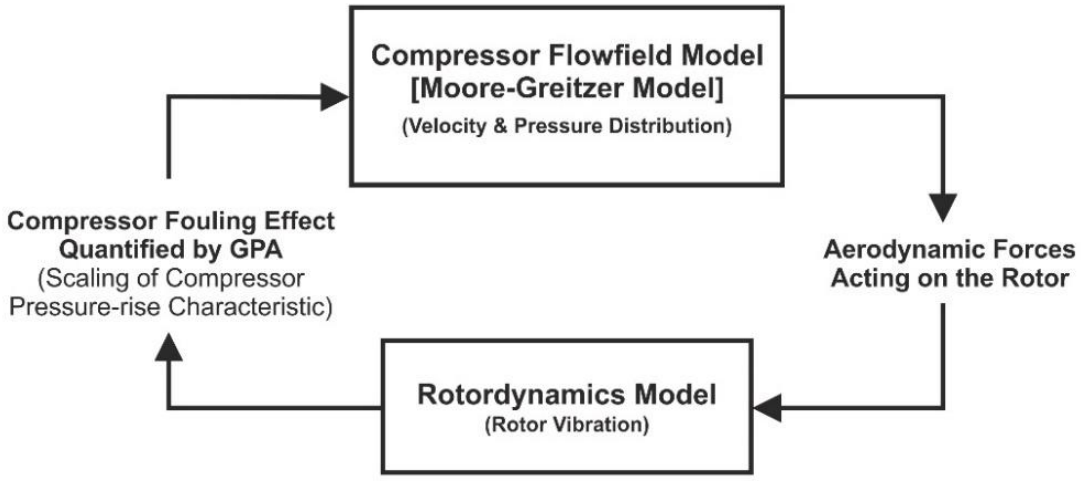

Figure 1-5 Schematic of the approach to study the interaction between the aerodynamic and rotordynamic domain in the compressor due to fouling

Firstly, gas path analysis is used to quantify the aero-thermal degradation of the compressor (reductions of massflow, isentropic efficiency & pressure ratio); together with the compressor maps, compressor geometry and the Moore-Greitzer compressor flow field model, the resulting flow field parameters, instantaneous pressure & axial flow coefficient in the compressor are predicted.

The Moore-Greitzer compression system flow model, which is described in detail in Chapter 2 is shown in Figure 1-6. The Moore-Greitzer model has been used by several investigators to successfully model and control stall, surge and rotordynamic instabilities in compressors (Fink, Cumpsty and Greitzer, 1992; Gravdahl and Egeland, 1997a, 1997b; Yoon, Lin and Allaire, 2013).

Based on the compressor flow field parameters and a momentum based aerodynamic force model, detailed in Chapter 3, the induced aerodynamic force due to fouling in the compressor is predicted. This force, then acts as a forcing function in a compressor rotordynamic model, generating the vibration response.

The detailed model development for the compression system model, aerodynamic force model and rotordynamic model is presented in Chapter 2 and Chapter 3 and the model validation results are presented in Chapter 5.

To summarise the overall methodology of this project, firstly, a virtual thermodynamic model of a gas turbine engine similar to LM2500+ is created with TurboMatch, a gas turbine performance modelling tool. The accuracy of the performance model is validated by comparing its performance parameters against that published in open literature by the engine manufacturer. The engine performance model is essential to performing gas path analysis. The creation and validation of the engine performance model is provided in Chapter 4.

Gas path analysis is used to quantify the extent of degradation in the gas turbine model and also to generate the compressor pressure characteristics when the gas turbine compressor is clean or fouled. Pythia is used to perform the gas path analysis and also implant faults in the engine performance model. Fouling degradation is implanted in the virtual engine by a reduction of the pressure ratio and massflow within the range of 1% - 5% in steps of 1% while keeping the reduction in isentropic efficiency constant at 1%. The fouling performance parameter simulation range is based on information in open literature (Li, 2016). The extent of the implanted fouling degradation is then determined with gas path analysis. There are two broad types of gas path analysis, which are linear and non-linear analysis. Section 4.2 in Chapter 4 provides an overview between both approaches. In this work the non-linear gas path analysis is used.

The degradation scaling factors from the gas path analysis for pressure ratio, mass flow and isentropic efficiency is uses to generated the rescaled compressor pressure characteristics.

The scaled pressure ratio characteristic is essential for the Moore-Greitzer model solution. The Moore-Greitzer compression system model is a lumped parameter model consisting of an inlet duct, a compressor, outlet duct and a plenum. The development and validation of the Moore-Greitzer model is performed in Chapter 2 and Chapter 5. The Moore-Greitzer model is used to determine the amplitudes of the disturbed flow coefficient.

The next part of the methodology involves the estimation of the aerodynamic forces due to the disturbed flow coefficient. The aerodynamic force model is based on the work by Al-Nahwi (2000) and it consist of three force component

which are turning force, pressure force and unsteady momentum storage force. The development and validation of the aerodynamic force is presented in Chapter 3 and Chapter 5 respectively.

The final bit of the methodology involves the determination of the rotordynamic response of the compressor rotor due to the aerodynamic force. A 2D rotordynamic model is developed based on the transfer matrix approach. The development and validation of the rotordynamic model is detailed in Chapter 3 and Chapter 5 respectively. Chapter 5 also presents result for the rotordynamic response of the compressor rotor under different conditions of fouling.

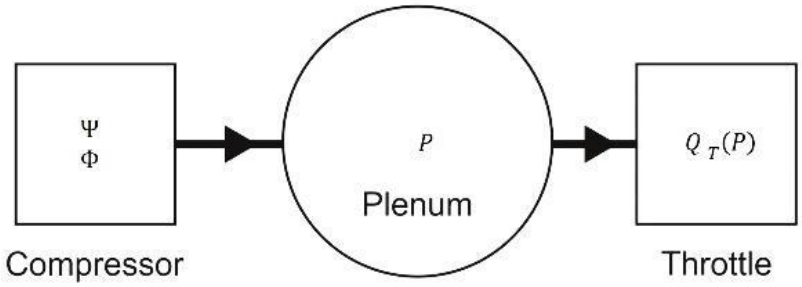

Figure 1-6 Schematic of the Moore-Greitzer compression system model

1.4 Modelling Assumptions and Limitations

1) A modification to the generic Moore-Greitzer model applied in this work, for the case of fouling in a gas turbine compressor is based on the premise that as a gas turbine compressor gets fouled, its pressure map gets modified or scaled; this compressor pressure map scaling effect is introduced to the Moore-Greitzer model by allowing the compressor pressure rise characteristic to scale linearly with the relative reduction in massflow due to fouling. This linear scaling assumption is based on the work by Grewal (1988). Nieuwenhuizen (2008) has performed a sensitivity analysis on the linearized Moore-Greitzer model and has reported an accuracy of about 7% of the linear model in predicting the compression system parameters.

2) The compression system model is based on the presence of an incompressible flow or low Mach number compressible flow in the compressor inlet.
3) The rotordynamic model is based on a 2D Euler-Bernoulli beam with consideration for shaft shear deflection.
4) The aerodynamic force model is developed based on the presence of a non-uniformity in the compressor flow field, as such, it's not suitable for the prediction of the aerodynamic force without the presence of degradation in the gas turbine.

- Aim

The aim of this research is to demonstrate the interaction between the aerodynamic and rotordynamic domain in a gas turbine compressor due to fouling, with the intent of understanding parameter dependencies for integrated condition monitoring involving gas path analysis and vibration response.

1.5 Research Objectives

In order to study the interaction between the aerodynamic and rotordynamic domain in the gas turbine compressor due to fouling, the following objectives where outlined:

1) Develop and validate a gas turbine performance model in TurboMatch (Cranfield University gas turbine performance analysis software), implant different cases of fouling degradation in the compressor and quantify the amount of degradation with gas path analysis using Pythia (Cranfield University gas turbine diagnostic software).
2) Develop a compression system model for the pre***diction of the modified flow field parameters (i.e. pressure and disturbed flow coefficient) in the compressor due to fouling.
3) Develop and validate an aerodynamic force model for the prediction of the modified aerodynamic forces in the compressor due to fouling.
4) Develop and validate a rotordynamic model for the forced response analysis of the compressor rotor system due to aerodynamic forces.

5) Investigate the possibility of integrating GPA and vibration response for fouling monitoring in a compressor by analysing the interaction between the aerodynamic and rotordynamic domain in a fouled compressor.

1.6 Contribution to Knowledge

This research makes the following contributions to knowledge:

1) A novel modelling approach involving the interaction between a compression system model, aerodynamic force model, rotordynamic model and gas turbine degradation model to study the aerodynamic-rotordynamic interaction in a fouled compressor.
2) This research showed that as the rate of fouling in the compressor increases there is a corresponding increase in the vibration amplitude at the first fundamental frequency of the compressor.
3) This research has demonstrated, with the aid of externally provided experimental data, the application of a Greitzer-type compression system model to predict the inception of unstable operations in a compressor due to fouling.
4) A new application for the non-dimensional pressure scale factor (λ_{pr}) is identified for accessing the effect of changing blade aspect ratio on a blade-row aerodynamic performance.

1.7 Thesis Structure

This thesis is structured as follows:

Chapter 1: Introduction

This chapter presents the motivation for this research. It also discusses the previous works by other investigators in the areas such as the interaction between the aerodynamic and rotordynamic domains in the compressor and also integrated diagnostic for compressors using performance and vibration diagnostics amongst other available techniques. It further gives an overview of the proposed methodology adopted in this research, the research aim, objectives and the contribution to knowledge. It closes with a thesis structure breakdown.

Chapter 2: Compression System Modelling

This chapter presents the development of the Moore-Greitzer compression system model used for the prediction of the disturbed flow field parameters such as the disturbed flow and pressure rise coefficient due to compressor fouling. In the Moore-Greitzer model, the compression system consists of a compressor operating between an intake and exit duct while discharging into a plenum with flow controlled by a throttle. The general equations for flow disturbance in the compression system is developed from which a closed form solution is determined suitable for describing the flow field parameters in a fouled compressor.

Chapter 3: Rotordynamic Model Development

This chapter presents the development of both the aerodynamic force model based on the Work by Al-Nahwi (2000) and the 2D transfer matrix rotordynamic model for the investigation of the forced response of the compressor rotor system due to aerodynamic forces. The total aerodynamic force in a compressor consist of the turning force due to the circumferential distribution of the flow coefficient, the pressure force due to pressure difference between stages and the unsteady momentum storage force in stage. As only steady state conditions are considered in this work, the unsteady momentum storage force is ignored in the total aerodynamic force expression presented finally in this chapter. Finally, the building blocks of a generalized 2D transfer matrix rotordynamic model is explained. In the 2D transfer matrix rotordynamic model, the rotor is considered as a series of interconnected field and point matrixes, where a field represents a massless shaft and a point could represent a bearing, shaft discontinuity, disc, coupling, impeller, etc. Free and forced response solution to the rotordynamic model is presented.

Chapter 4: Gas Turbine Fouling Degradation

This chapter begins by discussing the causes, effects and control of fouling in gas turbine compressors. It also presents the development of the LM2500+ gas turbine engine model in TurboMatch and the generation of the degraded

compressor pressure maps. Finally, Pythia has been used to both implant several cases of fouling degradation in the LM2500+ compressor and also to perform linear and non-linear gas path analysis on the fouled compressor operating data.

Chapter 5: Results for the Aerodynamic-Rotordynamic Model Integration

This chapter presents the results for the validation of the aerodynamic force model based on the work by Al-Nahwi (2000) on the MIT 3 stage experimental compressor rig and rotordynamic model based on the Kikuchi(1970) rotor experimental rotordynamic data. Finally, by integrating the aerodynamic and rotordynamic models for different fouling conditions and operating points in a fouled compressor, it is observed that, as the rate of fouling increases, typified by a decrease in compressor massflow, isentropic efficiency and pressure ratio, there is a corresponding increase in the vibration amplitude at the compressor rotor first fundamental frequency.

Chapter 6: Application of a Moore-Greitzer Type Model to a Fouling Experiment in a Small Jet Engine (TJ100)

This chapter demonstrates the application of a Moore-Greitzer type model for the prediction of the inception of unstable operations in a fouled TJ100 centrifugal compressor. The experimental data for model validation has been provided by an external collaborator, Lt. Col. Jiri Pecinka from the Engine Operation Group, Department of Air Force and Aircraft Technology, University of Defence, Czech Republic. The experimental setup is such that, fouling is simulated in the compressor by painting the centrifugal impeller blade with a micro glass ball and paint mixture. The roughness of the resulting texture is 6μm. The fouled gas turbine is test across its operational envelope and it actual frequency of plenum disturbance, and averaged flow coefficient, at the inception of unstable operations show is compared against the prediction from Greitzer model; the results show an agreement with the experimental data for the clean and fouled TJ100 engine.

Chapter 7: Conclusions & Future Work

This chapter gives an overview of the conducted research and areas for further model improvements such as the modification of the fundamental Moore-Greitzer compression system model to account for non-linearity, an extension to the rotordynamic analysis to include non-synchronous response of the rotor to an aerodynamic excitation and application of the Greitzer type model for the prediction of the flow and pressure rise coefficient at the inlet of the compressor when fouled.

2 COMPRESSION SYSTEM MODELLING

2.1 Introduction

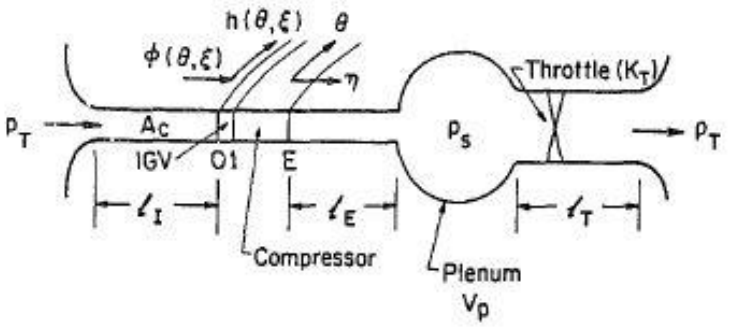

Figure 2-1 Detailed Moore-Greitzer compression system model with co-ordinate frame of reference (Source: Greitzer and Moore, 1986)

The mathematical model used to describe the flow dynamics in the compressor is formulated in this chapter. The model formulation is based on the work by Moore and Greitzer (1986), an approach that has been used by many investigators to successfully model and control stall, surge and rotordynamic instabilities in both axial and centrifugal compressors (Al-Nahwi, Paduano and Nayfeh, 2003; Fink, Cumpsty and Greitzer, 1992; Gravdahl and Egeland, 1997a; Yoon, Lin and Allaire, 2013).

The Moore-Greitzer model as shown in Figure 2-1, is a lumped parameter model of a compression system consisting of: an inlet duct, inlet guide vane (IGV), compressor, exit duct & guide vane, plenum volume and throttle (Greitzer and Moore, 1986).

2.2 Governing Equations of a General Disturbance in a Compression System

The governing equations of a general disturbance in a compression system is used to predict the changes in the pressure rise coefficient, average flow coefficient and the disturbed values of flow coefficient due to a generalised disturbance (e.g. surge, stall, tip clearance effect, fouling, etc.). The general disturbance can take the form of both temporal and spatial variations in the flow coefficient.

2.2.1 Non-dimensionalization of System Parameters

The non-dimensionalization scheme adopted by the Moore-Greitzer model for the system parameters are (Greitzer and Moore, 1986):

- Lengths: all lengths are non-dimensionalized by dividing with the mean compressor wheel radius, R.
  i. non-dimensional inlet duct length $l_I = L_I/R$
  ii. non-dimensional exit duct length $l_E = L_E/R$
- Time: expressed as radian of wheel travel ξ

$$\xi = Ut/R \qquad 2\text{-}1$$

  where U is the compressor wheel speed at the mean radius, t is time and R is the mean compressor wheel radius.
- Pressure: all pressures are non-dimensionalized by dividing with ρU^2. E.g. $P/(\rho U^2)$, where P is pressure, ρ is density and U is the compressor wheel speed at the mean radius.
- Velocity: all velocity values are non-dimensionalized by dividing with the compressor wheel speed at mean radius, U.
  i. Axial flow coefficient $\phi = C_x/U$, where C_x is axial flow velocity and U is the compressor wheel speed at the mean radius.
- Co-ordinate System: η represents the axial co-ordinate while θ represents the circumferential co-ordinate.

2.2.2 Inlet Flow Assumptions

The following assumptions have been shown to be valid for incompressible flows and low Mach number compressible flows in the axial compressor inlet (Moore, 1984; Yoon, Lin and Allaire, 2013):

1) The flow proceeding from upstream of the inlet duct, i.e. atmosphere, flowing through the inlet duct, to the entrance of the inlet guide vane (IGV), point '0' as shown in Figure 2-1, is assumed to be irrotational and inviscid.
2) There are generally two components of flow coefficients acting at the entrance of the IGV point '0': the first component is the axial flow coefficient ϕ acting in the η axis and the second is the circumferential flow coefficient, *h* acting in the

θ axis. The *h* component is only present when there is a disturbance in the axial flow coefficient (ϕ) i.e. temporal and spatial variation.

Thus,

$$\phi(\xi,\theta) = \Phi(\xi) + g(\xi,\theta)\ and\ h = h(\xi,\theta) \qquad 2\text{-}2$$

where g is the disturbed axial flow coefficient component and $\Phi(\xi)$ is the annulus averaged axial flow coefficient, defined as:

$$\Phi(\xi) = \frac{1}{2\pi}\int_0^{2\pi} \phi(\xi,\theta)d\theta \qquad 2\text{-}3$$

Based on continuity principle, the *g* component of ϕ must have a vanishing average and also due to the fact that no circulation should exist at the entrance of the IGV '0', *h* also should have a vanishing average.

Thus,

$$\int_0^{2\pi} g(\xi,\theta)d\theta = 0 \text{ and } \int_0^{2\pi} h(\xi,\theta)d\theta = 0 \qquad 2\text{-}4$$

2.2.3 Pressure Rise in the Compressor

The unsteady pressure rise in a single stage of compressor blade row (rotor and stator pair) can be modelled as (Moore, 1984):

$$\frac{\Delta P}{\frac{1}{2}\rho U^2} = F(\phi) - \tau\frac{d\phi}{dt} \qquad 2\text{-}5$$

where ΔP is the stage pressure rise, ϕ is the unsteady axial flow coefficient, $F(\phi)$ represents the axisymmetric pressure rise characteristic of a single stage and τ the coefficient of stage pressure rise lag due to fluid inertia in the stage passage, is defined as (Moore, 1984):

$$\tau = \frac{2l}{U\cos\gamma} \qquad 2\text{-}6$$

where l is the blade chord and γ is the blade stagger angle.

Assuming similar blade row stages, with N, number of blade row stages

$$\frac{P_E - P_1}{\frac{1}{2}\rho U^2} = \mathrm{N}F(\phi) - \tau N\frac{d\phi}{dt} \qquad 2\text{-}7$$

where P_E is the pressure at the exit of the compressor and P_1 is the pressure at the inlet of the compressor.

$\frac{d\phi}{dt}$ represents the unsteadiness of the flow in a rotor-stator passage and is expressed as:

$$\frac{d\phi}{\mathrm{dt}} = \left(\frac{d\phi}{\mathrm{dt}}\right)_{rotor} + \left(\frac{d\phi}{\mathrm{dt}}\right)_{stator} \quad \text{2-8}$$

From partial differential calculus, for a function such as this $\phi = \phi(\xi, \theta)$, then,

$$\frac{d\phi}{\mathrm{dt}} = \frac{\partial\phi}{\partial\xi}\frac{d\xi}{dt} + \frac{\partial\phi}{\partial\theta}\frac{d\theta}{dt} \quad \text{2-9}$$

Making use of $\xi = Ut/R$, $\theta = Ut/R$ and equation 2-9, and taking note that for the stator $\frac{d\theta}{dt} = 0$, then,

$$\left(\frac{d\phi}{\mathrm{dt}}\right)_{rotor} = \frac{U}{R}\left(\frac{\partial\phi}{\partial\xi} + \frac{\partial\phi}{\partial\theta}\right) \quad \text{2-10}$$

$$\left(\frac{d\phi}{\mathrm{dt}}\right)_{stator} = \frac{U}{R}\left(\frac{\partial\phi}{\partial\xi}\right) \quad \text{2-11}$$

Therefore,

$$\frac{d\phi}{\mathrm{dt}} = \frac{U}{R}\left(2\frac{\partial\phi}{\partial\xi} + \frac{\partial\phi}{\partial\theta}\right) \quad \text{2-12}$$

Substituting Equation 2-6 and 2-12 into Equation 2-7, and simplifying further,

$$\frac{P_E - P_1}{\rho U^2} = \mathrm{N}F(\phi) - \mu\frac{\partial\phi}{\partial\xi} - \lambda\frac{\partial\phi}{\partial\theta} \quad \text{2-13}$$

where μ and λ are inertia parameters, defined as:

$$\mu = \frac{2Nl}{R\cos\gamma} \quad \text{2-14}$$

$$\lambda = \frac{Nl}{R\cos\gamma} \quad \text{2-15}$$

2.2.4 Pressure Rise in the Inlet Duct and Guide Vanes

1) Inlet Guide Vane (IGV)

The pressure rise across the inlet guide vane, from point '0' to point '1' as shown in Figure 2-1, is expressed as (Greitzer and Moore, 1986):

$$\frac{P_1 - P_0}{\rho U^2} = \frac{1}{2} K_G h^2 \qquad 2\text{-}16$$

where K_G is the IGV pressure recovery coefficient. K_G = 1, for a lossless IGV, otherwise, $K_G < 1$.

2) Inlet Duct

Since the flow upstream of the IGV is assumed irrotational, a velocity potential $\tilde{\phi}$ exit, whose derivatives describes the flow velocity everywhere in the inlet duct.

Thus at the entrance of the IGV, point '0',

$$\left(\tilde{\phi}_\eta\right)_0 = \Phi(\xi) + g(\xi,\theta) \; and \; \left(\tilde{\phi}_\theta\right)_0 = h(\xi,\theta) \qquad 2\text{-}17$$

where the partial derivatives of $\tilde{\phi}$ with respect to η and θ are denoted by subscripts.

The pressure rise across the inlet duct is defined by applying Bernoulli's equation for unsteady flow as (Greitzer and Moore, 1986):

$$\frac{P_T - P_0}{\rho U^2} = \frac{1}{2}(\phi^2 + h^2) + \left(\tilde{\phi}_\xi\right)_0 \qquad 2\text{-}18$$

For a straight duct with a non-dimensional length l_I, the velocity potential $\tilde{\phi}$ can be represented as:

$$\tilde{\phi} = (\eta + l_I)\Phi(\xi) + \tilde{\phi}'(\xi,\theta) \qquad 2\text{-}19$$

where $\tilde{\phi}'(\xi,\theta)$ is the velocity potential disturbance, and satisfies the following conditions:

$$\tilde{\phi}'\big|_{\eta=-l_I} = 0 \,, \left(\tilde{\phi}'_\eta\right)_0 = g(\xi,\theta) \; and \; \left(\tilde{\phi}'_\theta\right)_0 = h(\xi,\theta) \qquad 2\text{-}20$$

From Equation 2-19,

$$\left(\tilde{\phi}_\xi\right)_0 = l_I \frac{d\Phi}{d\xi} + \left(\tilde{\phi}'_\xi\right)_0 \qquad 2\text{-}21$$

Substituting Equation 2-21 into Equation 2-18,

$$\frac{P_T - P_0}{\rho U^2} = \frac{1}{2}(\phi^2 + h^2) + l_I \frac{d\Phi}{d\xi} + \left(\tilde{\phi}'_\xi\right)_0 \qquad 2\text{-}22$$

where P_T is the pressure at the entrance of the inlet duct.

2.2.5 Pressure Rise in the Exit Duct and Guide Vanes

The flow downstream of compressor is complex and rotational; but if the pressure in the exit duct is assumed, to differ only slightly from the pressure in the plenum, the pressure rise coefficient would satisfy the Laplace's equation, and can then be represented as:

$$\frac{P_s - P_E}{\rho U^2} = -l_E \frac{d\Phi}{d\xi} - (m-1)\left(\tilde{\phi}'_\xi\right)_0 \qquad 2\text{-}23$$

where P_s is the plenum pressure, P_E is the compressor exit pressure, l_E non-dimensional exit duct length, m = 1 for a short or sudden expansion duct or m = 2 for a long duct.

2.2.6 Overall Pressure Rise at End of Compressor Exit Duct

The overall pressure rise at the end of the exit duct is gotten by combining the pressure rise in the inlet guide duct, inlet guide vane, compressor, exit duct and guide vanes, i.e. Equations 2-22, 2-16, 2-13 and 2-23.

Thus,

$$\frac{P_s - P_T}{\rho U^2} = -\left[\frac{P_T - P_0}{\rho U^2}\right] + \frac{P_1 - P_0}{\rho U^2} + \frac{P_E - P_1}{\rho U^2} + \frac{P_s - P_E}{\rho U^2}$$

$$\begin{aligned}\frac{P_s - P_T}{\rho U^2} = &-\left[\frac{1}{2}(\phi^2 + h^2) + l_I \frac{d\Phi}{d\xi} + \left(\tilde{\phi}'_\xi\right)_0\right] + \left[\frac{1}{2}K_G h^2\right] \\ &+ \left[\mathrm{N}F(\phi) - \mu\frac{\partial\phi}{\partial\xi} - \lambda\frac{\partial\phi}{\partial\theta}\right] + \left[-l_E \frac{d\Phi}{d\xi} - (m-1)\left(\tilde{\phi}'_\xi\right)_0\right]\end{aligned} \qquad 2\text{-}24$$

Recalling Equations 2-2 and 2-20, thus,

$$\phi(\xi,\theta) = \Phi(\xi) + g(\xi,\theta) \;\; and \;\; \left(\tilde{\phi}'_\eta\right)_0 = g(\xi,\theta) \qquad 2\text{-}25$$

Therefore,

$$\frac{\partial \phi}{\partial \xi} = \frac{\mathrm{d}\Phi}{d\xi} + \left(\tilde{\phi}'_{\xi\eta}\right)_0 \qquad 2\text{-}26$$

$$\frac{\partial \phi}{\partial \theta} = \left(\tilde{\phi}'_{\theta\eta}\right)_0 \qquad 2\text{-}27$$

Substituting Equations 2-26 and 2-27 into Equation 2-24 and simplifying,

$$\frac{P_s - P_T}{\rho U^2} = \left[\mathrm{N}F(\phi) - \frac{1}{2}\phi^2\right] - [l_I + \mu + l_E]\frac{d\Phi}{d\xi} - m\left(\tilde{\phi}'_{\xi}\right)_0 - \mu\left(\tilde{\phi}'_{\xi\eta}\right)_0 - \lambda\left(\tilde{\phi}'_{\theta\eta}\right)_0 - \frac{1}{2}[1 - K_G]h^2 \qquad 2\text{-}28$$

But the total-to-static pressure rise coefficient $\Psi(\xi)$ is defined as:

$$\Psi(\xi) = \frac{P_s - P_T}{\rho U^2} \qquad 2\text{-}29$$

and the quasi-steady axisymmetric compressor pressure rise characteristic is defined as:

$$\psi'_c(\phi) = \mathrm{N}F(\phi) - \frac{1}{2}\phi^2 \qquad 2\text{-}30$$

Thus,

$$\Psi(\xi) = \psi'_c(\phi) - [l_I + \mu + l_E]\frac{d\Phi}{d\xi} - m\left(\tilde{\phi}'_{\xi}\right)_0 - \mu\left(\tilde{\phi}'_{\xi\eta}\right)_0 - \lambda\left(\tilde{\phi}'_{\theta\eta}\right)_0 - \frac{1}{2}[1 - K_G]h^2 \qquad 2\text{-}31$$

Assuming, the inlet guide vane (IGV) is lossless i.e. the pressure recovery coefficient $K_G = 1$, therefore,

$$\Psi(\xi) = \psi'_c(\phi) - l_c\frac{d\Phi}{d\xi} - m\left(\tilde{\phi}'_{\xi}\right)_0 - \mu\left(\tilde{\phi}'_{\xi\eta}\right)_0 - \lambda\left(\tilde{\phi}'_{\theta\eta}\right)_0 \qquad 2\text{-}32$$

where $l_c = l_I + \mu + l_E$ is the non-dimensional effective flow path length through the compressor and its ducts.

Simplifying Assumption: $^{dh}/_{d\theta} = -g$ or $(\tilde{\phi}'_{\eta})_0 = -(\tilde{\phi}'_{\theta\theta})_0$

Equation 2-32 for the total-to-static pressure rise coefficient, depends on the flow potential disturbance $\tilde{\phi}'$ and its partial derivatives in $\xi, \eta \; and \; \theta$, therefore, an assumption is adopted to simplify its partial derivatives.

Since the flow upstream of the compressor is irrotational, the flow potential disturbance $\tilde{\phi}'$ would satisfy the Laplace equation (Greitzer and Moore, 1986).

Therefore,

$$\tilde{\phi}'_{\theta\theta} + \tilde{\phi}'_{\eta\eta} = 0 \qquad 2\text{-}33$$

To determine the form of the $\tilde{\phi}'$ expression that would satisfy Equation 2-33, we recall from Equation 2-20 that, $(\tilde{\phi}'_{\eta})_0 = g(\xi, \theta)$ and that from Equation 2-4 that *g* is a periodic function, since it must have a vanishing average in 2π; therefore, $\tilde{\phi}'$ must also be a periodic function with a vanishing average and based on continuity, vanishes when $\eta = -\infty$ (Greitzer and Moore, 1986).

The Fourier series of the form below satisfies the above conditions for $\tilde{\phi}'$ and also satisfies the Laplace equation (Greitzer and Moore, 1986):

$$\tilde{\phi}' = \sum_{n=1}^{\infty} \frac{1}{n} e^{n\eta} (a'_n \sin n\theta + b'_n \cos n\theta) \qquad 2\text{-}34$$

If an approximation is made to Equation 2-34, such that only the first term of the Fourier series is used in representing $\tilde{\phi}'$ i.e. $(n = 1)$, then simplifying Equation 2-34 results in:

$$(\tilde{\phi}'_{\eta})_0 = -(\tilde{\phi}'_{\theta\theta})_0 \qquad 2\text{-}35$$

Equation 2-35 can also be expressed in the form $^{dh}/_{d\theta} = -g$ by substituting Equation 2-20 into Equation 2-35.

For simplicity, let

$$(\tilde{\phi}')_0 = Y(\xi, \theta) \; and \; (\tilde{\phi}'_{\eta})_0 = -\mathrm{Y}_{\theta\theta} \qquad 2\text{-}36$$

Then Equation 2-32 for total-static pressure rise coefficient can be simplified as,

$$\Psi(\xi) = \psi_c'(\phi) - l_c \frac{d\Phi}{d\xi} - mY_\xi + \mu Y_{\xi\theta\theta} + \lambda Y_{\theta\theta\theta} \qquad 2\text{-}37$$

Equation 2-37 represents the first governing equation of a general disturbance in a compression system.

Since $\left(\tilde{\phi}'\right)_0 = Y(\xi, \theta)$, then an implication from Equation 2-34, is that,

$$\int_0^{2\pi} Y(\xi, \theta) d\theta = 0 \qquad 2\text{-}38$$

The second equation of general disturbance is gotten by integrating Equation 2-37 over one cycle with respect to θ, thus,

$$\Psi(\xi) + l_c \frac{d\Phi}{d\xi} = \frac{1}{2\pi} \int_0^{2\pi} \psi_c'(\phi)\, d\theta \qquad 2\text{-}39$$

2.2.7 Mass Balance in the Plenum and Throttle

The third and final equation of the general disturbance is gotten by balancing the following mass flows: the mass flow into plenum from the compressor, the mass flow leaving the plenum through the throttle and the mass accumulated in the plenum such that,

$$\frac{d}{dt}\left(\rho_p V_p\right) = \rho U A_c \Phi(\xi) - \rho U A_c \Phi_T(\xi) \qquad 2\text{-}40$$

where ρ_p density of gas accumulating in the plenum, V_p volume of the plenum, ρ density of gas entering and leaving the plenum, A_c compressor annulus area, $\Phi(\xi)$ and $\Phi_T(\xi)$ is the annulus averaged axial flow coefficient entering and leaving the plenum respectively.

If the change in gas density in the plenum with pressure is assumed isentropic, then,

$$\frac{dP_p}{dt} = \frac{a_s^2}{V_p}\left[\rho U A_c \Phi(\xi) - \rho U A_c \Phi_T(\xi)\right] \qquad 2\text{-}41$$

By non-dimensionalizing Equation 2-41, dividing pressure by ρU^2, converting time from *t* to ξ by considering Equation 2-1 and replacing R with $\frac{L_c}{l_c}$, the ratio of

dimensional effective flow path length L_c to the non-dimensional effective flow path length l_c, the resulting expression becomes (Greitzer and Moore, 1986):

$$l_c \frac{d\Psi}{d\xi} = \frac{1}{4B^2}[\Phi(\xi) - \Phi_T(\xi)] \quad \text{2-42}$$

where B, the Greitzer B-parameter is defined as,

$$\mathrm{B} = \frac{U}{2a_s}\sqrt{\frac{V_p}{A_c L_c}} \quad \text{2-43}$$

where U is the compressor speed at the mean wheel radius, a_s is the speed of sound, V_p is the plenum volume, A_c is the compressor annular area, L_c is the dimensional effective flow path length of the compressor and its duct.

The throttle characteristic $\Phi_T(\xi)$, can be modelled as (Gravdahl and Egeland, 1997a; Greitzer and Moore, 1986; Yoon, Lin and Allaire, 2013):

$$\Phi_T(\xi) = \gamma\sqrt{\Psi} \quad \text{2-44}$$

where γ is the throttle coefficient.

2.2.8 Governing Equations of a General Disturbance

Recalling Equations 2-37, 2-39 and 2-42, the governing equations of a general disturbance in a compression system can be summarised as:

$$\Psi(\xi) = \psi_c'(\phi) - l_c \frac{d\Phi}{d\xi} - mY_\xi + \mu Y_{\xi\theta\theta} + \lambda Y_{\theta\theta\theta} \quad \text{2-45}$$

$$\Psi(\xi) + l_c \frac{d\Phi}{d\xi} = \frac{1}{2\pi}\int_0^{2\pi} \psi_c'(\phi)\, d\theta \quad \text{2-46}$$

$$l_c \frac{d\Psi}{d\xi} = \frac{1}{4B^2}[\Phi(\xi) - \Phi_T(\xi)] \quad \text{2-47}$$

From Equation 2-25 and Equation 2-34, considering just the first term, $n = 1$, $\phi(\xi, \theta)$ can be simplified as:

$$\phi(\xi, \theta) = \Phi(\xi) + a' \sin\theta + b' \cos\theta \quad \text{2-48}$$

where ϕ is the axial flow coefficient, Φ is the averaged annular flow coefficient, $a'$and b' are amplitudes of the first harmonic in the Fourier series approximation for the disturbed axial flow coefficient.

2.2.9 Compressor Characteristic

1) Steady State Axisymmetric Compressor Pressure Rise Characteristic

The compressor steady state pressure rise characteristic depicts the relationship between the compressor pressure rise and flow coefficient under axisymmetric steady flow conditions.

In order to proceed with the solution for the general disturbance equations in Equations 2-45 - 2-47, a closed form expression for the steady state compressor pressure rise characteristic $\psi_c'(\phi)$ is required.

According to Greitzer and Moore (1986), the steady state compressor pressure rise characteristic $\psi_c'(\phi)$ can be described by a 3rd order polynomial of the form:

$$\psi_c'(\phi) = \psi_{c0} + H\left[1 + \frac{3}{2}\left(\frac{\phi}{W} - 1\right) - \frac{1}{2}\left(\frac{\phi}{W} - 1\right)^3\right] \qquad 2\text{-}49$$

where ϕ is the axial flow coefficient, $\psi_{c0}, H\ and\ W$ are parameters gotten from curve fitting the compressor pressure map as shown in Figure 2-2. In Figure 2-2, the x-axis is represented by the flow coefficient ϕ while y-axis is represented by the pressure rise coefficient ψ_c'.

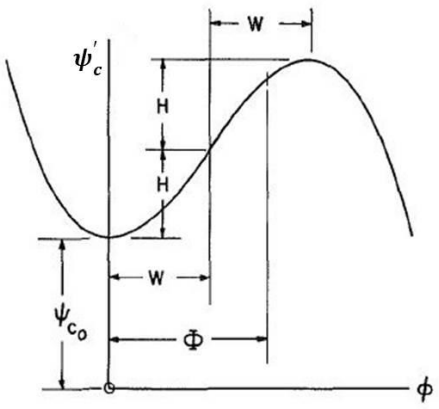

Figure 2-2 General attributes of the compressor axisymmetric pressure rise characteristics (Source: Greitzer and Moore, 1986)

Since the standard compressor pressure map is dependent on rotational speed, Al-Nahwi (2000) has proposed a transformation scheme that eliminates the dependence of the compressor characteristic on speed. This transformation scheme collapses all the different speed lines on the compressor pressure map into a single line.

The transformation scheme proposed by Al-Nahwi (2000) is represented as:

$$\mathrm{q} = \frac{\phi}{2W}\,;\mathrm{Q} = \frac{\Phi}{2W}\,;\,\psi_c = \frac{\psi_c'}{H}\,;P = \frac{\Psi}{H};\,\mathrm{a} = \frac{a'}{2W};\mathrm{b} = \frac{b'}{2W} \qquad \text{2-50}$$

where q is the transformed flow coefficient, Q is the transformed annulus averaged flow coefficient, ψ_c is the transformed compressor pressure rise characteristic, P is the transformed plenum pressure rise coefficient, a and b are the transformed amplitudes of the first harmonics in the Fourier series approximation for the disturbed axial flow coefficient.

The generalized format of the transformed compressor pressure rise characteristic is presented in Figure 2-3.

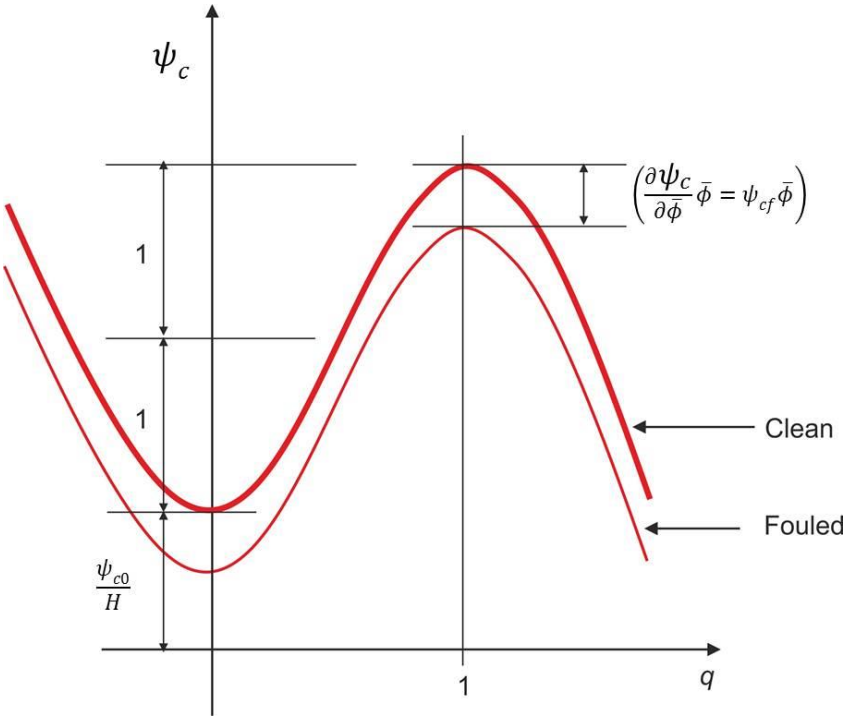

Figure 2-3 General attributes of the transformed compressor pressure rise characteristic

The expression for the transformed compressor pressure rise characteristic without the effect of fouling is:

$$\psi_c(q) = \left(\frac{\psi_{c0}}{H}\right) + 1 + 3(q - 0.5) - 4(q - 0.5)^3 \qquad 2\text{-}51$$

where q is determined by:

$$q = \mathrm{Q} + a\sin\theta + b\cos\theta \qquad 2\text{-}52$$

Equation 2-52 is determined by applying the transformation scheme in Equation 2-50 to Equation 2-48.

2) Effect of Fouling on Compressor Pressure Rise Characteristic

A modification and contribution of this work to the Moore-Greitzer model, is the inclusion of the scaling effect of fouling on the compressor pressure rise characteristic.

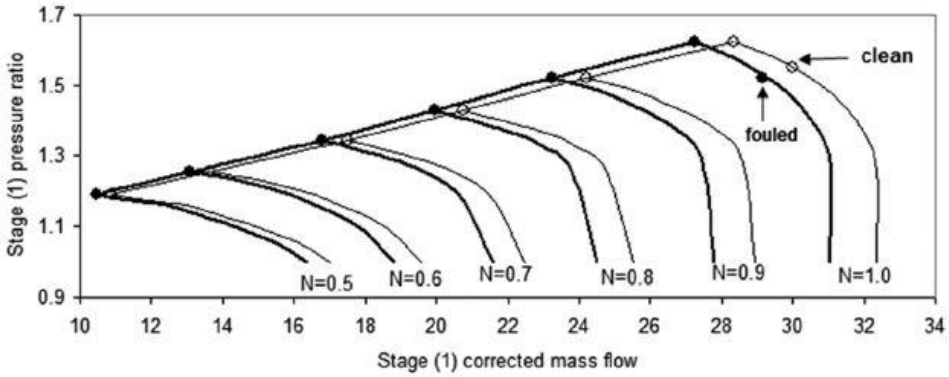

Figure 2-4 Plot of compressor pressure ratio vs corrected massflow for a clean and fouled engine stage (Source: Igie et al., 2014)

Although the scaling effect of fouling on the compressor pressure rise characteristic is non-linear as shown in Figure 2-4, a linear assumption is adopted as an approximate representation of the effect of fouling on the compressor pressure rise characteristic i.e. relative change in pressure rise coefficient equals the relative change in flow coefficient due to fouling (Grewal, 1988). This approximation is based on the findings by Grewal (1988); who showed that for a deteriorated compressor, the relative reduction of the compressor pressure ratio

is approximately equal to the relative reduction in the compressor massflow at lower speeds and high pressure ratios. Although Grewal (1988) noted that the nonlinear scaling effect would be best represented by an empirical relationship between pressure ratio, massflow and compressor speed.

Thus, the linear approximation is summarised as:

$$\Delta PR \approx \Delta MF \qquad \text{2-53}$$

where ΔPR is the relative change in pressure ratio and ΔMF is the relative change in massflow.

The modified expression for the compressor pressure rise characteristic, taking into consideration the effect of fouling as displayed in Figure 2-3 is:

$$\psi_c(q) = \left(\frac{\psi_{c0}}{H}\right) + 1 + 3(q - 0.5) - 4(q - 0.5)^3 + \frac{\partial \psi_c}{\partial \bar{\phi}}\bar{\phi} \qquad \text{2-54}$$

where $\partial \psi_c / \partial \bar{\phi}$ is the fouling sensitivity coefficient and $\bar{\phi}$ is the relative change in axial flow coefficient due to fouling.

Based on the linear approximation, $\partial \psi_c / \partial \bar{\phi}$ is represented by the constant parameter ψ_{cf}.

Therefore,

$$\psi_c(q) = \left(\frac{\psi_{c0}}{H}\right) + 1 + 3(q - 0.5) - 4(q - 0.5)^3 + \psi_{cf}\bar{\phi} \qquad \text{2-55}$$

where ψ_{cf} is the fouling sensitivity coefficient and $\bar{\phi}$ is the relative change in axial flow coefficient due to fouling with respect to θ.

The relative change in the axial flow coefficient $\bar{\phi}$ with respect to θ can be expressed approximately as:

$$\bar{\phi} = -\left(\frac{\Delta MF}{2}\right)\cos(\theta - \Gamma) - \left(\frac{\Delta MF}{2}\right) \qquad \text{2-56}$$

$$\bar{\phi} = -\left(\frac{\Delta MF}{2}\right)[\cos(\theta - \Gamma) + 1] \qquad \text{2-57}$$

where $\bar{\phi}$ is the relative change in axial flow coefficient due to fouling with respect to θ, ΔMF is the relative change in massflow due to fouling, θ is the angle around

the compressor and Γ is a phase angle. $\bar{\phi}$ is a periodic function such that $\bar{\phi}(\theta + 2\pi) = \bar{\phi}(\theta)$.

The proposed form of $\bar{\phi}$ in Equation 2-56, is based on the experimental results presented in Figure 2-5 and Figure 2-6 by Fouflias et al. (2010) and also similar findings by Back et al. (2010) on the influence of fouling on a blade row's downstream pitchwise velocity and pressure loss coefficient distribution in a compressor cascade test.

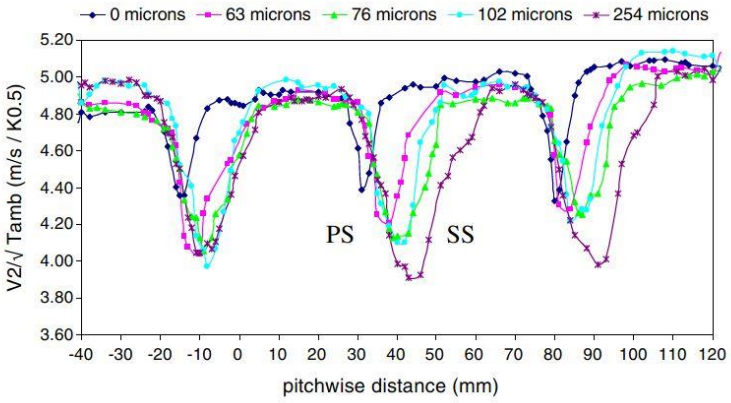

Figure 2-5 Pitchwise velocity distribution downstream of the cascade blade for different blade roughness (Source: Fouflias et al., 2010)

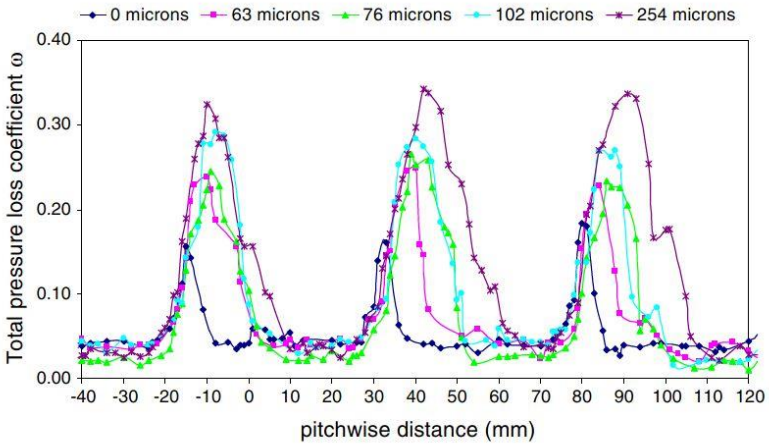

Figure 2-6 Pitchwise pressure loss coefficient distribution downstream of the cascade blade for different blade roughness (Source: Fouflias et al., 2010)

From Figure 2-5 and Figure 2-6, the following observation is made, and they form the basis for the proposed form of $\bar{\phi}$ presented in Equation 2-56:

i. The downstream pitchwise axial velocity distribution show periodicity for both the clean and fouled blades. Therefore, $\bar{\phi}$ is a periodic function with respect to θ and expressed as:

$$\bar{\phi}(\theta + 2\pi) = \bar{\phi}(\theta) \qquad 2\text{-}58$$

ii. With respect to the clean blade (roughness $0\mu m$), the increase in the blade roughness causes a shift in the profile for both the velocity and pressure loss coefficient distribution. This shift is due to the growth in boundary layer due to the increased blade roughness (Back, Sohn and Song, 2010; Fouflias et al., 2010). This effect is accounted for by the inclusion of the phase angle Γ in Equation 2-56.

iii. It is observed from Figure 2-5, at the blade trailing edge, the pitchwise velocity of the roughened blades is much reduced compared to the clean blade, while at the mean-line streamflow (centre of the space between any two neighbouring blade), the pitchwise velocity for both the clean and roughened blades are approximately equal. In addition, from Figure 2-6, it is observed that the pressure-loss coefficient at the mean-line streamflow is approximately the same for both the clean and all roughened blade. These trends are captured in equation 2-56 by the way the amplitude of the cosine term and the second term counteract themselves.

Substituting Equation 2-57 into equation 2-55, $\psi_c(q)$ becomes:

$$\psi_c(q) = \left(\frac{\psi_{c0}}{H}\right) + 1 + 3(q - 0.5) - 4(q - 0.5)^3 - \psi_{cf}\left(\frac{\Delta MF}{2}\right)[\cos(\theta - \Gamma) + 1] \qquad 2\text{-}59$$

3) <u>Integrated Compressor Pressure Rise Characteristic</u>

The integrated expressions of the compressor pressure rise characteristic is necessary for the Galerkin solution of the general disturbance equations, as such, they are presented below.

a)

$$\bar{\psi}_c^c = \frac{1}{2\pi}\int_0^{2\pi} \psi_c d\theta \qquad \text{2-60}$$

Recalling Equation 2-59 and Equation 2-52,

$$\psi_c(q) = \left(\frac{\psi_{c0}}{H}\right) + 1 + 3(q-0.5) - 4(q-0.5)^3 - \psi_{cf}\left(\frac{\Delta MF}{2}\right)[\cos(\theta - \Gamma) + 1]$$

$$q = \mathrm{Q} + a\sin\theta + b\cos\theta$$

Therefore,

$$\bar{\psi}_c^c = \left(\frac{\psi_{c0}}{H}\right) + 1 + 3(Q-0.5) - 4(Q-0.5)^3 - 6(a^2+b^2)(Q-0.5) - \psi_{cf}\left(\frac{\Delta MF}{2}\right) \qquad \text{2-61}$$

b)

$$\bar{\psi}_c^{cc} = \frac{1}{\pi}\int_0^{2\pi} \psi_c \cos\theta\, d\theta \qquad \text{2-62}$$

$$\therefore \bar{\psi}_c^{cc} = -3\mathrm{a}[4Q(Q-1) + (a^2+b^2)] - \psi_{cf}\left(\frac{\Delta MF}{2}\right)\cos\Gamma \qquad \text{2-63}$$

c)

$$\bar{\psi}_c^{cs} = \frac{1}{\pi}\int_0^{2\pi} \psi_c \sin\theta\, d\theta \qquad \text{2-64}$$

$$\therefore \bar{\psi}_c^{cs} = -3\mathrm{b}[4Q(Q-1) + (a^2+b^2)] - \psi_{cf}\left(\frac{\Delta MF}{2}\right)\sin\Gamma \qquad \text{2-65}$$

4) <u>Fouling Parameter (FP)</u>

The fouling parameter represents the difference between the pressure rise coefficient of the clean engine and the fouled engine in the transformed pressure rise coefficient plane when the transformed flow coefficient is one (i.e. q = 1).

Mathematically, the fouling parameter can be expressed as:

$$\mathrm{FP} = \left(\psi_c^{clean} - \psi_c^{fouled}\right)_{q=1} \quad \text{2-66}$$

From Figure 2-3, the pressure coefficient for the clean engine when q = 1 is:

$$\psi_c^{clean} = \left(\frac{\psi_{co}}{H} + 2\right) \quad \text{2-67}$$

where ψ_{co} the shut-off value of pressure coefficient and H is semi-height parameter from the compressor pressure rise characteristic.

But the relative change in pressure ratio due to fouling can be expressed as,

$$\Delta PR \approx \left\{\frac{\left(\psi_c^{clean} - \psi_c^{fouled}\right)}{\psi_c^{clean}}\right\}_{q=1} \quad \text{2-68}$$

Thus,

$$\left(\psi_c^{clean} - \psi_c^{fouled}\right) \approx \Delta PR \times \psi_c^{clean} \quad \text{2-69}$$

Substituting Equation 2-76 into Equation 2-78, it becomes:

$$FP \approx \Delta PR\left(\frac{\psi_{co}}{H} + 2\right) \quad \text{2-70}$$

Considering the linear approximation for the scaling effect of the pressure rise characteristic due to fouling expressed in Equation 2-53 (i.e. $\Delta PR \approx \Delta MF$), Equation 2-70 becomes:

$$FP \approx \Delta MF\left(\frac{\psi_{co}}{H} + 2\right) \quad \text{2-71}$$

From Figure 2-3, the Fouling Parameter can also be expressed as:

$$FP = \psi_{cf}[\bar{\phi}]_{max} \quad \text{2-72}$$

where ψ_{cf} is the fouling sensitivity coefficient and $[\bar{\phi}]_{max}$ is the maximum amplitude of the relative change in axial flow coefficient.

Since the relative change in axial flow coefficient ($\bar{\phi}$) is a periodic function, its maximum amplitude $[\bar{\phi}]_{max}$ gotten from simplifying Equation 2-57 is ΔMF.

Therefore, Equation 2-72 becomes,

$$FP = \psi_{cf}\Delta MF \quad \text{2-73}$$

Comparing Equations 2-71 and 2-73, the fouling sensitivity coefficient (ψ_{cf}) can be determined by:

$$\psi_{cf} = \left(\frac{\psi_{co}}{H} + 2\right) \qquad 2\text{-}74$$

where ψ_{co} is the shut-off value of pressure rise coefficient and H is a parameter gotten from curve fitting the compressor pressure rise characteristic.

The fouling parameter is determined based on a linear approximation of the effect of fouling on the compressor pressure rise characteristic i.e. relative change in the pressure rise coefficient equals the relative change in flow coefficient due to fouling (Grewal, 1988), as such, the fouling parameter describes the degradation for fouled compressor operating with incompressible inlet flow or compressible inlet flow at low Mach number.

2.2.10 Galerkin Solution of the General Disturbance Equations

1) <u>Final Model</u>

To simplify the final compression system model, the Galerkin method is applied to Equation 2-45, to transform it from a partial differential equation to an ordinary differential equation dependent only on time (Al-Nahwi, 2000; Gravdahl and Egeland, 1997a; Greitzer and Moore, 1986).

The Galerkin method is based on the following premise, if a variational problem (e.g. partial differential equation) is posed as a minimization problem such as $F(x) = 0$, with *x*, the basis function being continuous and infinite; In other to arrive at a solution to the minimization problem, a Fourier series approximation of *x* is first proposed, which on substituting into the minimization problem produces a residue R_g or error very close to zero. The final solution to the minimization problem is gotten by equating the integral of the inner product of the residue 'R_g and a weighting function 'w' to zero. The weighting function 'w' is such that it is of the same form as the approximate expression of *x*.

Recalling Equation 2-45,

$$\Psi(\xi) = \psi_c'(\phi) - l_c \frac{d\Phi}{d\xi} - mY_\xi + \mu Y_{\xi\theta\theta} + \lambda Y_{\theta\theta\theta}$$

The minimization problem residue R_g is:

$$\psi_c'(\phi) - l_c \frac{d\Phi}{d\xi} - mY_\xi + \mu Y_{\xi\theta\theta} + \lambda Y_{\theta\theta\theta} - \Psi(\xi) = 0 \qquad 2\text{-}75$$

Recalling Equation 2-34 and 2-36, the basis function Y is approximated by the first term of the Fourier series (i.e. n=1) as:

$$Y = a'(\xi)\sin\theta + b'(\xi)\cos\theta \qquad 2\text{-}76$$

The Galerkin method applied to this minimization problem results in:

$$\int_0^{2\pi} R_g \, d\theta = 0 \qquad 2\text{-}77$$

$$\int_0^{2\pi} R_g \, \cos\theta \, d\theta = 0 \qquad 2\text{-}78$$

$$\int_0^{2\pi} R_g \, \sin\theta \, d\theta = 0 \qquad 2\text{-}79$$

Simplifying Equation 2-77,

$$\frac{d\Phi}{d\xi} = \frac{1}{l_c}\left[\frac{1}{2\pi}\int_0^{2\pi} \psi_c'(\phi)\, d\theta - \Psi(\xi)\right] \qquad 2\text{-}80$$

The result from the simplification of Equation 2-77 is the same as Equation 2-46.

Simplifying Equation 2-78,

$$\frac{da'}{d\xi} = \frac{1}{\mathrm{m} + \mu}\left[\frac{1}{\pi}\int_0^{2\pi} \psi_c'(\phi)\cos\theta \, d\theta - \lambda b'\right] \qquad 2\text{-}81$$

Simplifying Equation 2-79,

$$\frac{db'}{d\xi} = \frac{1}{\mathrm{m} + \mu}\left[\frac{1}{\pi}\int_0^{2\pi} \psi_c'(\phi)\sin\theta \, d\theta + \lambda a'\right] \qquad 2\text{-}82$$

From Equations 2-47, 2-80, 2-81 and 2-82, the summary of the simplified general disturbance equations are:

$$\frac{d\Phi}{d\xi} = \frac{1}{l_c}\left[\frac{1}{2\pi}\int_0^{2\pi} \psi_c'(\phi)\, d\theta - \Psi(\xi)\right] \qquad 2\text{-}83$$

$$\frac{d\Psi}{d\xi} = \frac{1}{4B^2 l_c}[\Phi(\xi) - \Phi_T(\xi)] \quad \text{2-84}$$

$$\frac{da'}{d\xi} = \frac{1}{\mathrm{m}+\mu}\left[\frac{1}{\pi}\int_0^{2\pi} \psi_c'(\phi)\cos\theta\, d\theta - \lambda b'\right] \quad \text{2-85}$$

$$\frac{db'}{d\xi} = \frac{1}{\mathrm{m}+\mu}\left[\frac{1}{\pi}\int_0^{2\pi} \psi_c'(\phi)\sin\theta\, d\theta + \lambda a'\right] \quad \text{2-86}$$

By applying the Al-Nahwi transformation scheme from Equation 2-50, the integrated compressor characteristic expressions in Equations 2-61, 2-63 and 2-65 and substituting $m = 2$ (i.e. long exit duct approximation) into Equations 2-83, 2-84, 2-85 and 2-86, the final governing equations of a general disturbance in a compression system are:

$$\frac{d\mathrm{Q}}{d\xi} = \frac{S}{2l_c}[\bar{\psi}_c^c - P] \quad \text{2-87}$$

$$\frac{dP}{d\xi} = \frac{1}{2SB^2 l_c}[\mathrm{Q} - \mathrm{Q}_T] \quad \text{2-88}$$

$$\frac{d\mathrm{a}}{d\xi} = \frac{1}{(2+\mu)}\left[\frac{\mathrm{S}}{2}\bar{\psi}_c^{cc} - \lambda\mathrm{b}\right] \quad \text{2-89}$$

$$\frac{d\mathrm{b}}{d\xi} = \frac{1}{(2+\mu)}\left[\frac{\mathrm{S}}{2}\bar{\psi}_c^{cs} + \lambda\mathrm{a}\right] \quad \text{2-90}$$

where $dQ/d\xi$ is the instantaneous transformed averaged flow coefficient, $dP/d\xi$ is the instantaneous transformed plenum pressure rise coefficient, $da/d\xi$ and $db/d\xi$ are the transformed amplitudes of disturbance flow coefficient, P is the transformed plenum pressure rise coefficient, Q is the transformed averaged flow coefficient, $\mathrm{Q}_T(P) = \gamma\sqrt{P}$ represents the throttle characteristic and S is the pressure rise characteristic aspect ratio expressed as H/W; with H and W representing parameters gotten from the curve fitting of the compressor pressure rise map as shown in Figure 2-2.

2) <u>Steady State Solution of the Final Model</u>

The steady state solution of the general equations of flow disturbance is gotten by setting time derivative terms in the left hand side of Equations 2-87, 2-88, 2-89 and 2-90 to zero and the resulting set of equations solved simultaneously.

$$0 = \frac{S}{2l_c}[\bar{\psi}_c^c - P] \qquad 2\text{-}91$$

$$0 = \frac{1}{2SB^2 l_c}[\mathrm{Q} - \mathrm{Q}_T(P)] \qquad 2\text{-}92$$

$$0 = \frac{1}{(2+\mu)}\left[\frac{\mathrm{S}}{2}\bar{\psi}_c^{cc} - \lambda\mathrm{b}\right] \qquad 2\text{-}93$$

$$0 = \frac{1}{(2+\mu)}\left[\frac{\mathrm{S}}{2}\bar{\psi}_c^{cs} + \lambda\mathrm{a}\right] \qquad 2\text{-}94$$

A further simplification is possible, since P is absent in both Equation 2-93 and 2-94, it is possible to only solve Equations 2-93 and 2-94 simultaneously for a and b by choosing just an operating point Q on the compressor pressure rise characteristic.

For brevity, only the final solution of above mention simplification technique is presented here, the full proof is given in Appendix A:

$$\mathrm{A}^6 + 8Q(Q-1)A^4 + \left[16Q^2(Q-1)^2 + \left(\frac{2\lambda}{3S}\right)^2\right]A^2 - \left[\frac{\psi_{cf}\Delta MF}{6}\right]^2 = 0 \qquad 2\text{-}95$$

$$\mathrm{A}^6 + 8Q(Q-1)A^4 + \left[16Q^2(Q-1)^2 + \left(\frac{2\lambda}{3S}\right)^2\right]A^2 - \left[\frac{FP}{6}\right]^2 = 0 \qquad 2\text{-}96$$

$$A = \sqrt{a^2+b^2}\,;\, a \approx A\cos\eta^*\,;\, b \approx A\sin\eta^*\,;$$
$$\eta^* = \sin^{-1}\left(\frac{4\mathrm{A}}{\psi_{cf}\Delta MF}\frac{\lambda}{S}\right) = \sin^{-1}\left(\frac{4\mathrm{A}}{(\mathrm{FP})}\frac{\lambda}{S}\right) \qquad 2\text{-}97$$

where A, a and b are amplitudes of the disturbed axial flow coefficient, Q is the transformed averaged flow coefficient, S is the pressure rise characteristic aspect ratio (H/W), λ is a compressor inertia parameter, FP is the fouling parameter $\left(FP = \psi_{cf} \times \Delta MF\right)$, ψ_{cf} is the fouling sensitivity coefficient and ΔMF is the relative change in massflow due to fouling.

Figure 2-7 provides a summary of the overall methodology for determining the amplitudes of the disturbed flow coefficients.

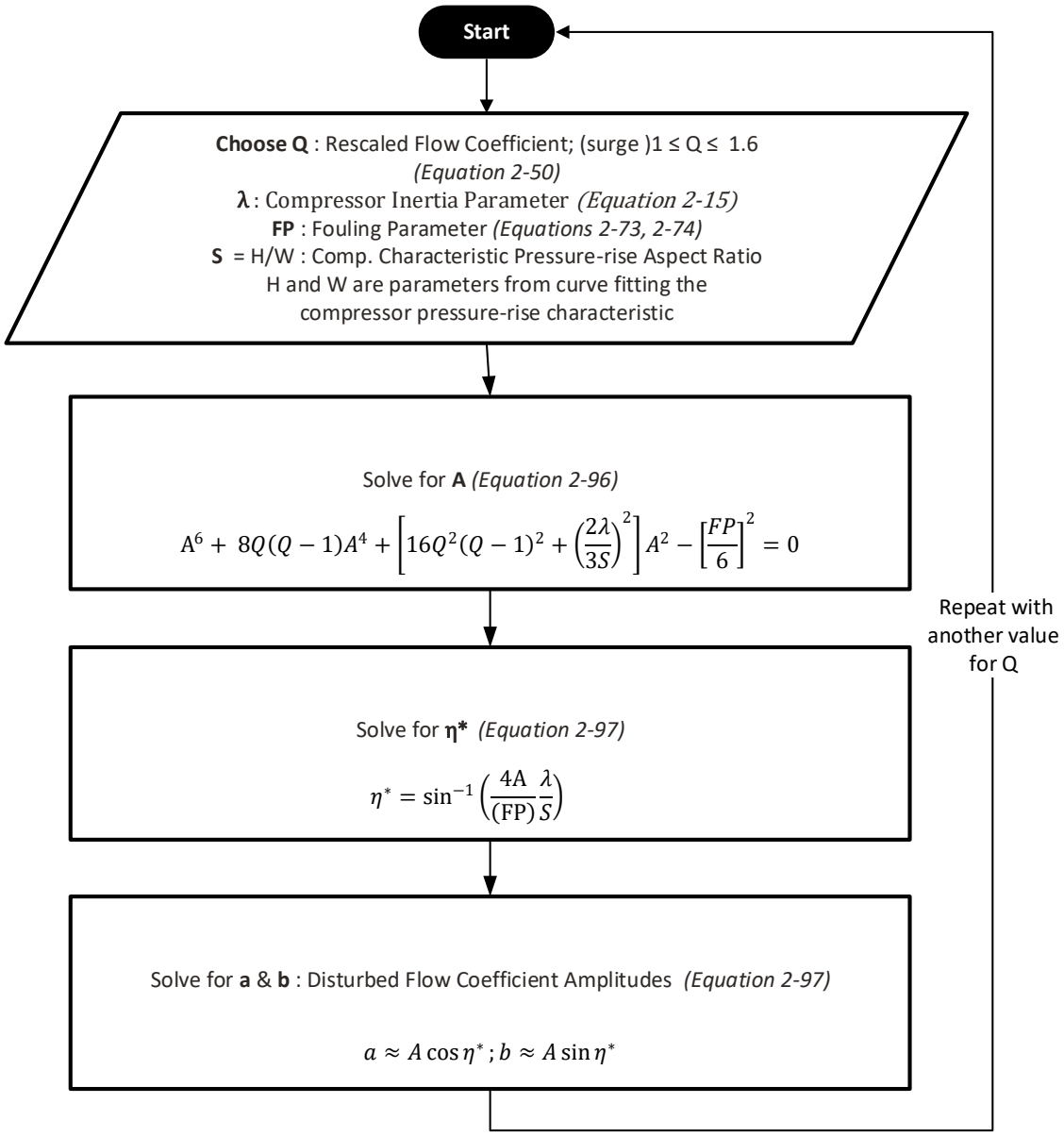

Figure 2-7 Flow chart summarizing the overall methodology for determining the amplitudes of the disturbed flow coefficient

2.3 Conclusion

This chapter paints a complete picture of the development of a flow field model for an axial compressor subjected to fouling. The output from this model (i.e. amplitudes of disturbed flow coefficient [a & b]) are used in the aerodynamic force prediction model.

Results for the model validation and parametric studies when integrated with the aerodynamic force model and compressor rotordynamic model are presented in Chapter 5 Section 5.3.

3 ROTORDYNAMIC MODEL DEVELOPMENT

3.1 Introduction

There are several reasons why rotating equipment vibrate. This results from the presence of an unbalance mass, alignment problems, fouled impellers, bearing problems, etc.; one thing is certain, measuring or trending the vibration amplitudes at specific frequencies can provide significant diagnostic information about the nature of the fault. Vibration analysis therefore, provides a valuable technique for rotating equipment condition monitoring (Scheffer and Girdhar, 2004).

In other to study the vibration characteristics of a rotor bearing system, rotordynamics provides the tools and insights.

Rotordynamics as a specialized field of study in applied mechanics provides a set of modelling approaches for rotating structures, used to provide insight into the general nature of their dynamics. With rotordynamics, the following predictions about the dynamic behaviour of rotating structures can be made: rotor critical speed prediction, rotor mode shape prediction, rotor unbalance/forced response analysis, rotor threshold of instability analysis, rotor torsional frequency prediction and the necessary design modifications needed to alter the critical or torsional speeds and supress rotor instabilities (Vance, 1988).

Although there are several approaches to rotordynamic modelling, the two widely used techniques are the finite element method and the transfer matrix method (Marcorio and Menezes, 2012; Murphy and Vance, 1983).

Predictions from both approaches are always in close agreement; therefore, the choice of which particular approach to adopt is based on a careful balance of the level of complexity involved and the computational speed required. While the finite element method has the added benefit of the ability to consider complex geometries, the transfer matrix method is several orders of magnitudes faster in computation time than the finite element method (Marcorio and Menezes, 2012).

A program dubbed “RotorMatch” has been written in MATLAB for this research to perform rotordynamic analysis of rotating structures e.g. gas turbine. The MATLAB code for this program is provided in Appendix D.

3.2 Transfer Matrix Method

To lay the foundation for the more involved complex 2D transfer matrix method, the 1D transfer matrix method is explained below.

The transfer matrix method as used today is the cumulative effort of the work by four different investigators: Holzer (1921), Myklestad (1944), Prohl (1945) and Lund (1967).

Holzer (1921) first developed the transfer matrix approach for predicting the natural frequencies of torsional systems. Holzer’s work formed the basis of Myklestad (1944) and Prohl (1945) further improvement. Concurrently, Myklestad (1944) adapted the transfer matrix approach to predict the natural frequencies of aeroplane wings while Prohl (1945) adapted the transfer matrix approach to predict the natural frequencies of rotor-bearing systems. Lund (1967) performed the final tuning of the bells and whistle of the transfer matrix method as applied to any rotor bearing configuration.

In the transfer matrix method, the rotor bearing system is assumed to consist of a series of concentrated masses or inertias referred to as points connected by massless elastic shafts called fields. The point masses could refer to any machine element such as a bearing, impeller, gears, bladed disc, flywheel, change in cross-sectional area etc.

A basic rotor configuration for the transfer matric method is presented in Figure 3-1.

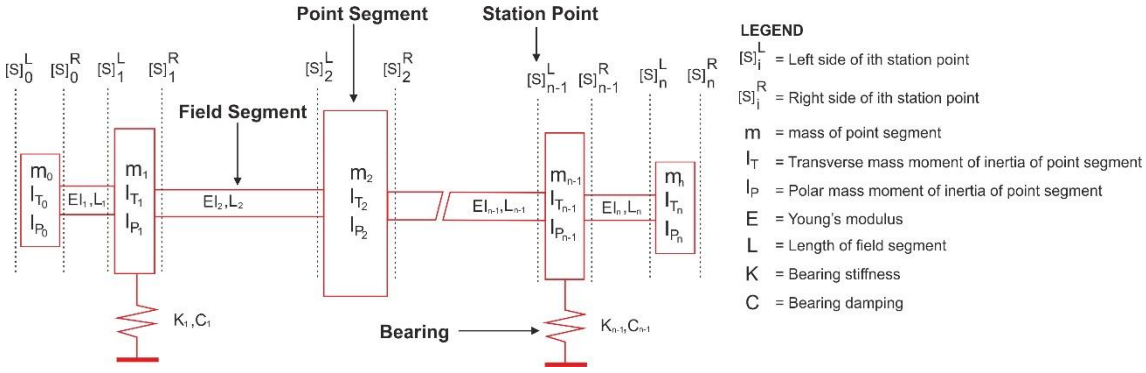

Figure 3-1 Basic rotor structure of the transfer matrix method

With the rotor bearing system broken down into a series of connected points (concentrated masses) and fields (massless elastic shafts), the entire rotor bearing system is then represented as matrices.

The matrix system in the transfer matrix method consists of three main parts: the state vector, the field matrix and the point matrix.

3.2.1 The State Vector

The state vector represents the value of the displacement, slope, bending moment and shear force at a particular location in the rotor bearing system.

Mathematically, the state vector is represented as:

$$[S] = \begin{bmatrix} -y \\ \theta \\ M \\ V \end{bmatrix} \qquad 3\text{-}1$$

where *y, θ, M & V* are the rotor deflection, slope, bending moment & shear force at a particular location along the rotor.

3.2.2 The Field Matrix

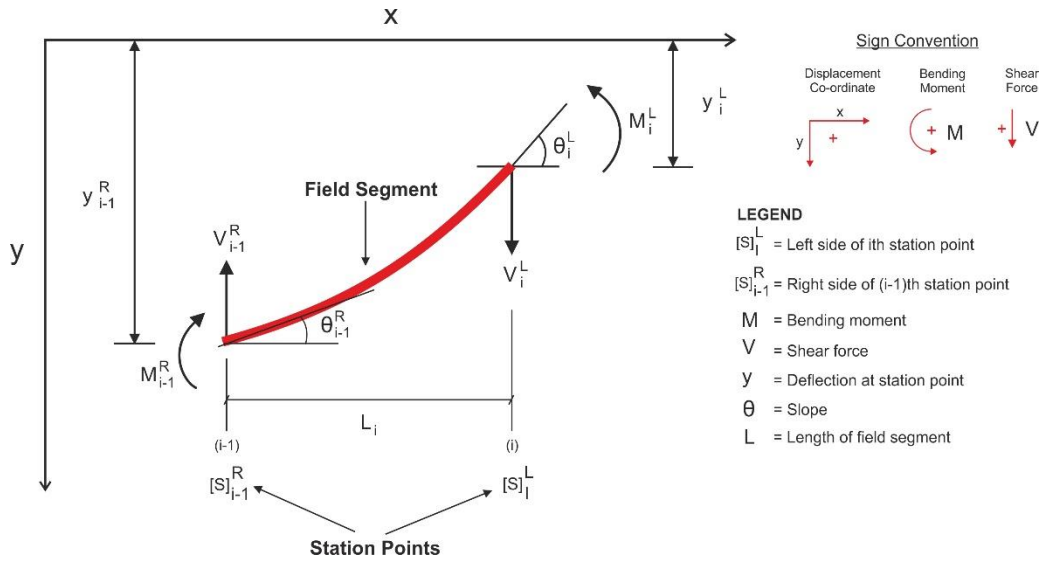

Figure 3-2 Deformation of an elastic shaft

The field matrix represents the behaviour of deformation of an elastic shaft segment. The elastic shaft segment is represented as either an Euler-Bernoulli beam or a Timoshenko beam.

To develop the basic form of the field matrix, the shaft segment would be treated first as an Euler-Bernoulli beam, and then later, the effect of shaft shear deflection would be included as a consequence of the Timoshenko beam theory.

As shown in Figure 3-2, for the shaft segment in elastic deformation to be equilibrium, summation of all moments about any point such as (i-1) is zero and the summation of all forces is zero.

This equilibrium condition can be expressed mathematically as:

$$V_i^L = V_{i-1}^R \qquad 3\text{-}2$$

$$M_i^L = M_{i-1}^R + V_i^L L_i \qquad 3\text{-}3$$

where V represents the shear forces and M represents the bending moment.

From the theory of strength of materials, the deflection and slope of a cantilever beam subjected to an end bending moment and load is given by (Young and Budynas, 2011):

$$y = -\frac{ML^2}{2EI} + \frac{VL^3}{3EI} \quad \text{3-4}$$

$$\theta = \frac{ML}{EI} - \frac{VL^2}{2EI} \quad \text{3-5}$$

where M is bending moment, V is shear force, L is beam segment length, E is modulus of elasticity and I is the beam area moment of inertia.

Framing the elastic shaft segment under deformation in Figure 3-2 as a cantilever beam; location (i-1) is considered to be fixed but possesses a deflection of y_{i-1}^R and slope of θ_{i-1}^R while the location 'i' is considered to be free and subjected to a shear force and bending moment of V_i^L and M_i^L respectively; the deflection and slope expression for this elastic shaft segment under deformation in Figure 3-2 with the application of Equations 3-4 and 3-5 to the problem at hand is:

$$y_i^L = y_{i-1}^R - \theta_{i-1}^R L_i - M_i^L \frac{L_i^2}{2EI_i} + V_i^L \frac{L_i^3}{3EI_i} \quad \text{3-6}$$

$$\theta_i^L = \theta_{i-1}^R + M_i^L \frac{L_i}{EI_i} - V_i^L \frac{L_i^2}{2EI_i} \quad \text{3-7}$$

Furthermore, to make Equations 3-6 and 3-7 in terms of only $(i-1)^R$ state variables, Equations 3-2 and 3-3 are substituted into Equations 3-6 and 3-7.3-2

Therefore,

$$y_i^L = y_{i-1}^R - \theta_{i-1}^R L_i - M_{i-1}^R \frac{L_i^2}{2EI_i} - V_{i-1}^R \frac{L_i^3}{6EI_i} \quad \text{3-8}$$

$$\theta_i^L = \theta_{i-1}^R + M_{i-1}^R \frac{L_i}{EI_i} + V_{i-1}^R \frac{L_i^2}{2EI_i} \quad \text{3-9}$$

Re-ordering Equations 3-2, 3-3, 3-8 and 3-9 in the following format: displacement, slope, bending moment and shear force results in:

$$y_i^L = y_{i-1}^R - \theta_{i-1}^R L_i - M_{i-1}^R \frac{L_i^2}{2EI_i} - V_{i-1}^R \frac{L_i^3}{6EI_i}$$

$$\theta_i^L = \theta_{i-1}^R + M_{i-1}^R \frac{L_i}{EI_i} + V_{i-1}^R \frac{L_i^2}{2EI_i}$$

$$M_i^L = M_{i-1}^R + V_i^L L_i$$

$$V_i^L = V_{i-1}^R$$

The above expressions can be rewritten in the matrix form as:

$$\begin{bmatrix} -y \\ \theta \\ M \\ V \end{bmatrix}_i^L = \begin{bmatrix} 1 & L & \frac{L^2}{2EI} & \frac{L^3}{6EI} \\ 0 & 1 & \frac{L}{EI} & \frac{L^2}{2EI} \\ 0 & 0 & 1 & L \\ 0 & 0 & 0 & 1 \end{bmatrix} \begin{bmatrix} -y \\ \theta \\ M \\ V \end{bmatrix}_{i-1}^R \quad \text{3-10}$$

$$[S]_i^L = [F]_i \, [S]_{i-1}^R \quad \text{3-11}$$

where $[S]_i^L$ is state vector at the left of the i-th station, $[F]_i$ is field matrix of the ith shaft section and $[S]_{i-1}^R$ is state vector at the right of the (i-1)-th station.

3.2.3 The Field Matrix with Shaft Shear Deflection

Thus far, the deflection of the beam has been due to bending only, which is the basis of the Euler-Bernoulli beam theory.

But for some rotor configurations, especially short shafts with large diameters, the effect of shear deflections becomes significant and therefore have to be accounted for in other to improve the accuracy of predicting the deflection by the transfer matrix method (Vance, 1988).

The effect of shear deflection on a beam's total deflection is a further improvement which owes itself to the Timoshenko beam theory.

The shear deflection of a beam as shown in Figure 3-3 is brought about by the sliding action of the beam elements on a plane normal to the beams axis due to shear stress.

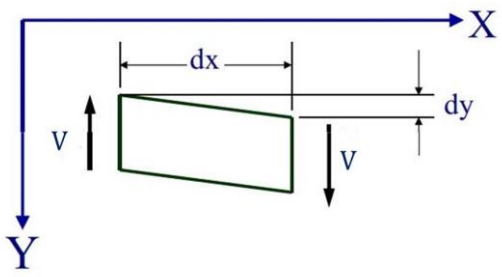

Figure 3-3 Shear deflection of a beam element due to shear stress (Source: Mba, 2012)

For the shearing deflection of the beam element in Figure 3-3 (Mba, 2012),

$$\frac{dy}{dx} = \alpha_F \frac{V}{A_b G} \tag{3-12}$$

where V is the shear force, A_b is the beam cross-sectional area, G is the shear modulus and α_F is a form factor which is equal to $^4/_3$ for circular sections and 1.5 for rectangular sections.

For a cantilever beam, the resulting expression from simplifying Equation 3-90 is (Mba, 2012):

$$y = \alpha_F \frac{VL}{A_b G} \tag{3-13}$$

where y is the deflection due to shearing, α is the form factor, V is the shear force, L is the length of the beam segment, A_b is the beam cross-sectional area and G is the shear modulus.

To include the effect of shear deflection in the prediction of the deflection by the transfer matrix method, Equation 3-91 is substituted into Equation 3-86, the result is:

$$y_i^L = y_{i-1}^R - \theta_{i-1}^R L_i - M_{i-1}^R \frac{L_i^2}{2EI_i} - V_{i-1}^R \frac{L_i^3}{6EI_i} + V_{i-1}^R \frac{\alpha_F L_i}{A_{bi} G} \tag{3-14}$$

Therefore, the modified field matrix presenting the massless elastic shaft is,

$$\begin{bmatrix} -y \\ \theta \\ M \\ V \end{bmatrix}_i^L = \begin{bmatrix} 1 & L & \frac{L^2}{2EI} & \left(\frac{L^3}{6EI} - \frac{\alpha_F L}{A_b G}\right) \\ 0 & 1 & \frac{L}{EI} & \frac{L^2}{2EI} \\ 0 & 0 & 1 & L \\ 0 & 0 & 0 & 1 \end{bmatrix} \begin{bmatrix} -y \\ \theta \\ M \\ V \end{bmatrix}_{i-1}^R \tag{3-15}$$

$$[S]_i^L = [F]_i \, [S]_{i-1}^R \tag{3-16}$$

where $[S]_i^L$ is state vector at the left of the i-th station, $[F]_i$ is field matrix of the ith shaft section and $[S]_{i-1}^R$ is state vector at the right of the (i-1)-th station.

3.2.4 The Point Matrix

The point matrix is used to represent any discontinuity along the rotor causing a change in the state vector. Examples of such discontinuities are inertia of discs, bearings, shaft cross-sectional area changes, unbalance, disc gyroscopic couple, etc.

Since the point matrix is made-up of a number of components or discontinuities; for clarity, the matrix representation of the individual discontinuity would be discussed first before the combined point matrix representing all the discontinuous effects.

1) Rotary Inertia Matrix

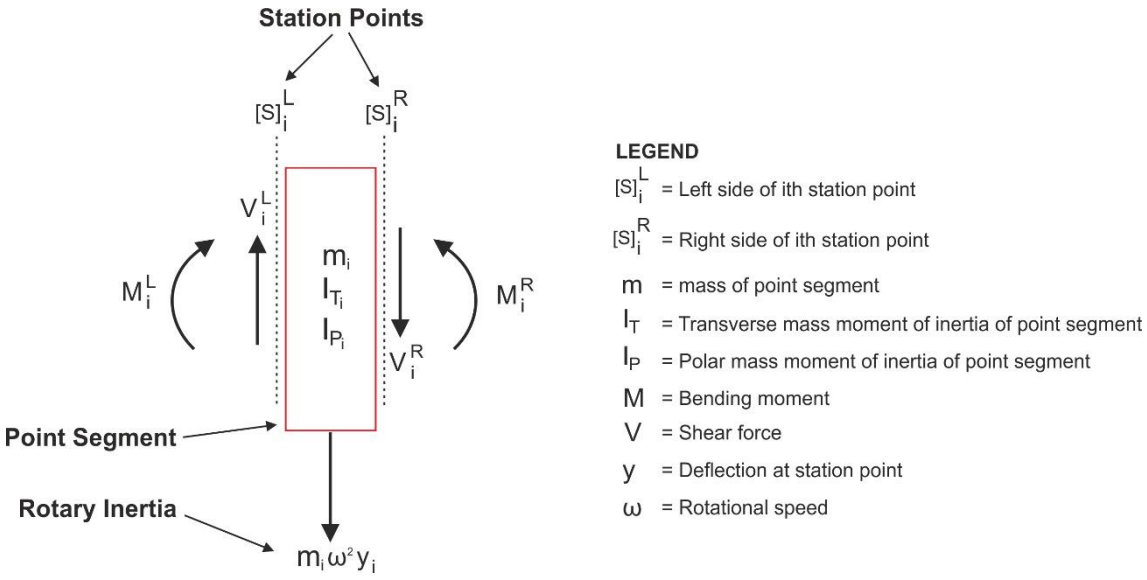

Figure 3-4 Rotary inertia loading free body diagram

In Figure 3-4, m_i is the concentrated mass, I_{Ti} is the transverse mass moment of inertia and I_{Pi} is the polar mass moment of inertia.

For a disc or concentrated mass subjected to rotary inertia loading as shown in Figure 3-4, to maintain continuity in the state vector, the deflection, slope and bending moment at the stations left $(i)^L$ and right $(i)^R$ of the disc or concentrated mass must be equal.

This is mathematically expressed as:

$$y_i^R = y_i^L \qquad 3\text{-}17$$

$$\theta_i^R = \theta_i^L \quad \text{3-18}$$

$$M_i^R = M_i^L \quad \text{3-19}$$

where y_i^R, θ_i^R & M_i^R are the deflection, slope and bending moment at the right side of the disc respectively and y_i^L, θ_i^L & M_i^L are the deflection, slope and bending moment at the left side of the disc respectively.

Although for the rotary inertia loading there is continuity in deflection, slope and bending moment, it causes a discontinuity in the shear force.

This is represented mathematically as:

$$V_i^R = V_i^L - m_i\omega^2 y_i \quad \text{3-20}$$

where V is shear force, m is mass of disc, ω is the rotary speed and y_i is the deflection.

Rearranging Equations 3-17, 3-18, 3-19 and 3-20 into the matrix form, results in:

$$\begin{bmatrix} -y \\ \theta \\ M \\ V \end{bmatrix}_i^R = \begin{bmatrix} 1 & 0 & 0 & 0 \\ 0 & 1 & 0 & 0 \\ 0 & 0 & 1 & 0 \\ m\omega^2 & 0 & 0 & 1 \end{bmatrix} \begin{bmatrix} -y \\ \theta \\ M \\ V \end{bmatrix}_i^L \quad \text{3-21}$$

$$[S]_i^R = [P]_i\,[S]_i^L \quad \text{3-22}$$

where $[S]_i^R$ is the state vector at the right side of the i-th station, $[S]_i^L$ is the state vector at the left side of the i-th station and $[P]_i$ is the point matrix of the i-th station.

2) Gyroscopic Couple Matrix

When a disc rotates on a shaft, apart from its rotary inertia loading contribution, it further imposes a gyroscopic couple on the shaft as shown in Figure 3-5. The nature of the gyroscopic couple is such that it tends to stiffen the shaft.

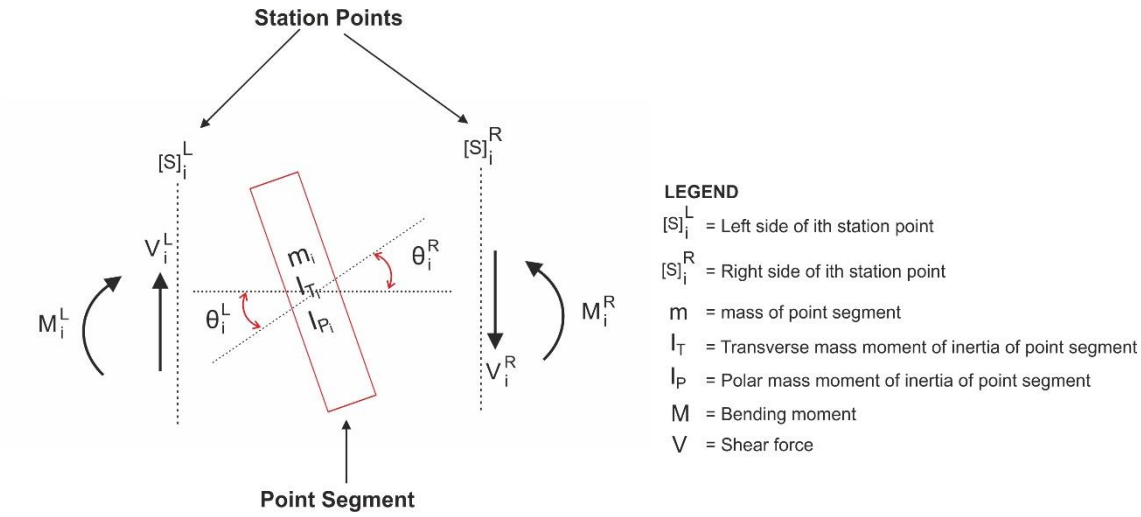

Figure 3-5 Rotating disc imposing gyroscopic couple on shaft

From the free body diagram in Figure 3-5, the relationship between the bending moment and the gyroscopic couple is:

$$M_i^R - M_i^L = I_T\ddot{\theta}_i = -\omega^2 I_T\theta_i \quad 3\text{-}23$$

$$M_i^R = M_i^L - \omega^2 I_T\theta_i \quad 3\text{-}24$$

where M_i^R & M_i^L are the bending moment at the right and left side of the disc respectively, θ_i is the slope, ω is rotor speed and I_T is transverse mass moment of inertia.

Since the gyroscopic couple affects the bending moment only, for there to be continuity of the state vector, the deflection, slope and shear force at the left and right side of the disc must be equal.

Thus,

$$y_i^R = y_i^L \quad 3\text{-}25$$

$$\theta_i^R = \theta_i^L \quad 3\text{-}26$$

$$M_i^R = M_i^L - \omega^2 I_T\theta_i \quad 3\text{-}27$$

$$V_i^R = V_i^L \quad 3\text{-}28$$

Expressing Equations 2-25, 2-26, 2-27 and 2-28 in the matrix form, they become:

$$\begin{bmatrix} -y \\ \theta \\ M \\ V \end{bmatrix}_i^R = \begin{bmatrix} 1 & 0 & 0 & 0 \\ 0 & 1 & 0 & 0 \\ 0 & -\omega^2 I_T & 1 & 0 \\ 0 & 0 & 0 & 1 \end{bmatrix} \begin{bmatrix} -y \\ \theta \\ M \\ V \end{bmatrix}_i^L \quad \text{3-29}$$

3) Unbalance Matrix

For rotating machineries, unbalance occurs when there is an offset between the rotor centre of rotation and its centre of mass.

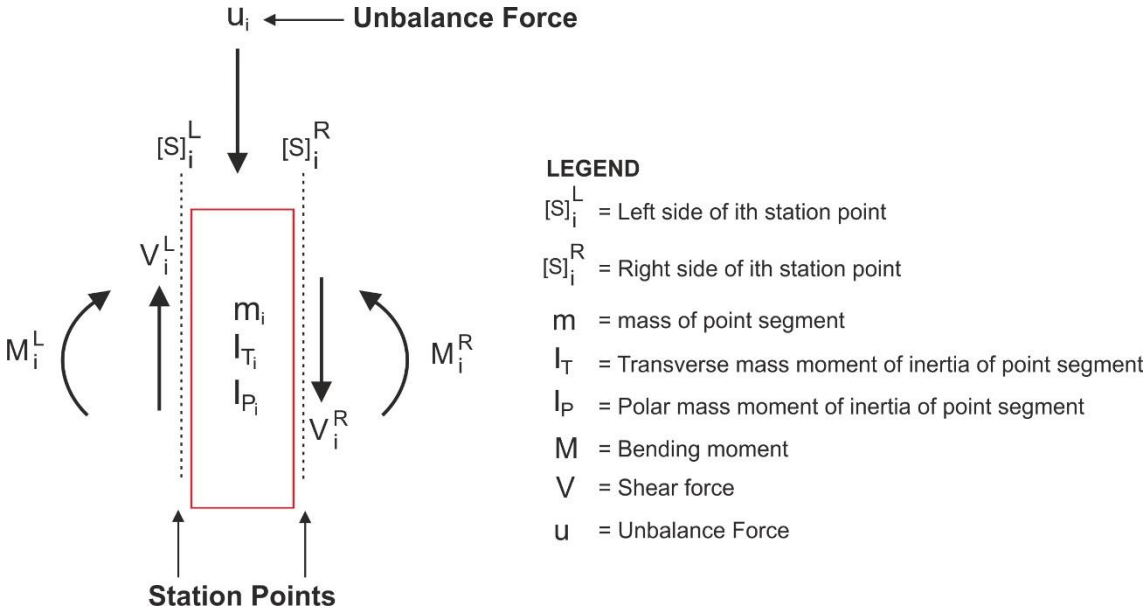

Figure 3-6 Unbalance acting on a disc or concentrated mass

For a disc or concentrated mass with an unbalance load as shown in Figure 3-6, a discontinuity in the shear force is created traversing from the left to the right side of the disc or concentrated load.

The relationship between the shear force and the unbalance is:

$$V_i^R = V_i^L - u_i \quad \text{3-30}$$

where V_i^R & V_i^L are the shear force at the right and left side of the disc or concentrated mass and u_i is the amount of unbalance.

Since the unbalance affects the shear force only, for there to be continuity in the state vector, the deflection, slope and bending moment on the right and left side of the disc or concentrated mass must be equal.

Thus,

$$y_i^R = y_i^L \tag{3-31}$$

$$\theta_i^R = \theta_i^L \tag{3-32}$$

$$M_i^R = M_i^L \tag{3-33}$$

$$V_i^R = V_i^L - u_i \tag{3-34}$$

The inclusion of the unbalance effect in the point matrix also causes the transformation of the state vector from a 4x1 matrix given in Equation 3-1 to a 5x1 matrix presented below:

$$[S] = \begin{bmatrix} -y \\ \theta \\ M \\ V \\ 1 \end{bmatrix} \tag{3-35}$$

From Equations 3-45, 3-46, 3-47, 3-48 and 3-49, the unbalance matrix is represented as:

$$\begin{bmatrix} -y \\ \theta \\ M \\ V \\ 1 \end{bmatrix}_i^R = \begin{bmatrix} 1 & 0 & 0 & 0 & 0 \\ 0 & 1 & 0 & 0 & 0 \\ 0 & 0 & 1 & 0 & 0 \\ 0 & 0 & 0 & 1 & -u \\ 0 & 0 & 0 & 0 & 1 \end{bmatrix} \begin{bmatrix} -y \\ \theta \\ M \\ V \\ 1 \end{bmatrix}_i^L \tag{3-36}$$

As a result of the transformation of the state vector to a 5x1 matrix, the field matrix also has to be enlarged to accommodate the extra row.

Therefore, the modified field matrix is represented as:

$$[F]_i = \begin{bmatrix} 1 & L & \frac{L^2}{2EI} & \left(\frac{L^3}{6EI} - \frac{\alpha_F L}{AG}\right) & 0 \\ 0 & 1 & \frac{L}{EI} & \frac{L^2}{2EI} & 0 \\ 0 & 0 & 1 & L & 0 \\ 0 & 0 & 0 & 1 & 0 \\ 0 & 0 & 0 & 0 & 1 \end{bmatrix} \quad \text{3-37}$$

4) Flexible Support Matrix

A flexible support can be used to represent the effect of a flexible foundation, bearing pedestal stiffness, simplified rolling-element bearing, etc.

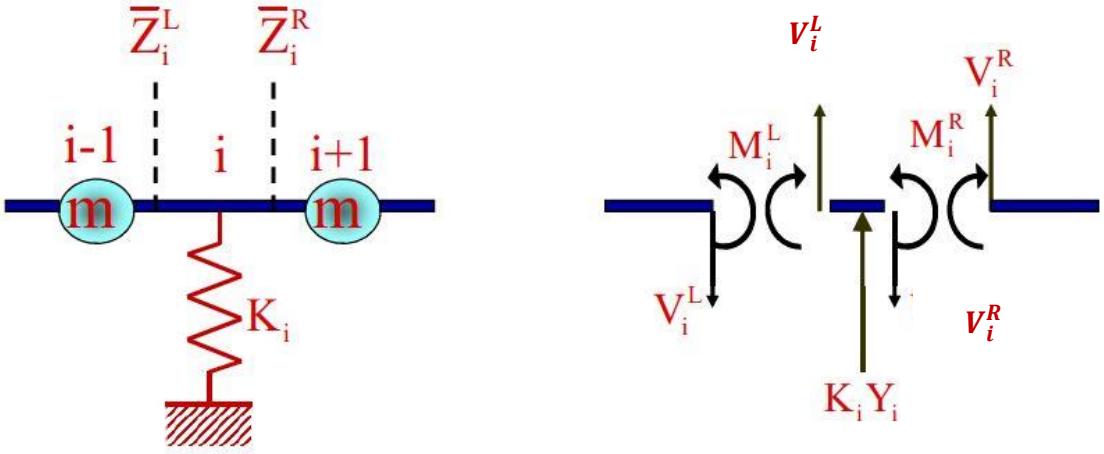

Figure 3-7 Flexible support free body diagram (Source: Mba, 2012)

The flexible support is viewed as a flexible spring with the restoring force such as:

$$F_i = K_i y_i \quad \text{3-38}$$

where K_i is the spring stiffness and y_i is the segment deflection.

The spring stiffness restoring force creates a discontinuity in the shear force; the relationship between the shear force and the spring stiffness restoring force is:

$$V_i^R = V_i^L + K_i y_i \quad \text{3-39}$$

where V_i^R & V_i^L are the shear forces at the right and left side of the point station, K_i is the stiffness of the support and y_i is the deflection at the point station.

Since the flexible support affects only the shear force, to ensure continuity of the state vector across the point station, the deflection, slope and bending moment across the point station are equal.

Thus,

$$y_i^R = y_i^L \quad \text{3-40}$$

$$\theta_i^R = \theta_i^L \quad \text{3-41}$$

$$M_i^R = M_i^L \quad \text{3-42}$$

$$V_i^R = V_i^L + K_i y_i \quad \text{3-43}$$

Rewriting Equations 3-40, 3-41, 3-42 and 3-43 into the matrix form:

$$\begin{bmatrix} -y \\ \theta \\ M \\ V \\ 1 \end{bmatrix}_i^R = \begin{bmatrix} 1 & 0 & 0 & 0 & 0 \\ 0 & 1 & 0 & 0 & 0 \\ 0 & 0 & 1 & 0 & 0 \\ -K & 0 & 0 & 1 & 0 \\ 0 & 0 & 0 & 0 & 1 \end{bmatrix} \begin{bmatrix} -y \\ \theta \\ M \\ V \\ 1 \end{bmatrix}_i^L \quad \text{3-44}$$

5) Combined Point Matrix

The combined point matrix is generated by combining the matrices of each discontinuity such as the rotor inertia matrix, gyroscopic couple matrix, unbalance matrix and the flexible support matrix.

The combined point matrix is represented as:

$$[P]_i = \begin{bmatrix} 1 & 0 & 0 & 0 & 0 \\ 0 & 1 & 0 & 0 & 0 \\ 0 & -\omega^2 I_T & 1 & 0 & 0 \\ (m\omega^2 - K) & 0 & 0 & 1 & -u \\ 0 & 0 & 0 & 0 & 1 \end{bmatrix} \quad \text{3-45}$$

3.2.5 Transfer Matrix Elimination Procedure

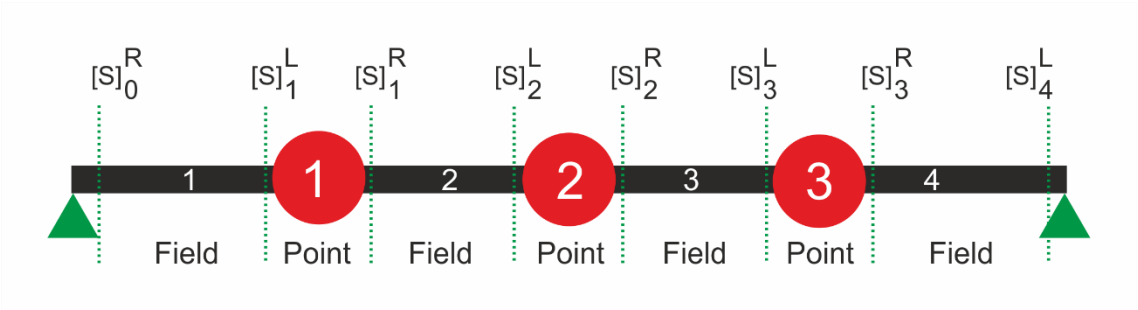

Figure 3-8 Representation of the intermediate state vector

As shown in Figure 3-8, a rotor in the transfer matrix method is viewed as a series of alternating field and point segments connected together.

The individual fields and points are first represented as individual field and point matrices from which the overall system matrix is derived.

The process of generating the overall system matrix leads to the elimination of the intermediate point and field matrices.

To further clarify the transfer matrix elimination method, the rotor model shown in Figure 3-8 is used as an example and its transfer matrix elimination procedure is shown in Table 3-1.

Table 3-1 Transfer matrix elimination procedure

Field Matrix	Point Matrix
$[S]_1^L = [F]_1\,[S]_0^R$	$[S]_1^R = [P]_1\,[S]_1^L$
$[S]_2^L = [F]_2\,[S]_1^R$	$[S]_2^R = [P]_2\,[S]_2^L$
$[S]_3^L = [F]_3\,[S]_2^R$	$[S]_3^R = [P]_3\,[S]_3^L$
$[S]_4^L = [F]_4\,[S]_3^R$	

The aim of the intermediate matrix elimination exercise is to arrive at a final expression that is a function of only the right and left boundary state vector, which in this case is $[S]_4^L$ and $[S]_0^R$ respectively as shown in Figure 3-8.

Starting with the field matrix equation $[S]_4^L$, the point matrix expression for $[S]_3^R$ is substituted into it and the result is:

$$[S]_4^L = [F]_4\,[P]_3\,[S]_3^L \qquad 3\text{-}46$$

The equation for the field matrix $[S]_3^L$ is also substituted into Equation 3-124, resulting in:

$$[S]_4^L = [F]_4\,[P]_3\,[F]_3\,[S]_2^R \qquad 3\text{-}47$$

If this process of substituting for the intermediate field and point equations is continue, the result overall state vector is:

$$[S]_4^L = [F]_4\,[P]_3\,[F]_3\,[P]_2\,[F]_2\,[P]_1\,[F]_1\,[S]_0^R \qquad 3\text{-}48$$

where $[S]_0^R$ and $[S]_4^L$ are boundary state matrices or conditions.

Equation 3-48 can further be expressed as:

$$[S]_4^L = [B][S]_0^R \qquad 3\text{-}49$$

$$\begin{bmatrix} -y \\ \theta \\ M \\ V \\ 1 \end{bmatrix}_4^L = \begin{bmatrix} b_{11} & b_{12} & b_{13} & b_{14} & b_{15} \\ b_{21} & b_{22} & b_{23} & b_{24} & b_{25} \\ b_{31} & b_{32} & b_{33} & b_{34} & b_{35} \\ b_{41} & b_{42} & b_{43} & b_{44} & b_{45} \\ 0 & 0 & 0 & 0 & 1 \end{bmatrix} \begin{bmatrix} -y \\ \theta \\ M \\ V \\ 1 \end{bmatrix}_0^R \qquad 3\text{-}50$$

where $[B]$ is the overall rotor matrix.

3.2.6 Frequency Matrix & Critical Speed Determination

The frequency matrix is a reduced form of the overall rotor system matrix used to determine the rotor natural frequencies or critical speeds.

The frequency matrix is generated by imposing boundary conditions on the overall rotor system matrix.

The possible boundary conditions for a 1D beam element are:

1. **Pinned End**

   For the pinned end boundary condition, the deflection and bending moment are zero at the end boundary.

   This is represented in the matrix form as:

$$[S] = \begin{bmatrix} -y \\ \theta \\ M \\ V \\ 1 \end{bmatrix} = \begin{bmatrix} 0 \\ \theta \\ 0 \\ V \\ 1 \end{bmatrix} \qquad 3\text{-}51$$

2. Free End

For the free end boundary condition, the bending moment and shear force are zero at the end boundary.

In the matrix form, this is represented as:

$$[S] = \begin{bmatrix} -y \\ \theta \\ M \\ V \\ 1 \end{bmatrix} = \begin{bmatrix} -y \\ \theta \\ 0 \\ 0 \\ 1 \end{bmatrix} \quad \text{3-52}$$

3. Fixed End

For the fixed end boundary condition, the deflection and slope are zero at the end boundary

$$[S] = \begin{bmatrix} -y \\ \theta \\ M \\ V \\ 1 \end{bmatrix} = \begin{bmatrix} 0 \\ 0 \\ M \\ V \\ 1 \end{bmatrix} \quad \text{3-53}$$

4. Flexible Support End

For the flexible support end boundary condition, the bending moment and shear force are zero at the end boundary.

This is represented in the matrix form as:

$$[S] = \begin{bmatrix} -y \\ \theta \\ M \\ V \\ 1 \end{bmatrix} = \begin{bmatrix} -y \\ \theta \\ 0 \\ 0 \\ 1 \end{bmatrix} \quad \text{3-54}$$

The boundary condition is first applied from the left end boundary station then the right end boundary condition is applied.

The application of the boundary condition for a simply supported rotor (pin-pin ends) is presented below to provide more clarity on the end boundary condition application.

Applying the condition of a pin-pin end boundary (simply supported) given in Equation 3-51 to the overall rotor matrix in Equation 3-50, results in:

$$\begin{bmatrix} 0 \\ \theta \\ 0 \\ V \\ 1 \end{bmatrix}_4^L = \begin{bmatrix} b_{11} & b_{12} & b_{13} & b_{14} & b_{15} \\ b_{21} & b_{22} & b_{23} & b_{24} & b_{25} \\ b_{31} & b_{32} & b_{33} & b_{34} & b_{35} \\ b_{41} & b_{42} & b_{43} & b_{44} & b_{45} \\ 0 & 0 & 0 & 0 & 1 \end{bmatrix} \begin{bmatrix} 0 \\ \theta \\ 0 \\ V \\ 1 \end{bmatrix}_0^R \quad \text{3-55}$$

The simplification of Equation 3-55 results in the frequency determinant, given as:

$$\begin{vmatrix} b_{12} & b_{14} \\ b_{32} & b_{34} \end{vmatrix} = 0 \quad \text{3-56}$$

where some of the terms b_{ij} in the determinant are function of the critical speed.

The solutions of the frequency determinant in Equation 3-56 would involve an iterative process for finding the roots of the equation. Numerical methods like the secant method, false position method, etc. lend themselves useful in this scenario.

A summary of the iterative steps for determining critical speed via the transfer matrix method is:

- Step 1: Guess a trial speed
- Step 2: Generate the intermediate field and point matrices
- Step 3: Determine the overall rotor matrix
- Step 4: Apply the boundary conditions
- Step 5: Determine the determinant of the frequency matrix. If its value is within the error tolerance, then the guess speed is the critical speed otherwise repeat the process with an improved guess based on the adopted numerical root searching technique.

3.2.7 Determination of Rotor Mode Shape or Forced Response

The mode shape of a rotor is a specific pattern of rotor displacement or vibration synonymous with a particular natural frequency (Azima, 2009).

To highlight the process of determining a rotor's mode shape or forced response, the rotor configuration in Figure 3-8 is used as an example.

Recalling Equation 3-55, the overall matrix of the rotor with the boundary conditions (pinned-pinned) applied is:

$$\begin{bmatrix} 0 \\ \theta \\ 0 \\ V \\ 1 \end{bmatrix}_4^L = \begin{bmatrix} b_{11} & b_{12} & b_{13} & b_{14} & b_{15} \\ b_{21} & b_{22} & b_{23} & b_{24} & b_{25} \\ b_{31} & b_{32} & b_{33} & b_{34} & b_{35} \\ b_{41} & b_{42} & b_{43} & b_{44} & b_{45} \\ 0 & 0 & 0 & 0 & 1 \end{bmatrix} \begin{bmatrix} 0 \\ \theta \\ 0 \\ V \\ 1 \end{bmatrix}_0^R \quad \text{3-57}$$

From Equation 3-57, considering the 1st and 3rd rows only:

$$\begin{bmatrix} b_{12} \\ b_{32} \end{bmatrix} \begin{bmatrix} \theta \\ V \end{bmatrix}_0^R = \begin{bmatrix} -b_{15} \\ -b_{35} \end{bmatrix} \quad \text{3-58}$$

$$\begin{bmatrix} \theta \\ V \end{bmatrix}_0^R = \begin{bmatrix} b_{12} \\ b_{32} \end{bmatrix}^{-1} \begin{bmatrix} -b_{15} \\ -b_{35} \end{bmatrix} \quad \text{3-59}$$

From Equation 3-57, considering the 2nd and 4th rows only:

$$\begin{bmatrix} \theta \\ V \end{bmatrix}_4^L = \begin{bmatrix} b_{22} & b_{24} \\ b_{42} & b_{44} \end{bmatrix} \begin{bmatrix} \theta \\ V \end{bmatrix}_0^R + \begin{bmatrix} b_{25} \\ b_{45} \end{bmatrix} \quad \text{3-60}$$

Depending on the nature of the vibration analysis i.e. free or forced, Equations 3-59 and 3-60 is then used to determine the rotor mode shape or forced vibration response.

3.2.8 2D Transfer Matrix Method

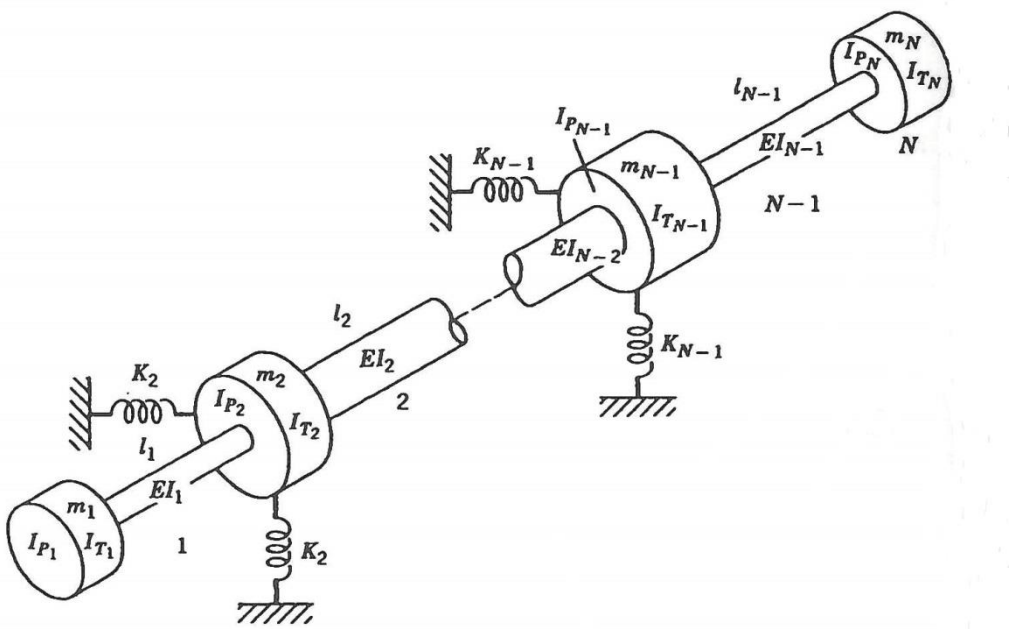

Figure 3-9 2D rotor configuration (Source: Vance, 1988)

The 1D transfer matrix method presented previously was mainly to illustrate the transfer matrix method. In other to account for the coupling between the horizontal and vertical plane which exist due to the presence of gyroscopic effects from disc and stiffness & damping forces from bearings e.g. journal bearings, the 2D transfer matrix method is the preferable choice. The 2D transfer matrix method has been adopted in this research for the development of the rotordynamic code.

All the expressions for the field matrix, point matrix, overall rotor matrix and state vector developed for the 1D transfer matrix method still hold for the 2D transfer matrix method; to avoid repetition, a more concise presentation is adopted.

1. Standard Rotor Element

The standard rotor element shown in Figure 3-10 represents the basic building block of the transfer matrix rotor. It is made up of a state vector [S], field matrix [F] and point matrix [P]. The point matrix acts as a point of attachment of the bearing, unbalance mass and other external forces.

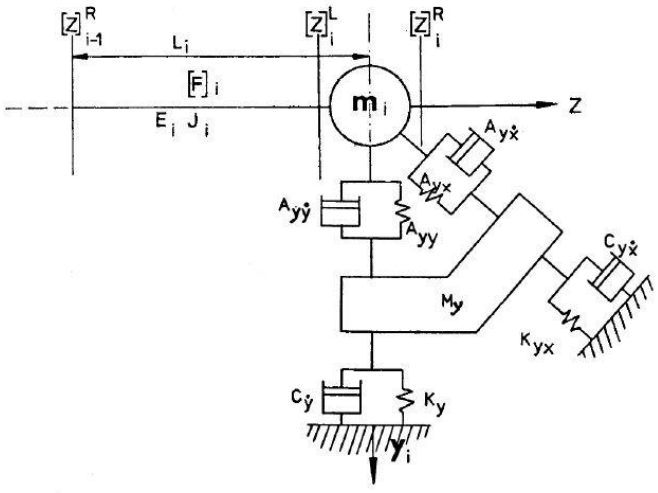

Figure 3-10 Standard element of the transfer matrix rotor (Source: Mba, 2012)

2. State Vector

The state vector in Equation 3-1 is extended to the current 2D form (Mba, 2012):

$$[S]_i = [-y \quad \varphi \quad M_y \quad V_y \quad \vdots \quad -x \quad \theta \quad M_x \quad V_x \quad \vdots \quad 1]_i \qquad 3\text{-}61$$

where y, φ, M_y & V_y are the displacement, slope, bending moment & shear force along the y-axis respectively and x, θ , M_x & V_x are the displacement, slope, bending moment & shear force along the x-axis respectively.

3. Field Matrix

The field matrix in Equation 3-15 is extended to the current 2D form to account for the elastic deformation of a shaft segment and the effect of shear deflection in the shat segment (Mba, 2012):

$$\begin{bmatrix} -y \\ \varphi \\ M_y \\ V_y \\ \cdots \\ -x \\ \theta \\ M_x \\ V_x \\ \cdots \\ 1 \end{bmatrix}_i^L = \left[\begin{array}{cccc:cccc:c} 1 & L & \frac{L^2}{2EI} & \left(\frac{L^3}{6EI}-\frac{\alpha_F L}{A_b G}\right) & 0 & 0 & 0 & 0 & 0 \\ 0 & 1 & \frac{L}{EI} & \frac{L^2}{2EI} & 0 & 0 & 0 & 0 & 0 \\ 0 & 0 & 1 & L & 0 & 0 & 0 & 0 & 0 \\ 0 & 0 & 0 & 1 & 0 & 0 & 0 & 0 & 0 \\ \cdots & \cdots & \cdots & \cdots & \cdots & \cdots & \cdots & \cdots & \cdots \\ 0 & 0 & 0 & 0 & 1 & L & \frac{L^2}{2EI} & \left(\frac{L^3}{6EI}-\frac{\alpha_F L}{A_b G}\right) & 0 \\ 0 & 0 & 0 & 0 & 0 & 1 & \frac{L}{EI} & \frac{L^2}{2EI} & 0 \\ 0 & 0 & 0 & 0 & 0 & 0 & 1 & L & 0 \\ 0 & 0 & 0 & 0 & 0 & 0 & 0 & 1 & 0 \\ \cdots & \cdots & \cdots & \cdots & \cdots & \cdots & \cdots & \cdots & \cdots \\ 0 & 0 & 0 & 0 & 0 & 0 & 0 & 0 & 1 \end{array}\right] \begin{bmatrix} -y \\ \varphi \\ M_y \\ V_y \\ \cdots \\ -x \\ \theta \\ M_x \\ V_x \\ \cdots \\ 1 \end{bmatrix}_{i-1}^R \quad \text{3-62}$$

$$[S]_i^L = [F]_i\,[S]_{i-1}^R \quad \text{3-63}$$

4. Point Matrix

The combined point matrix in Equation 3-45 is extended to the current 2D complex form to account for rotary inertia, bearing stiffness and damping coefficients, gyroscopic couple from disk, unbalance and aerodynamic forces (Mba, 2012):

$$\begin{bmatrix} -y \\ \varphi \\ M_y \\ V_y \\ \cdots \\ -x \\ \theta \\ M_x \\ V_x \\ \cdots \\ 1 \end{bmatrix}_i^R = \left[\begin{array}{cccc:cccc:c} 1 & 0 & 0 & 0 & 0 & 0 & 0 & 0 & 0 \\ 0 & 1 & 0 & 0 & 0 & 0 & 0 & 0 & 0 \\ 0 & -\Omega^2 I_T & 1 & 0 & 0 & -j\Omega^2 I_P & 0 & 0 & 0 \\ \begin{pmatrix} m\Omega^2 - K_{yy} \\ -j\Omega C_{yy} \end{pmatrix} & 0 & 0 & 1 & -\begin{pmatrix} K_{yx} \\ +j\Omega C_{yx} \end{pmatrix} & 0 & 0 & 0 & -(\Omega^2 u_y + \bar{F}_y^{ae}) \\ \cdots & \cdots & \cdots & \cdots & \cdots & \cdots & \cdots & \cdots & \cdots \\ 0 & 0 & 0 & 0 & 1 & 0 & 0 & 0 & 0 \\ 0 & 0 & 0 & 0 & 0 & 1 & 0 & 0 & 0 \\ 0 & -j\Omega^2 I_P & 0 & 0 & 0 & -\Omega^2 I_T & 1 & 0 & 0 \\ -\begin{pmatrix} K_{xy} \\ +j\Omega C_{xy} \end{pmatrix} & 0 & 0 & 0 & \begin{pmatrix} m\Omega^2 - K_{xx} \\ -j\Omega C_{xx} \end{pmatrix} & 0 & 0 & 1 & -(\Omega^2 u_x + \bar{F}_x^{ae}) \\ \cdots & \cdots & \cdots & \cdots & \cdots & \cdots & \cdots & \cdots & \cdots \\ 0 & 0 & 0 & 0 & 0 & 0 & 0 & 0 & 1 \end{array}\right] \begin{bmatrix} -y \\ \varphi \\ M_y \\ V_y \\ \cdots \\ -x \\ \theta \\ M_x \\ V_x \\ \cdots \\ 1 \end{bmatrix}_i^L \quad \text{3-64}$$

$$[S]_i^R = [P]_i\,[S]_i^L \quad \text{3-65}$$

5. Overall Matrix

From Equations 3-63 and 3-65, the relationship between the state vector and either the point or field matrix is summarised below:

$$[S]_i^L = [F]_i\,[S]_{i-1}^R$$

$$[S]_i^R = [P]_i\,[S]_i^L$$

Thus,

$$[S]_i^L = [P]_i\,[F]_i\,[S]_{i-1}^R \quad 3\text{-}66$$

$$[S]_i^L = [B]_i\,[S]_{i-1}^R \quad 3\text{-}67$$

where $[B]_i = [P]_i\,[F]_i$ is the standard element overall matrix

Based on the number of field and point elements, the overall rotor matrix is generated by continuous alternating matrix multiplication of a point matrix followed by a field matrix and the process repeats itself.

This is represented mathematically as,

$$[B] = [P]_i\,[F]_i[P]_{i-1}\,[F]_{i-1}[P]_{i-2}\,[F]_{i-2}\cdots[P]_1\,[F]_1 \quad 3\text{-}68$$

Since the point matrix is complex as seen in Equation 3-140, the overall rotor matrix would also be complex.

A simple technique to generate the overall rotor matrix and resolve the 2D transfer matrix from the complex matrices (i.e. point) is presented below.

Let the state vector, overall rotor matrix and forcing function due to unbalance and aerodynamic force be expressed as:

$$[S]_i = [S]_i^r + j[S]_i^i \quad 3\text{-}69$$

$$[B]_i = B_i^r + j[B]_i^i \quad 3\text{-}70$$

$$[g]_i = g_i^r + j[g]_i^i \quad 3\text{-}71$$

where $[S]_i$ is the state vector, $[S]_i^r$ & $[S]_i^i$ are the real and imaginary components of the state vector respectively, $[B]_i$ is the overall rotor matrix, $[B]_i^r$ & $[B]_i^i$ are the real and imaginary component of the overall rotor matrix respectively, $[g]_i$ is the forcing function matrix, $[g]_i^r$ & $[g]_i^i$ are the real and imaginary component of the forcing function matrix respectively.

Then,

$$\begin{bmatrix} S^r \\ \cdots \\ S^i \\ \cdots \\ 1 \end{bmatrix}_i = \begin{bmatrix} B^r & \vdots & -B^i & \vdots & g^r \\ \cdots & \vdots & \cdots & \vdots & \cdots \\ B^i & \vdots & B^r & \vdots & g^i \\ \cdots & \vdots & \cdots & \vdots & \cdots \\ 0 & \vdots & 0 & \vdots & 1 \end{bmatrix} \begin{bmatrix} S^r \\ \cdots \\ S^i \\ \cdots \\ 1 \end{bmatrix}_{i-1} \qquad 3\text{-}72$$

The resulting overall rotor matrix in the above expression in Equation 3-72 is a 17x17 matrix.

The processes of simplifying the overall rotor matrix in Equation 3-72 is the same as that outlined in the 1D transfer matrix method.

Step1: Generation of the overall rotor matrix as represented in Equation 3-72.

Step 2: Application of the boundary condition.

For example, for a free-free boundary support recalling the boundary condition in Equation 3-52 (Mba, 2012):

$$[S]_0 = [-y^r \quad \varphi^r \quad 0 \quad 0 \quad -x^r \quad \theta^r \quad 0 \quad 0 \; \vdots -y^i \quad \varphi^i \quad 0 \quad 0 \quad -x^i \quad \theta^i \quad 0 \quad 0 \quad \vdots \quad 1]_0 \qquad 3\text{-}73$$

$$[S]_n = [-y^r \quad \varphi^r \quad 0 \quad 0 \quad -x^r \quad \theta^r \quad 0 \quad 0 \; \vdots -y^i \quad \varphi^i \quad 0 \quad 0 \quad -x^i \quad \theta^i \quad 0 \quad 0 \quad \vdots \quad 1]_n \qquad 3\text{-}74$$

The final reduced matrix for a free-free boundary condition is (Mba, 2012),

$$\begin{bmatrix} b_{31} & b_{32} & b_{35} & b_{36} & b_{3,9} & b_{3,10} & b_{3,13} & b_{3,14} \\ b_{41} & b_{42} & b_{45} & b_{46} & b_{4,9} & b_{4,10} & b_{4,13} & b_{4,14} \\ b_{71} & b_{72} & b_{75} & b_{76} & b_{7,9} & b_{7,10} & b_{7,13} & b_{7,14} \\ b_{81} & b_{82} & b_{85} & b_{86} & b_{8,9} & b_{8,10} & b_{8,13} & b_{8,14} \\ b_{11,1} & b_{11,2} & b_{11,5} & b_{11,6} & b_{11,9} & b_{11,10} & b_{11,13} & b_{11,14} \\ b_{12,1} & b_{12,2} & b_{12,5} & b_{12,6} & b_{12,9} & b_{12,10} & b_{12,13} & b_{12,14} \\ b_{15,1} & b_{15,2} & b_{15,5} & b_{15,6} & b_{15,9} & b_{15,10} & b_{15,13} & b_{15,14} \\ b_{16,1} & b_{16,2} & b_{16,5} & b_{16,6} & b_{16,9} & b_{16,10} & b_{16,13} & b_{16,14} \end{bmatrix} \begin{bmatrix} -y_0^r \\ \varphi_0^r \\ -x_0^r \\ \theta_0^r \\ -y_0^i \\ \varphi_0^i \\ -x_0^i \\ \theta_0^i \end{bmatrix} + \begin{bmatrix} g_3^r \\ g_4^r \\ g_7^r \\ g_8^r \\ g_{11}^i \\ g_{12}^i \\ g_{15}^i \\ g_{16}^i \end{bmatrix} = 0 \qquad 3\text{-}75$$

$$\begin{bmatrix} b_{31} & b_{32} & b_{35} & b_{36} & b_{3,9} & b_{3,10} & b_{3,13} & b_{3,14} \\ b_{41} & b_{42} & b_{45} & b_{46} & b_{4,9} & b_{4,10} & b_{4,13} & b_{4,14} \\ b_{71} & b_{72} & b_{75} & b_{76} & b_{7,9} & b_{7,10} & b_{7,13} & b_{7,14} \\ b_{81} & b_{82} & b_{85} & b_{86} & b_{8,9} & b_{8,10} & b_{8,13} & b_{8,14} \\ b_{11,1} & b_{11,2} & b_{11,5} & b_{11,6} & b_{11,9} & b_{11,10} & b_{11,13} & b_{11,14} \\ b_{12,1} & b_{12,2} & b_{12,5} & b_{12,6} & b_{12,9} & b_{12,10} & b_{12,13} & b_{12,14} \\ b_{15,1} & b_{15,2} & b_{15,5} & b_{15,6} & b_{15,9} & b_{15,10} & b_{15,13} & b_{15,14} \\ b_{16,1} & b_{16,2} & b_{16,5} & b_{16,6} & b_{16,9} & b_{16,10} & b_{16,13} & b_{16,14} \end{bmatrix} \begin{bmatrix} -y_0^r \\ \varphi_0^r \\ -x_0^r \\ \theta_0^r \\ -y_0^i \\ \varphi_0^i \\ -x_0^i \\ \theta_0^i \end{bmatrix} = - \begin{bmatrix} g_3^r \\ g_4^r \\ g_7^r \\ g_8^r \\ g_{11}^i \\ g_{12}^i \\ g_{15}^i \\ g_{16}^i \end{bmatrix} \quad \text{3-76}$$

Equation 3-76 can be simply represented as:

$$[E]\{S\}_0 = \{G\} \quad \text{3-77}$$

The critical speeds are determined by equating the matrix $[E]$ to zero.

The state vector at the left most boundary condition $\{S\}_0$ is determined by:

$$\{S\}_0 = [E]^{-1}\{G\} \quad \text{3-78}$$

Once the state vector of the left most boundary condition has been determined, the state vector at other points along the rotor can then be found by stepping through the transfer matrix.

For example, the state vector at the first and second station from the left most boundary condition can be found by:

$$\{S\}_1^r = [P]_1[F]_1\{S\}_0$$

$$\{S\}_2^r = [P]_2[F]_2[P]_1[F]_1\{S\}_0$$

3.3 External Forces

Although there are several sources of vibration excitation which may be internal or external to the rotor-bearing system, in this research, only two excitation sources are considered: unbalance force and aerodynamic force.

The unbalance force contribution to the rotordynamic model has been discussed earlier during the development of the transfer matrix method; therefore, attention would now shift to the development of the aerodynamic force contribution.

3.3.1 Aerodynamic Force

Aerodynamic forces also called fluid-induced forces are generated due to the contact and interaction between a fluid (liquid or gas) and a solid object.

In modelling the aerodynamic forces present in an axial compressor, the approach by Al-Nahwi (2000) is adopted. According to Al-Nahwi (2000), the aerodynamic force in an axial compressor is due to the presence of a non-uniform flow field in the compressor, surrounding and exchanging momentum with the compressor rotor. The non-uniform compressor flow field generates an aerodynamic force that is made up of three different force components, which are:

a) **Turning Force**

   The turning force is due to the presence of a non-uniform circumferential distribution of the axial flow velocity coefficient caused by the non-uniform flow field. The non-uniform circumferential flow velocity coefficient causes the rotor blades to be subjected to uneven loads, the integrated effect of this uneven blade loads is the turning force.

b) **Pressure Force**

   The pressure force is due to the hydrostatic pressure distribution around the compressor rotor.

c) **Unsteady Momentum Force**

   The unsteady momentum force is due to the storage of unsteady momentum within the compressor rotor.

3.3.2 Modelling of the Compressor Aerodynamic Force

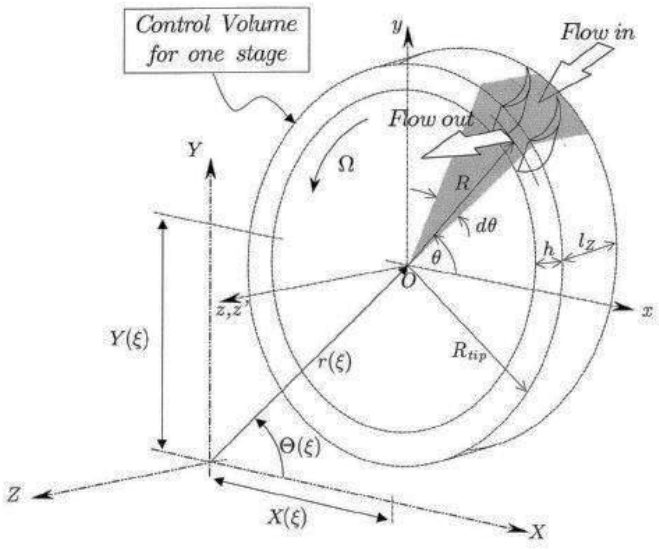

Figure 3-11 Control volume for modelling the aerodynamic force (Source: Al-Nahwi, 2000)

To derive the expressions for the aerodynamic force components, a stationary control volume attached to the geometric centre 'O' of the compressor rotor and fixed to the translating frame of reference, xyz, is chosen as shown in Figure 3-11, with the flow entering and leaving the compressor rotor stage as shown in Figure 3-11. The translating frame of reference, xyz, is chosen to ensure compatibility with the frame of reference of the Moore-Greitzer compressor flow field model described and developed in Chapter 2.

Based on control volume in Figure 3-11 and the conservation of momentum, Al-Nahwi (2000) proposed the following general expressions for the three aerodynamic component forces:

1) Turning Force

$$\bar{F}_{tu} = -\int_{cs} \bar{\mathrm{v}}_{xyz}\bar{\mathrm{v}}_{xyz}\rho d\mathcal{A} \qquad 3\text{-}79$$

where $\bar{F}_{tu}$ is the dimensional turning force, $\bar{\mathrm{v}}_{xyz}$ is the dimensional flow field velocity and ρ is the density of the fluid.

2) Pressure Force

$$\bar{F}_{pr} = -\int_{cs} p d\mathcal{A} \qquad 3\text{-}80$$

where $\bar{F}_{pr}$ is the dimensional pressure force and p is the dimensional pressure.

3) Unsteady Momentum Force

$$\bar{F}_{un} = -\frac{\partial}{\partial t}\int_{cv} \bar{\mathrm{v}}_{xyz}\rho d\mathcal{V} \qquad 3\text{-}81$$

where $\bar{F}_{un}$ is the dimensional unsteady momentum force, $\bar{\mathrm{v}}_{xyz}$ is the dimensional flow field velocity and ρ is the density of the fluid.

Thus, the total dimensional aerodynamic force $\bar{F}_{ae}$ is given by,

$$\bar{F}_{ae} = \bar{F}_{tu} + \bar{F}_{pr} + \bar{F}_{un} \qquad 3\text{-}82$$

$$\bar{F}_{ae} = -\int_{cs} \bar{\mathrm{v}}_{xyz}\bar{\mathrm{v}}_{xyz}\rho d\mathcal{A} - \int_{cs} p d\mathcal{A} - \frac{\partial}{\partial t}\int_{cv} \bar{\mathrm{v}}_{xyz}\rho d\mathcal{V} \qquad 3\text{-}83$$

To evaluate the integrals in Equation 3-83, knowledge of the pressures p and velocity $\bar{\mathrm{v}}_{xyz}$ of the flowfield at the inlet, exit and inter-stages of the compressor is required. The Moore-Greitzer model developed in Chapter 2, provides the flowfield pressures and flow velocity coefficient at the inlet and exit of the compressor. Since the inter-stage flowfield parameters cannot be gotten from the Moore-Greitzer model, a linear distribution of the flow field parameters at the various inter-stage is assumed in other to relate the inter-stage flowfield parameters with the inlet and exit flow field parameters gotten from the Moore-Greitzer model. This assumption has also been adopted by Al-Nahwi (2000).

3.3.3 Non-dimensionalization of the Aerodynamic Force Expressions

The non-dimensionalization of the aerodynamic force integral in Equation 3-83 is necessary to ensure compatibility with the Moore-Greitzer flow field model. The non-dimensionalization process involves transforming dimensional flow velocity $\bar{\mathrm{v}}_{xyz}$ to flow velocity coefficient ϕ and pressure p to a function of $p_I \; and \; p_E$.

The non-dimensionalization of the components of the aerodynamic force in equations 3-79, 3-80 and 3-81 is based on the non-dimensionalization scheme for the Moore-Greitzer model described in Chapter 2 where,

- **Time:** is expressed as radian of wheel travel ξ

$$\xi = Ut/R$$

$$\therefore \xi = \Omega t$$

  where $U = \Omega R$ is the compressor wheel speed at the mean radius, Ω is compressor wheel spin speed, R is the mean compressor wheel radius and t is time.

- **Pressure:** all pressures are non-dimensionalized by dividing with ρU^2. E.g. $p/(\rho U^2)$, where p is pressure, ρ is density and U is the compressor wheel speed at the mean radius.
- **Velocity:** all velocity values are non-dimensionalized by dividing with the compressor wheel speed at mean radius, $U = \Omega R$.
  i. Non-dimensional flow velocity $v_{xyz} = \bar{v}_{xyz}/\Omega R$, where $\bar{v}_{xyz}$ is the dimensional flow velocity, Ω is the compressor wheel spin speed and R is mean compressor wheel radius.

Thus, the non-dimensionalization of Equations 3-79, 3-80 and 3-81 is given by (Al-Nahwi, 2000):

$$\bar{F}_{tu} = -\rho R^2 \Omega^2 A_{tu} \int_{cs} v_{xyz} v_{xyz} \frac{d\mathcal{A}}{A_{tu}} \qquad 3\text{-}84$$

$$\bar{F}_{pr} = -\rho R^2 \Omega^2 A_{pr} \int_{cs} \frac{p}{\rho R^2 \Omega^2} \frac{d\mathcal{A}}{A_{pr}} \qquad 3\text{-}85$$

$$\bar{F}_{un} = -\rho R \Omega^2 V_{un} \frac{\partial}{\partial \xi} \int_{cv} v_{xyz} \frac{d\mathcal{V}}{V_{un}} \qquad 3\text{-}86$$

where $\bar{F}_{tu}, \bar{F}_{pr}$ & $\bar{F}_{tu}$ are the dimensional turning, pressure and unsteady force respectively, v_{xyz} is the non-dimensional flow velocity, A_{tu} is a factor proportional to the area through which the flow passes, A_{pr} is a factor proportional to the area upon which the pressure acts and V_{tu} is a factor proportional to the volume within which momentum is stored.

From Figure 3-11, A_{tu}, A_{pr} and V_{un} can be expressed as (Al-Nahwi, 2000):

$$A_{tu} = 2\pi \mathrm{NRh} \tag{3-87}$$

$$A_{pr} = 2\pi(2\mathrm{N})\mathrm{R}l_z = 4\pi \mathrm{NR}l_z \tag{3-88}$$

$$V_{un} = 2\pi \mathrm{NRh}l_z \tan\gamma \tag{3-89}$$

Where N is the number of blade row stages, R is the mean compressor wheel radius, h is the blade span, $l_z = l\cos\gamma$ is the axial blade chord, l is the blade chord and γ is the blade stagger angle.

The factor $(2\mathrm{N})$ is included in the expression for the pressure force area A_{pr} in Equation 3-88 because, the pressure acts both within the hub in a blade row and on the hub between blade rows.

The final non-dimensionalized expressions for the aerodynamic component forces is gotten by dividing Equations 3-84, 3-85 and 3-86 by $Ml\Omega^2$ and substituting for A_{tu}, A_{pr} and V_{un} into Equations 3-84, 3-85 and 3-86.

$$F_{tu} = -\chi\,\lambda_{tu}\int_{cs} v_{xyz}v_{xyz}\frac{d\mathcal{A}}{A_{tu}} \tag{3-90}$$

$$F_{pr} = -\chi\,\lambda_{pr}\int_{cs} \frac{p}{\rho R^2\Omega^2}\frac{d\mathcal{A}}{A_{pr}} \tag{3-91}$$

$$F_{un} = -\chi\,\lambda_{un}\frac{\partial}{\partial\xi}\int_{cv} v_{xyz}\frac{d\mathcal{V}}{V_{un}} \tag{3-92}$$

$$F_{ae} = F_{tu} + F_{pr} + F_{un}$$

$$F_{ae} = -\chi\left[\lambda_{tu}\int_{cs} v_{xyz}v_{xyz}\frac{d\mathcal{A}}{A_{tu}} + \lambda_{pr}\int_{cs} \frac{p}{\rho R^2\Omega^2}\frac{d\mathcal{A}}{A_{pr}} + \lambda_{un}\frac{\partial}{\partial\xi}\int_{cv} v_{xyz}\frac{d\mathcal{V}}{V_{un}}\right] \tag{3-93}$$

where F_{tu}, F_{pr}, F_{un} & F_{ae} are the non-dimensional turning force, pressure force, unsteady momentum force and total aerodynamic force respectively, χ is the aerodynamic-rotordynamic domain coupling factor, λ_{tu}, λ_{pr} & λ_{un} are the scale

factors for the turning force, pressure force and unsteady momentum force respectively.

3.3.4 Aerodynamic Force Coupling and Scale Factors

The aerodynamic-rotordynamic domain coupling factor χ, defines the nature of the link between the aerodynamic domain and the rotordynamic domain in an axial compressor.

Mathematically, it is defined as (Al-Nahwi, 2000):

$$\chi = \frac{N\rho(2\pi Rhl_z)}{NM_{st}} = \frac{mass\ of\ fluid\ within\ control\ volume}{mass\ of\ \ compressor\ rotor} \qquad 3\text{-}94$$

When $\chi = 0$, it means there is no link between the two domain, while a larger number implies a strong link between both domains.

The aerodynamic-rotordynamic domain coupling factor can also be viewed as the ratio between the mass of the fluid in a single blade-row to the mechanical mass of that blade-row. This results in a further simplification as the ratio between the fluid density ρ and the density of the blade row material ρ_s, i.e. $\chi = {}^{\rho}/_{\rho_s}$ based on the assumption that the mechanical mass of a blade-row is proportional to $\rho_s(2\pi Rhl_z)$.

An implication of the above density ratio definition for the aerodynamic-rotordynamic domain coupling factor χ is, a strong connection between both domains is favoured by either a denser fluid or a lighter rotor.

On the other hand, the scale factors for the turning force λ_{tu}, pressure force λ_{pr} and unsteady momentum force λ_{un} are defined as:

$$\lambda_{tu} = \left(\frac{R}{l_z}\right)^2 \cos\gamma = \frac{1}{(AR)_s^2}\cos\gamma \qquad 3\text{-}95$$

$$\lambda_{pr} = 2\left(\frac{R}{l_z}\right)^2\left(\frac{l}{h}\right)\cos^2\gamma = 2\frac{1}{(AR)_s^2}\frac{1}{(AR)_b}\cos^2\gamma \qquad 3\text{-}96$$

$$\lambda_{un} = \left(\frac{R}{l_z}\right)\cos\gamma\tan\gamma = \frac{1}{(AR)_s}\cos\gamma\tan\gamma \qquad 3\text{-}97$$

where $(AR)_s$ and $(AR)_b$ are the stage and blade aspect ratio respectively, R is the mean compressor wheel radius, l_z is the blade axial chord, l is the blade chord, h is the blade height and γ is the blade stagger angle.

3.3.5 Significance of the Aerodynamic Force Scale Factors

The scale factors λ_{tu}, λ_{pr} and λ_{un} are responsible for scaling the turning force, pressure force and the unsteady momentum force respectively. From Equations 3-95, 3-96 and 3-97, these scaling factors are shown to depend on the stage aspect ratio $(AR)_s$, blade aspect ratio $(AR)_b$ and the blade stagger angle.

The results presented in Figure 3-12 and Figure 3-13 is a Matlab implementation of Equations 3-95, 3-96 and 3-97 for the parametric study of effect of the blade and stage aspect ratio on the aerodynamic force scale factors in the well documented MIT 3-stage axial compressor reported by Gamache (1985). A summary of the geometric dimensions of the MIT 3-stage axial compressor is provided in Appendix B. These parametric studies provide clarity into the general nature and significance of the aerodynamic force scale factors.

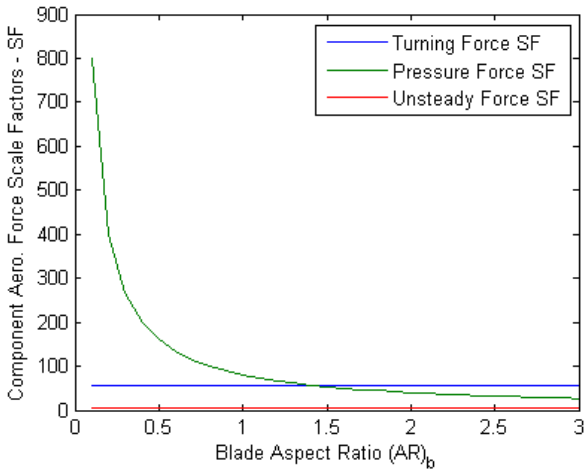

Figure 3-12 Effect of blade aspect ratio on the aerodynamic force component scale factors

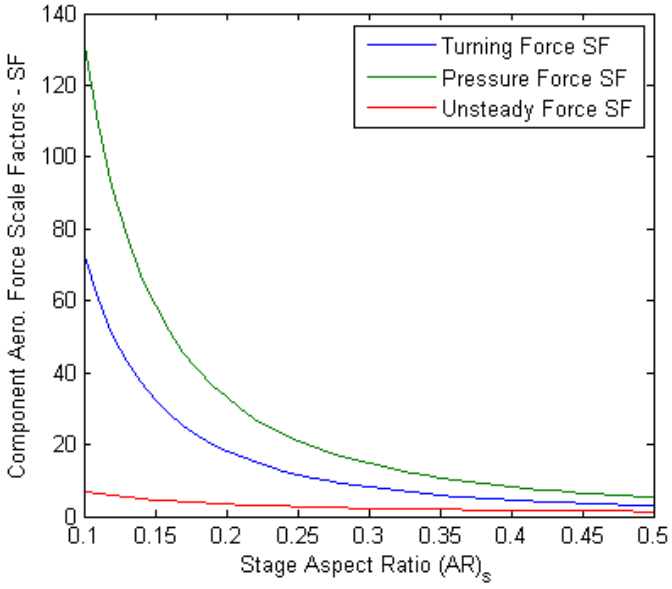

Figure 3-13 Effect of stage aspect ratio on the aerodynamic force component scale factors

From Figure 3-12, keeping the stage aspect ratio constant, while varying the blade aspect ratio, it becomes obvious that both the turning force and unsteady momentum force are not affected by a variation in the blade aspect ratio. The pressure force is the only force that is affected by a variation in the blade aspect ratio.

Another point observed from Figure 3-12, at low blade aspect ratio $(AR)_b < 1$ i.e. shorter blades, the pressure force scale factor experiences a sharp rise. On the other hand, as the blade aspect ratio increases, there is a subsequent decrease in the pressure force scale factor.

The observation of the adverse effect of increase in blade aspect ratio on the performance of an axial compressor has been reported by Horlock and Fahmi (1966) with further experimental evidence in Horlock et. al. (1964) and Emery et al. (1958). According to Horlock and Fahmi (1966), the adverse effect of blade aspect ratio increase on axial compressor performance can be attributed to one or more of the following reasons: the difference in the nature of secondary and tip clearance flows, the difference in the 3D axisymmetric flow and difference in performance of the different blade-row acting as a diffuser.

Thus, the pressure force scale factor lends itself as a suitable non-dimensional parameter that can be used to access and compare the effect of blade aspect ratio variation on the performance of a blade row.

On the other hand, from Figure 3-13, the stage aspect ratio affects all the components of the aerodynamic force, more so for the pressure and turning force than the unsteady momentum force. The smaller the stage aspect ratio, the higher the scale factors for the pressure and turning force and vice versa.

3.3.6 General Aerodynamic Force Expressions

Recalling Equations 3-90, 3-91 and 3-92, the non-dimensional components of the aerodynamic force is given as:

$$F_{tu} = \chi[F_{tu}]_i = \chi \left[-\lambda_{tu} \int_{cs} \mathrm{v}_{xyz} \mathrm{v}_{xyz} \frac{d\mathcal{A}}{A_{tu}} \right] \quad 3\text{-}98$$

$$F_{pr} = \chi\left[F_{pr}\right]_i = \chi \left[-\lambda_{pr} \int_{cs} \frac{p}{\rho R^2 \Omega^2} \frac{d\mathcal{A}}{A_{pr}} \right] \quad 3\text{-}99$$

$$F_{un} = \chi[F_{un}]_i = \chi \left[-\lambda_{un} \frac{\partial}{\partial \xi} \int_{cv} \mathrm{v}_{xyz} \frac{d\mathcal{V}}{V_{un}} \right] \quad 3\text{-}100$$

where $[F_{tu}]_i$, $\left[F_{pr}\right]_i$ and $[F_{un}]_i$ are the non-dimensional average turning, pressure and unsteady momentum force per stage respectively.

3.3.7 Simplified Form of the Aerodynamic Force Expressions

Applying a similar assumption used by Spakovszky (2000a) and Al-Nahwi (2000) of an incompressible flow through a constant height compressor annulus of similar stages and Equations 3-98, 3-99 & 3-100 to the adopted control volume presented in Figure 3-11, Equations 3-98, 3-99 and 3-100 are simplified as:

$$F_{tu} = \chi[F_{tu}]_i = \chi \left[-\lambda_{tu} \frac{NRh}{A_{tu}} \int_0^{2\pi} \phi \left[(\mathrm{v}_{XYZ}^{out})_i - \left(\mathrm{v}_{XYZ}^{in}\right)_i \right] d\theta \right] \quad 3\text{-}101$$

$$F_{pr} = \chi\left[F_{pr}\right]_i = \chi \left[-\lambda_{pr} \frac{2NRl_z}{A_{pr}} \int_0^{2\pi} \frac{1}{2} \frac{p_I + p_E}{\rho R^2 \Omega^2} (\cos\theta\, \mathbf{i} + \sin\theta\, \mathbf{j}) d\theta \right] \quad 3\text{-}102$$

$$F_{un} = \chi[F_{un}]_i = \chi \left[-\lambda_{un} \frac{NRhl_z}{V_{un}} \frac{\partial}{\partial \xi} \int_0^{2\pi} \bar{\bar{\mathrm{v}}}_{XYZ} d\theta \right] \quad 3\text{-}103$$

To proceed with a closed form solution of the above equations, knowledge of the compressor flowfield parameters of velocity and pressure distribution is very important. For the turning force, the inlet and outlet flowfield velocity at each stage is required, together with the axial flow velocity. For the pressure force, the average static pressure distribution is required which is gotten from the average of the compressor inlet and out pressure. On the other hand, to determine the unsteady force, the average flow velocity at each stage is required.

To determine the relationship for the flowfield velocity at each stage in terms of the blade angles, the 2D and 3D stage velocity triangle for a single stage presented in Figure 3-14 and Figure 3-15 provides guidance.

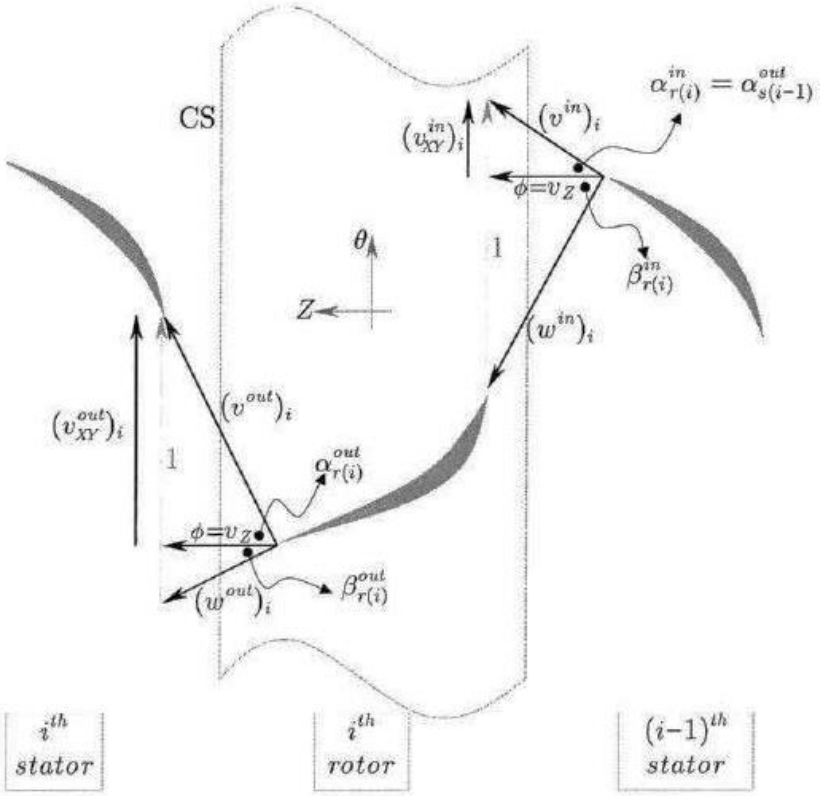

Figure 3-14 Compressor 2D velocity triangle (Source: Al-Nahwi, 2000)

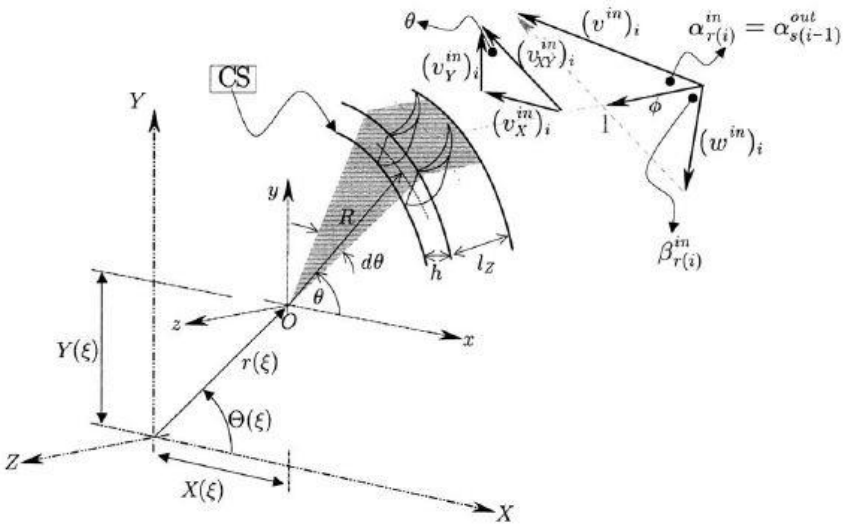

Figure 3-15 Compressor 3D velocity triangle (Source: Al-Nahwi, 2000)

Figure 3-15 shows clearly the two reference frames at play in the compressor system, first is the relative reference frame attached to the compressor rotor geometric centre and the second is the absolute reference frame, attached to the bearing centre line.

The compressor flowfield velocity is attached to the relative reference frame, but the aerodynamic forces are required in the absolute reference frame; so a transformation of the compressor flowfield velocity from the relative reference frame to the absolute frame is required.

By considering Figure 3-15, the relationship between the absolute and relative velocity is:

$$\mathrm{v}_{xyz} = \mathrm{v}_{XYZ} - \frac{l}{R}\frac{dr}{d\xi} \qquad 3\text{-}104$$

But $\mathbf{v}_{XYZ} \gg \frac{l}{R}\frac{dr}{d\xi}$ based on order of magnitude estimates, therefore,

$$\mathrm{v}_{xyz} \approx \mathrm{v}_{XYZ} \qquad 3\text{-}105$$

From Figure 3-15 and Figure 3-14, the expressions for the compressor flowfield inlet and outlet velocity is given as:

$$\left(\mathrm{v}_{XYZ}^{in}\right)_i = -\mathrm{v}_X^{in}\,\mathbf{i} + \mathrm{v}_Y^{in}\,\mathbf{j} + \phi\,\mathbf{k}$$

$$\left(\mathrm{v}_{XYZ}^{in}\right)_i = \phi\tan\alpha_{r(i)}^{in}\left(-\sin\theta\ \mathbf{i} + \cos\theta\ \mathbf{j}\right) + \phi\,\mathbf{k} \qquad 3\text{-}106$$

$$\left(\mathrm{v}_{XYZ}^{out}\right)_i = -\mathrm{v}_X^{out}\,\mathbf{i} + \mathrm{v}_Y^{out}\,\mathbf{j} + \phi\,\mathbf{k}$$

$$\left(\mathrm{v}_{XYZ}^{out}\right)_i = \phi\tan\alpha_{r(i)}^{out}\left(-\sin\theta\ \mathbf{i} + \cos\theta\ \mathbf{j}\right) + \phi\,\mathbf{k} \qquad 3\text{-}107$$

Thus,

$$\left(\mathrm{v}_{XYZ}^{out}\right)_i - \left(\mathrm{v}_{XYZ}^{in}\right)_i = \phi\left(\tan\alpha_{r(i)}^{out} - \tan\alpha_{r(i)}^{in}\right)\left(-\sin\theta\ \mathbf{i} + \cos\theta\ \mathbf{j}\right) \qquad 3\text{-}108$$

From the compressor velocity triangle in Figure 3-14, we derive the following relationships:

$$\alpha_{r(i)}^{in} = \alpha_{s(i-1)}^{out} \qquad 3\text{-}109$$

$$\tan\alpha_{r(i)}^{out} = \frac{1}{\phi} - \tan\beta_{r(i)}^{out} \qquad 3\text{-}110$$

Substituting Equations 3-109 and 3-110 into Equation 3-108,

$$\left(\mathrm{v}_{XYZ}^{out}\right)_i - \left(\mathrm{v}_{XYZ}^{in}\right)_i = \left[1 - \phi\left(\tan\alpha_{s(i-1)}^{out} + \tan\beta_{r(i)}^{out}\right)\right]\left(-\sin\theta\ \mathbf{i} + \cos\theta\ \mathbf{j}\right) \qquad 3\text{-}111$$

For the unsteady momentum storage force integral, the average flowfield velocity is expressed as:

$$\left(\hat{\mathrm{v}}_{XYZ}\right)_i = \frac{\left(\mathrm{v}_{XYZ}^{out}\right)_i + \left(\mathrm{v}_{XYZ}^{in}\right)_i}{2} \qquad 3\text{-}112$$

Substituting Equations 3-106 and 3-107 into Equation 3-112,

$$\left(\hat{\mathrm{v}}_{XYZ}\right)_i = \phi\left[\frac{\tan\alpha_{r(i)}^{in} + \tan\alpha_{r(i)}^{out}}{2}\right]\left(-\sin\theta\ \mathbf{i} + \cos\theta\ \mathbf{j}\right) + \phi\,\mathbf{k} \qquad 3\text{-}113$$

From the compressor velocity triangle in Figure 3-14,

$$\tan \alpha_{r(i)}^{in} = \frac{1}{\phi} - \tan \beta_{r(i)}^{in} \qquad 3\text{-}114$$

Substituting Equations 3-110 and 3-114 into Equation 3-113,

$$(\hat{\mathrm{v}}_{XYZ})_i = \left(1 - \phi\left[\frac{\tan \beta_{r(i)}^{in} + \tan \beta_{r(i)}^{out}}{2}\right]\right)(-\sin\theta\ \mathbf{i} + \cos\theta\ \mathbf{j}) + \phi\ \mathbf{k} \qquad 3\text{-}115$$

1) Turning Force Expression

Substituting A_{tu} from Equation 3-87 into Equation 3-101

$$F_{tu} = \chi[F_{tu}]_i = \chi\left[-\lambda_{tu}\frac{1}{2\pi}\int_0^{2\pi}\phi\left[(\mathrm{v}_{XYZ}^{out})_i - \left(\mathrm{v}_{XYZ}^{in}\right)_i\right]d\theta\right] \qquad 3\text{-}116$$

From the Euler turbine equation for a steady state axisymmetric flowfield, we have the following expression:

$$\frac{1}{2}(\tau_c)_i = \phi\left((\mathrm{v}_{XY}^{out})_i - \left(\mathrm{v}_{XY}^{in}\right)_i\right) \qquad 3\text{-}117$$

$$= \phi\left(1 - \phi\left[\tan \alpha_{s(i-1)}^{out} + \tan \beta_{r(i)}^{out}\right]\right) \qquad 3\text{-}118$$

Where $(\tau_c)_i$ is the non-dimensional stage torque, ϕ is the axial flow coefficient, $\left(\mathrm{v}_{XY}^{in}\right)_i$ and $(\mathrm{v}_{XY}^{out})_i$are the input and output velocity vector though a compressor blade row.

Thus, Equation 3-116 can be re-expressed as:

$$F_{tu} = \chi[F_{tu}]_i = \chi\ \left[-\lambda_{tu}\frac{1}{2\pi}\int_0^{2\pi}\frac{1}{2}(\tau_c)_i(-\sin\theta\ \mathbf{i} + \cos\theta\ \mathbf{j})d\theta\right] \qquad 3\text{-}119$$

Based on the experimental measurements of compressor stage torque reported by Day (1976), Gamache (1985) and Lavrich (1988), Al-Nahwi (2000) proposed the following closed form expression for the stage torque in conformity with the Moore-Greitzer compressor flowfield model as:

$$(\tau_c)_i = \frac{(\bar{\tau}_c)_i}{\frac{1}{2}\rho\Omega^2 R^3 A_c} \qquad 3\text{-}120$$

where $(\bar{\tau}_c)_i$ is the dimensional stage torque, ρ is the density, R is the compressor wheel mean radius, Ω is the compressor rotational speed and A_c is the compressor flow through annulus area.

$$(\tau_c)_i = \tau_{c0} + \tau_{c1}q + \tau_{c2}q^2 + \tau_{c3}q^3 \qquad 3\text{-}121$$

where the coefficients $\tau_{c0}, \tau_{c1}, \tau_{c2}$ and τ_{c3} in Equation 3-121 are gotten from a polynomial curve fitting of the experimental compressor stage torque data. Gamache (1985) provides experimental data of typical compressor stage torque.

By substituting Equation 3-121 and the expression for *q* in Equation 2-52 into Equation 3-119 and simplifying the integral, the following closed form expression for the turning force is obtained:

$$F_{tu} = \chi[F_{tu}]_i = \chi \left[\frac{1}{4}\lambda_{tu}([bF_{tu}^c(Q,a,b)]\,\mathbf{i} + [-aF_{tu}^c(Q,a,b)]\,\mathbf{j})\right] \qquad 3\text{-}122$$

where $F_{tu}^c(Q,a,b)$ is defined as:

$$F_{tu}^c(Q,a,b) = \tau_{c1} + 2\tau_{c2}Q + 3\tau_{c3}\left[Q^2 + \frac{1}{4}(a^2+b^2)\right] \qquad 3\text{-}123$$

$\tau_{c1}, \tau_{c2} \& \tau_{c3}$ are the coefficients from the compressor stage torque expression, a and b are the amplitudes of the Fourier series approximation of the disturbed flow coefficient.

2) Pressure Force Expression

Substituting A_{pr} from Equation 3-88 into Equation 3-102

$$F_{pr} = \chi\left[F_{pr}\right]_i = \chi \left[-\lambda_{pr}\frac{1}{2\pi}\int_0^{2\pi}\frac{1}{2}\frac{p_I + p_E}{\rho R^2\Omega^2}(\cos\theta\,\mathbf{i} + \sin\theta\,\mathbf{j})d\theta\right] \qquad 3\text{-}124$$

Recalling Equation 2-22 from the Moore-Greitzer compressor flowfield model in Chapter 2, the pressure rise across the inlet duct is:

$$\frac{P_T - P_0}{\rho U^2} = \frac{1}{2}(\phi^2 + h^2) + l_I\frac{d\Phi}{d\xi} + \left(\tilde{\phi}_\xi'\right)_0 \qquad 3\text{-}125$$

Assuming a lossless inlet guide vane, then:

$$\mathrm{P}_I = \mathrm{P}_0 \qquad \text{3-126}$$

Thus,

$$\frac{P_T - P_\mathrm{I}}{\rho U^2} = \frac{1}{2}(\phi^2 + h^2) + l_I \frac{d\Phi}{d\xi} + \left(\tilde{\phi}'_\xi\right)_0 \qquad \text{3-127}$$

Rearranging,

$$\frac{P_\mathrm{I}}{\rho U^2} = \frac{P_\mathrm{T}}{\rho U^2} - \frac{1}{2}(\phi^2 + h^2) - l_I \frac{d\Phi}{d\xi} - \left(\tilde{\phi}'_\xi\right)_0 \qquad \text{3-128}$$

Applying order of magnitude approximation between ϕ & h, with $\phi \gg h$, therefore,

$$\frac{P_\mathrm{I}}{\rho U^2} = \frac{P_\mathrm{T}}{\rho U^2} - \frac{1}{2}(\phi^2) - l_I \frac{d\Phi}{d\xi} - \left(\tilde{\phi}'_\xi\right)_0 \qquad \text{3-129}$$

Recalling Equation 2-23 in Chapter 2, the pressure rise in the compressor exit duct is:

$$\frac{P_s - P_E}{\rho U^2} = -l_E \frac{d\Phi}{d\xi} - (m-1)\left(\tilde{\phi}'_\xi\right)_0 \qquad \text{3-130}$$

$$\frac{P_E}{\rho U^2} = \frac{P_s}{\rho U^2} + l_E \frac{d\Phi}{d\xi} + (m-1)\left(\tilde{\phi}'_\xi\right)_0 \qquad \text{3-131}$$

Combining Equations 3-129 and 3-131, substituting for m = 2 (long exit duct approximation), and averaging both sides results in:

$$\frac{P_\mathrm{I} + P_E}{2\rho U^2} = \frac{P_\mathrm{T}}{\rho U^2} + \frac{1}{2}\Psi - \frac{1}{4}(\phi^2) - \frac{1}{2}(l_I + l_E)\frac{d\Phi}{d\xi} + \frac{1}{2}(m-2)\left(\tilde{\phi}'_\xi\right)_0 \qquad \text{3-132}$$

With $U = R\Omega$, therefore,

$$\frac{P_\mathrm{I} + P_E}{2\rho R^2\Omega^2} = \frac{P_\mathrm{T}}{\rho U^2} + \frac{1}{2}\Psi - \frac{1}{4}(\phi^2) - \frac{1}{2}(l_I + l_E)\frac{d\Phi}{d\xi} + \frac{1}{2}(m-2)\left(\tilde{\phi}'_\xi\right)_0 \qquad \text{3-133}$$

To simplify the pressure force integral in Equation 3-124, any term in Equation 3-133 that is not a function of θ will not contribute to the integral solution, thus,

$$F_{pr} = \chi\left[F_{pr}\right]_i = \chi\ \left[-\lambda_{pr}\frac{1}{2\pi}\int_0^{2\pi} -\frac{1}{4}(\phi^2)(\cos\theta\ \mathbf{i} + \sin\theta\ \mathbf{j})d\theta\right] \qquad \text{3-134}$$

where ϕ is an expression gotten from combining Equations 2-50 and 2-52, defined as:

$$\phi = 2\mathrm{W}(\mathrm{Q} + a\sin\theta + b\cos\theta) \qquad 3\text{-}135$$

By substituting Equation 3-135 into Equation 3-134 and simplifying the integral, we have:

$$F_{pr} = \chi\left[F_{pr}\right]_i = \chi\ \left[-\lambda_{pr}W^2Q(a\,\mathbf{i} + b\,\mathbf{j})\right] \qquad 3\text{-}136$$

where W is a parameter gotten from the compressor steady state pressure rise characteristics, Q is the non-dimensional flow coefficient, a and b are the amplitudes of the Fourier series approximation of the disturbed flow coefficient.

3) Unsteady Momentum Force Expression

Substituting V_{un} from Equation 3-89 into Equation 3-103

$$F_{un} = \chi[F_{un}]_i = \chi\ \left[-\lambda_{un}\frac{1}{2\pi\tan\gamma}\int_0^{2\pi}\bar{\bar{\mathrm{v}}}_{XYZ}d\theta\right] \qquad 3\text{-}137$$

Substituting Equation 3-115 into Equation 3-137,

$$\begin{aligned} F_{un} = \chi[F_{un}]_i = \chi\ \Bigg[-\lambda_{un}\frac{1}{2\pi\tan\gamma}\int_0^{2\pi}\Bigg\{\Bigg(1 \\ -\phi\left[\frac{\tan\beta_{r(i)}^{in} + \tan\beta_{r(i)}^{out}}{2}\right]\Bigg)(-\sin\theta\ \mathbf{i} + \cos\theta\ \mathbf{j}) \\ +\phi\,\mathbf{k}\Bigg\}d\theta\Bigg] \end{aligned} \qquad 3\text{-}138$$

Based on the experimental results by Lavrich (1988) for the time resolved flow measurements of an axial compressor in rotating stall, for the unstalled flow region, the following approximation holds:

$$\frac{\left(\tan\beta_{r(i)}^{in} + \tan\beta_{r(i)}^{out}\right)}{2} \approx \tan\gamma \qquad 3\text{-}139$$

where $\beta_{r(i)}^{in}$ and $\beta_{r(i)}^{out}$ are the inlet and outlet relative velocity angle and γ is the blade stagger angle.

Substituting Equation 3-139 into Equation 3-138,

$$F_{un} = \chi[F_{un}]_i = \chi \left[-\lambda_{un} \frac{1}{2\pi \tan\gamma} \int_0^{2\pi} \{(1-\phi\tan\gamma)(-\sin\theta\ \mathbf{i} + \cos\theta\ \mathbf{j}) + \phi\ \mathbf{k}\} d\theta \right] \quad \text{3-140}$$

By substituting Equation 3-135 into Equation 3-140 and simplifying the integral, we have:

$$F_{un} = \chi[F_{un}]_i = \chi \left[\lambda_{un} W \left(-\frac{db}{d\xi}\ \mathbf{i} + \frac{da}{d\xi}\ \mathbf{j} + \frac{1}{\tan\gamma}\frac{dQ}{d\xi}\ \mathbf{k} \right) \right] \quad \text{3-141}$$

where χ is the aerodynamic-rotordynamic domain coupling factor, λ_{un} is the unsteady momentum storage force scale factor, W is a parameter gotten from the compressor steady state pressure rise characteristics, Q is the non-dimensional flow coefficient, a and b are the amplitudes of the Fourier series approximation of the disturbed flow coefficient.

3.4 Summary

This chapter outlines the development of both the rotordynamic and aerodynamic force models.

In summary, the general expressions for aerodynamic force are presented below.

$$\bar{F}_{ae} = Ml\Omega^2 F_{ae} \quad \text{3-142}$$

where $\bar{F}_{ae}$ is the dimensional total aerodynamic force, M is the mass of the compressor rotor, l is the blade chord length, Ω is the compressor rotational speed in rad/s and F_{ae} is the non-dimensional total aerodynamic force

The non-dimensional total aerodynamic force F_{ae} is further expressed as:

$$F_{ae} = F_{tu} + F_{pr} + F_{un} \quad \text{3-143}$$

$$F_{ae} = \chi\left([F_{tu}]_i + \left[F_{pr}\right]_i + [F_{un}]_i\right) \quad \text{3-144}$$

where χ is the aerodynamic-rotordynamic domain coupling factor, $[F_{tu}]_i$, $\left[F_{pr}\right]_i$ & $[F_{un}]_i$ are the stage turning force, pressure force and unsteady momentum force respectively.

The X and Y component force expression of the turning force are:

$$[F_{tu}^X]_i = \frac{1}{4}\lambda_{tu} b \left\{\tau_{c1} + 2\tau_{c2}Q + 3\tau_{c3}\left[Q^2 + \frac{1}{4}(a^2 + b^2)\right]\right\} \quad \text{3-145}$$

$$[F_{tu}^Y]_i = -\frac{1}{4}\lambda_{tu} a \left\{\tau_{c1} + 2\tau_{c2}Q + 3\tau_{c3}\left[Q^2 + \frac{1}{4}(a^2 + b^2)\right]\right\} \quad \text{3-146}$$

The X and Y component force expression of the pressure force are:

$$\left[F_{pr}^X\right]_i = \lambda_{pr} W^2 Q\ a \quad \text{3-147}$$

$$\left[F_{pr}^Y\right]_i = \lambda_{pr} W^2 Q\ b \quad \text{3-148}$$

The X and Y component force expression of the unsteady momentum force are:

$$[F_{un}^X]_i = -\lambda_{un} W \frac{db}{d\xi} \quad \text{3-149}$$

$$[F_{un}^Y]_i = \lambda_{un} W \frac{da}{d\xi} \quad \text{3-150}$$

The overall methodology for computing the turning force, pressure force and the total aerodynamic force in the compressor are presented in Figure 3-16, Figure 3-17 and Figure 3-18 respectively.

The results for model validation of the rotordynamic model and aerodynamic model are presented in Chapter 5. Section 5.2

Lastly, the MATLAB code implementation for both the 2D transfer matrix rotordynamic model and the compressor aerodynamic force model is provided in Appendix D and Appendix E respectively.

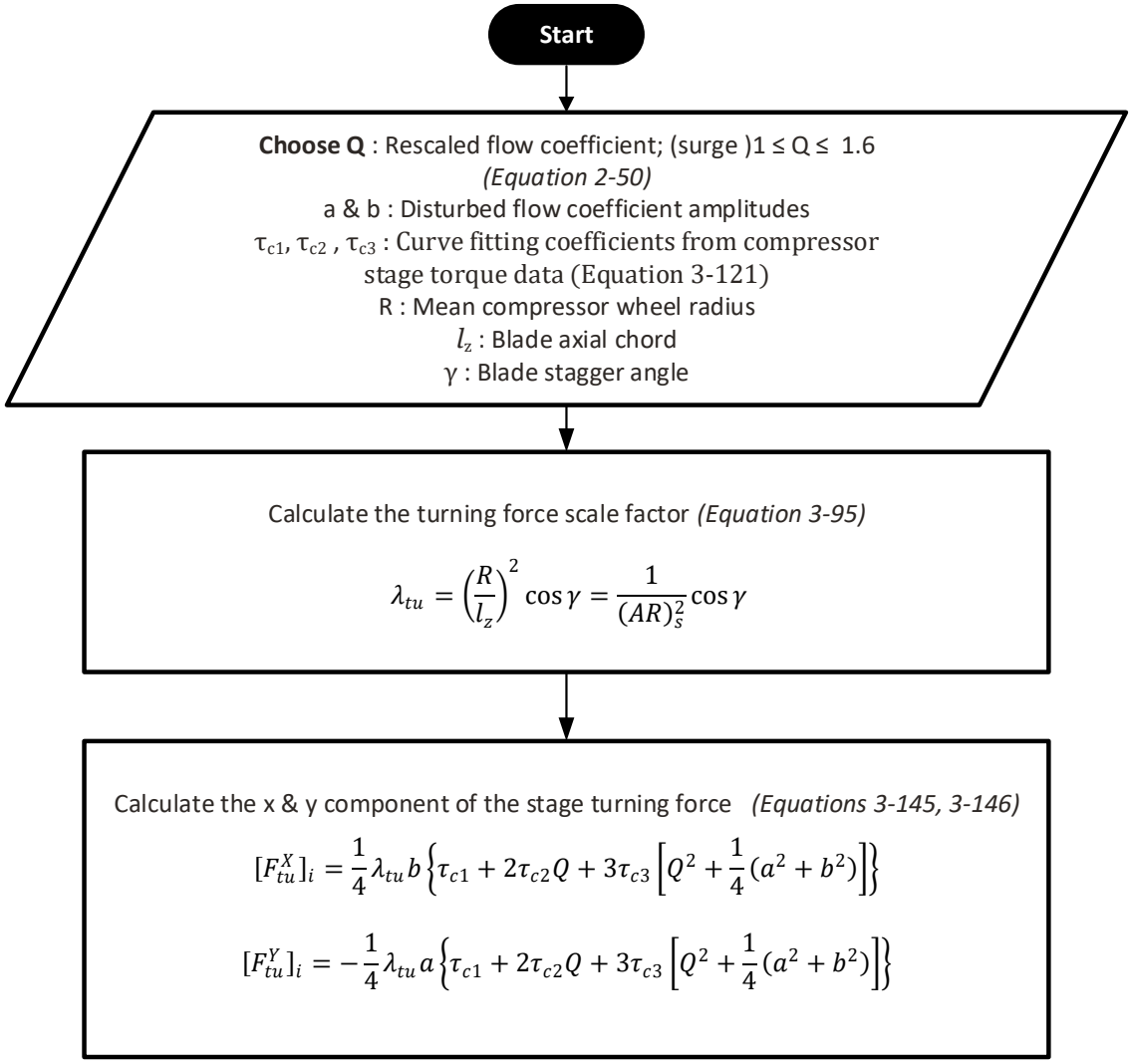

Figure 3-16 Flowchart for stage turning force calculation

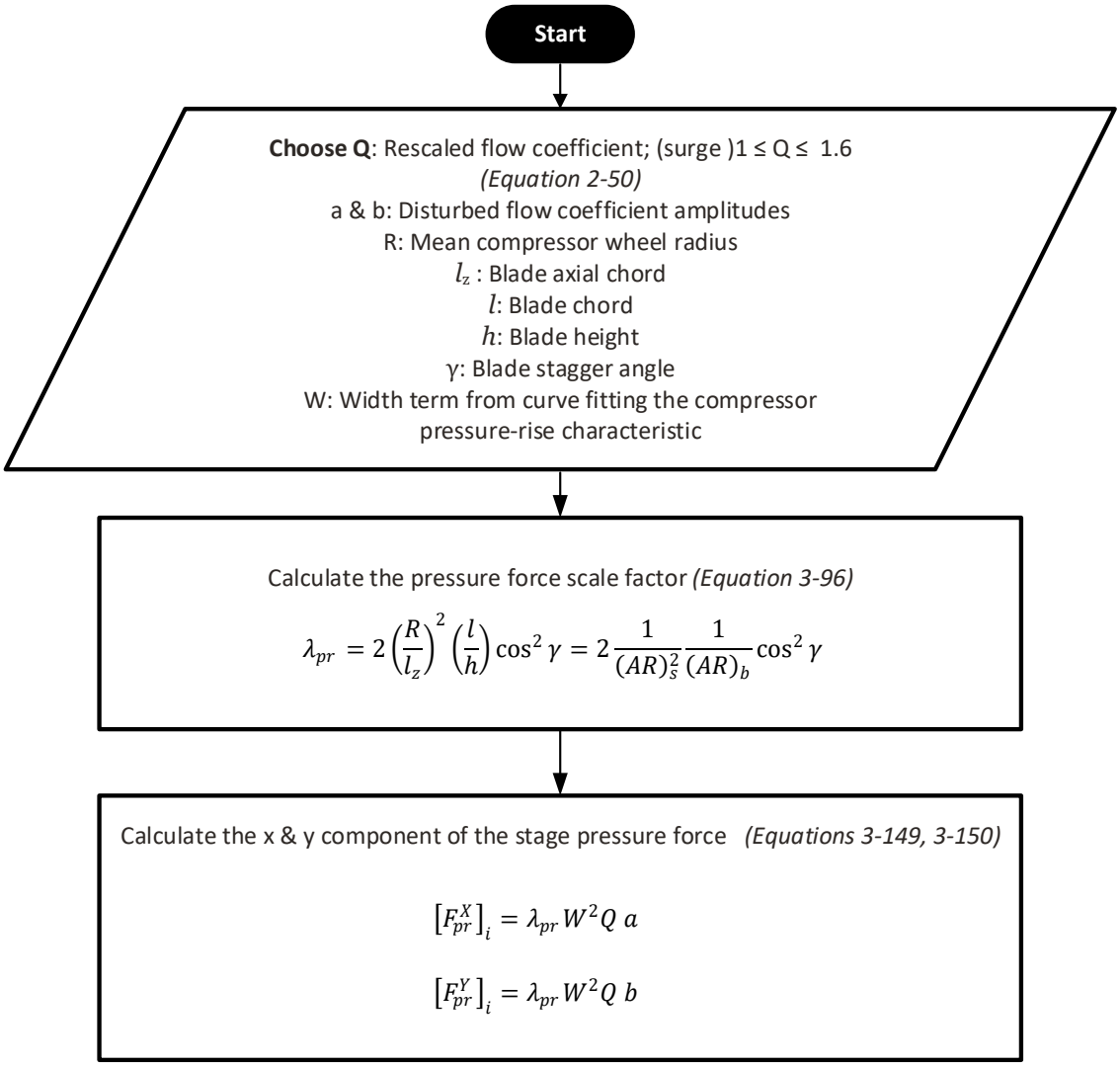

Figure 3-17 Flowchart for stage pressure force calculation

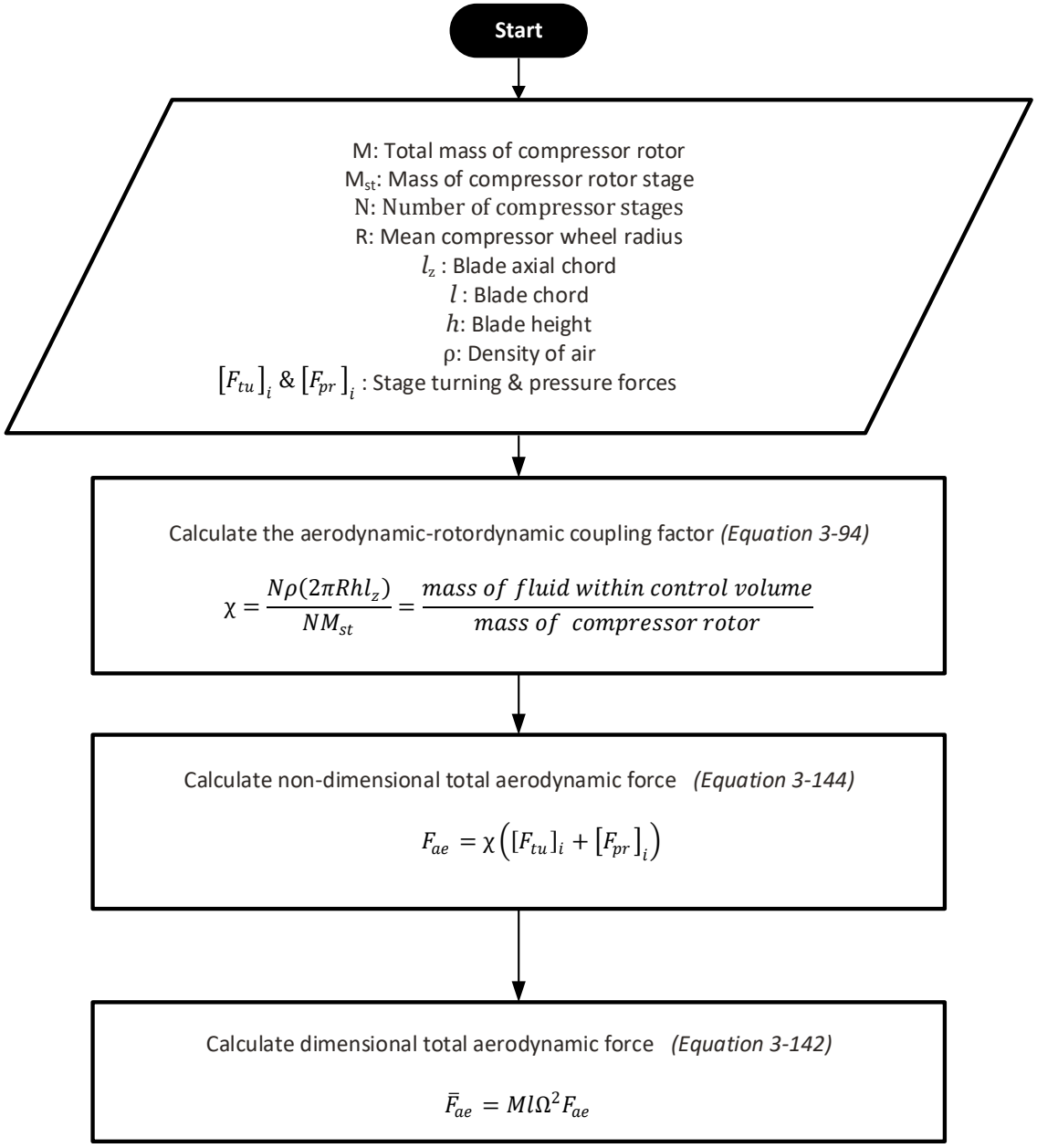

Figure 3-18 Flowchart for total aerodynamic force calculation

4 GAS TURBINE FOULING DEGRADATION

4.1 Introduction

Fouling is the deposition of airborne contaminates on the surface of the compressor blades, stators and annulus walls (Igie et al., 2014). The effect of fouling on the compressor's performance is manifested by a drop in its massflow, isentropic efficiency and pressure ratio; in very severe cases, fouling has been known to cause surge in the compressor due to a reduction in the compressor surge margin (Meher-homji, Focke and Wooldridge, 1989).

Generally, the rate of fouling in the compressor is affected by the type of environment (e.g. desert, offshore, tropical or artic), the type of location (e.g. industrial, urban or countryside), the atmospheric condition (e.g. rain, humidity or fog) and position & elevation of the intake (Igie, 2015). This is further emphasized in Table 4-1 where the different air dust concentration and particle sizes at various locations is summarised. It has been observed that particle sizes less than 10 microns cause fouling while particle sizes greater than 10 microns cause erosion (Meher-homji, Chaker and Motiwala, 2001).

The causative agents identified as the major cause of fouling in compressors are (Meher-homji, Chaker and Motiwala, 2001):

- Airborne contaminants such as sand, dust, plant stuff, insecticide, fertilizers, insects, coal dust, fly ash, cement dust etc.
- Airborne salt occurring mostly in marine and offshore environment.
- Gas turbine exhaust ingestion and lube oil from internal lube leaks in the gas turbine.
- Impure water carryover from evaporative coolers.

In other to mitigate the effect of compressor fouling on the performance of the gas turbine, two techniques have become prevalent; the first involves the use of intake filtration while the second involves the application of compressor cleaning.

Table 4-1 Effect of the Environment on Compressor Fouling (Source: Meher-homji, Focke and Wooldridge, 1989)

ENVIRONMENT	*COUNTRY SIDE*	*COASTAL*	*LARGE CITIES* (Power Stations) (Chemical Plants)	*INDUSTRIAL AREAS* (Steel Works) (Petro-Chemical) (Mining)	*DESERTS* (Sand Storms) (Dusty Ground)	*TROPICAL*	*ARTIC*	*MOBILE INSTALLATIONS*
Types of Dust	Dry-Non Erosive	Dry-Non Erosive but Salt Particles. Corrosive Mist.	Sooty-Oily. May be Erosive, also Corrosive.	Sooty-Oily Erosive. May be Corrosive.	Dry-Erosive in sand storm areas. Fine talc-like in areas of non-sand storms but dusty ground.	Non-Erosive May cause fouling	Non-Erosive	Dry-Erosive Sooty-Oily Corrosive
Dust Concentration								
mg/cu.m.	0.01-0.1	0.01-0.1	0.03-10	0.1-10	0.1-700	0.01-0.25	0.01-0.25	0.01-700
Grains/cu.ft. 10^{3}	0.004-0.0436	0.004-0.436	0.01-0.13	0.043-4.35	0.04-300	0.004-0.10	0.004-0.10	0.04-300
Particle Size	0.01-3	0.1-3 Salt <5	0.1-10	0.1-(50)[1]	1-(500)[2]	0.1-10	0.1-10	0.1-(500)[3]
Effection on G.T.	*Minimal*	*Corrosion*	*Fouling* Sometimes corrosion and fouling.	*Erosion* Sometimes corrosion and fouling.	*Erosion* Plugging of filter with insect swarms.	*Fouling*	Plugging of air intake system with snow and ice.	*Fouling Erosion Corrosion*
Temperature								
Range °C	−20 to +30	−20 to +25	−20 to +35	−20 to +35	−5 to +45	5 to 45	−40 to +5	−30 to +45
Weather Conditions	Dry and sunny Rain Snow Fog	Dry and sunny Rain, snow, sea mist. Freezing fog in winter.	Dry and sunny Rain snow Hail stones Smog	Dry and sunny Rain Snow Hail stones Smog	Long dry sunny spells. High winds Sand and dust storms. Some rain.	High humidity Tropical rain Insect and mosquito swarms.	Heavy snow High winds Icing conditions. Insect swarms in summertime in some areas.	All possible weather conditions

NOTES: 1. In emission areas of chimney.
2. During severe sand storms.
3. At track level and during dust storms.

4.1.1 Intake Filtration

As the modern gas turbine becomes more sensitive to the quality of the inlet air, the design and selection of the intake filtration system is increasingly becoming important.

The intake filtration system is responsible for the removal of solid,liquid contaminants in the air and also salts when present. Poor design and selection of the intake filtration can lead to fouling, corrosion, foreign object damage, blockage of the turbine blade cooling holes, particle fusion and erosion (Wilcox et al., 2010).

In the modern gas turbine, the intake filtration system comprises of several stages as shown in Figure 4-1, with the various stages selected based on the required inlet air quality and the air contaminant present at a particular location; thus, the intake filtration system design is site specific.

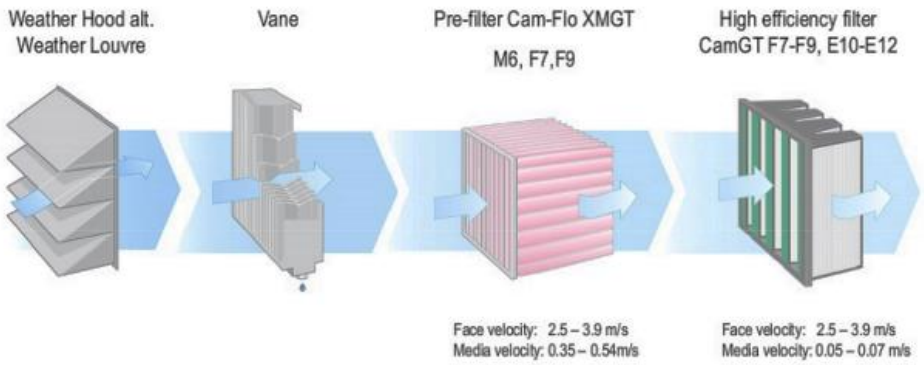

Figure 4-1 4 stage inlet air filtration system (Source: Camfil, 2014)

With regards to the nature or grade of the air contaminate at a particular location, Table 4-2 provides guidance on the selection of a suitable stage filter based on the ASHRAE 52.2 and EN 779/EN 1822 standards.

Table 4-2 Inlet air filter selection based on the grade of air contaminant (Source: Wilcox et al., 2010)

Grade	ASHRAE Filter Class MERV	EN Filter Class	Particles Separated
Coarse > 10 micron	1	G1	Leaves, insects, textile fibers, sand, flying ash, mist, rain
	2	G2	
	3	G2	
	4	G2	
	5	G3	Pollen, fog, spray
	6	G3	
	7	G4	
	8	G4	
	9	G4	
Fine > 1 micron	10	F5	Spore, cement dust, dust sedimentation
	11	F6	Clouds, fog
	12	F6	
	13	F7	Accumulated carbon black
	14	F8	Metal oxide smoke, oil smoke
	15	F9	
EPA and HEPA > 0.01 micron	16	E10	Metal oxide smoke, carbon black, smog, mist, fumes
	16	E11	
	16	E12	Oil smoke in the initial stages, aerosol micro particles, radioactive aerosol
	17	H13	
	18	H13	
	19	H14	Aerosol micro particles
	20	H14	
ULPA Micro particles		U15	Aerosol micro particles
		U16	
		U17	
Note: Correlations between ASHRAE and EN standards classifications and particle size are approximate.			

The different types of intake air filters are (Wilcox et al., 2010):

1. Weather Protection and Trash Screens

Weather hood and weather louvre are used to protect the filtration system from rain and snow. Although the weather hood and weather louvre serve similar functions, they are different in construction. As shown in Figure 4-2, the weather hood is constructed such its entrance faces downward constraining the inlet air to flow upwards in other to enter the filtration system. This upward turning effect prevents the entrance of either rain or snow into the filtration system.

Figure 4-2 Intake filtration weather hood (Source: Pneumafil, 2016)

On the other hand, the weather louvre as shown in Figure 4-3, is constructed with its entrance made of louvres, which provides a convoluted path for the inlet air stream; it is this turning effect that prevents the entrance of rain or snow into the filtration system.

Figure 4-3 Intake filtration weather louvre (Source: Voetec, 2016)

Trash screens and insect screens are used to capture large foreign objects like birds, leaves, insects, etc.

2. Inertial Separators

Inertial separators are suitable for removing air contaminants greater than 10 microns. They operate based on the principle of momentum, impingement, centrifugal forces and gravity to separate solid and liquid contaminants from the inlet air stream.

The two basic types of the inertial separators are (Wilcox et al., 2010):

- Vane-type inertial separator

  As shown in Figure 4-4, the vane-type inertial separator operates in an axial flow direction, with pockets or hocks along its side walls which serves the purpose of extracting the water from the air stream based on the momentum difference between water and air. As the air flows through the continuous strip of v-shaped vanes, water impinges on the hocks or pockets and are captured. The clean air then continues through the convoluted path provided by the continuous strip of v-shaped vane.

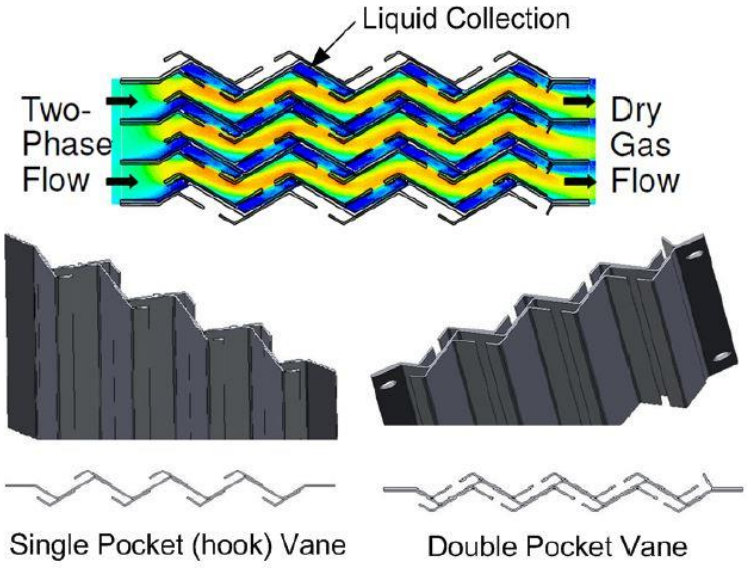

Figure 4-4 Vane-type inertial separator (Source: Wilcox et al., 2010)

- Cyclone-type inertial separator

  In the cyclone-type inertial separator as shown in Figure 4-5, the inlet air is given a spin by a stationary centrifugal-like blade; this spinning effect, causes the heavier particles to congregate at the outer part of the tube which is then retrieved by a bleed fan system. The clean air stream is then captured from the centre of the tube.

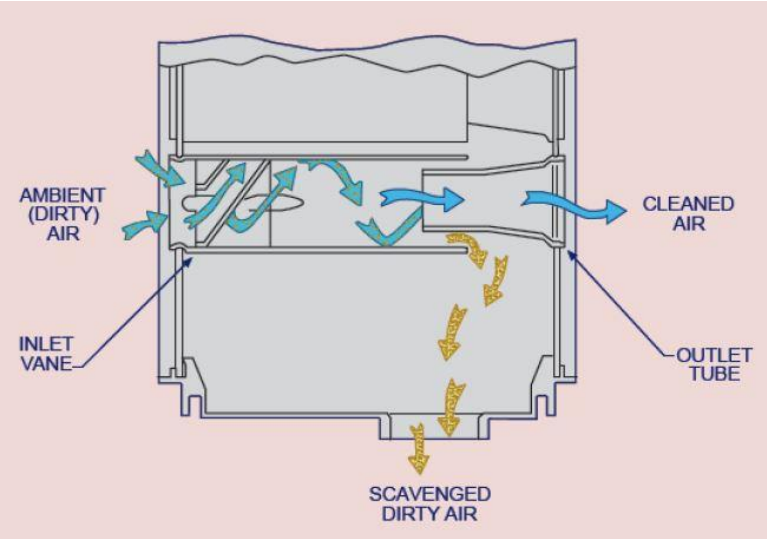

Figure 4-5 Cyclone-type inertial separator (Source: Wilcox et al., 2010)

Compared to the vane-type separator, the cyclone-type has a larger frontal area, and by extension, larger size, which could be a disadvantage in applications where space usage is limited such as in the offshore environment.

Despite its size limitation, the cyclone-type separator is useful for the removal of both water and solid contaminants in the inlet air unlike the vane-type separator which is more suited for removing water only from the inlet air.

3. Moisture Coalescers

The moisture coalescers are used in the filtration system to remove moisture from the inlet air. They function by causing aerosols or tiny droplets of water to combine into larger droplets as they pass through the fibre matrix of the filter. The larger droplets are eventually collected through a drain pipe.

4. Pre-filters

Pre-filters are used to extend the life of high efficiency particle air (HEPA) filters by capturing the larger sized particles in the inlet air stream. The nominal size of particles captured is around 10 microns (Wilcox et al., 2010). The bag type filter shown in Figure 4-6 is a good example of a pre-filter. It is normal practice to place the pre-filter before the HEPA filters for optimum HEPA filter capture efficiency and life (Loud and Slaterpryce, 1991).

Figure 4-6 Bag type pre-filter (Source: Camfil, 2016a)

It is also possible for the pre-filter to be given an electrostatic charge during its manufacture; this further improves the filtration efficiency of the pre-filters. Although with use, the effect of the electrostatic charge decays.

5. High Efficiency Filters

The high efficiency filters are used to remove particles of size less than 0.3 microns. This sub-micron removal of particles is possible based on the nature of

the filter fibre which is made up of either fibre glass or treated paper arranged in a pleat format. The pleats on the filter material further increase the filter surface area, thereby increasing its capture efficiency

The high efficiency filters are broadly classified as EPA (efficiency particle air filter), HEPA (high efficiency particle air filter) and ULPA (ultra-low particle air filter) (Wilcox et al., 2010).

The minimum capture efficiency of the EPA and HEPA are 85% and 99.95% for particles sizes above 0.3 microns while that of the ULPA is 99.9995% for particle sizes above 0.12 microns (Wilcox et al., 2010).

The high efficiency filters come in two basic constructions, which are the rectangular panel filter shown in Figure 4-7 and the cylindrical cartridge filter shown in Figure 4-8 (Loud and Slaterpryce, 1991).

Figure 4-7 Rectangular panel high efficiency filter (Source: Camfil, 2016b)

Figure 4-8 Cylindrical cartridge high efficiency filter (Source: Camfil, 2016c)

6. Self-Cleaning Filters

As shown in Figure 4-9, the self-cleaning filter operates by allowing air particles to accumulate on the filter surface; when the pressure-drop across the filter reaches a pre-determined level, a reverse blast of air from the compressor or a supplementary source is feedback through the filter to dislodge the air particles thereby returning the filter to its original performance. The cleaning process is performed on a few filters per time; this is to ensure a continuous uninterrupted supply of air to the gas turbine.

The self-cleaning filter is suitable for desert location where sand storms are a regular occurrence or locations with high air loading. The self-cleaning filters in these applications ensure that the life of the filtration system is maximized.

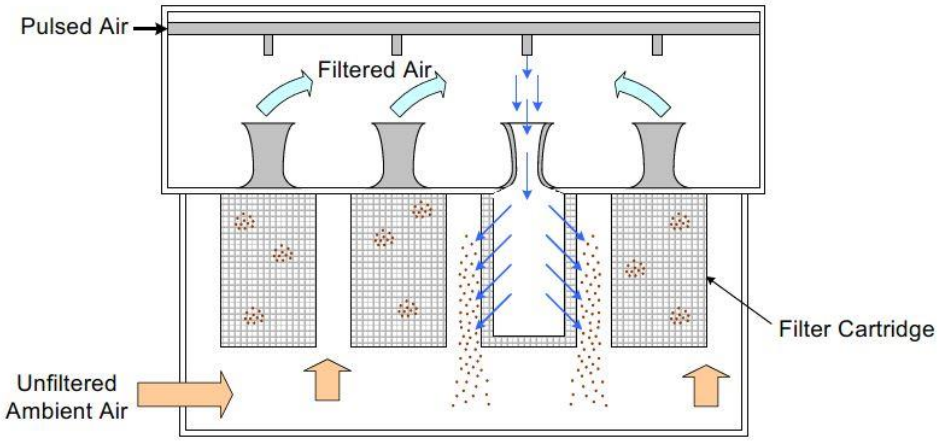

Figure 4-9 The operation of a self-cleaning filter (Source: Wilcox et al., 2010)

4.1.2 Compressor Cleaning

Irrespective of the presence of an inlet filtration system in a gas turbine engine, smaller sized contaminants such as dust, water or aerosols would still find their way through the filters and deposit themselves on the compressor blades and stators resulting in a reduction of the gas turbine's performance (EthosEnergy, 2016; GE, 2008).

Compressor cleaning is a means of recovering the lost performance in a fouled gas turbine through the application of a wash fluid i.e. demineralized water and detergent or solid particles such as rice or nutshell to remove the contaminants on the compressor blades and stators.

Historically, compressor cleaning was performed by injecting solid particles like rice or nutshell into the gas turbine compressor to dislodge the dirt on the compressor blades; with the introduction of coated compressor blades, this approach has fallen in popularity due to concerns with pitting corrosion (Stalder, 2000).

The current state of the art approach with regards compressor cleaning involves the use of a wet or liquid wash (Stalder, 2000).

Compressor washing involves the injection of a wash fluid into the gas turbine compressor, where it dislodges the dirt by dissolving them. Compressor washing can be performed either online or offline. The online approach is normally performed when the gas turbine is on load and at full speed and it is intended to avoid the build-up of dirt while the offline wash also called a crank wash, which is a more rigorous wash, is performed with the gas turbine on crank (GE, 2008).

A typical compressor washing system is shown in Figure 4-10.

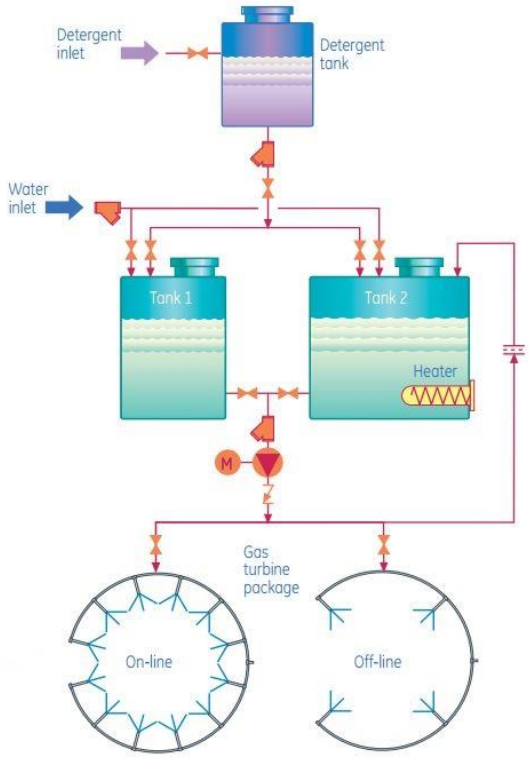

Figure 4-10 A typical compressor washing system (Source: GE, 2008)

Adopting a combination of online and offline wash is the recommend best practice which should be based on the site environmental conditions and the OEM recommendation. As a guideline, online wash can be performed daily while offline wash should be performed at least 4 – 6 times a year (Marcus, 2011).

For the compressor wash fluid, the choice is either demineralized water or a mixture of a detergent and demineralized water. Demineralized water alone is mostly effective for removing water soluble contaminants such as salts.

There are several options for the detergents, they are: water-based solvent detergent, petroleum-based solvent detergent and surfactants (Meher-homji, Chaker and Motiwala, 2001).

Water-based solvent detergent is effective against water soluble contaminants while petroleum-based solvent detergent is effective against oily contaminants.

While the solvent based detergents dislodge the contaminants by dissolving them, there is the possibility of the contaminants being redeposited at the later

stages, .surfactants have been developed to overcome this limitation (Meher-homji, Chaker and Motiwala, 2001).

Surfactant removes the contaminants on the compressor blade and stator surfaces by breaking the bond between the contaminants and the blade/stator surfaces and finally holds them in a suspension which allows their easy removal.

4.2 Gas Path Analysis

During the operational service life of a gas turbine engine, several faults do occur which adversely affects its performance and reduces its availability.

The faults in the gas turbine can be grouped into the two broad headings (Meher-Homji and Bhargava, 1994; Stamatis, 2013):

- **Gas path component faults:** Gas path component faults are faults in the compressor, combustor, turbine or other components along the gas path. Examples of gas path component faults are: fouling, erosion, corrosion, foreign object damage, increase in blade clearances, wholly or partially missing blades, hot section problems, etc.,
- **Rotating mechanical component faults:** Examples of rotating mechanical component faults are cracked rotor or disc, wear in bearings, gearbox & seals, problems with coupling, etc.

Gas path analysis was developed by Urban (1973) to detect single or multiple faults simultaneously in a gas turbine engine and their relative severity.

Gas path analysis is based on the premises that, as the gas turbine components degrade while in-service, an indication of such degradation is reflected by changes in each component's performance parameter such as isentropic efficiency, massflow, pressure ratio, etc.

Although these component parameters are not directly measureable, with the aid of measurable changes in engine gas path parameters such as pressure, temperature, fuel flow and rotational speed from that of an healthy engine state and a thermodynamic model relating the measured parameters to the component parameters, component faults can be detected, isolated and quantified.

Mathematically, the relationship between the measured engine parameters and the component performance parameters is expressed as (Li et al., 2014; Stamatis, 2013):

$$\bar{z} = f(\bar{u}, \bar{x}) \qquad 4\text{-}1$$

where $\bar{z}$ is a vector representing the measured engine parameter, $\bar{u}$ represents the ambient & operating conditions, $\bar{x}$ is a vector representing the component performance parameters and f is a function representing the thermodynamic model of the gas turbine.

Since the intent of gas path analysis is to determine the changes in the component parameters from the measurable parameters, this is performed through an inverse operation of equation 4-1.

Thus,

$$\bar{x} = DM(\bar{u}, \bar{z}) \qquad 4\text{-}2$$

where $DM(\quad)$ represents the type of diagnostic inverse approximation method used.

A graphical representation of the gas path analysis is shown in Figure 4-11.

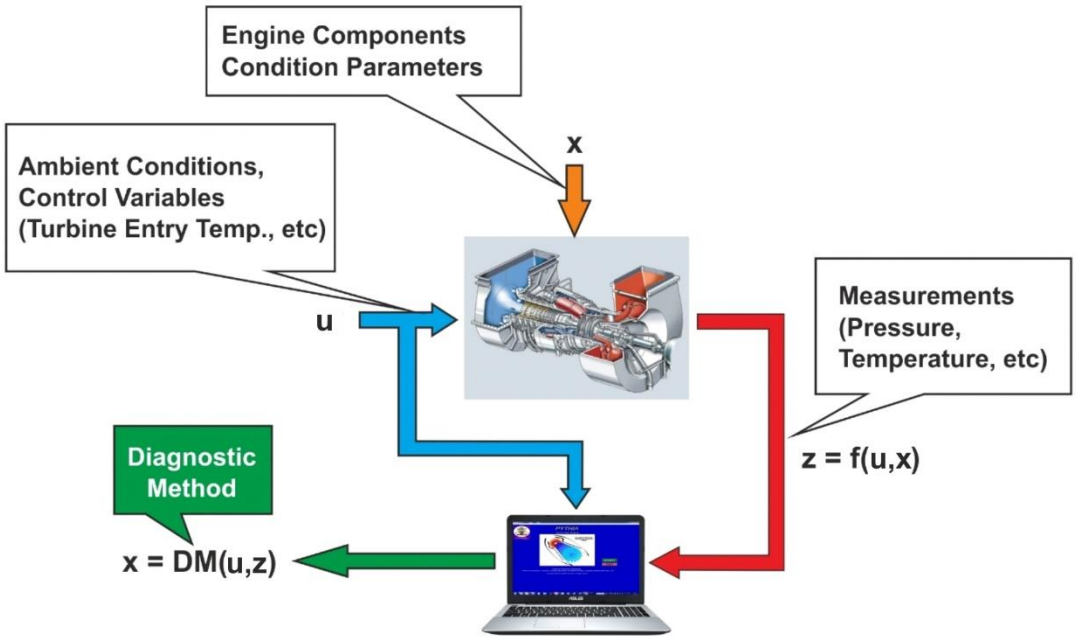

Figure 4-11 An overview of the gas path analysis technique

Based on the choice for the diagnostic inverse approximation method, there are two basic ways to perform gas path analysis and they are: linear gas path analysis and non-linear gas path analysis (Li, 2010).

4.2.1 Linear Gas Path Analysis

For a given operating point, assuming all measurement uncertainties such as measurement noise and sensor faults are neglected, the relationship between the measured engine parameters $(\bar{z})$ and component performance parameters $(\bar{x})$ in Equation 4-1 can be rewritten as (Li, 2010):

$$\bar{z} = f(\bar{x}) \qquad 4\text{-}3$$

From Taylor series, the series expansion of a function about a point 'a' for a small variable change 'h' can be expressed as (Stroud, 2003):

$$f(a+h) = f(a) + hf'(a) + \frac{h^2}{2!}f''(a) + \cdots + \frac{h^n}{n!}f^n(a) + \cdots \qquad 4\text{-}4$$

If $\bar{x}_0 = a$, $\bar{x} = (a+h) \therefore h = \bar{x} - \bar{x}_0$ and $f(a+h) = \bar{z}$, then,

$$\bar{z} = \bar{z}_0 + (\bar{x} - \bar{x}_0)\frac{\partial \bar{z}}{\partial \bar{x}}\Big|_0 + HOT \quad \text{4-5}$$

where HOT stands for the higher order terms in the Taylor series expansion. Assuming very small $(\bar{x} - \bar{x}_0)$ difference, the HOT terms is neglected.

Equation 4-5 can be rewritten as (Li, 2016),

$$\bar{z} = \bar{z}_0 + (\bar{x} - \bar{x}_0)\frac{\partial \bar{z}}{\partial \bar{x}}\Big|_0 \quad \text{4-6}$$

$$\Delta \bar{z} = H\Delta \bar{x} \quad \text{4-7}$$

where $\Delta \bar{z}$ is the deviation vector for the measured parameters represented as (Li, 2016),

$$\Delta \bar{z} = (\bar{z} - \bar{z}_0) = \begin{bmatrix} \Delta \bar{z}_1 \\ \Delta \bar{z}_2 \\ \cdots \\ \Delta \bar{z}_M \end{bmatrix} \quad \text{4-8}$$

$\Delta \bar{x}$ is the deviation vector for the components parameters represented as (Li, 2016),

$$\Delta \bar{x} = (\bar{x} - \bar{x}_0) = \begin{bmatrix} \Delta \bar{x}_1 \\ \Delta \bar{x}_2 \\ \cdots \\ \Delta \bar{x}_N \end{bmatrix} \quad \text{4-9}$$

H is the influence coefficient matrix represented as (Li, 2016),

$$H = \begin{bmatrix} \frac{\partial f_1(\bar{x})}{\partial \bar{x}_1} & \frac{\partial f_1(\bar{x})}{\partial \bar{x}_2} & \cdots & \frac{\partial f_1(\bar{x})}{\partial \bar{x}_N} \\ \frac{\partial f_2(\bar{x})}{\partial \bar{x}_1} & \frac{\partial f_2(\bar{x})}{\partial \bar{x}_2} & \cdots & \frac{\partial f_2(\bar{x})}{\partial \bar{x}_N} \\ \cdots & \cdots & \cdots & \cdots \\ \frac{\partial f_M(\bar{x})}{\partial \bar{x}_1} & \frac{\partial f_M(\bar{x})}{\partial \bar{x}_2} & \cdots & \frac{\partial f_M(\bar{x})}{\partial \bar{x}_N} \end{bmatrix} \quad \text{4-10}$$

From Equation 4-7, the deviations in the component performance parameters $(\Delta \bar{x})$ can be determined by,

$$\Delta \bar{x} = H^{-1}\Delta \bar{z} \quad \text{4-11}$$

where H^{-1} is the inverse of the influence coefficient matrix otherwise called the fault coefficient matrix. The inversion of the influence coefficient matrix is possible when the number of component performance parameters required equals the number of measured parameters i.e. H is a square matrix.

For situations where H is not a square matrix i.e. fewer equations than required unknowns, a pseudo inverse is used.

The pseudo inverse of H when H has more rows than columns is (Ghaoui, 2014):

$$H^{\#} = (H^T H)^{-1} H^T \qquad 4\text{-}12$$

where H^T is the transpose of H and $H^{\#}$ is the pseudo inverse of H.

The pseudo inverse of H when H has more columns than rows is (Ghaoui, 2014):

$$H^{\#} = H^T (H^T H)^{-1} \qquad 4\text{-}13$$

where H^T is the transpose of H and $H^{\#}$ is the pseudo inverse of H.

The accuracy of the measured parameters is affected by measurement noise and sensor faults, so they need to be accounted for (Li, 2016).

The measurement noise is originated as a result of the harsh operating environment found in the gas turbine and it has been reported that the measurement noise is often of same magnitude as the fault sought after, thus making it increasing important to consider its effect during the gas path analysis (Li, 2016).

On the other hand, the sensor faults could be constant with time called a bias or time varying called a drift. In the case of a drift, instrument calibration can be used to rectify it. To ensure the accuracy of the measurement parameter it is best practice to consider the sensor faults during gas path analysis (Li, 2016).

Mathematically, to account for the measurement noise and sensor faults vector in the linear gas path analysis problem, Equation 4-3 is rewritten as (Li, 2016):

$$\bar{z} = f(\bar{x}) + \bar{v} + \bar{b} \qquad 4\text{-}14$$

where $\bar{v}$ is a zero mean measurement vector and $\bar{b}$ is the sensor error vector.

4.2.2 Non-Linear Gas Path Analysis

To better predict the non-linear behaviour of the gas turbine, the non-linear gas path analysis adopts an iterative approach such as the Newton-Ralphson method to solve the relationship between the measured gas path parameters and the engine component performance parameters as presented in Equation 4-7 (Escher and Singh, 1995; Li, 2002).

The idea of the non-linear gas path analysis is such that component parameter vector guesses are used to predict the engine measurement parameter vector. Using an optimization technique such as the Newton-Ralphson approach iteratively, the difference between the measured parameter and the predicted measurement parameter is minimized (Escher and Singh, 1995).

The convergence criteria for the minimization procedure is (Escher and Singh, 1995):

$$\Delta\bar{z} = \sum_{j=1}^{M} |\Delta\bar{z}_{meas} - \Delta\bar{z}_{cal}| < \delta \qquad 4\text{-}15$$

where $\Delta\bar{z}_{meas}$ is the measured parameter deviation vector, $\Delta\bar{z}_{cal}$ is the predicted or calculated measurement deviation vector, M is the number of measurements and δ is convergence criteria.

To summarize the circumstance under which linear or non-linear gas path analysis would be suitable, from Equation 4-5, because the higher order terms (HOT) are ignored for linear gas path analysis, it is accurate for estimating engine health parameters when the engine performance deteriorations are small . However, when the engine operates far away from its design point, the higher order terms in Equation 4-5 becomes significant in determining the performance deterioration, as such, linear gas path analysis becomes less accurate. For this situation, non-linear gas path analysis provides better accuracy. Yang et al.

(2014) has provided a comparative analysis between linear and nonlinear gas path analysis for gas turbine engine health status estimation.

4.3 Engine Performance Model and Fouling Degradation Studies

4.3.1 TurboMatch Gas Turbine Engine Model

1. Overview of an Engine Thermodynamically Similar to LM2500+ Gas Turbine Engine

In this research, a gas turbine engine model thermodynamically similar to LM2500+ gas turbine engine has been chosen based on the availability of its engine performance parameters in open literature.

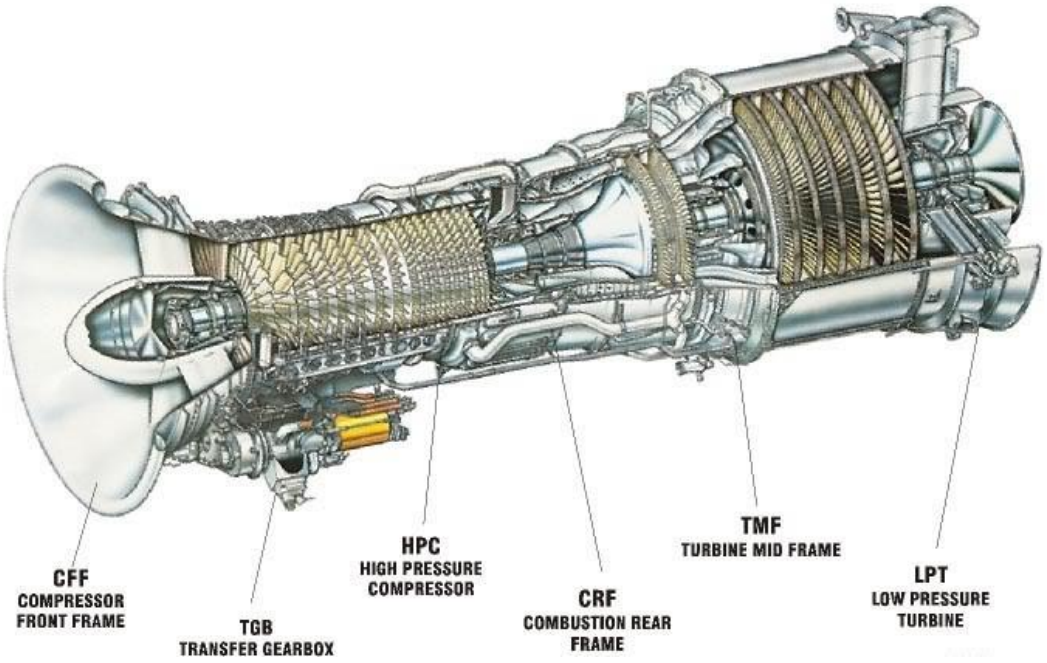

Figure 4-12 A cut-out of an LM2500+ gas turbine engine (Source: Afoggyeye, 2016)

The LM2500+ gas turbine engine shown in Figure 4-12 is an aero-derivative gas turbine produced by GE Aviation; it consists of a gas generator aerodynamically coupled to a power turbine.

The gas generator is made up of (GE Aviation, 2017):

- A 17-stage axial compressor with a pressure ratio of 23.1:1
- An annular combustor featuring externally mounted fuel nozzles
- A 2-stage air cooled high pressure turbine which drives the compressor, the auxiliary systems and also provides a high pressure exhaust gas for the power turbine.

On the other hand, the power turbine responsible for driving the external load is made up of a 6-stage low pressure turbine (GE Aviation, 2017). The power turbine is aerodynamically coupled and driven by the high pressure exhaust gas from the gas generator.

A summary of the performance parameters of the LM2500+ gas turbine engine is presented in Table 4-3.

Table 4-3 Performance datasheet for LM2500+ at ISO conditions (Source: GE Aviation, 2017)

S/N	Performance Parameter	Value
1	Output Power	30,200 KW
2	Specific Fuel Consumption	215 g/KWh
3	Heat Rate	9,277 KJ/KWh
4	Thermal Efficiency	39%
4	Exhaust Gas Flow Rate	85.9 Kg/s
5	Exhaust Gas Temperature	518^{o}C
6	Power Turbine Rotational Speed	3600rpm

Note: An ISO condition signifies an ambient temperature of 15^{o}C at sea level static, 60% relative humidity and no inlet and exhaust losses.

2. TurboMatch Implementation of an Engine Thermodynamically Similar to LM2500+ Gas Turbine Engine

In other to assess the performance degradation of a gas turbine engine, the first step involved is to create a baseline model of the engine. This first step in this

research is performed with TurboMatch for an engine thermodynamically similar to LM2500+.

TurboMatch is a gas turbine performance simulation tool created in Cranfield University with use and validation ranging over 40 years; it has the capability to perform design point analysis, off-design point analysis and transient analysis for any gas turbine configuration and application (Nikolaidis, 2015).

TurboMatch employs a modular modelling technique, where each component is viewed as a black block called a brick.

A bricks is a pre-programed sub-routine based on the aero-thermodynamic theory for the particular component such as: intake, compressor, burner, turbine, power turbine, heat exchanger, convergent nozzle, etc.

The final outputs from the TurboMatch simulation of the virtual engine are: the gas path parameters (e.g. total temperature, total pressure, etc.) along various stations in the gas turbine, overall thermal efficiency, specific fuel consumption, fuel flow, power output or thrust, specific work and component characteristic map for the compressor and turbine.

Figure 4-13 shows the TurboMatch brick structure for an engine thermodynamically similar to LM2500+.

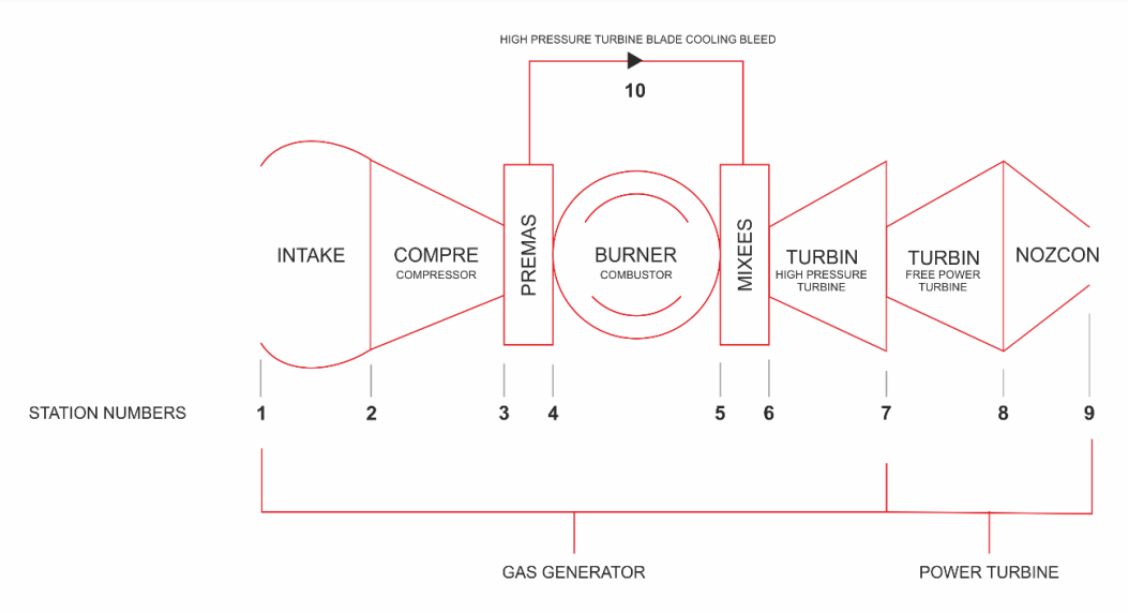

Figure 4-13 TurboMatch brick structure for an engine thermodynamically similar to LM2500+

In other to validate the TurboMatch engine model before the performance degradations studies can be performed, its design point and off-design point performance analysis is performed and the results compared with the performance data for LM2500+ in open literature.

1. Design Point Performance Simulation

The operating parameters, performance parameters and compressor maps of the TurboMatch simulated engine which is thermodynamically similar to LM2500+ is presented in Table 4-4, Figure 4-14 and Figure 4-15.

Table 4-4 Design point performance parameters of simulated engine

Parameter	Value	Parameter	Value
Intake			
Ambient temperature	288.15 K	Ambient pressure	1.01325 bar
Total pressure recovery	99.5%	Intake mass flow	84.1 kg/s
Compressor			
Compressor efficiency	84%	Compressor pressure ratio	23.1
Compressor exit temperature	770 K	Number of stages	17
Compressor surge margin	0.85	Cooling bypass flow	1%
Burner			
Combustion efficiency	99.8%	Burner pressure loss	5%
Fuel flow	1.7 kg/s		
Turbine (Compressor)			
Turbine inlet temperature	1500 K	Turbine efficiency	87%
Relative to max. enthalpy drop	0.8	Relative non-dimensional speed	0.6
Turbine (Free Power)			
Relative non-dim. speed	0.6	Turbine efficiency	87%
Relative to max. enthalpy drop	0.8		
Overall Performance			
Net power output	30.4 MW	Exhaust gas temperature	806 K
Thermal efficiency	37.9%		

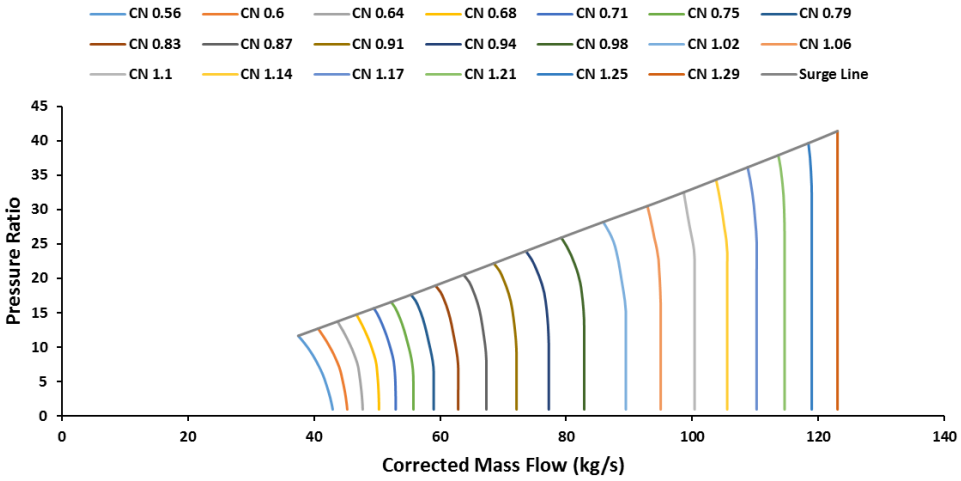

Figure 4-14 Compressor pressure map of TurboMatch baseline engine model

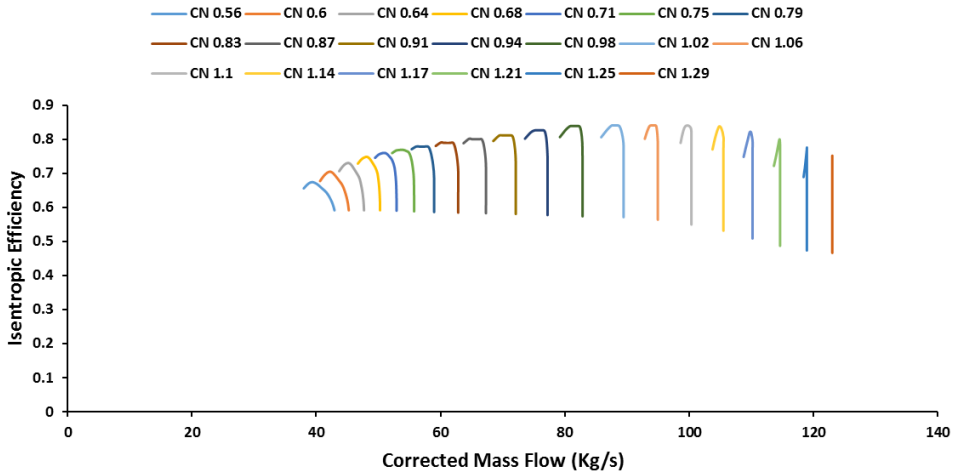

Figure 4-15 Compressor efficiency map of TurboMatch baseline engine model

Figure 4-14 and Figure 4-15 have been generated by the scaling of one of the standard maps embedded in TurboMatch. The scaling factors are determined by the following equations (Igie et al., 2014):

$$PRSF = \frac{PR_{DP} - 1}{PR_{DP,map} - 1} \quad 4\text{-}16$$

$$ETASF = \frac{\eta_{DP}}{\eta_{DP,map}} \quad 4\text{-}17$$

$$WASF = \frac{\phi_{DP}}{\phi_{DP,map}} \quad 4\text{-}18$$

where PRSF, ETASF and WASF are the pressure ratio, isentropic efficiency and mass flow scaling factors respectively, PR_{DP}, η_{DP} and ϕ_{DP} are the specified design point pressure ratio, isentropic efficiency and flow coefficient of the simulated engine while $PR_{DP,map}$, $\eta_{DP,map}$ and $\phi_{DP,map}$ are the corresponding design point pressure ratio, isentropic efficiency and flow coefficient of the specified TurboMatch standard compressor map.

The simulation result comparing the performance of the TurboMatch LM2500+engine to the published performance data of LM2500+ in open literature is presented in Table 4-5.

Table 4-5 Comparison of the design point performance parameters between TurboMatch LM2500+ engine model and LM2500+ datasheet (Source: GE Aviation, 2017)

S/N	Performance Parameters	TurboMatch LM2500+ (A)	LM2500+ Datasheet (B)	Delta % (A-B)/B
1	Output Power (kW)	30,387	30,200	10.6%
2	Inlet Mass Flow (Kg/s)	84.1	-	-
3	Turbine Entry Temperature (K)	1500	-	-
4	Exhaust Mass Flow (Kg/s)	85.8	85.9	-0.1%
5	Exhaust Gas Temperature (°C)	533	518	2.9%
6	Overall Pressure Ratio	23.1:1	23.1:1	0
7	Thermal Efficiency	38%	38%	0

The result shown in Table 4-5 comparing the design point performance parameters of the TurboMatch LM2500+ engine and that published in open literature for the LM2500+ engine by GE Aviation show good agreement.

No further attempt was made to close the exhaust gas temperature delta, as evidence from the work by Kostyuk and Karpunin (2016) show that an exhaust gas temperature error margin of ~15°C is acceptable for an accurate gas turbine

engine performance model. Similar result is reported by Visser et al. (2004), where an exhaust gas temperature delta of 23K is found to be acceptable for an accurate gas turbine performance model.

The input file for the TurboMatch LM2500+ design point analysis is provided in Appendix F

2. Off-Design Point Performance Simulation

To further validate that the TurboMatch LM2500+ virtual engine model and prove that it is a true representation of the real LM2500+ engine, an off-design performance simulation (i.e. when the gas turbine engine is operating at operating point conditions other than what it was designed to) is performed and the results shown in Figure 4-16

The input file for the TurboMatch LM2500+ off-design point analysis is provided in Appendix F.

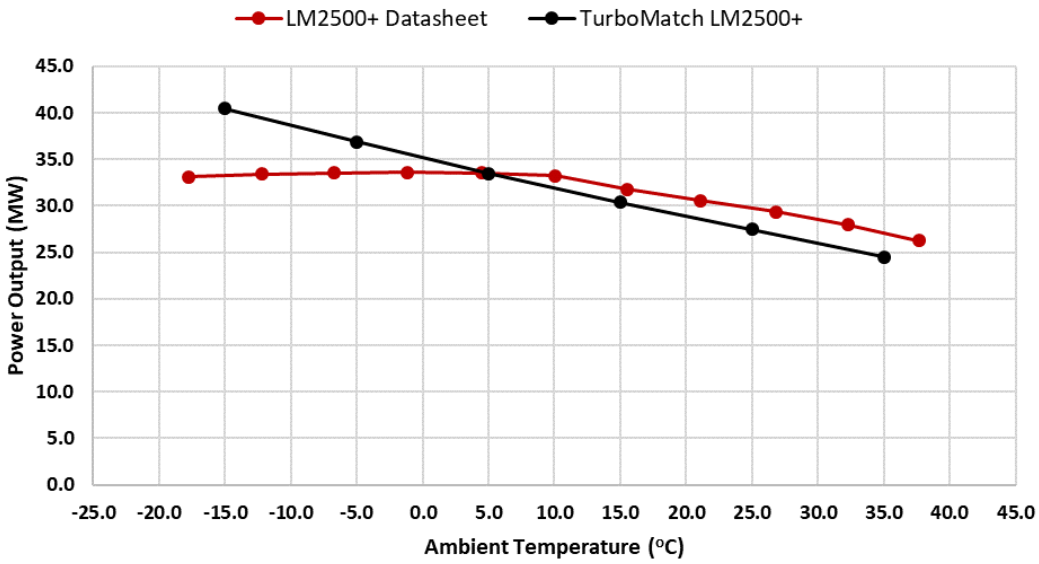

Figure 4-16 Comparison of the effect of ambient temperature variation on the power output in TurboMatch LM2500+ virtual engine and LM2500+ (Source: GE Aviation, 2017)

4.3.2 Result Discussion for the TurboMatch LM2500+ Virtual Engine Design Point and Off-design Point Analysis

The result presented in Table 4-5 shows that the TurboMatch LM2500+ virtual engine can accurately predict the design point performance of the real LM2500+ engine.

Comparing the off-design performance plot of the effect of the variation of the ambient temperature on the power output of the TurboMatch LM2500+ virtual engine and the real LM2500+ in Figure 4-16, it can be observed that they both follow the same trend i.e. a decreasing power output with increasing ambient temperature for temperatures above 10^{o}C.

Below 10^{o}C, there is a difference between the TurboMatch thermodynamic engine model prediction and the actual LM2500+ engine behaviour; this is as a result of the control system for LM2500+ ensuring the engine does not exceed its operational limit i.e. rated power as the ambient temperature continue to drop.

Overall, the validation results from both the design point and off-design point analysis show that the TurboMatch LM2500+ virtual engine is a good representative of the real LM2500+ engine and therefore, can be used to represent it in a performance degradation study.

4.3.3 Pythia Gas Path Analysis Results

Using Pythia (Cranfield University gas turbine diagnostic software), the fouling degradation shown in Table 4-6 is implanted into baseline TurboMatch LM2500+ engine.

Pythia is a gas turbine diagnostic software created in Cranfield University and it operates based on the following steps below which are also summarized in Figure 4-17 (Li et al., 2014):

- **Step 1** *Performance model setup:* A virtual engine model is built, comprising of bricks representing the thermodynamic characteristic of each component, the gas turbine engine configuration and the design & operating parameters.

- **Step 2** *Instrumentation selection:* Gas path parameters at critical locations for the interested components and faults to be monitored are selected.
- **Step 3** *Data acquisition and noise reduction:* Multiple measurements are acquired and feed into the diagnostic system and averaging is performed to reduce the noise in the data.
- **Step 4** *Data correction:* The measured parameters are corrected to the nominal ambient conditions.
- **Step 5** *Sensor diagnosis:* Measurement from faulty sensors are eliminated.
- **Step 6** *Component diagnosis:* Linear and non-linear gas path diagnostic is performed on the measured data to isolate, identify and quantify the faults.

Although in Figure 4-17 model adaptation is listed as a step in the gas path analysis process, model adaption has not been performed in this work, as such, it is skipped in the above listed steps.

However, Pythia has the capability to perform model adaptation. Model adaption finds use in tuning a performance model from gas turbine field or operational data.

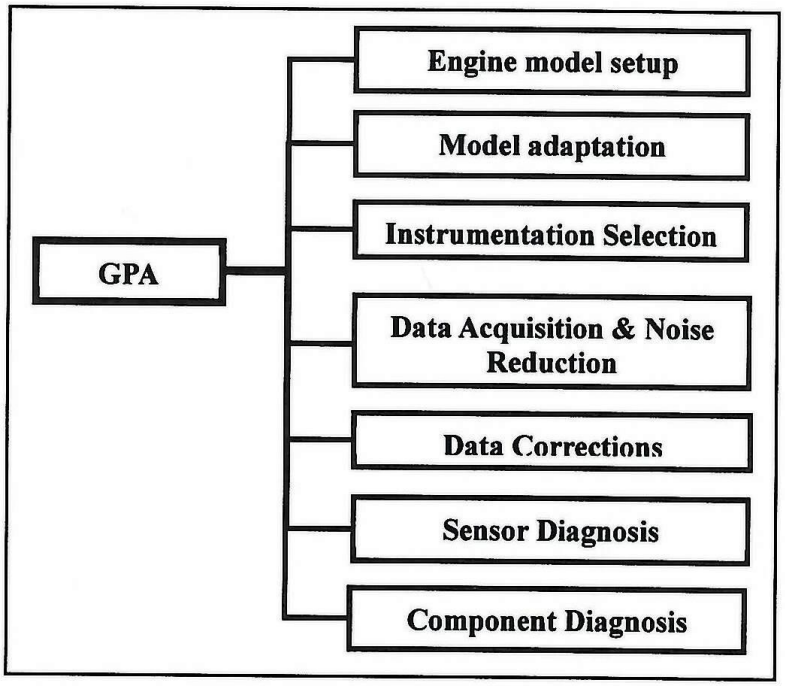

Figure 4-17 A schematic of the Pythia diagnostic process (Source: Li et al., 2014)

The conditions presented in Table 4-6 are different scenarios of fouling degradation in the gas turbine compressor.

Linear and non-linear gas path analysis (LGPA & NGPA) is then performed with Pythia on the degraded TurboMatch Lm2500+ engine simulated operating data to quantify the implanted degradation, which represents the effect of fouling on the compressor performance parameters (i.e. massflow, pressure ratio and isentropic efficiency).

The justification of this step is to overcome the absence of actual gas turbine compressor fouling degradation operating data. In an actual case, gas path analysis would be performed on gas turbine degradation operating field data of unknown degradation levels and the gas path analysis would isolate and quantify the fault. To overcome this, Pythia has been used to generate a simulated gas turbine degradation operating data based on the different cases in Table 4-6 and Pythia has also been used as a form of counter checking, to quantify the presence of the implanted degradation using the linear and non-linear gas path analysis technique.

Table 4-6 Different compressor fouling operating conditions

Cases	% ΔNDMF Reduction	% ΔPR Reduction	% ΔETA Reduction
Case 0 (Clean Engine)	0%	0%	0%
Case 1	1%	1%	1%
Case 2	2%	2%	1%
Case 3	3%	3%	1%
Case 4	4%	4%	1%
Case 5	5%	5%	1%

Note: NDMF is non-dimensional mass flow, PR is pressure ratio & ETA is isentropic efficiency

The plots comparing the implanted and diagnosed faults using linear and non-linear gas path analysis of the fouled gas turbine compressor is presented in Figure 4-18, Figure 4-19, Figure 4-20, Figure 4-21 and Figure 4-22 below.

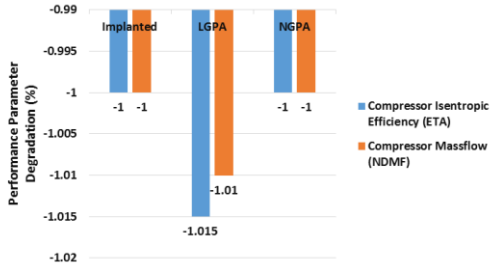

Figure 4-18 GPA results for Case 1

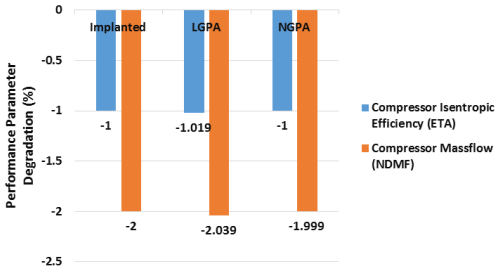

Figure 4-19 GPA results for Case 2

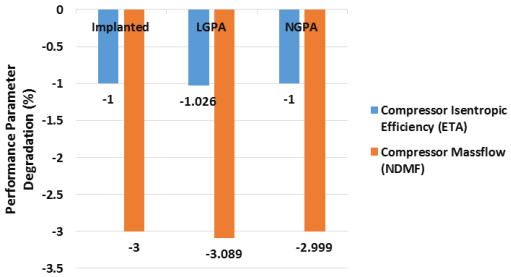

Figure 4-20 GPA results for Case 3

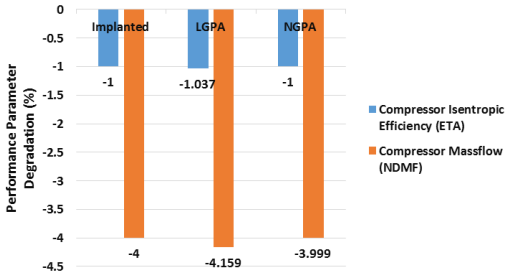

Figure 4-21 GPA results for Case 4

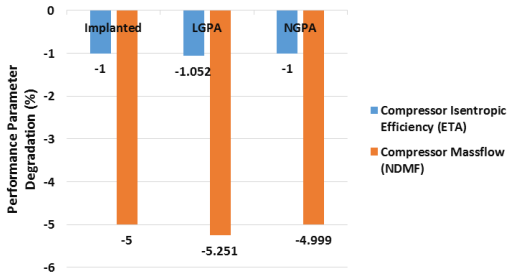

Figure 4-22 GPA results for Case 5

The plots above show the effectiveness of both the linear and non-linear gas path analysis technique in diagnosing the presence of faults in a gas turbine. From the plots above, the non-linear gas path analysis is more accurate than the linear gas path analysis. This observation is as expected judging from the inherent non-linear behaviour of the dependences between the gas path parameters.

The importance of the gas path analysis step to the current methodology for investigating the aerodynamic-rotordynamic interaction due to fouling in a compressor is to quantify the relative reduction in compressor massflow and pressure ratio, which is feed into the Moore-Greitzer compressor flowfield model through the modified compressor pressure rise characteristic.

4.3.4 Degraded/Fouled Compressor Map

TurboMatch provides the data for the baseline/clean compressor map or characteristic.

However, in other to determine the fouled compressor map for the different cases, the following scaling relationship is applied to the baseline compressor map:

$$PR_{[deg.]} = (1 - |\Delta PR|\%) \times \left(PR_{[clean]} - 1\right) + 1 \quad \text{4-19}$$

$$\eta_{is[deg.]} = (1 - |\Delta \eta|\%) \times \eta_{is[clean]} \quad \text{4-20}$$

$$\phi_{[deg.]} = (1 - |\Delta \phi|\%) \times \phi_{[clean]} \quad \text{4-21}$$

where $PR_{[deg.]}$ & $PR_{[clean]}$ are the fouled and clean compressor pressure ratio at a particular operating point respectively, ΔPR is the relative reduction in pressure ratio due to compressor fouling, $\eta_{is[deg.]}$& , $\eta_{is[clean]}$ are the fouled and clean compressor isentropic efficiency at a particular operating point respectively, $\Delta\eta$ is the relative reduction in isentropic efficiency due to compressor fouling, $\phi_{[deg.]}$ & $\phi_{[clean]}$ are the fouled and clean compressor massflow at a particular operating point respectively and $\Delta\phi$ is the relative reduction in massflow due to compressor fouling.

Applying Equations 4-19 and 4-21 to the baseline compressor pressure map in Figure 4-14, the resulting maps for the fouled compressor for all the cases are presented in Figure 4-23 to Figure 4-27.

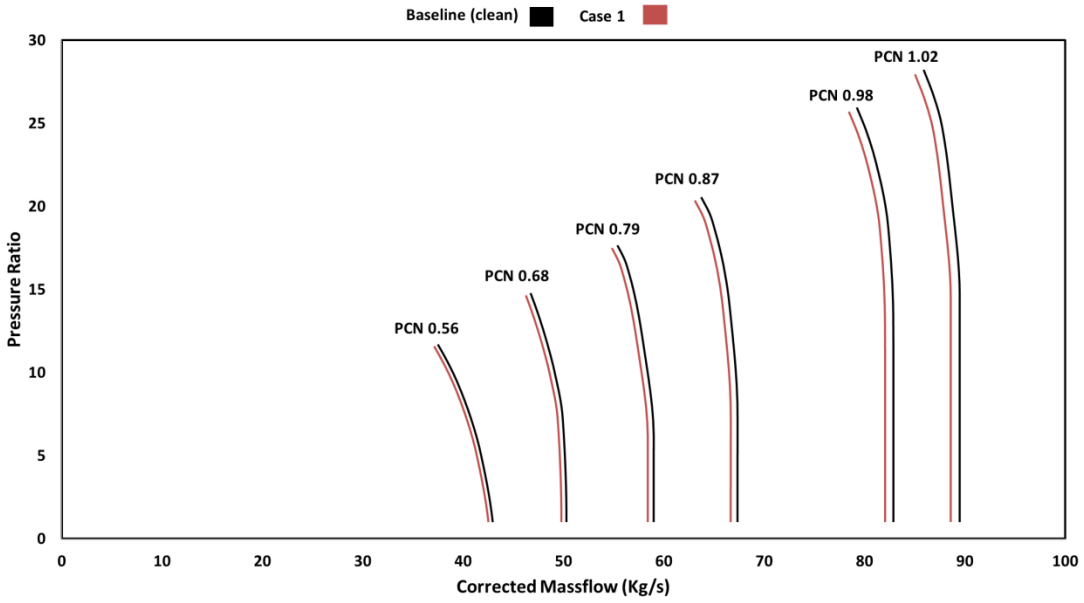

Figure 4-23 Compressor pressure maps for baseline and Case 1

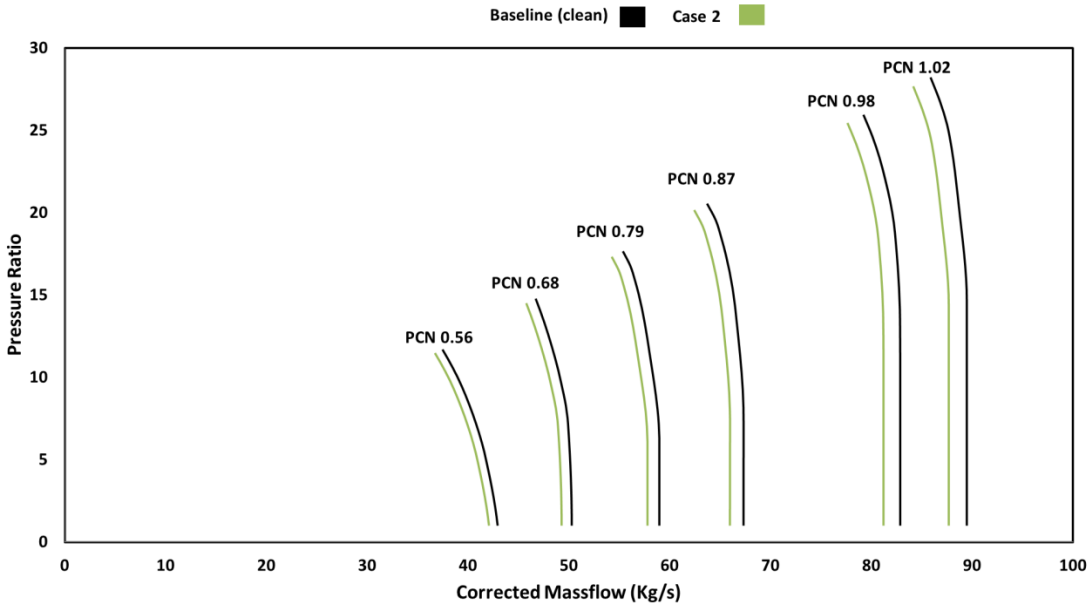

Figure 4-24 Compressor pressure maps for baseline and Case 2

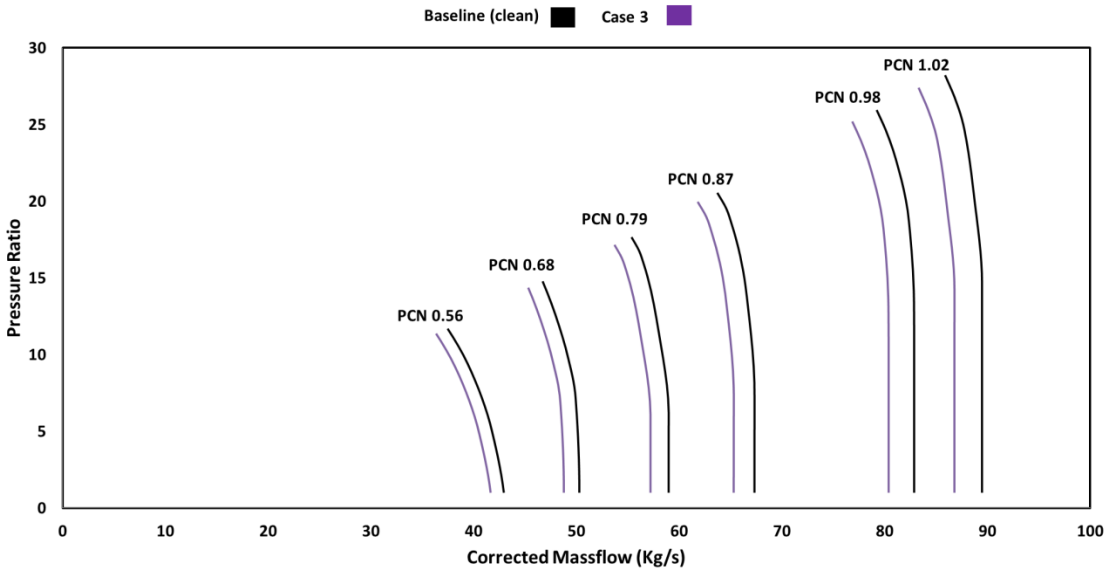

Figure 4-25 Compressor pressure maps for baseline and Case 3

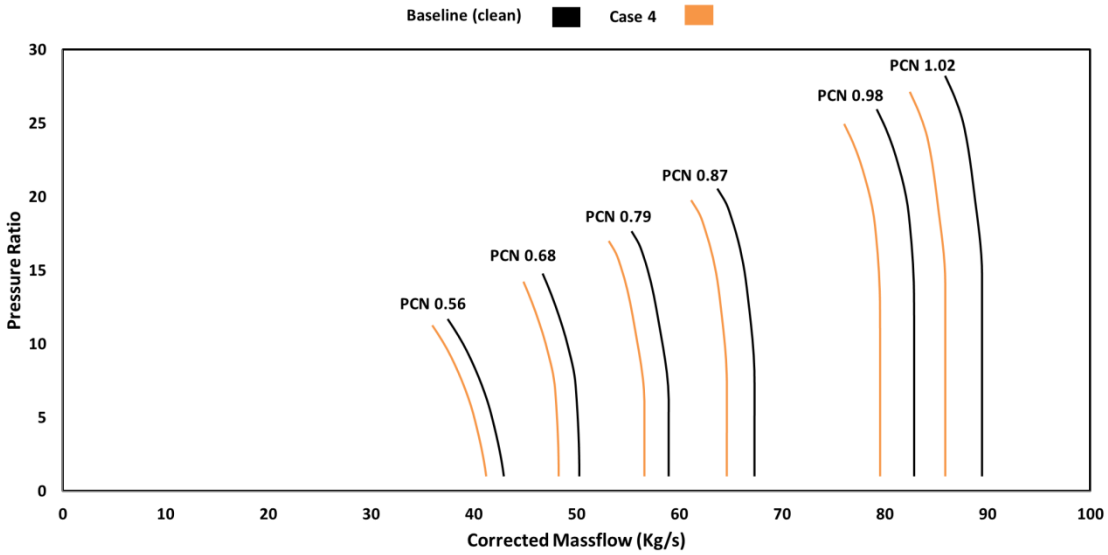

Figure 4-26 Compressor pressure maps for baseline and Case 4

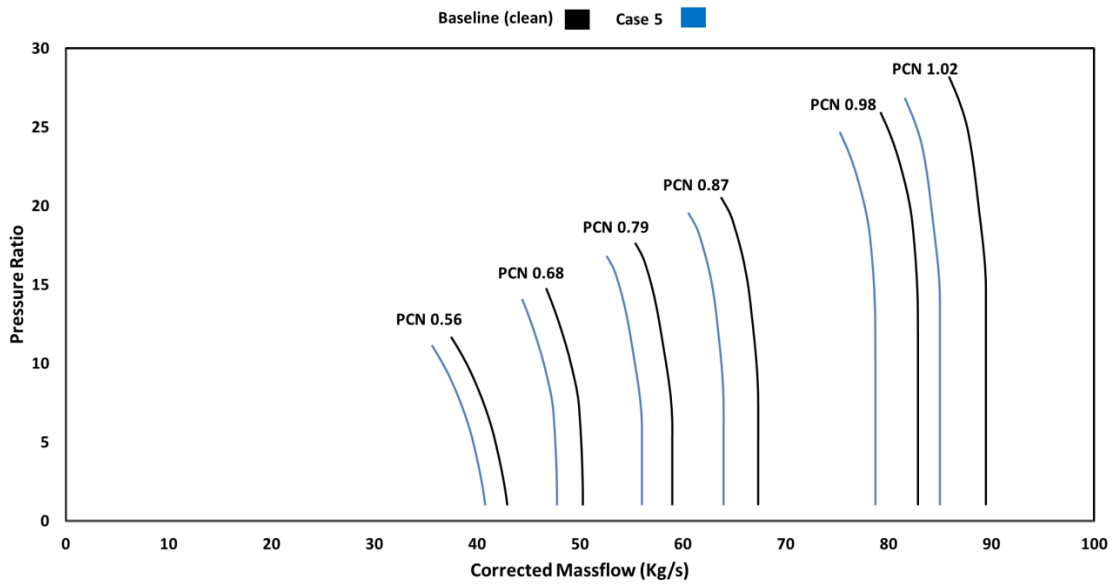

Figure 4-27 Compressor pressure maps for baseline and Case 5

4.4 Conclusion

This chapter outlines the effectiveness of both the linear and non-linear gas path analysis technique for the detection and quantification of gas path faults.

Furthermore, a virtual engine in TurboMatch for the LM2500+ was created and validated against performance data in open literature for the real LM2500+ engine. This validated virtual engine was the basis for the fouling degradation studies carried out it in this chapter.

Apart from the use of this virtual engine in Pythia to generate degradation operational data for the gas path analysis, it was also used to generate the modified compressor maps for the different degradation cases considered for use in the Moore-Greitzer compressor flowfield model.

5 RESULTS FOR THE AERODYNAMIC-ROTORDYNAMIC MODEL INTEGRATION

5.1 Introduction

This chapter presents the results for the following:

- Validation for the 2D transfer matrix rotordynamic modelling MATLAB code.
- Validation for the Al-Nahwi's compressor aerodynamic force model.
- Results for the parametric study of the model integration for the aerodynamic and rotordynamic models as applied to a fouled gas turbine compressor thermodynamically similar to LM2500+.

5.2 Rotordynamic Model Validation

To validate the 2D transfer matrix rotordynamic model MATLAB code given in Appendix D, programmed based on the first principles detailed in Chapter 3, its prediction of the critical speed and unbalance response of the Kikuchi rotor-bearing system is compared against that published by Kikuchi (Kikuchi, 1970).

5.2.1 Kikuchi Rotor-Bearing System

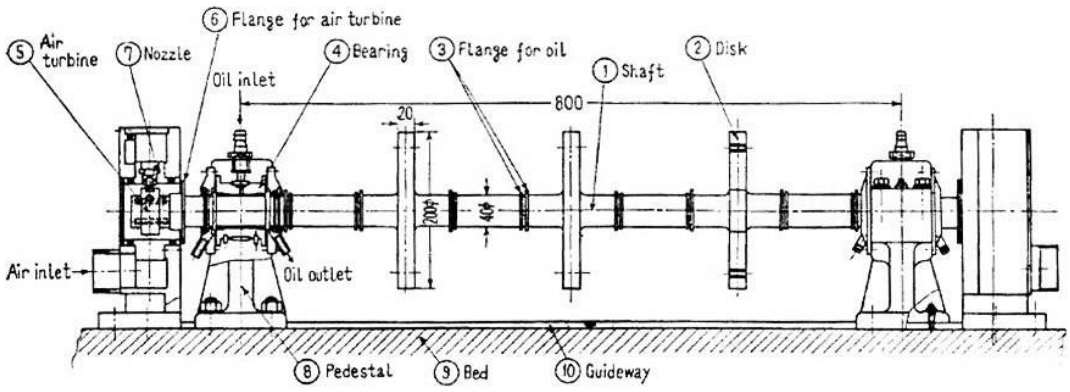

Figure 5-1 Kikuchi rotor-bearing test rig (Source: Kikuchi, 1970)

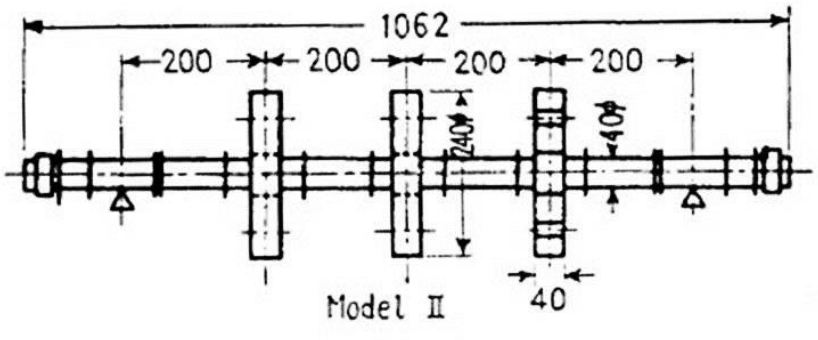

Figure 5-2 Schematic of the Kikuchi rotor-bearing system (Source: Kikuchi, 1970)

The Kikuchi rotor configuration shown in Figure 5-2 consists of three interspaced disks of equal masses, shrink fitted to a uniform shaft and driven by an air turbine at its left end. The rotor shaft has a minimal residual unbalance that can only excite about 5μm at any rotational speed (Kikuchi, 1970).

The rotor is supported at its end by two split cylindrical journal bearing made of brass and lined with white metal. The bearings are lubricated from the top using the turbine oil No. 90 lubricant.

For the unbalance response experiment, the unbalance mass is attached to the central disk, the amplitude of the both the vertical and horizontal components of the shaft vibration at the central disk for different journal bearing configuration is pickup using a vibration capacitive probe.

Details of the rotor and journal bearing dimensions and other necessary input parameter for the rotordynamic model are presented below in Table 5-1.

Table 5-1 Kikuchi rotor-bearing configuration data (Source: Kikuchi, 1970)

Items \ Conditions			Ⅱ-0.6-0.001		Ⅱ-0.6-0.003		Ⅱ-0.6-0.01	
Bearings	Position		Left	Right	Left	Right	Left	Right
	Length	L mm	24	24	24	24	24	24
	Diameter	D mm	40.045	40.044	40.112	40.113	40.396	40.393
	Clearance	C mm	0.024	0.026	0.058	0.061	0.200	0.200
	Viscosity	μ cP	28	26	29	28	42	47
	Static load	F_0 kg	25.9	25.9	25.9	25.9	25.9	25.9
Shaft	Model		Ⅱ					
	Total weight	kg	51.8					
	Disks Position		Left, Right			Middle		
		Mg kg	13.47			13.44		
		I_{pg} kg-mm²	1.02×10^5			1.02×10^5		
		I_{dg} kg-mm²	5.11×10^4			5.11×10^4		
	Span length	mm	800					
	Natural frequency (1st mode)	c/sec	48.7					
Unbalances			Middle disk 0°, 120 kg·μ					
Type			Symmetric rotating shaft system with two bearings					

5.2.2 Determination of Journal Bearing Stiffness and Damping Coefficients

The journal bearing stiffness and damping coefficients is gotten from the solution of the Reynolds equation for hydrodynamic lubrication.

Since the accurate numerical modelling of the journal bearing is not the primary aim of this work, results from an already existing solution for the Reynolds equation in open literature is used. The published results for bearing stiffness and damping coefficients shown in Figure 5-4 and Figure 5-5 are used to create a lookup table for the bearing stiffness and damping in terms of the bearing eccentricity ratio.

To determine the bearing eccentricity ratio which is a function of the bearing Sommerfeld number and bearing L/D ratio (bearing length/ bearing diameter), the data published by Pinkus and Sternlicht (1961) also shown in Figure 5-3 is used.

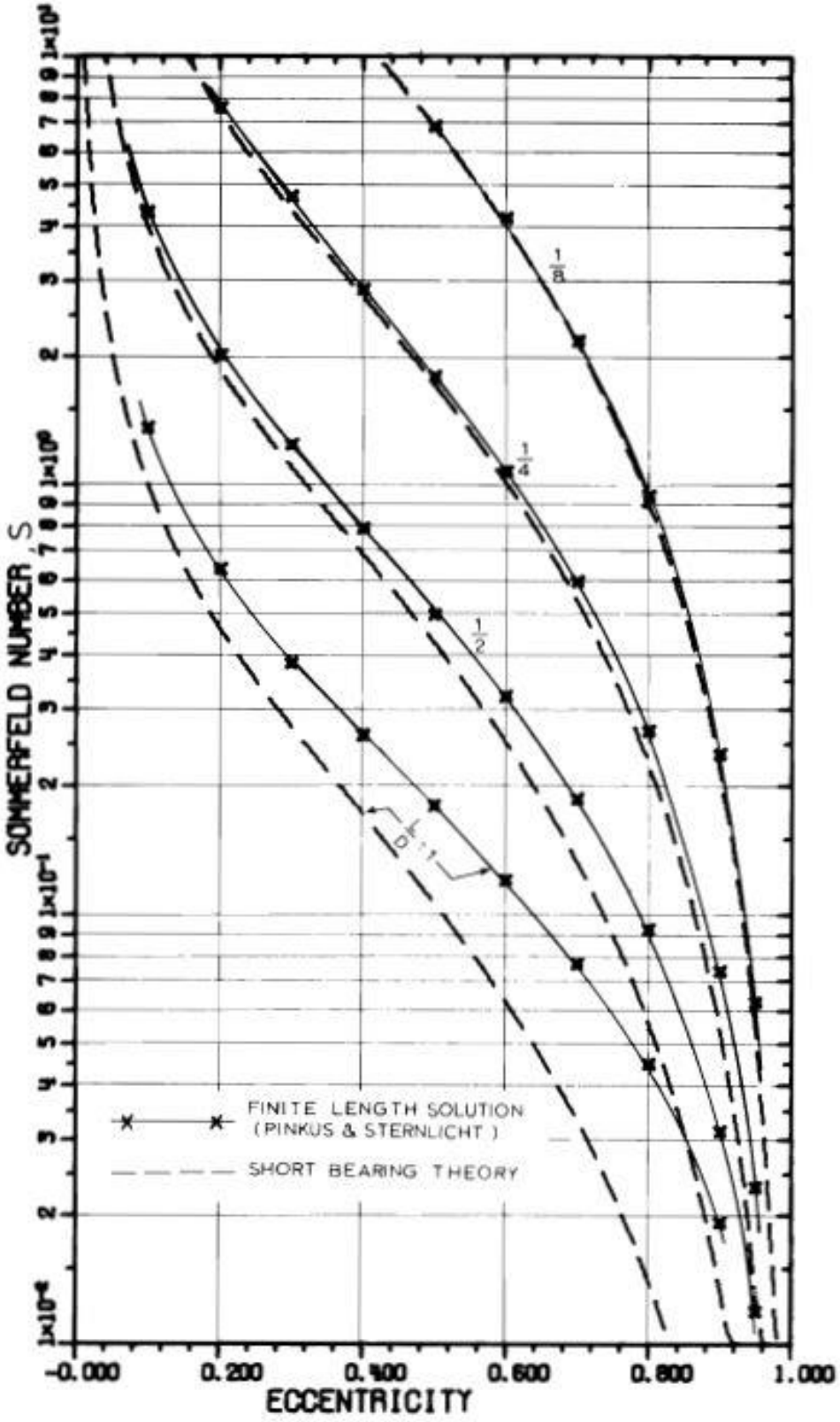

Figure 5-3 A graph of journal bearing Sommerfeld number and eccentricity

(Source: Kirk and Gunter, 1976)

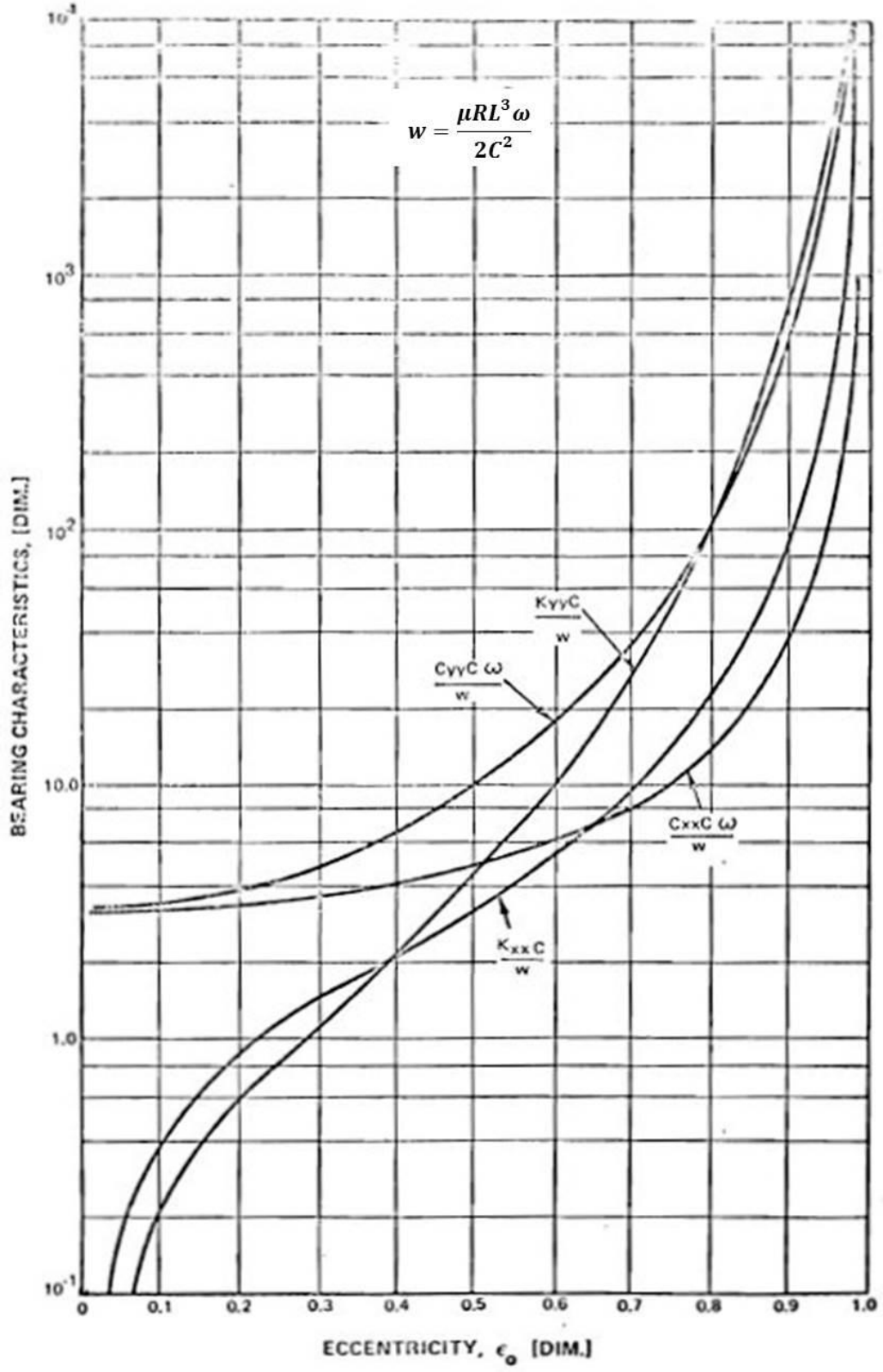

Figure 5-4 Direct stiffness and damping coefficient (Source: Kirk and Gunter, 1976)

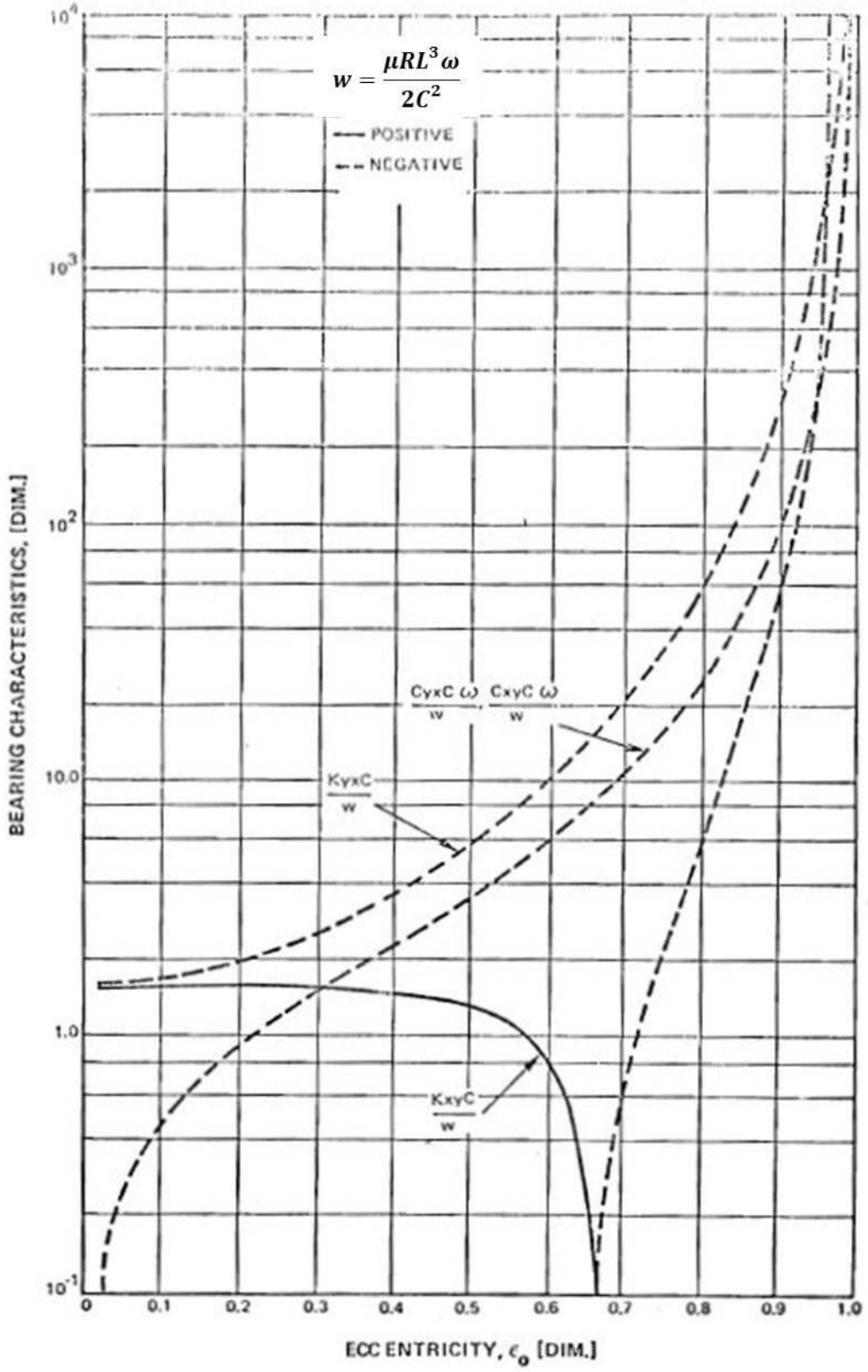

Figure 5-5 Cross-coupled stiffness and damping coefficients (Source: Kirk and Gunter, 1976)

5.2.3 Results for Rotor-Bearing System Unbalance Response

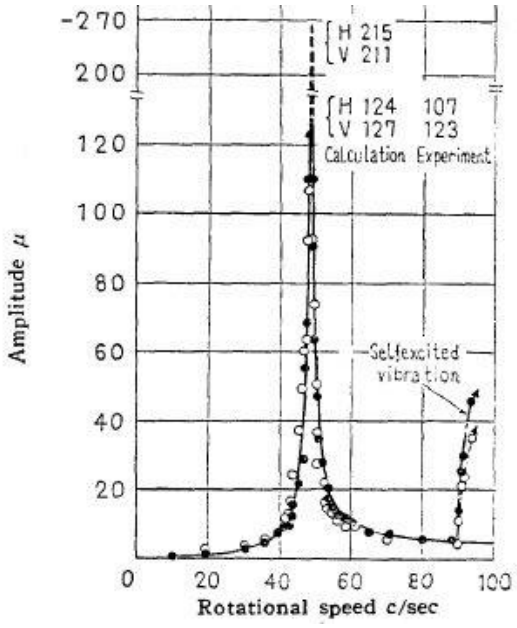

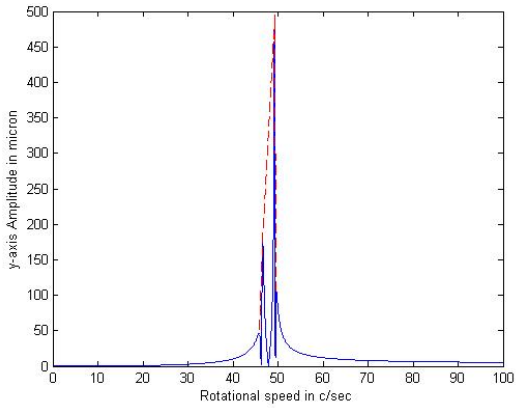

(a) (Source: Kikuchi, 1970)

(b)

Figure 5-6 Unbalance response of rotor-bearing configuration II-0.6-0.001

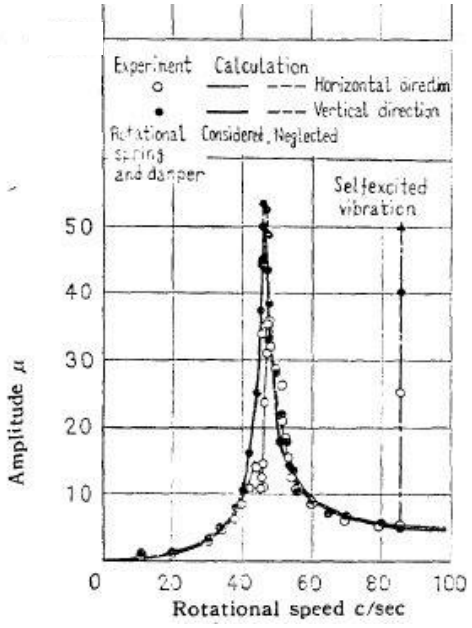

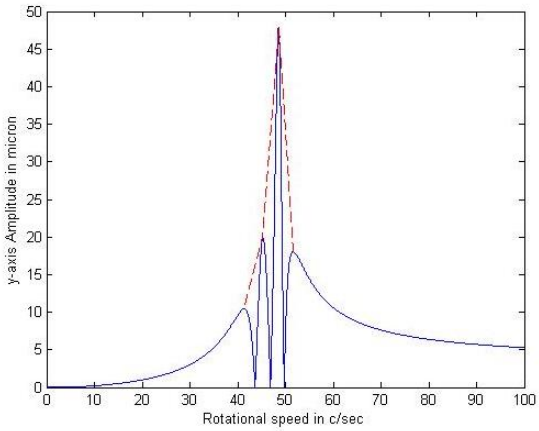

(a) (Source: Kikuchi, 1970)

(b)

Figure 5-7 Unbalance response of rotor-bearing configuration II-0.6-0.003

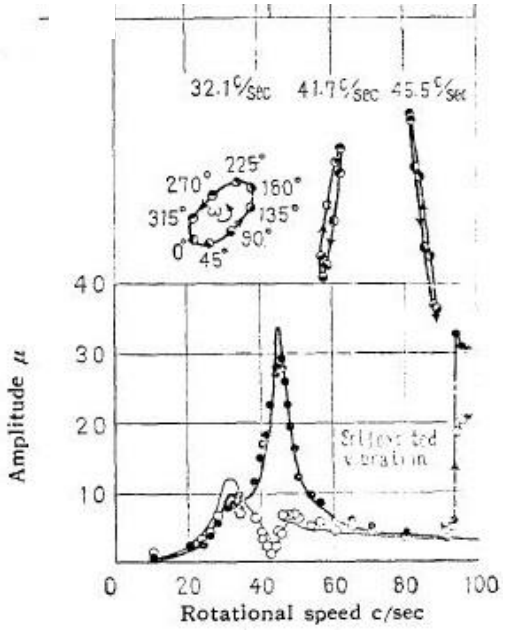

(a) (Source: Kikuchi, 1970)

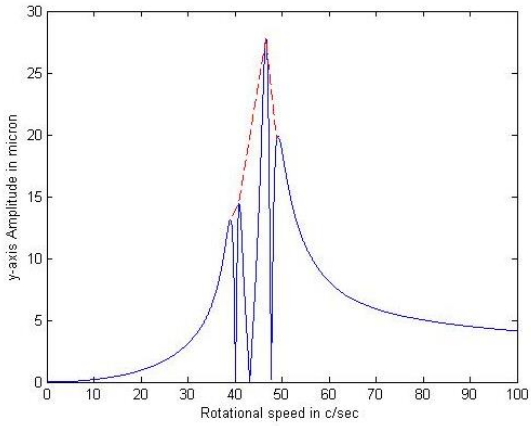

(b)

Figure 5-8 Unbalance response of rotor-bearing configuration II-0.6-0.01

5.2.4 Discussion of Results for Rotordynamic Model Code Validation

Comparing Kikuchi's unbalance response results in 'a' to the predicted response from the MATLAB code in 'b' found in Figure 5-6, Figure 5-7 and Figure 5-8, the following observation is made:

- The predicted critical speed (i.e. peak frequency response) and the Kikuchi's peak frequency response are the same.
- The trend of the unbalance response both in Kikuchi's result and that predicted by the MATLAB code is similar.
- Apart from the result in Figure 5-6 where the MATLAB code over predicts the peak response amplitude, all other cases in Figure 5-7 and Figure 5-8, the amplitude of the peak response show good agreement.

The discrepancy between the MATLAB code response prediction and Kikuchi's response in Figure 5-6 is mainly due to errors from curve fitting approximation in creating the journal bearing stiffness and damping coefficient look up table. However, this curve fitting approximation error in the model is limited to only when the bearing on the rotor is a journal bearing. For rotor bearing configuration where

the bearing is a rolling-element bearing like in the investigated engine which is similar to the LM2500+, such modelling error would not suffice, as only a constant stiffness coefficient in the X and Y axis are required for its modelling (Vance, 1988).

In summary, the MATLAB rotordynamic model implementation shows good agreement with Kikuchi's result for the prediction of critical speed and unbalance response.

The MATLAB codes for the Kikuchi rotor simulation are presented in Appendices D.7, D.8 and D.9.

5.3 Aerodynamic Force Model Validation

To validate the aerodynamic force MATLAB code presented in Appendix E, which has been programmed based on the first principles detailed in Chapter 3, its prediction of the aerodynamic forces is compared to that published by Al-Nahwi (2000) for the aerodynamic forces generated due to the effect of rotor blade tip clearance asymmetry in an axial compressor. This indirect means of validation is adopted due to the dearth of experimental data of aerodynamic force measurements in an axial compressor due to fouling in the open literature.

5.3.1 MIT 3-stage experimental compression system

In following with the work by Al-Nahwi(2000), the prediction from the aerodynamic force MATLAB code is compared to that published for the MIT 3-stage compressor for a fixed rotor displacement tip clearance condition.

The MIT 3-stage experimental compression system consists basically of a 3-stage axial compressor, a plenum and a throttle.

To proceed with the aerodynamic force validation, the following data is required: compressor pressure rise characteristic, compressor torque characteristic, compressor geometry and inertia parameters.

Plots of the compressor pressure rise and torque characteristics, compressor geometry and the determination of other geometrical parameters are provided in Appendix B.

Presented below is a summary of the key parameters needed for the aerodynamic force validation.

Table 5-2 Summary of MIT 3-stage test compressor data (Source: Al-Nahwi, 2000)

Parameter	Value
H	0.27
W	0.25
S	1.08
λ	0.68
μ	1.01
ψ_{CE}	14.82
λ_{tu}	54.74
λ_{pr}	98.89
$\tau_{c0}, \tau_{c1}, \tau_{c2}, \tau_{c3}$	0.4472, -0.8254, 1.9392, -0.88774

5.3.2 Results for Fixed Compressor Rotor Offset

Al-Nahwi(2000) showed that, for a fixed offset of the compressor rotor, the steady state flowfield in the compressor is governed by the following relationship:

$$\mathrm{A}^6 + 8Q(Q-1)A^4 + \left[16Q^2(Q-1)^2 + \left(\frac{2\lambda}{3S}\right)^2\right]A^2 - \left[\frac{\psi_{ce}\mathrm{r}}{3}\right]^2 = 0 \qquad 5\text{-}1$$

$$A = \sqrt{a^2 + b^2}\,;\, a \approx A\cos\eta^*\,;\, b \approx A\sin\eta^*\,;\, \eta^* = \sin^{-1}\left(\frac{2\mathrm{A}}{\psi_{ce}\mathrm{r}}\frac{\lambda}{S}\right) \qquad 5\text{-}2$$

where A is the disturbed flow coefficient amplitude, a & b are also components of the disturbed flow coefficient amplitude, Q is the rescaled flow coefficient, λ is the compressor rotor inertia parameter, S is the compressor pressure rise aspect ratio, ψ_{ce} is the sensitivity of the compressor pressure rise coefficient to tip clearance variation and r is the relative rotor radial displacement.

Applying the parameters in Table 5-2 into Equation 5-1 for a relative rotor radial displacement of 1% (i.e. r = 0.01); with the resulting values for a and b inputted

into the expressions for aerodynamic force developed in Chapter 3 which has been implemented in MATLAB and provided in Appendix E. Plots of the corresponding aerodynamic force prediction are compared with that published by Al-Nahwi for the flow regime $-0.4 \leq Q \leq 1.6$.

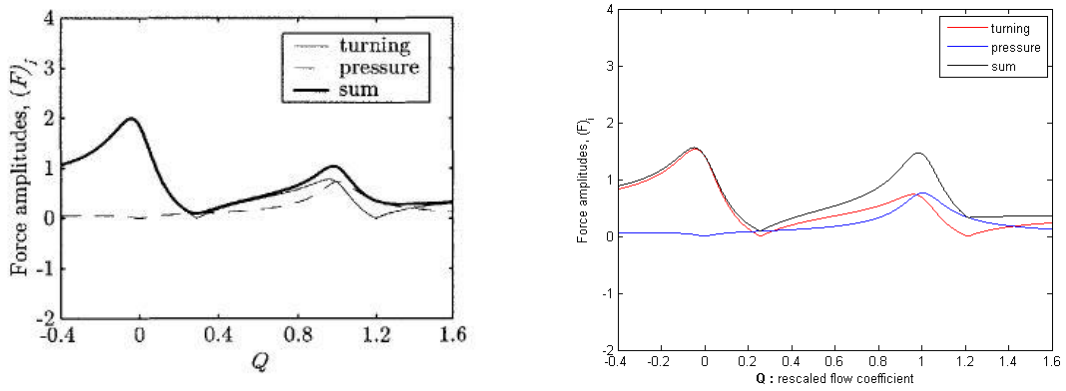

(a) (Source: Al-Nahwi, 2000) (b)

Figure 5-9 Resultant aerodynamic force plot (a) Al-Nahwi's result (b) MATLAB code prediction

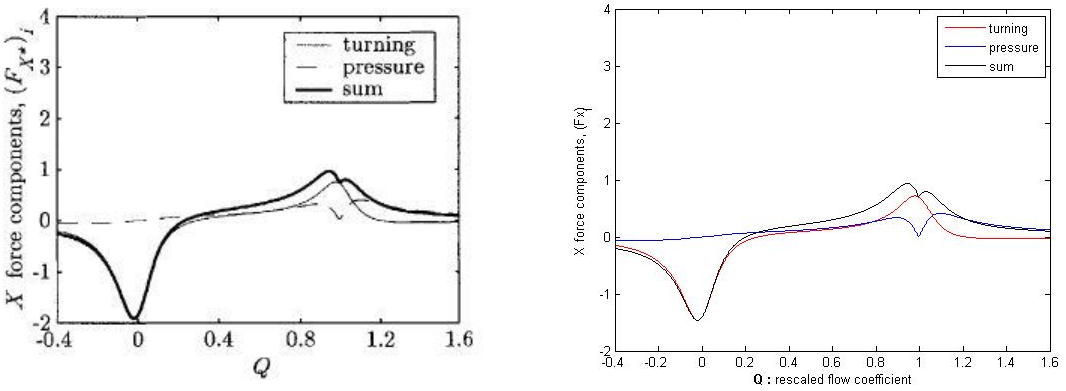

(a) (Source: Al-Nahwi, 2000) (b)

Figure 5-10 X-component aerodynamic force plot (a) Al-Nahwi's result (b) MATLAB code prediction

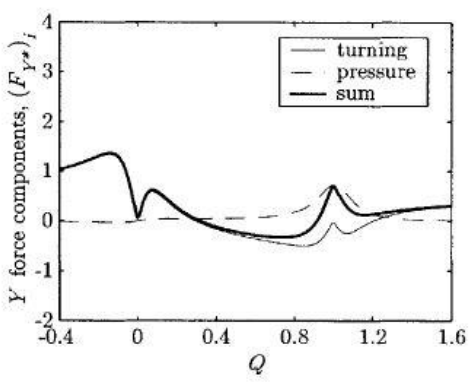

(a) (Source: Al-Nahwi, 2000)

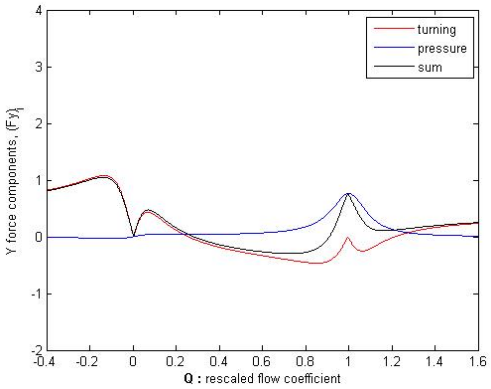

(b)

Figure 5-11 Y-component aerodynamic force plot (a) Al-Nahwi's result (b) MATLAB code prediction

5.3.3 Discussion of Results for Aerodynamic Force MATLAB Code Validation

The following observations are made from the aerodynamic force simulation:

Firstly, from Figure 5-9, it is observed from both plots, that the turning force is the dominant contributor to the total aerodynamic force. A point that is also corroborated by Alford (1965).

Secondly, from Figure 5-9, in both plots, at Q = 1, which correspond to the surge point, the total aerodynamic force is maximum. This point is as expected, with the surge point being a point of instability in the compressor, the amplitude of disturbed flow is a maximum.

Considering the X and Y aerodynamic component force plot in Figure 5-10 and Figure 5-11 respectively, with the X force component serving as the restoring force and the Y force component serving as the whirling inducing force, it can be observed that when Q < 0.4, the X force component is negative in both plots and thus acts in opposite direction to the compressor rotor, but when Q > 0.4, the X force component is positive in both plots and acts in same direction of the rotor displacement.

Lastly, when Q = 1 in Figure 5-11, the pressure force part of the total Y component force is maximum in both plots and changes the backward whirling tendency of the turning force part at that operating point to a forward whirling motion.

In conclusion, the MATLAB code for the aerodynamic force prediction shows good agreement with the results published by Al-Nahwi for the MIT 3-stage experimental compressor.

5.4 Parametric Studies of the Integration of the Aerodynamic and Rotordynamic Models

5.4.1 Determination of the Compressor Pressure Rise Parameters and the Fouling Parameters

From the TurboMatch compressor fouling degradation studies conducted in Chapter 4, the compressor pressure map for all cases of compressor fouling in Table 4-6 for the speed line CN.= 1.02 is displayed in Figure 5-12.

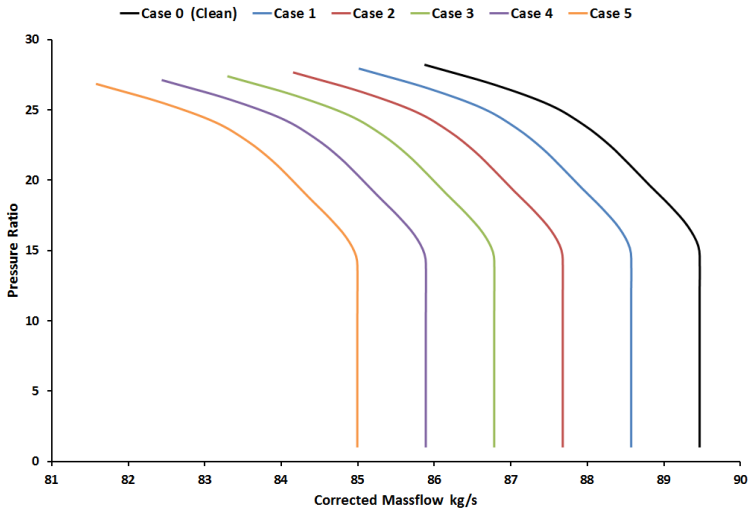

Figure 5-12 Clean & fouled compressor pressure map for CN=1.02

In other to convert Figure 5-12 to the form required by the Moore-Greitzer model, i.e. pressure coefficient versus flow coefficient, the following conversion is applied:

$$\Psi = \frac{P_1(PR-1)}{\rho U^2} \qquad 5\text{-}3$$

$$\phi = \frac{CM}{\rho A_c U} \qquad 5\text{-}4$$

where Ψ is the pressure rise coefficient, Φ is the flow coefficient, P_1 is the compressor inlet pressure, PR is the pressure ratio, ρ is the inlet air density, CM is the corrected mass flow, U is the spool speed at mean radius and A_c is the compressor flow area at inlet.

The determination of the geometrical parameters for the similar to LM2500+ engine is provided in Appendix C The resulting compressor pressure rise characteristic after applying Equations 5-3 and 5-4 to Figure 5-12 is presented in Figure 5-13.

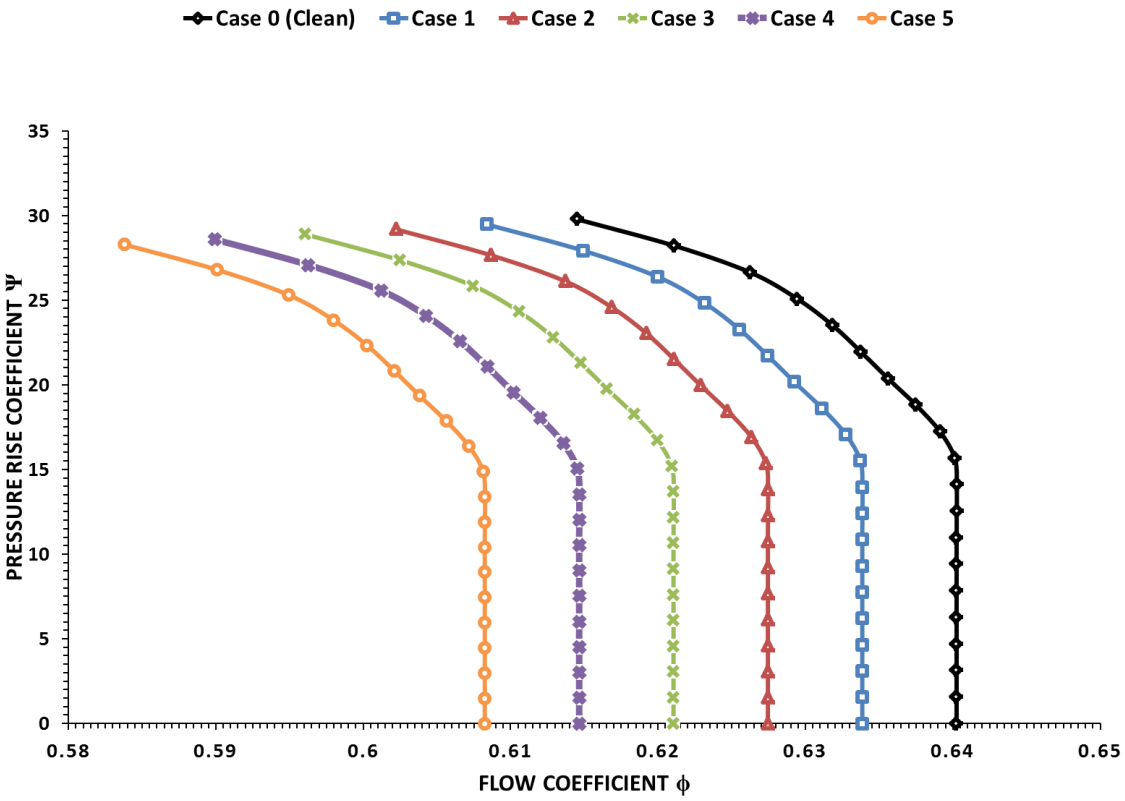

Figure 5-13 Converted compressor pressure map for CN=1.02

The final transformation required for Figure 5-13 is:

$$\phi^* = \phi - \phi_{co} \qquad 5\text{-}5$$

where ϕ^* is the transformed xial flow coefficient, ϕ the actual axial flow coefficient and ϕ_{co} the flow coefficient at the minimum or shut-off value of the pressure rise coefficient.

The resulting figure after applying Equation 5-5 is presented in Figure 5-14

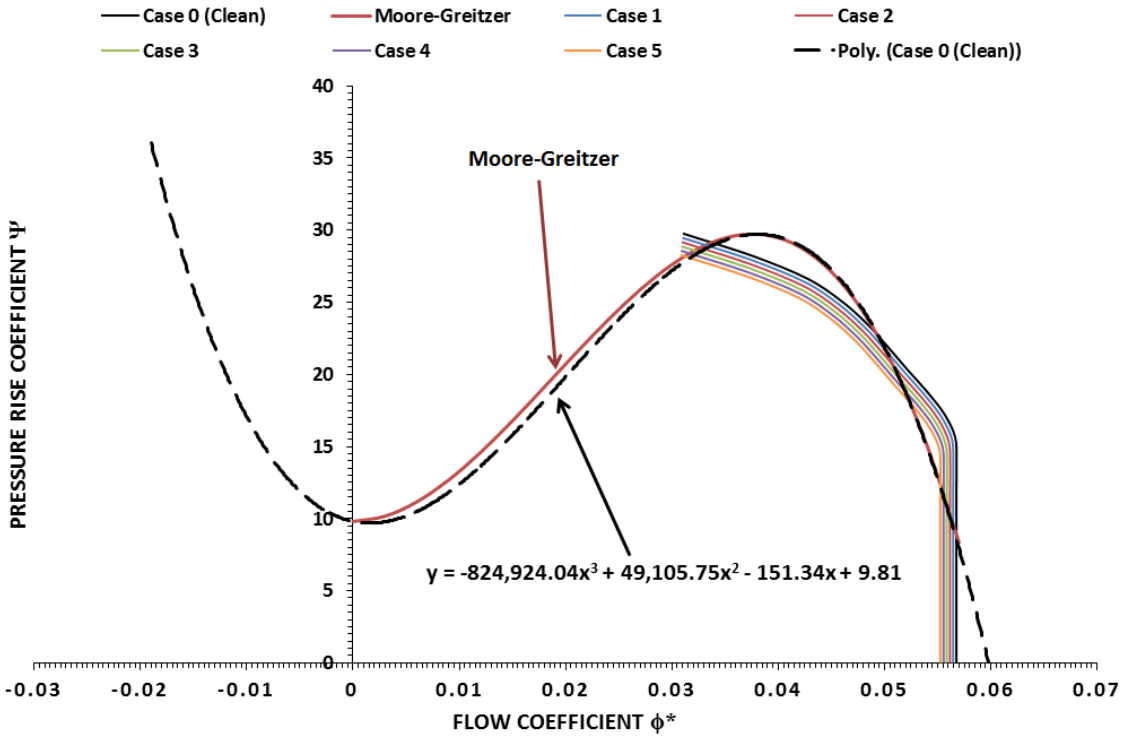

Figure 5-14 Transformed compressor pressure map for CN=1.02

Figure 5-14 is compared with the general polynomial form proposed by Moore and Greitzer (1986) shown in Figure 5-15 and the relevant parameters from this comparison describing the compressor pressure rise characteristic is presented in Table 5-3.

From Figure 5-14, the Moore-Greitzer compressor pressure rise characteristic curve fit uses a single expression to map both the normal steady-state compressor operation and the reverse flow compressor operation (post surge) (Greitzer and Moore, 1986). The negative flow coefficient in Figure 5-14 signifies reverse flow conditions.

Although the Moore-Greitzer compressor pressure rise characteristic describes both normal steady state and reverse flow and unstable operations, this work has focused only on the normal steady state operating regime.

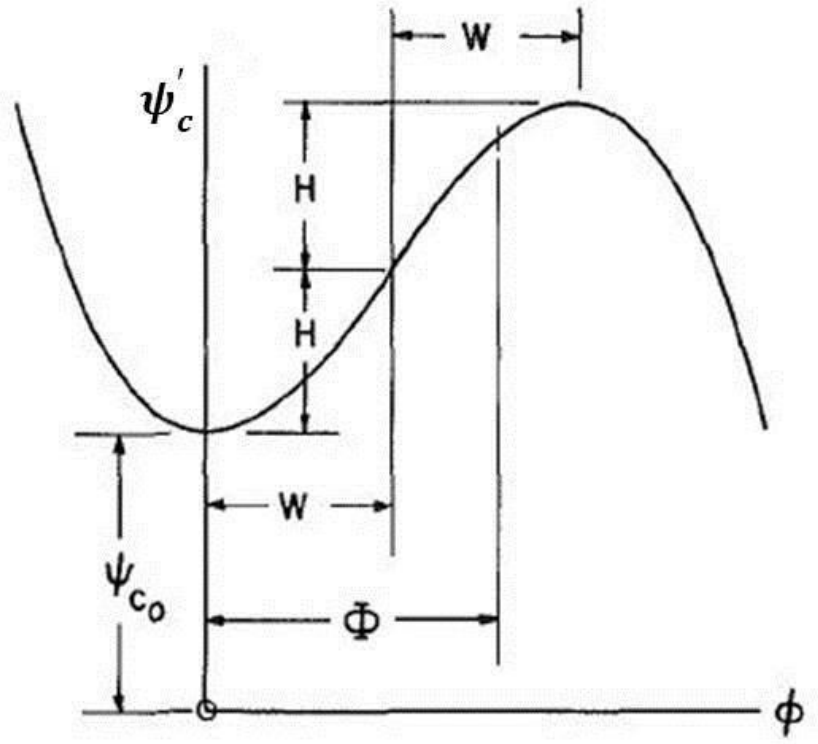

Figure 5-15 Moore-Greitzer Compressor Pressure rise Characteristic (Source: Greitzer and Moore, 1986)

Table 5-3 Compressor pressure rise characteristics parameters

S/N	Parameters	Value
1	Semi-height of the cubic axisymmetric characteristic (H)	9.96
2	Semi-width of the cubic axisymmetric characteristic (W)	0.0188
3	Aspect ratio of the pressure rise characteristic (S = H/W)	529.787
4	Shut-off value of the pressure rise coefficient ψ_{co}	9.811

Recalling from Chapter 2, the fouling parameter (FP) assuming a linear scaling effect of fouling on the compressor pressure rise characteristic is defined as:

$$\mathrm{FP} = \psi_{cf} \times \Delta MF = \left(2 + \frac{\psi_{co}}{H}\right) \Delta PR \qquad 5\text{-}6$$

where ψ_{cf} is the fouling sensitivity coefficient, ΔMF and $\Delta\mathrm{PR}$ are the relative change in massflow and pressure ratio respectively, ψ_{co} is the shut-off value of the pressure rise coefficient and H is a parameter gotten from the pressure rise characteristics.

Applying Equation 5-6 to the data in **Error! Reference source not found.** and parameters in Table 5-3, the fouling parameters for the different cases of engine fouling is presented in the table below.

Table 5-4 Fouling parameters for different cases of engine fouling

S/N	Cases	Fouling Parameter (FP)
1	Case 1	0.0299
2	Case 2	0.0597
3	Case 3	0.0896
4	Case 4	0.1194
5	Case 5	0.1493

5.4.2 Compressor Flow Field Analysis

The aim of the compressor flow field analysis is the determination of the evolution of the amplitudes of disturbed flow coefficient.

On the other hand, the amplitudes of the disturbed flow coefficient are necessary for the determination of the aerodynamic force.

The compressor flow field analysis is based on the steady state solution of the Moore-Greitzer compression system model modified for a fouled compressor developed in Chapter 2.

Table 5-5 Inertia parameter for simulated LM2500+

S/N	Parameter	Value
1	Inertia Parameter λ	2.8243

Applying the data in Table 5-4 and Table 5-5 into Equation 2-95, results for the steady state evolution of the amplitude of the disturbed flow coefficient in presented in Figure 5-16, Figure 5-17 and Figure 5-18. The MATLAB implementation of the solution to the steady state flow field equation is presented in Appendix E.

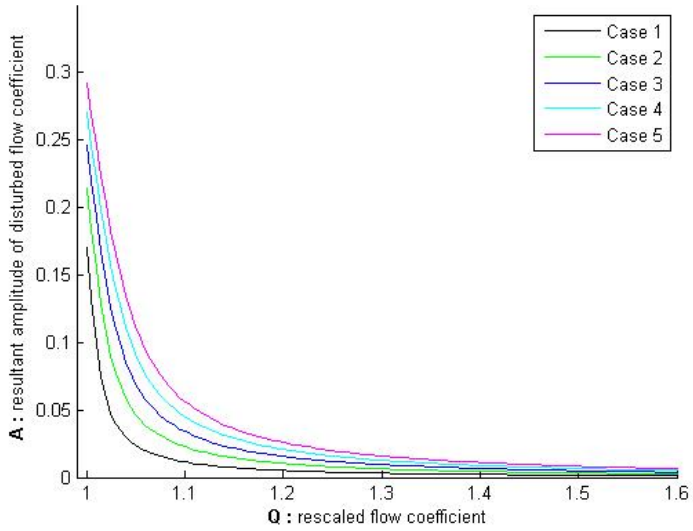

Figure 5-16 Resultant amplitude 'A' of disturbed flow coefficient for different cases of fouling in simulated gas turbine engine

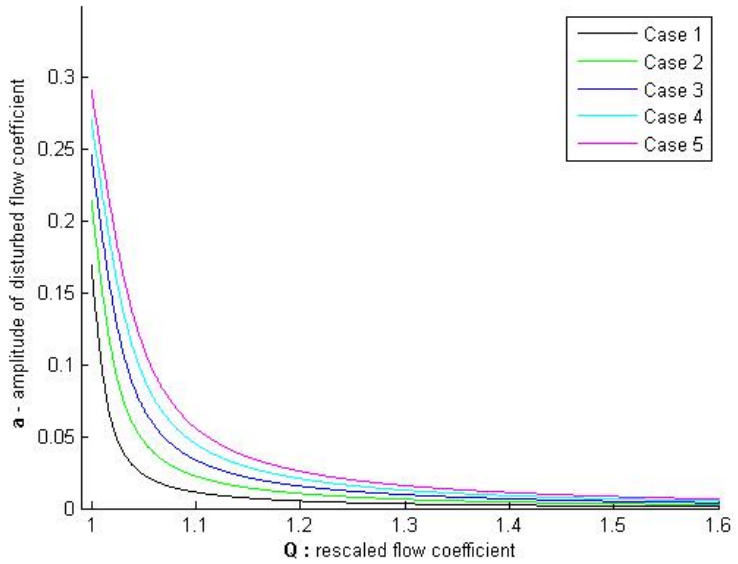

Figure 5-17 'a' Amplitude of disturbed flow coefficient for different cases of fouling in simulated gas turbine engine

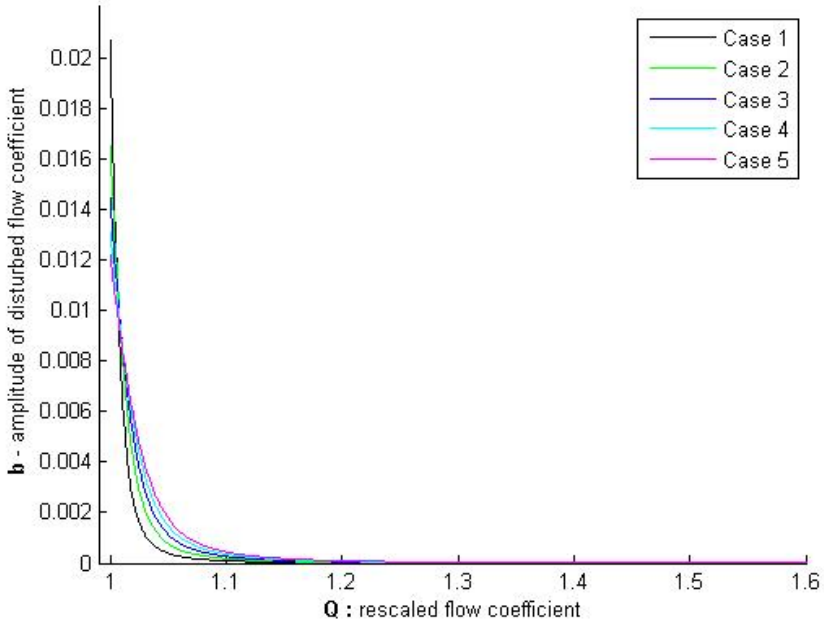

Figure 5-18 'b' Amplitude of disturbed flow coefficient for different cases of fouling in simulated gas turbine engine

Figure 5-16, Figure 5-17 and Figure 5-18 show the evolution of the amplitudes of disturbed flow coefficient for different levels of fouling in the thermodynamically simulated LM2500+ engine.

Over the operating flow range from 1<Q <1.6, with Q = 1.2 being the design point and Q = 1 the surge point, it is observed that for every case of fouling considered, the amplitude of the disturbed flow coefficient increases as the massflow is reduced or engine is throttled down.

Also, comparing Figure 5-17 and Figure 5-18, it can be observed that the a-component of the amplitude of the disturbed flow coefficient is several order of magnitude higher than the b – component. This observation is one of the reasons the turning force is the predominant force with respect to the pressure force. Furthermore, from Equations 3-145 and 3-146 representing the turning force and Equations 3-147 and 3-148 representing the pressure force, it is shown mathematically that the turning force scales with the square of ‘a’, while the pressure force scales linearly with ‘a’.

In Figure 5-18, a damping effect is observed near the surge point Q = 1, when the massflow is throttled down, as the level of fouling increases, the amplitude of the b-component of the disturbed flow coefficient is reduced.

Finally, Figure 5-16 shows an exponential like increase in the resultant amplitude of the disturbed flow coefficient as the mas flow is throttled down. The marked increase in the amplitude of the flow coefficient is indicative of unstable operations in the compressor typical with surge or when the stall limit has been exceeded.

5.4.3 Aerodynamic Force Analysis

The aerodynamic force analysis is based on the non-dimensional force expressions in Equations 3-145, 3-146, 3-147 and 3-148 for the x and y component of the turning and pressure force respectively.

The unsteady momentum force is ignored as only a steady state operating condition is considered in this analysis.

The non-dimensional force is the preferred form for the parametric analysis to be considered as it shows the general nature and trends of each of the components of the total aerodynamic force.

For the rotordynamic response analysis presented in the next section 5.4.4, the dimensional form of the aerodynamic force in Equation 3-142 is more suitable.

From Chapter 3, the flow-induced aerodynamic force is made up of three components, although the focus here is just on the turning and pressure force.

To proceed with the non-dimensional turning force simulation, the compressor stage torque characteristic is required.

Al-Nahwi (2000) proposed a 3rd order polynomial expression for the stage torque characteristic. In other to determine the coefficients of the torque characteristic expression, a curve fitting of the experimental data by Gamache (1985) for the stage torque characteristic of an axial compressor is performed. The criteria for curve fitting the stage torque characteristic is based on similar constraint for curve fitting the compressor characteristic given by Moore and Greitzer (1986) which is shown in Figure 2-2 This approach has also been used by Al-Nahwi (1985).

Furthermore, a single expression describing the entire stage torque is essential for simplification of the integration process required to compute the aerodynamic forces.

Presented in Figure 5-19, is the curve-fit of Gamache's data for stage torque characteristic. The curve fit is essential for the determination of the coefficients of the polynomial expression for the stage torque characteristic shown in Equation 3-121. The coefficients for the stage torque expression are summarized in

Table 5-6.

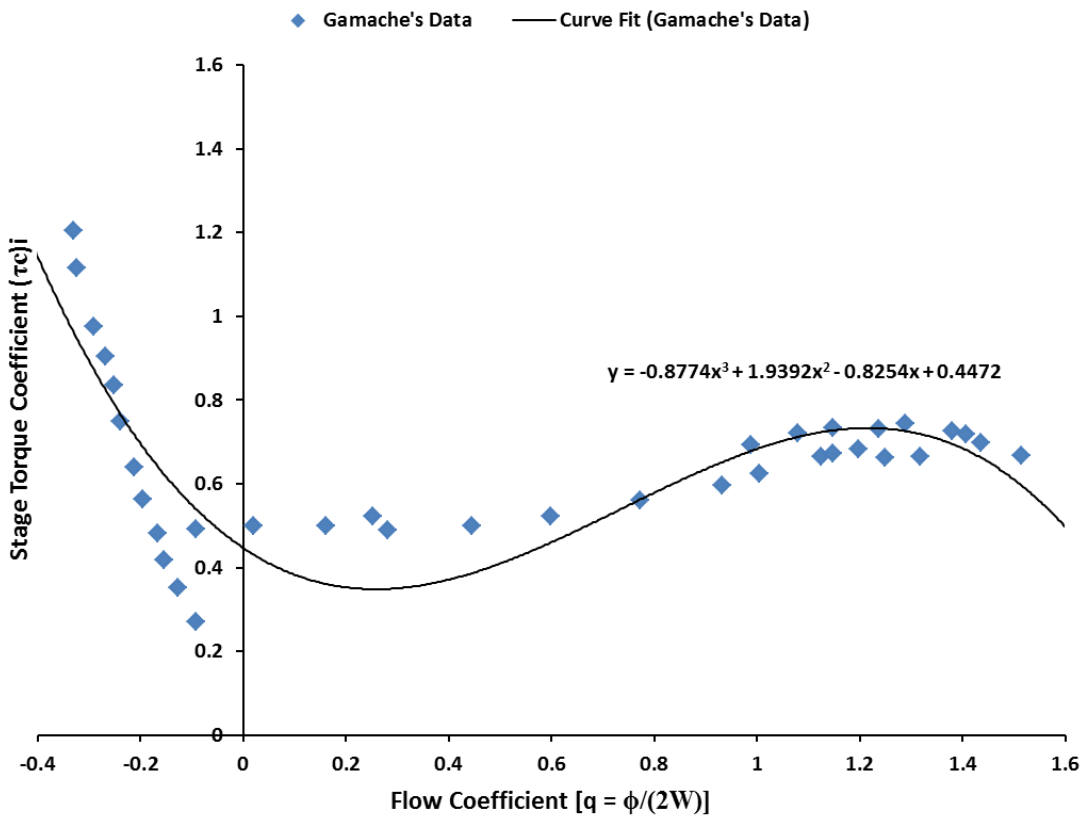

Figure 5-19 Stage torque characteristic

Table 5-6 Coefficients of stage torque expression

Stage Torque Expression Coefficients	Values
τ_{c0}	0.4472
τ_{c1}	-0.8254
τ_{c2}	1.9392
τ_{c3}	-0.8774

Other parameters needed to perform the aerodynamic force analysis are the turning force scale factor λ_{tu} and the pressure force scale factor λ_{pr} . Table 5-7 summarizes the turning force scale factor and pressure force scale factor for the simulated engine inspired by LM2500+ based on Equations 3-95 and 3-96. The geometric parameters of the simulated engine are given in Appendix C.

Table 5-7 Coefficients of stage torque expression

Parameters	Values
λ_{tu} (Turning Force Scale Factor)	92.6150
λ_{pr} (Pressure Force Scale Factor)	34.4968

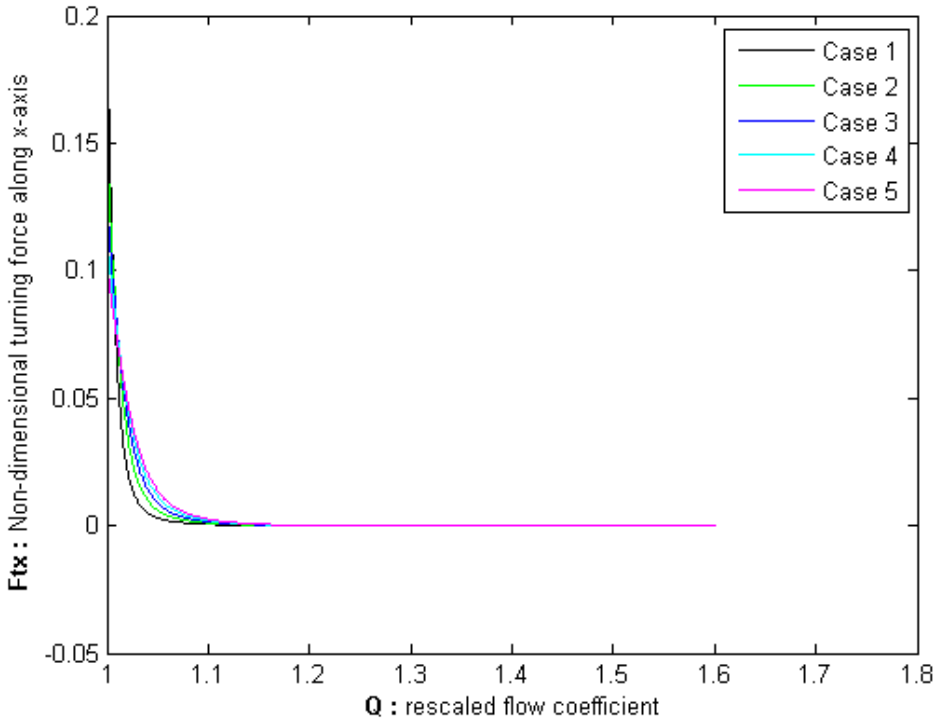

Figure 5-20 X-axis component of non-dimensional turning force

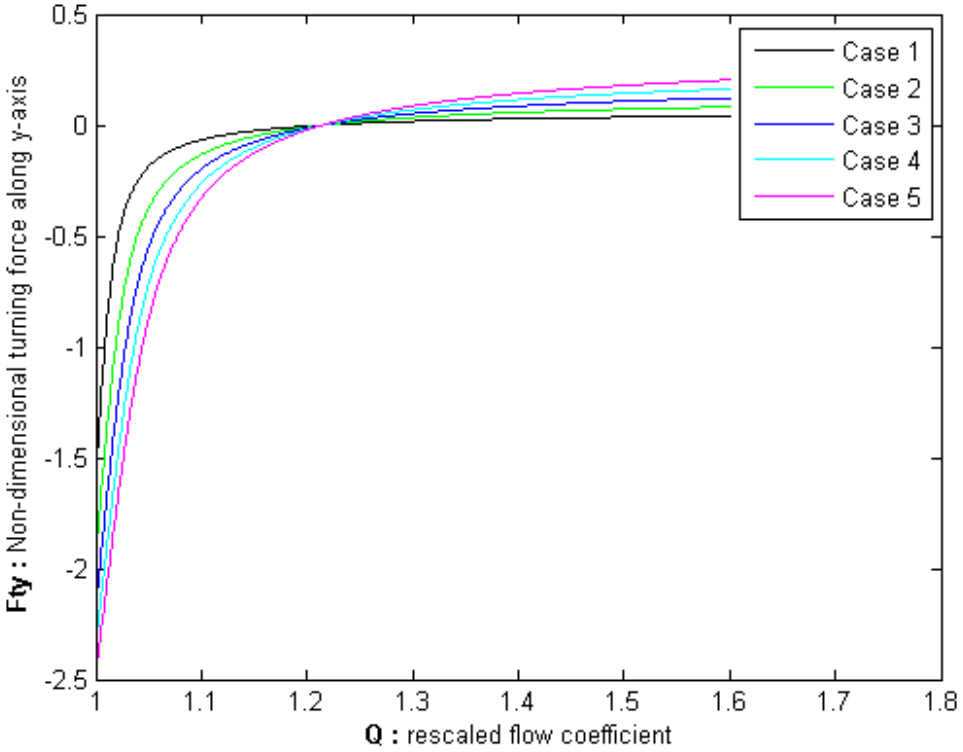

Figure 5-21 Y-axis component of non-dimensional turning force

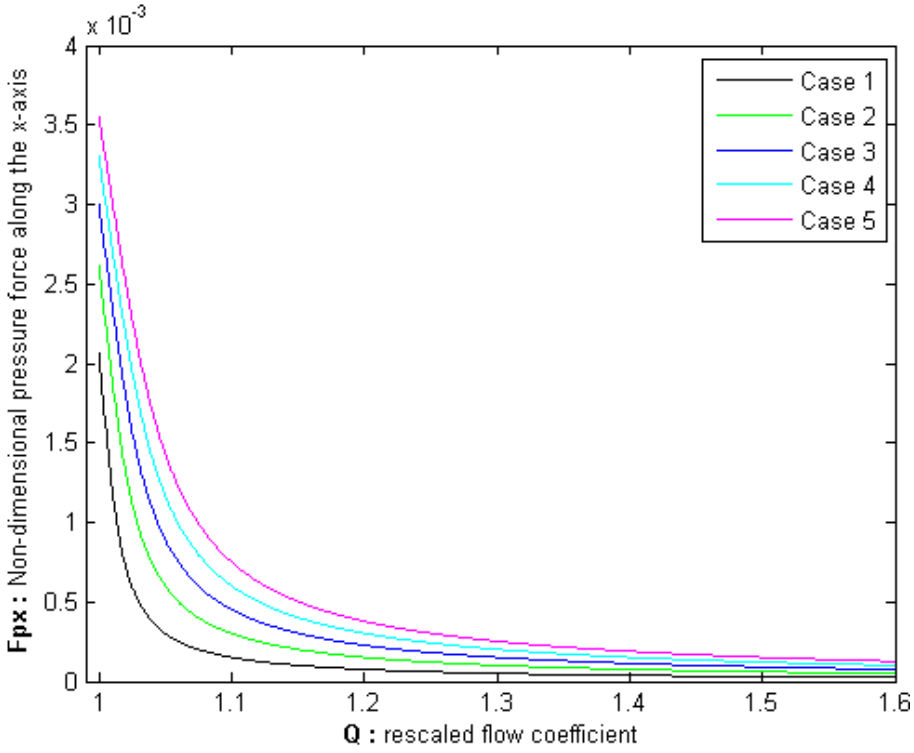

Figure 5-22 X-axis component of non-dimensional pressure force

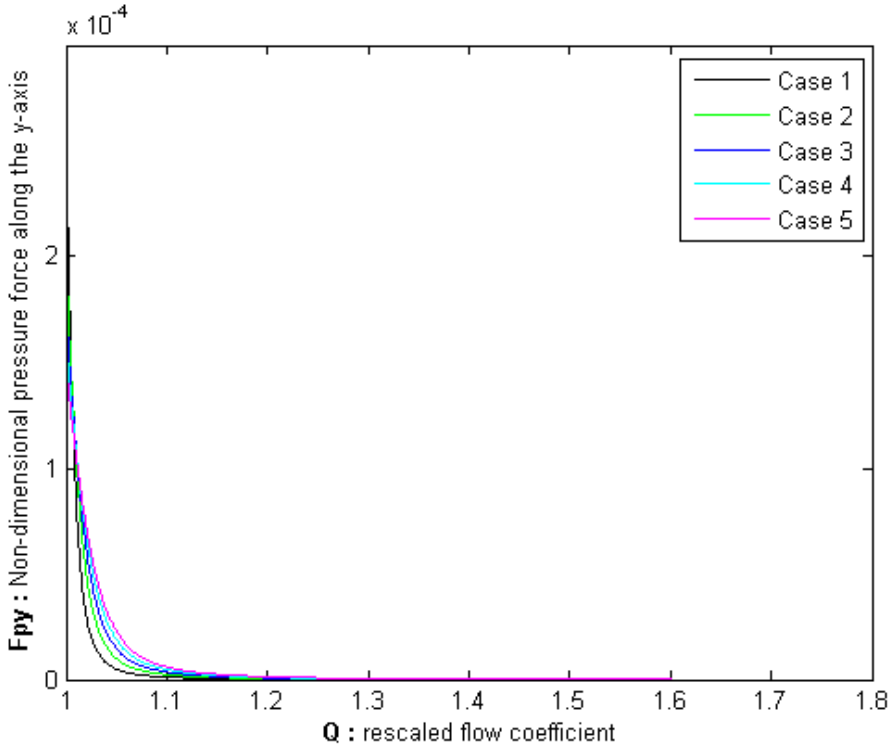

Figure 5-23 Y-axis component of non-dimensional pressure force

The nature of the force components of the aerodynamic force is such that, component forces acting along the x-axis are restoring forces while component forces acting along the y-axis are whirling inducing forces.

Considering the x-axis component of the non-dimensional turning force in Figure 5-20, for $Q > 1.1$ its effect is negligible. On the other hand, for $Q < 1.1$, its effect becomes predominant. Thus, as the compressor approaches the surge point $Q = 1.0$, the effect of fouling manifested through the turning force increases.

From Figure 5-21, the y-axis component of the non-dimensional turning force, it can be observed that for $Q < 1.2$ the turning force is negative, while for $Q > 1.2$, the turning force is positive. A similar trend has been report by Al-Nahwi (2000) albeit for the effect of compressor tip clearance asymmetry on compressor aerodynamic force

Comparing the components of the turning force in Figure 5-20 & Figure 5-21 and the components of the pressure force in Figure 5-22 & Figure 5-23, it's quite clear that the turning force is several orders of magnitude greater than the pressure

force and therefore the predominant source of the aerodynamic force experienced in the compressor rotor. This observation also falls in line with the findings by Alford (1965) in his work on the destabilizing aerodynamic forces in a turbine rotor due to clearance changes around its periphery.

5.4.4 Rotordynamic Response Analysis

The final piece of the puzzle is the rotordynamic forced response analysis due to the aerodynamic forces acting on the compressor rotor which caused the rotor vibration.

For this analysis, the 2D transfer matrix MATLAB code presented in Appendix D has been used. The code in Appendix D has been developed based on the rotordynamic theory detailed in Chapter 3.

Figure 5-24 presents a schematic of the rotordynamic model of the simulated LM2500+ compressor as a modified Jeffcott rotor used for the forced response rotordynamic analysis.

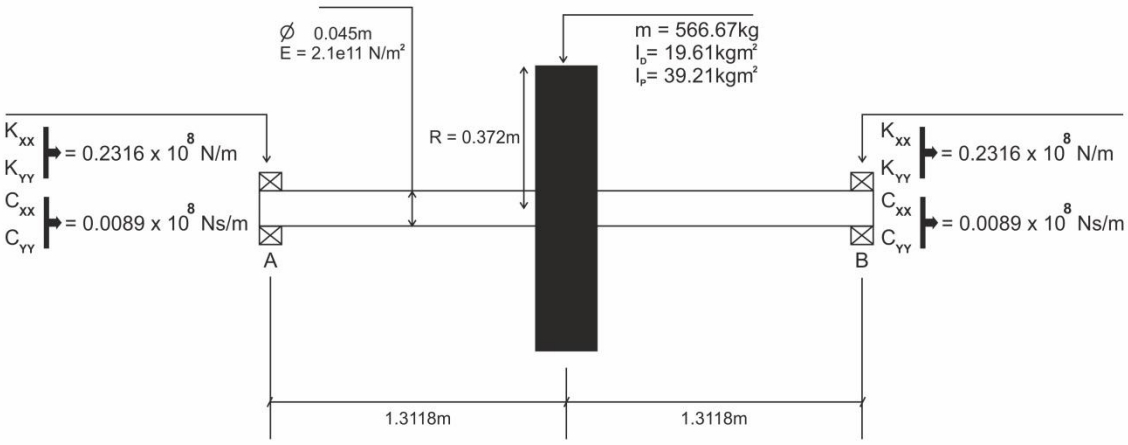

Figure 5-24 Simulated engine as a modified Jeffcott rotor

The parametric investigation of the vibration response at bearing location B for the rotordynamic model shown in Figure 5-24 for the different cases of fouling presented in **Error! Reference source not found.** operating at the design and s urge point are presented below.

The summary of the vibration trend for the operating point Q = 1.2 (design point).

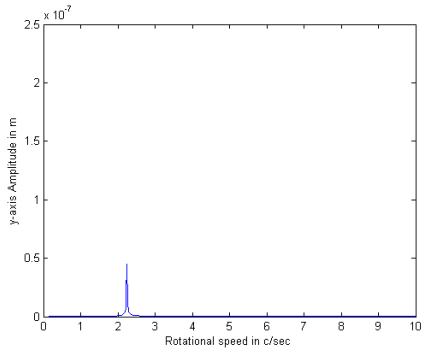

Figure 5-25 Case 1 engine vibration response @ Q = 1.2 (design point)

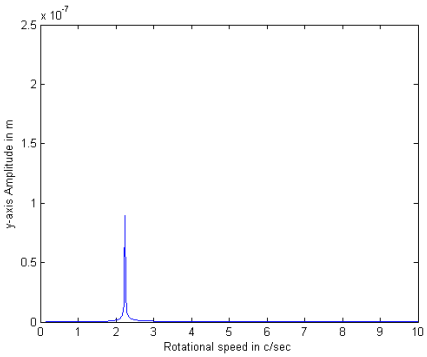

Figure 5-26 Case 2 engine vibration response @ Q = 1.2 (design point)

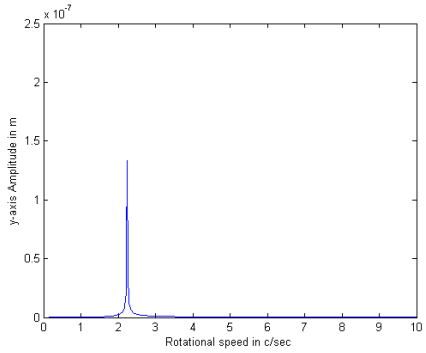

Figure 5-27 Case 3 engine vibration response @ Q = 1.2 (design point)

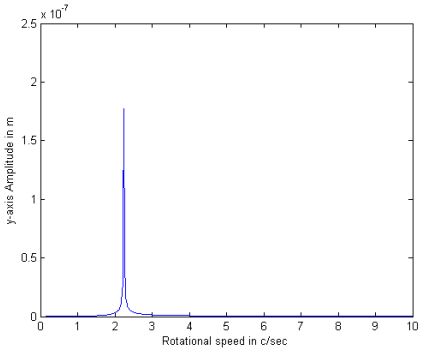

Figure 5-28 Case 4 engine vibration response @ Q = 1.2 (design point)

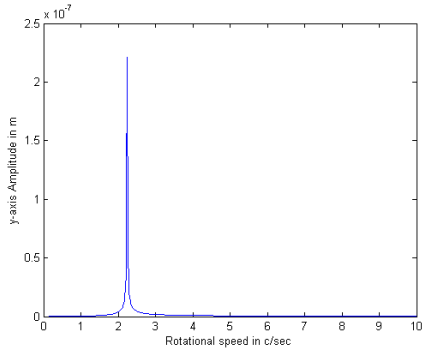

Figure 5-29 Case 5 engine vibration response @ Q = 1.2 (design point)

The summary of the vibration trend for the operating point Q = 1.0 (surge point).

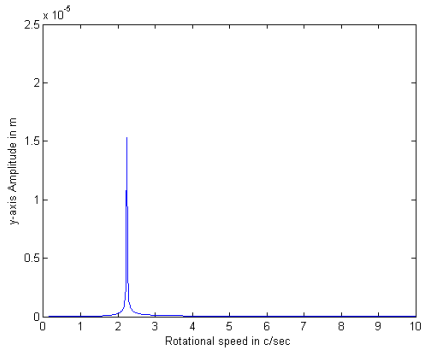

Figure 5-30 Case 1 engine vibration response @ Q = 1.0 (surge point)

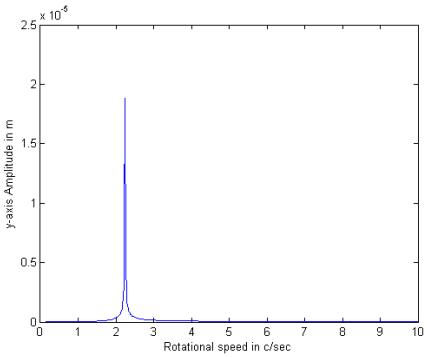

Figure 5-31 Case 2 engine vibration response @ Q = 1.0 (surge point)

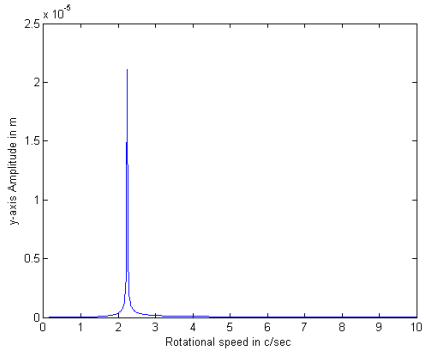

Figure 5-32 Case 3 engine vibration response @ Q = 1.0 (surge point)

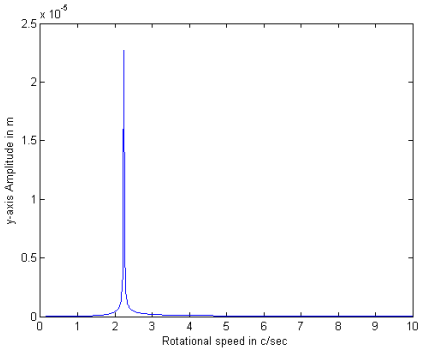

Figure 5-33 Case 4 engine vibration response @ Q = 1.0 (surge point)

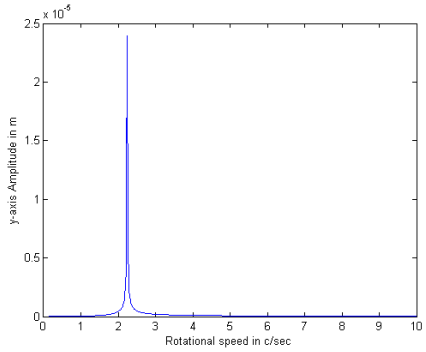

Figure 5-34 Case 5 engine vibration response @ Q = 1.0 (surge point)

5.4.5 Discussion of Results from the Integration of the Aerodynamic and Rotordynamic Compressor Model

Integrating the aerodynamic force model as a forcing function into the rotordynamic model of the fouled compressor reveals the following key finding:

1) **Effect of fouling on the vibration amplitude at the compressor rotor first fundamental frequency**

With the flow field parameters non-dimensionalized based on the modified Moore-Greitzer model transformation scheme described in Chapter 2, the design point is represented as Q = 1.2, while surge point is represented as Q = 1.0.

From Figure 5-25 to Figure 5-29 representing the design point forced response analysis and Figure 5-30 to Figure 5-34 representing the surge point forced response analysis, it is observed that as the rate of fouling increased marked by a continuous drop in the compressor mass-flow, isentropic efficiency and pressure ratio, there was a corresponding increase in the vibration amplitude at the compressor rotor first fundamental frequency. For the rotor configuration studied, the first fundamental frequency was approximately 2.24 Hz.

Also, the vibration amplitude is several orders of magnitude greater for the surge cases presented from Figure 5-30 to Figure 5-34 than the design point cases presented from Figure 5-25 to Figure 5-29. This is due to unstable compressor operations during surge.

While it is possible to consider other operating points in the flowfield regime, which most like would fall under the off-design operating condition for the gas turbine, only the design point and surge operating point is considered. This is aimed at avoiding needless repetition of similar plots as similar trends observed at the design and surge point would hold at the off-design points.

In conclusion, increased fouling causes the vibration amplitude at the compressor's rotor first fundamental frequency to increase.

6 APPLICATION OF MOORE-GREITZER TYPE MODEL TO A FOULING EXPERIMENT IN A SMALL JET ENGINE (TJ100)

6.1 Overview

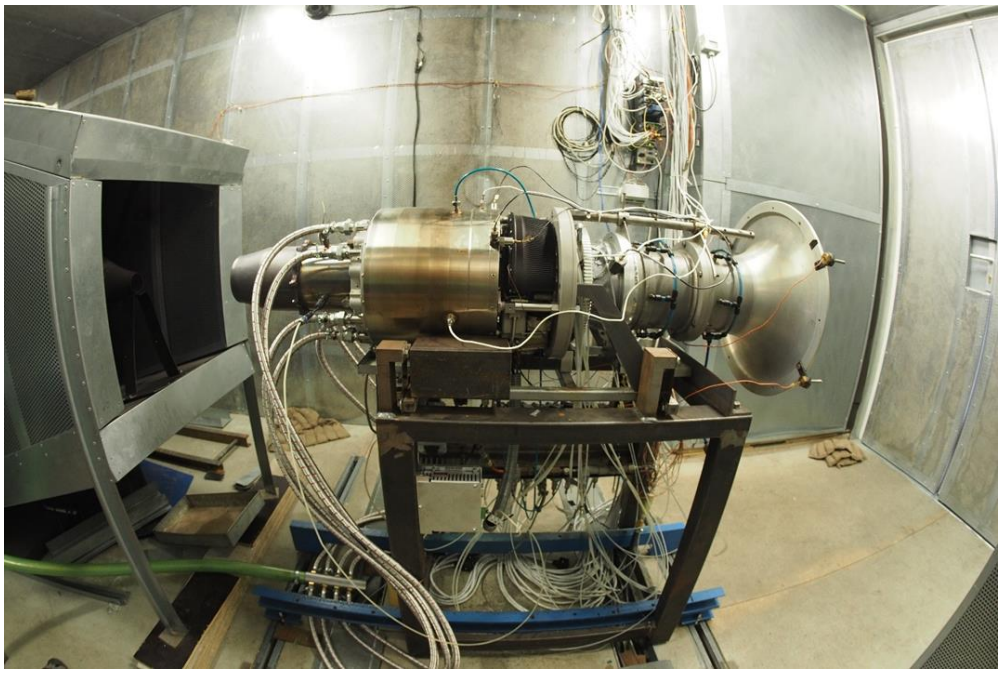

Figure 6-1 Modified TJ100 jet engine test rig (Source: Jiri, 2016a)

Compressor fouling experimental data performed on a modified TJ100 small jet engine test rig shown in Figure 6-1 was provided by a visiting academic to Cranfield University, Lt. Col Jiri Pecinka; who is from the Engine Operation Group, Department of Air Force and Aircraft Technology, University of Defence, Czech Republic. The externally provided experimental data was used to test the validity of the Greitzer-type model in predicting the flowfield parameters of the compressor during unstable operating conditions.

The experimental investigation covered the measurements of different unsteady gas path and vibration parameters at different engine locations for both a clean and fouled engine operating under different throttle settings and speeds. The fouling experiments were carried out with the intent of providing diagnostic insights into the dynamics of a fouled compressor.

The contribution of this research to this project was in the development and validation of a dynamic compression system model for the prediction of the inception of unstable operating conditions (surge/ stall) in the clean and fouled TJ100 test rig engine.

The dynamic compression system model developed for the TJ100 compression system was based on the Greitzer compression system model (i.e. a 1D Moore-Greitzer model).

The prediction of the inception of unstable operation in the compressor by the developed model for both the clean and fouled engine in terms of the frequency of the plenum pressure disturbance and mean flow coefficient at inception of unstable operations show good agreements with the experimental data.

An overview of the testing and measurements carried out, the mathematical rudiments of the compression system model and results are presented below.

6.2 Experimental Setup and Measurements

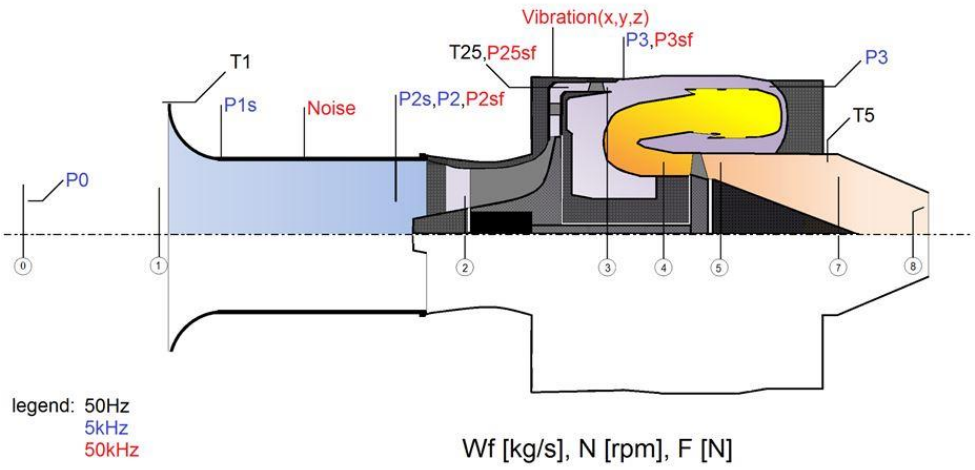

- 50 Hz – 30 channels (14 parameters)
- 5 kHz – 12 (4) channels
- 50kHz – 9 (5) channels

Figure 6-2 Measurement points on the TJ100 jet engine test rig (Source: Jiri, 2016a)

The fouling experiment was carried out on a refitted TJ100 jet engine test rig.

The TJ100 is a small turbojet manufactured by PBS Velka Bites; it is mostly used in light air vehicles e.g. unmanned air vehicles (UAV), light sport planes, sail planes, etc. (PBS, 2016).

The TJ100 gas turbine consists of a one-stage centrifugal compressor, radial and axial diffuser, annular combustor and a one-stage axial turbine (PBS, 2016).

A summary of the performance parameters for the TJ100 jet engine is presented in Table 6-1.

Table 6-1 TJ100 performance parameters (Source: PBS, 2016)

Main parameters – performance (ISA SL)		
Thrust: take - off (max. 5 min.)	1,300 N	292 lbf
Power supply	24 V DC	
Electrical power output	750 W	
Specific fuel consumption at max. thrust	≤ 0.112 kg/N/h	≤ 1.0983 lb/lbf/hr
Dimensions and weight		
Outside diameter	272 mm	10.7 in
Engine length	625 mm	24.6 in
Engine weight	19.5 kg	43.0 lb
Weight of accessories	depending on configuration	
Other data		
Amount of air intake	1.7 kg/sec	3.75 lb/sec
Revolutions max.	60,000 RPM	
Fuel	JET-A, JET-A1, JP4, JP8, TS-1, T2, RT	
Oil	according to MIL-L-23699 (Mobil Jet Oil II, AEROSHELL 560)	
Operating range		
Max. operating altitude	10,000 m	32,800 ft
Max. starting altitude	8,000 m	26,000 ft
Flight speed range	< Mach 0.8	
Speed range for startup	< Mach 0.6	
Temperature operating range	-40°C to +50°C	-40°F to +122°F

Four sets of measurements where obtained simultaneously during the fouling experiment, they are:

- Fast response unsteady pressures with 50kHz pressure probes located in P2, P25 and P3 in Figure 6-2

- Slow response unsteady pressures with 5kHz pressure probes located in P0, P1, P2 and P3 in Figure 6-2
- Temperature measurements sampled at 50Hz at locations T1, T25 and T5 in Figure 6-2
- Horizontal, vertical and axial casing vibrations using accelerometers mounted at the compressor discharge casing at P25 in Figure 6-2

To simulate fouling in the compressor, the compressor blade surfaces were roughened by painting with a texturized paint to a roughness value of $R_a = 6\mu m$ as shown in Figure 6-3.

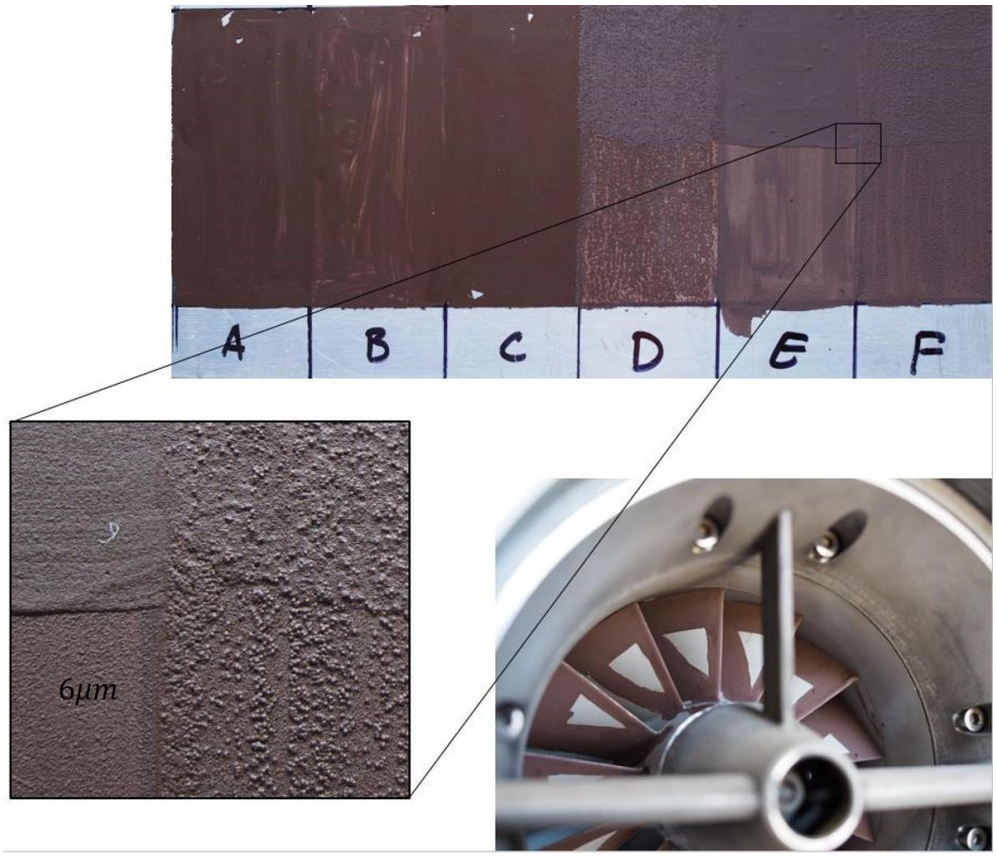

Figure 6-3 Simulating fouling in the compressor blade (Source: Jiri, 2016a)

All measurements of the gas path parameters and vibration where taken at different throttle settings and rotational speeds (i.e. 95%, 90%, 85%, 80% and 51%).

6.3 Modelling

6.3.1 Greitzer Compression System Model

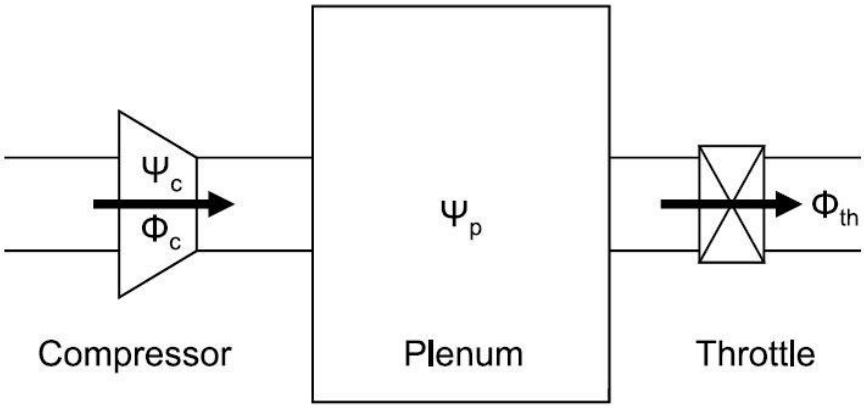

Figure 6-4 Schematic of a Greitzer compression system model (Source: Yoon, Lin and Allaire, 2013)

The Greitzer compression system model as show in Figure 6-4 is a lumped parameter model consisting of a compressor operating in a duct and discharging to plenum with a throttle to control the flow through the compression system. It's suitable for modelling the surge dynamics in a compressor.

The governing equation for the Greitzer compression system are (Greitzer, 1976):

$$\frac{d\Phi_c}{dt} = \mathrm{B}\left(\Psi_c - \Psi_p\right) \quad 6\text{-}1$$

$$\frac{d\Phi_{th}}{dt} = \left(\frac{\mathrm{B}}{G}\right)\left(\Psi_p - \Psi_{th}\right) \quad 6\text{-}2$$

$$\frac{d\Psi_p}{dt} = \left(\frac{1}{B}\right)\left(\Phi_c - \Phi_{th}\right) \quad 6\text{-}3$$

$$\frac{d\Psi_c}{dt} = \left(\frac{1}{\tau}\right)\left(\Psi_{c,ss} - \Psi_c\right) \quad 6\text{-}4$$

where Φ_c & Φ_{th} are the flow coefficient in the compressor & throttle respectively, Ψ_p & Ψ_c are pressure rise coefficient for the plenum and compressor respectively, $\Psi_{c,ss}$ is the steady state compressor pressure rise characteristics, B is the Greitzer parameter, G is a geometric parameter and τ is the compressor flow relaxation time.

The non-dimensional compressor flow coefficient (Φ_c) is expressed as (Greitzer, 1976):

$$\Phi_c = \frac{C_x}{U} = \frac{\rho C_x A_c}{\rho U A_c} = \frac{\dot{m}}{\rho U A_c} \qquad 6\text{-}5$$

where C_x is the axial velocity, U is the impeller tip speed, ρ is the average density of the air between inlet and outlet of the impeller, A_c is the compressor inlet annulus area and $\dot{m}$ is the massflow.

The non-dimensional compressor pressure rise coefficient (Ψ_c) is expressed as (Greitzer, 1976):

$$\Psi_c = \frac{\Delta P}{\frac{1}{2}\rho U^2} = \frac{P_1(PR-1)}{\frac{1}{2}\rho U^2} \qquad 6\text{-}6$$

where ΔP is the pressure rise from the compressor inlet to the plenum, U is the impeller tip speed, ρ is the average density of the air between inlet and outlet of the impeller, P_1 is the compressor inlet pressure and PR is the compressor pressure ratio.

The throttle pressure rise coefficient (Ψ_{th}) is expressed as (Hansen et al., 1981):

$$\Psi_{th} = S\Phi_{th}^2 \qquad 6\text{-}7$$

where S is the throttle parameter and Φ_{th} is the throttle flow coefficient.

The Greitzer parameter (B) is expressed as (Greitzer, 1976):

$$B = \frac{\mathrm{U}}{2a}\sqrt{\frac{V_p}{A_c L_c}} \qquad 6\text{-}8$$

where U is the tip speed of the impeller, a is the speed of sound at the ambient condition, V_p is the plenum volume, A_c is the compressor inlet flow area, L_c is the effective length of the compressor and the ducting.

The geometric parameter (G) is expressed as (Greitzer, 1976):

$$G = \frac{\left(\frac{\mathrm{L}_T}{A_T}\right)}{\left(\frac{\mathrm{L}_c}{A_c}\right)} \qquad 6\text{-}9$$

where L_T & L_c are the effective length of the throttle and compressor respectively and A_T & A_c are the flow areas of the throttle and compressor respectively.

The compressor flow relaxation time (τ) is expressed as (Greitzer, 1976):

$$\tau = \frac{\pi RN}{L_c B} \qquad 6\text{-}10$$

where R is the compressor mean radius, N is the time lag in revolution, L_c is the effective length of the compressor and B is the Greitzer B parameter.

The time lag parameter N was chosen based on the recommendation of Hansen et al. (Hansen et al., 1981), where N = 0.5 for centrifugal compressors. Although in the original Greitzer (Greitzer, 1976) axial compression system model, the time lag parameter was 2; Hansen et al. (Hansen et al., 1981) argued based on their experimental data, that for centrifugal compressors, the time lag for transitioning from unstalled to fully stalled mode was quite shorter as compared to the axial compressor.

6.4 Results and Discussion

6.4.1 +TJ100 Geometric Parameters

Figure 6-5 presents the relevant geometric parameters for the TJ100 compression system to be used in the Greitzer compression system model.

The determination of the geometrical parameters for the TJ100 compression system is presented in Appendix G.

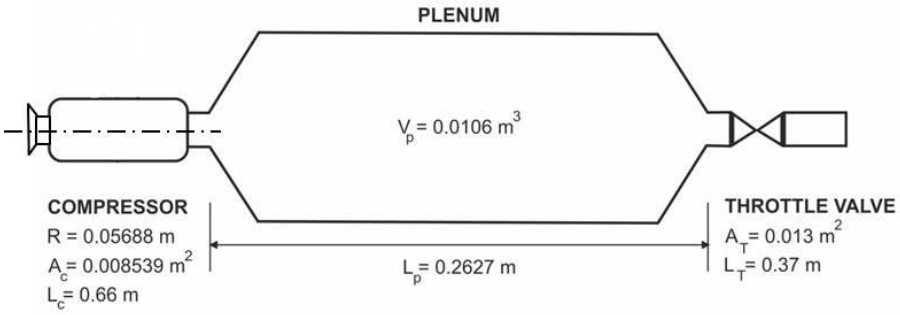

Figure 6-5 Simplified TJ100 compression test rig geometry

6.4.2 Generalized Steady-State Compressor Pressure Rise Characteristic for the Baseline and Fouled Engine

The generalized steady-state compressor pressure rise characteristic is a graphical representation of the relationship between the non-dimensional pressure rise coefficient and the non-dimensional flow coefficient in the compressor when operating in steady state conditions.

The generalised pressure rise characteristic for the clean and fouled TJ100 engine is presented in Figure 6-6 based on experimental data for the speed lines 0.8, 0.85, 0.9 and 0.95.

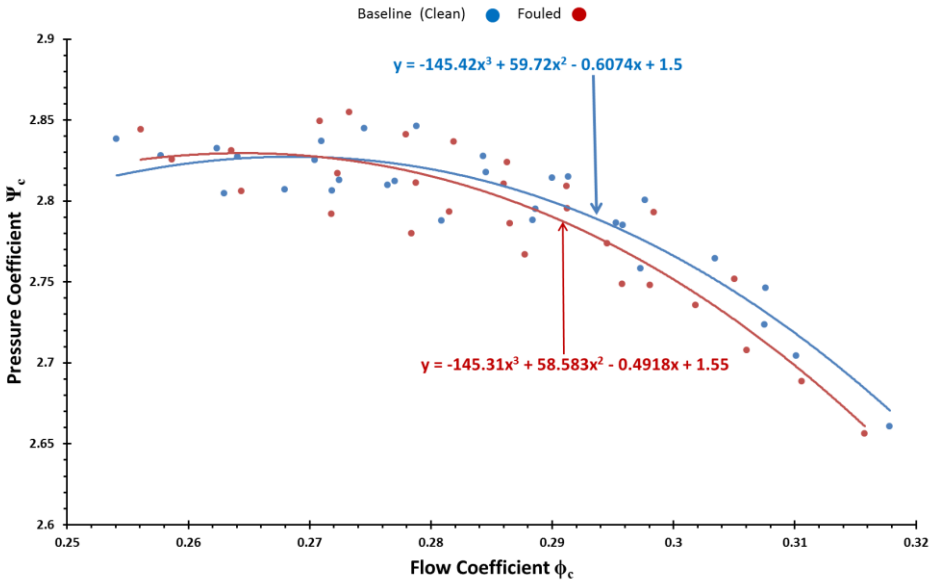

Figure 6-6 Best-Fit generalised pressure rise characteristic for TJ100 based on experimental data

The polynomial curve fit of the data is based on the Moore and Greitzer recommendation for the general form of the compressor pressure rise characteristic presented in Figure 2-2. A more detailed polynomial curve fit of the experimental data for both the baseline and fouled TJ100 engine is presented in Appendix G.

From Figure 6-6, the polynomial expressions representing the steady state pressure rise characteristic for the baseline and fouled TJ100 compressor are:

$$\Psi_{c,ss}^{base} = -145.42\,\Phi_c^3 + 59.72\Phi_c^2 - 0.6074\Phi_c + 1.5 \qquad 6\text{-}11$$

$$\Psi_{c,ss}^{fouled} = -145.31\,\Phi_c^3 + 58.583\Phi_c^2 - 0.4918\Phi_c + 1.55 \qquad 6\text{-}12$$

6.4.3 Model Validation and Simulation

The governing equations for the Greitzer compression system given in Equations 6-1 to 6-4 have been implemented in MATLAB using the ODE45 module to simultaneously solve the 4 sets of first-order differential equations. The MATLAB code is presented in Appendix G.

The Greitzer model prediction for the following parameters: frequency of plenum pressure disturbance and average disturbance flow coefficient at the inception of unstable operation in the compressor is compared against the experimental data.

The range of experimental data considered involved all the operating points within the speed lines PCN 0.8, PCN 0.85, PCN 0.9 and PCN 0.95.

The experimental data for the plenum pressure time series and its synchronous average fast Fourier transform analysis is presented in Appendix G.4.

Table 6-2 to Table 6-5 summarizes the experimental data and model prediction for the frequency of plenum pressure disturbance and the average flow coefficient at the inception of unstable operations in the compressor (baseline and fouled).

For clarity, this data is also presented in the graphical form shown in Figure 6-7 to Figure 6-10.

Table 6-2 Summary of experimental and model prediction of inception parameters for compressor unstable operation at the speed line 0.80

Baseline						Fouled				
PCN 0.80		S (Throttle Parameter) =39.8				PCN 0.80		S (Throttle Parameter) = 41.2		
S/N	**Parameter**	**Experiment**	**Model**	**Delta %**		**S/N**	**Parameter**	**Experiment**	**Model**	**Delta %**
1	Freq. of Press. Fluctuation (Hz)	58.54	58.27	0.46		1	Freq. of Press. Fluctuation (Hz)	57.31	56.39	1.6
2	Ave. Flow Coeff.	0.2541	0.2663	-4.8		2	Ave. Flow Coeff.	0.2561	0.2616	-2.1

Table 6-3 Summary of experimental and model prediction of inception parameters for compressor unstable operation at the speed line 0.85

Baseline						Fouled				
PCN 0.85		S (Throttle Parameter) = 39.7				PCN 0.85		S (Throttle Parameter) = 41.9		
S/N	**Parameter**	**Experiment**	**Model**	**Delta %**		**S/N**	**Parameter**	**Experiment**	**Model**	**Delta %**
1	Freq. of Press. Fluctuation (Hz)	58.54	58.27	0.46		1	Freq. of Press. Fluctuation (Hz)	47.56	46.99	1.2
2	Ave. Flow Coeff.	0.2588	0.2665	-2.98		2	Ave. Flow Coeff.	0.2587	0.2584	0.11

Table 6-4 Summary of experimental and model prediction of inception parameters for compressor unstable operation at the speed line 0.90

Baseline						Fouled				
PCN 0.90		S (Throttle Parameter) = 40				PCN 0.90		S (Throttle Parameter) = 41.8		
S/N	**Parameter**	**Experiment**	**Model**	**Delta %**		**S/N**	**Parameter**	**Experiment**	**Model**	**Delta %**
1	Freq. of Press. Fluctuation (Hz)	52.44	52.63	-0.36		1	Freq. of Press. Fluctuation (Hz)	42.63	43.23	-1.4
2	Ave. Flow Coeff.	0.2629	0.2652	-0.87		2	Ave. Flow Coeff.	0.2815	0.2577	8.5

Table 6-5 Summary of experimental and model prediction of inception parameters for compressor unstable operation at the speed line 0.95

Baseline						Fouled				
PCN 0.95		S (Throttle Parameter) = 39.5				PCN 0.95		S (Throttle Parameter) = 40.6		
S/N	**Parameter**	**Experiment**	**Model**	**Delta %**		**S/N**	**Parameter**	**Experiment**	**Model**	**Delta %**
1	Freq. of Press. Fluctuation (Hz)	58.54	58.27	0.46		1	Freq. of Press. Fluctuation (Hz)	53.66	56.39	-5
2	Ave. Flow Coeff.	0.271	0.2676	1.25		2	Ave. Flow Coeff.	0.2708	0.2640	2.5

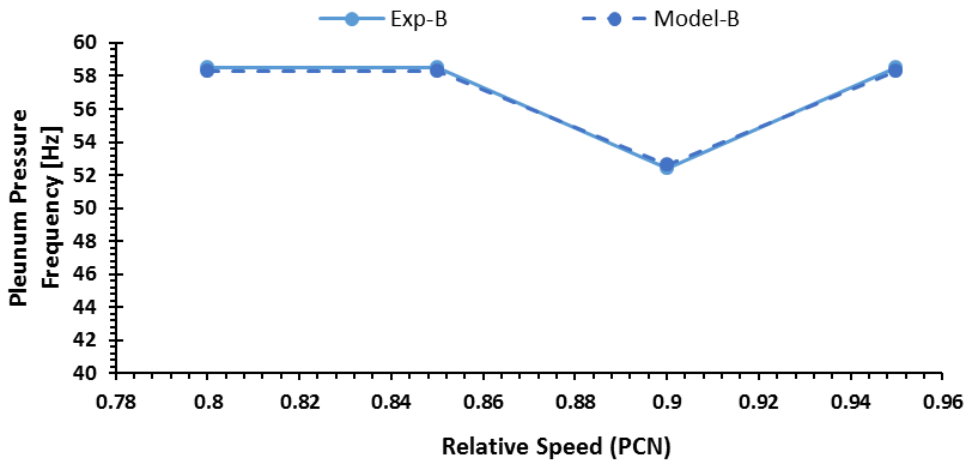

Figure 6-7 Plenum pressure disturbance frequency (clean)

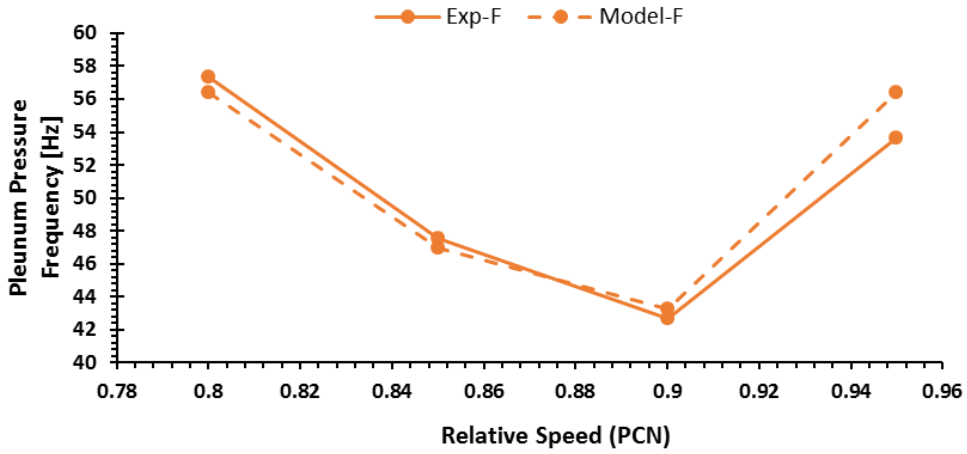

Figure 6-8 Plenum pressure disturbance frequency (fouled)

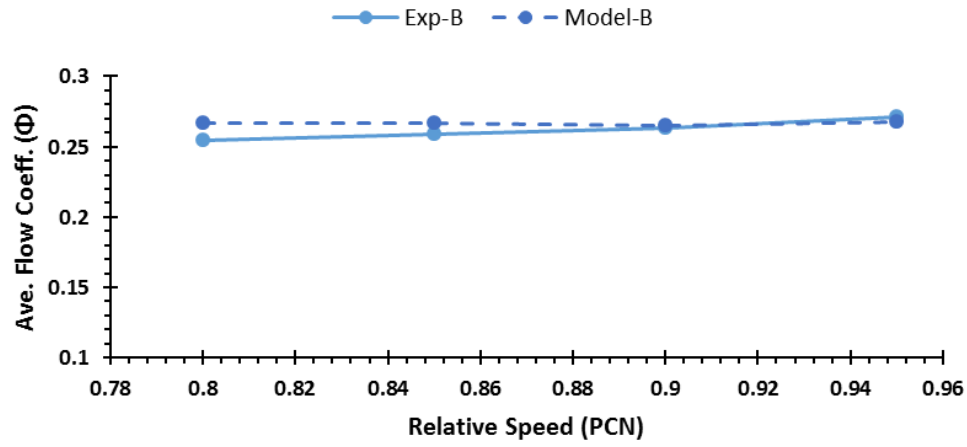

Figure 6-9 Disturbance average flow coefficient (clean)

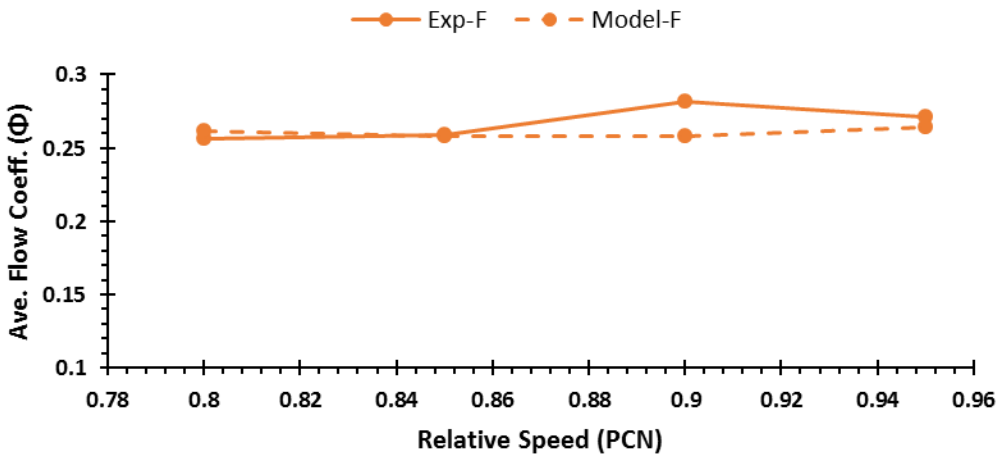

Figure 6-10 Disturbance average flow coefficient (fouled)

Figure 6-7 and Figure 6-8 show the frequency of the plenum pressure disturbance at the inception of unstable operations in the compressor for both the clean and fouled engine respectively. They also compare the experimental data and the Greitzer model prediction for the frequency of plenum pressure disturbance at different relative speeds (i.e. PCN 0.8, PCN 0.85, PCN 0.9 and PCN 0.95).

For the TJ100 compression system modelled, it was observed that it behaved differently in terms of the frequency of the plenum pressure disturbance when operating at 90% of its rated speed as seen in Figure 6-7 and Figure 6-8; the Greitzer model was able to capture this peculiar behaviour.

Figure 6-9 and Figure 6-10 compare the average flow coefficient at the inception of unstable compressor operation for the clean and fouled compressor respectively at different relative speed (i.e. PCN 0.8, PCN 0.85, PCN 0.9 and PCN 0.95).

The almost flat shape model prediction for the average flow coefficient stems from the data averaging employed in generating the generalised compressor pressure rise characteristic.

From Figure 6-6, it can be seen that the generalized compressor pressure rise characteristics is a best-fit relationship between the pressure rise coefficient and flow coefficient for a particular compressor and health state; this makes the point

of inception of unstable operation in the compressor for all the speed lines to collapse to a single point.

The model then predicts an almost constant flow coefficient for the clean and fouled compressor based also on the choice of the throttle parameter. A little deviation in the experimental values for the average flow coefficient at the inception of a disturbance is observed in Figure 6-9 and Figure 6-10.

6.5 Conclusion

This study demonstrates the suitability of the Greitzer (1976) compression system model to simulate the dynamic behaviour of a clean and fouled compressor when operating in unstable conditions.

The validation of the Greitzer model has been based on comparing its prediction of the plenum pressure disturbance frequency and the average flow coefficient at the inception of unstable operations in the compressor against experimental values from the TJ100 centrifugal gas turbine test rig. The Greitzer model predictions are in good agreement with the experimental values.

Finally, this study lends support for the use of the Greitzer compression system model for the determination of the flowfield parameters in a fouled compressor.

7 CONCLUSIONS & FUTURE WORK

7.1 Summary

The focus of this research has been on studying the effect of fouling on the interaction between aerodynamic and rotordynamic domain in a compressor with the intent of integrating thermodynamic performance monitoring via gas path analysis and vibration via the rotordynamic response of the rotor to monitor the effect of fouling in the compressor.

A methodology to carry out such study has been proposed involving the interaction of four different models. The models are: Moore-Greitzer compression system model, Al-Nahwi aerodynamic force model, 2D transfer matrix rotordynamic model and gas turbine performance and diagnostic model.

The proposed methodology in a nutshell is based on the premise that fouling deterioration in the compressor is evident in the rescaling of the compressor maps which is also a performance indication of changes in the aerodynamic forces acting within the compressor. The predications of these modified aerodynamic forces now act as forcing functions on the compressor rotor, producing vibration.

The Moore-Greitzer compression system model is a lumped parameter model consisting of a compressor operating in a duct and discharging to a plenum with the overall flow controlled by a throttle valve.

Four governing equations for the Moore-Greitzer compression system where derived from which the amplitudes of disturbed flow coefficient due to fouling in the compressor were predicted.

A modification to the general expression for Moore-Greitzer model compressor pressure rise characteristic is introduced in this work. The modification is included to account for the scaling effect of fouling on the compressor pressure rise characteristic. A linear scaling effect has been assumed in the modification of the generalised compressor pressure rise characteristic.

The aerodynamic force model adopted for this study is that proposed by Al-Nahwi (2000). According to Al-Nahwi (2000), the aerodynamic force in the compressor is made up of three components, which are the turning force, the pressure force and the unsteady momentum force.

Since only steady state conditions are considered in this research, the focus was mainly on the turning force and pressure force components.

A 2D transfer matrix rotordynamic MATLAB code dubbed 'RotorMatch' has been developed for the compressor rotordynamic response conducted in this study. Although at its early stages, it performs critical speed and forced response analysis on any rotor-bearing configuration. The accuracy of this code has been validated against the test data by Kikuchi (1970) and it shows good agreement with the Kikuchi (1970) test results.

Lastly, a clean and fouled virtual LM2500+ engine has been modelled in TurboMatch and Pythia. The design point and off-design point performance analysis of the baseline engine compares favourably with the published performance data for the LM2500+ engine. A compressor fouling degradation analysis has been performed both in TurboMatch and Pythia. The TurboMatch analysis is used to derive the rescaled compressor maps due to several cases of compressor fouling in terms of performance deterioration i.e. reduction in massflow, pressure ratio and isentropic efficiency while Pythia analysis was use to perform both linear and non-linear gas path analysis on the degraded virtual LM2500+ engine.

From the aerodynamic-rotordynamic interaction studies conducted on the fouled virtual test engine (LM2500+), it is observed that as the rate of fouling increases in the compressor evident by a reduction in compressor massflow, isentropic efficiency and pressure ratio, there is a corresponding increase in the amplitude of the frequency at the rotors first fundamental frequency.

Another finding from this work is the identification of a non-dimensional parameter called the pressure scale factor that is useful in comparing the effect of blade aspect ratio on a blade-row aerodynamic performance.

Also demonstrated in this work with the aid of experimental data is the ability to apply a Moore-Greitzer type model to predict the inception of unstable operation in a gas turbine compressor due to fouling. This aspect of this research was in collaboration with Lt. Col Jiri Pecinka from the Engine Operation Group, Department of Air Force and Aircraft Technology, University of Defence, Czech Republic. The test data for the fouling experiments conducted on a modified TJ100 test rig has been provided by him.

Finally, this work lays a foundation for developing a diagnostic physics based model for gas turbine compressor fouling monitoring by exploiting the interaction between the rotordynamic and aerodynamic domain in the compressor. Although the full realization of a prognostic system is not made in this work, several key findings to that regards are presented, as a first step. Major progress is made in validating and tuning a modelling approach which showed that the rate of fouling degradation corresponds to an increase in amplitude of the compressor's rotor fundamental frequency. The importance of this insight lies in its use as a diagnostic tool.

7.2 Recommendations for Future Work

The following is a list of further model improvements and research interests stemming from this work:

- In modelling the interaction between the aerodynamic and rotordynamic domain in a fouled gas turbine compressor, linear simplifications have been adopted in the compression system model. A single term Fourier series has been used to approximate the resulting disturbed flow coefficient. This approximation is reasonable for weakly nonlinear systems such as compressor operating with either an incompressible inlet flow or low Mach number compressible inlet flow (Gamache, 1985; Moore and Greitzer, 1985). To truly account for nonlinearity in the model, further improvements is possible, such as adopting a second order or two-term Fourier series to approximate the disturbed flow coefficient. Moore and Greitzer(1985) provide the Two-Harmonic Galerkin method as a further refinement to the

fundamental Moore-Greitzer compression system model (Greitzer and Moore, 1986).

- For the analysis of the rotordynamic response of the compressor rotor, only a synchronous response analysis was performed. It would be interesting to consider the asynchronous response of the rotor with regards to an aerodynamic excitation. Aerodynamic forces have been reported to also generate non-synchronous rotor vibrations (Spakovszky, 2000a). As a first step in this regard, the rotordynamic model can be extended to perform steady-state non-synchronous harmonic response. Chen (2015) describe a model to perform non-synchronous harmonic response for rotors.
- In demonstrating the application of a Moore-Greitzer type model to the prediction of the inception of unstable operation in the compressor due to fouling, a Greitzer-type model was developed to look at the disturbances in the plenum. It would be interesting to extend this model to the 2D Moore-Greitzer (1986) model to look at the disturbances at the inlet of the compressor; as the TJ100 test data showed a high sensitivity of the compressor inlet parameters to fouling in the compressor.

REFERENCES

Afoggyeye (2016) *GE LM2500+*. Available at: http://s308.photobucket.com/user/afoggyeye/media/Engine and drydock/LM2500.jpg.html (Accessed: 27 November 2016).

Aker, G.F. and Saravanamuttoo, H.I.H. (1989) 'Predicting Gas Turbine Performance Degradation Due to Compressor Fouling Using Computer Simulation Techniques', *Journal of Engineering for Gas Turbines and Power*, 111(2) ASME, pp. 343–350.

Al-Nahwi, A.A. (2000) *Aerodynamic-Rotordynamic Interaction in Axial Compression System. PhD Thesis*. Massachusetts Institute of Technology.

Al-Nahwi, A.A. et al. (2003) 'Aerodynamic-Rotordynamic Interaction in Axial Compression Systems—Part I: Modeling and Analysis of Fluid-Induced Forces', *Journal of Turbomachinery*, 125, pp. 405–415.

Alford, J.S. (1965) 'Protecting Turbomachinery From Self-Excited Rotor Whirl', *Journal of Engineering for Power*, 87(4), pp. 333–343.

Aretakis, N. and Mathioudakis, K. (1998) 'Classification of Radial Compressor Faults Using Pattern-Recognition Techniques', *Control Engineering Practice*, 6, pp. 1217–1223.

Azima (2009) *Mode Shape*. Available at: http://azimadli.com/vibman/gloss_modeshape1.htm (Accessed: 2 December 2016).

Back, S.C. et al. (2010) 'Impact of Surface Roughness on Compressor Cascade Performance', *Journal of Fluids Eningeering*, 132, pp. 64502–1.

Biliotti, D. et al. (2015) 'Analysis of the Rotordynamic Response of a Centrifugal Compressor Subject to Aerodynamic Loads Due to Rotating Stall', *Journal of Turbomachinery*, 137(2), p. 21002.

Boyce, M.P. (2012) *Gas Turbine Engineering Handbook*. 4th edn. Oxford, UK: Elsevier.

Boyce, M.P. and Latcovich, J.A. (2002) ‘Condition Monitoring and Its Effect on the Life of New Advanced Gas Turbines’, *ASME-IGTI Glob. Gas Turbine News*, 42(3), pp. 4–10.

Camfil (2014) *Gas Turbines technology and the importance of air filtration*. Available at: http://www.slideshare.net/Camfil_Farr/gas-turbines-technology-and-the-importance-of-air-filtration (Accessed: 20 November 2016).

Camfil (2016a) *Cam-Flo GT X7*. Available at: http://www.camfil.com/Products/Air-filters-for-gas-turbines/Bag-filters/Cam-Flo-GT-X7-en-BZ/ (Accessed: 21 November 2016).

Camfil (2016b) *CamGT 3V-600 CamBrane*. Available at: http://www.camfil.com/ps/Air-inlet-filters-and-parts-for-gas-turbines/Air-filters-for-gas-turbines/Compact-filters/CamGT-3V-600-CamBrane-en-BZ/ (Accessed: 22 November 2016).

Camfil (2016c) *CamPulse CamBrane*. Available at: http://www.camfil.com/ps/Air-inlet-filters-and-parts-for-gas-turbines/Air-filters-for-gas-turbines/Pulse-filters/CamPulse-CamBrane-en-BZ/#tab-2-tab (Accessed: 22 November 2016).

Chen, W.J. (2015) *Practical Rotordynamics and Fluid Film Bearing Design*. TRAFFORD PUB.

Childs, D. (1993) *Turbomachinery Rotordynamics Phenomena Modeling and Analysis*. USA: Wiley.

Day, I. (1976) *Axial Compressor Stall. PhD Thesis*. Cambridge University.

Emery, J.C. et al. (1958) *naca-report-1368: Systematic two-dimensional cascade tests of NACA 65-series compressor blades at low speeds*.

Escher, P.C. and Singh, R. (1995) ‘An Object-Oriented Diagnostics Computer Program Suitable for Industrial Gas Turbines’, *(CIMAC) International Congress of Combustion Engines, Switzerland, May 15-18, 1995*., pp. 15–18.

EthosEnergy (2016) *Compressor Water Wash (Online / Offline)*. Available at: http://www.ethosenergygroup.com/products-services/gas-turbines-heavy-

industrial/upgrades-life-extension/compressor-water-wash-online-offline (Accessed: 22 November 2016).

Fink, D.A. et al. (1992) ‘Surge Dynamics in a Free Spool Centrifugal Compressor System’, *Journal of Turbomachinery*, 114, pp. 321–332.

Fouflias, D. et al. (2010) ‘Experimental investigation of the influence of fouling on compressor cascade characteristics and implications for gas turbine engine performance’, *Journal of Power and Energy*, 224, pp. 1007–1018.

Gamache, R. (1985) *Axial Compressor Reversed Flow Performance. PhD thesis*. Massachusetts Institute of Technology.

GE (2008) *Axial Compressor On/Off-line Washing*.

GE Aviation (2017) *LM2500+ Marine Gas Turbine Datasheet*. Available at: https://www.geaviation.com/sites/default/files/datasheet-lm2500plus.pdf (Accessed: 11 November 2017).

Ghaoui, L. El (2014) *Pseudo-Inverse of a Matrix*. Available at: https://inst.eecs.berkeley.edu/~ee127a/book/login/def_pseudo_inv.html (Accessed: 25 November 2016).

Gravdahl, J.T. and Egeland, O. (1997a) ‘A Moore-Greitzer axial compressor model with spool dynamics’, *Proceedings of the 36th Conference on Decision & Control, San Diego, California, USA. December, 1997*. IEEE.

Gravdahl, J.T. and Egeland, O. (1997b) ‘Control of the Three-State Moore-Greitzer Compressor Model Using a Close-Coupled Valve’, *Proceedings of the 1997 European Control Conference, July 1997*.

Greitzer, E.M. (1976) ‘Surge and Rotating Stall in Axial Flow Compressors Part 1: Theoretical Compresson System Model’, *Journal of Engineering for Power*, 98, pp. 199–211.

Greitzer, E.M. and Moore, F.K. (1986) ‘A Theory of Post-Stall Transients in Axial Compression Systems : Part I — Development of Equations’, *Transactions of the ASME*, 108(68)

Grewal, M.S. (1988) *Gas Turbine Engine Performance Deterioration Modelling and Analysis. PhD Thesis*. SME, Cranfield Institute of Technology.

Hansen, K.E. et al. (1981) 'Experimental and Theoretical Study of Surge in a Small Centrifugal Compressor', *Journal of Fluids Engineering*, 103(3), pp. 391–395.

Holzer, H. (1921) *DIE BERECHNUNG DER DREHSCHWINGUNGEN*. Springer Berlin Heidelberg.

Horlock, H.H. et al. (1964) 'Reynolds Number Effects in Cascades and Axial Flow Compressors', *ASME. Journal of Engineering Power*, 86(3), pp. 236–242.

Horlock, J.H. and Fahmi, G.J. (1966) *C.P. No. 943: A Theoretical Investigation of the Effect of Aspect Ratio on Axial Flow Compressor Performance*.

Igie, U. (2015) *Gas Turbine: Performance Degradation & Enchancement* Lecture notes distributed in Gas Turbine Appreciation Short Course at Cranfield University on 2-6 March 2015,

Igie, U. et al. (2014) 'Industrial Gas Turbine Performance: Compressor Fouling and On-Line Washing', *Journal of Turbomachinery*, 136(10), pp. 101001–13.

Jiri, P. (2016a) *Small Jet Fouling* [Unpublished work]. PowerPoint slides presented at Cranfield University by Lt. Col. Jiri Pecinka,

Jiri, P. (2016b) *TJ100 Fouling Experiment Dataset* [Unpublished dataset]. Presented at Cranfield University by Lt. Col. Jiri Pecinka for a collaboration project at the Centre for Propulsion Engineering,

Kikuchi, K. (1970) 'Analysis of Unbalance Vibration of Rotating Shaft System with Many Bearings and Disks', *Bulletin of the JSME*, 13(61), pp. 864–872.

Kirk, R.G. and Gunter, E.J. (1976) 'Short Bearing Analysis Applied to Rotor Dynamics—Part I: Theory', *Journal of Lubrication Technology*, 98(1), pp. 47–56.

Kostyuk, A.G. and Karpunin, A.P. (2016) 'Calculation of gas temperature at the outlet of the combustion chamber and in the air-gas channel of a gas-turbine unit by data of acceptance tests in accordance with ISO', *Thermal Engineering*, 63(1),

pp. 24–27.

Kyriazis, A. et al. (2006) ‘Gas Turbine Diagnosis From Fast Response Data Using Probabilistic Methods and Information Fusion’, *Proceesings of GT2006 ASME Turbo Expo 2006: Power for Land, Sea and Air, May 8-11, 2006, Barcelona, Spain*., pp. 1–9.

Lavrich, P. (1988) *Time Resolved Measurements of Rotating Stall in Axial Compressors. PhD Thesis*. Massachusetts Institute of technology.

Li, Y.G. (2002) ‘Performance Analysis Based Gas Turbine Diagnostics: A Review’, *Journal of Power and Energy*, 216(5), pp. 363–377.

Li, Y.G. (2016) *Gas Turbine Diagnostics (Ed. 1.5.2)* lecture notes distributed in Gas Turbine Diagnostics at Cranfield University, Thermal Power MSc. on 25 November 2016,

Li, Y.G. (2010) ‘Gas Turbine Performance and Health Status Estimation Using Adaptive Gas Path Analysis’, *Journal of Engineering for Gas Turbines and Power*, 132(4), p. (041701-1)-(9).

Li, Y.G. et al. (2014) ‘Application of Gas Path Diagnostics to Gas Turbine Engines’, *Singapore Aerospace Technology and Engineering Conference*. Singapore: SIAE, pp. 1–11.

Loud, R.L. and Slaterpryce, A.A. (1991) *Gas Turbine Inlet Air Treatment*.

Loukis, E. et al. (1991) ‘A Procedure for utomated Gas Turbine Blade Fault Identification Based on Spectral Pattern Analysis’, *Proceedings of ASME International Gas Turbine and Aeroengine Congress and Exposition, Orlando, FL, June 3-6, 1991*. Orlando, FL, pp. 1–9.

Loukis, E. et al. (1991) ‘Combination of Different Unsteady Quantity Measurements for Gas Turbine Blade Fault Diagnosis’, *ASME 36th Gas Turbine and Aeroengine Congress, Orlando, FL, June 3-6, 1991*., pp. 1–8.

Lund, J.W. and Orcutt, F.K. (1967) ‘Calculations and Experiments on the Unbalance Response of a Flexible Rotor’, *Journal of Engineering for Industry*,

89(4), pp. 785–796.

Macdougal, I. and Elder, R.L. (1983) ‘Simulation of Centrifugal Compressor Transient Performance for Process Plant Applications’, *Journal of Engineering for Power*, 105(4) ASME, pp. 885–890.

Marcorio, G. and Menezes, J.C. (2012) ‘Dynamical Evaluation of Gas Turbine Rotors’, *12th Pan-American Congress of Applied Mechanics, January 02-06, 2012, Port of Spain, Trinidad*. Trinidad, Spain.

Marcus, G. (2011) *Advanced Compressor Cleaning System for Siemens Gas Turbines*.

Mathioudakis, K; Tsalavoutas, A. (1995) ‘Identification of mechanical alterations from their effect on performance of a radial compressor’, *Proceedings of the International Gas Turbine and Aeroengine Congress and Exposition, Houston, Texas - June 5-8, 1995*. Houston, Texas: ASME, pp. 1–9.

Mba, D. (2012) *Rotor Dynamics* lecture notes distributed in Rotor Dynamics at Cranfield University, Design of Rotating Machines MSc. on 5 December 2012,

Meher-Homji, C.B. and Bhargava, R. (1994) ‘Condition Monitoring and Diagnostic Aspects of Gas Turbine Transient Response’, *International Journal of Turbo and Jet Engine*, 11(1), pp. 99–111.

Meher-Homji, C.B. and Bromley, A. (2004) ‘Gas Turbine Axial Compressor Fouling and Washing’, *Proceedings of the Thirty-Third Turbomachinery Symposium*., pp. 163–191.

Meher-homji, C.B. et al. (2001) ‘Gas Turbine Performance Deterioration’, *30th Turbomachinery Symposium, Texas A&M University, Texas*. Texas A&M University, Texas, USA, pp. 139–176.

Meher-homji, C.B. and Cullen, J.P. (1992) ‘Integration of Condition Monitoring Technologies for the Health Monitoring of Gas Turbines’, *ASME 1992 International Gas Turbine and Aeroengine Congress and Exposition*. Cologne, Germany: ASME, p. V005T15A007.

Meher-homji, C.B. and Focke, A.B. (1985) ‘Performance & Vibration Monitoring for the Prevention of Gas Turbine Airfoil Failures’, *6th Bi annual ASME Conference on Failure Prevention & Reliability, September, 1985 ASME Vol H-331*.

Meher-homji, C.B. et al. (1989) ‘Fouling of Axial Flow Compressors - Causes, Effcets, Detention, And Control’, *Proceedings of the Eighteenth Turbomachinery Symposium*. Texas A&M University, Texas, USA, pp. 55–76.

Melino, F. et al. (2010) ‘Development and Validation of a Model for Axial Compressor Fouling Simulation’, *ASME Turbo Expo 2010: Power for Land, Sea, and Air Volume 5: Industrial and Cogeneration; Microturbines and Small Turbomachinery; Oil and Gas Applications; Wind Turbine Technology Glasgow, UK, June 14–18, 2010*. Glasgow, UK: ASME, pp. 87–98.

Moore, F.K. (1984) ‘A Theory of Rotating Stall of Multistage Compressors, Part I, II, III’, *ASME Journal of Engineering for Power*, 106(2), pp. 313–336.

Moore, F.K. and Greitzer, E.M. (1985) *A Theory of Post-Stall Transients in Multistage Axial Compression Systems*.

Murphy, B.T. and Vance, J.M. (1983) ‘An improved method for calculating critical speeds and rotordynamic stability of turbomachinery’, *Proceedings of the Tenth Turbomachinery Symposium*. Texas A&M University, Texas, USA: Texas A&M University, pp. 141–146.

Myklestad, N.O. (1944) ‘A New Method of Calculating Natural Modes of uncoupled Bending Vibrations of Airplane Wings and Other Types of Beams’, *Journal of the Aeronautical Sciences*, 11(2), pp. 153–162.

Nieuwenhuizen, M.J. (2008) *Parameter analysis and identification of the Greitzer model by analogy with the Van der Pol equation*. Technische Universiteit Eindhoven.

Nikolaidis, T. (2015) *The TurboMatch Scheme* lecture notes distributed in Gas Turbine Performance Simulation at Cranfield University, Thermal Power MSc. on 25 November 2016,

PBS (2016) *TJ100 Turbojet Engine*. Available at: http://www.pbsvb.com/getattachment/Zakaznicka-odvetvi/Letectvi/Aircraft-UAV-engines/Proudovy-motor-TJ-100/Turbojet-engine_TJ100.pdf.aspx (Accessed: 14 December 2016).

Pinkus, O. and Sternlicht, B. (1961) *Theory of Hydrodynamic Lubrication*. New York: Mc Graw Hill.

Pneumafil (2016) *Rain and Mist Control*. Available at: http://www.pneumafil.com/gas_turbine_inlet_air_filtration/details/mist_control/ (Accessed: 20 November 2016).

Prohl, M.A. (1945) 'A General Method for Calculating Critical Speeds of Flexible Rotors', *Journal of Applied Mechanics*, 67, p. A-142-A-148.

Ramsden, K. (2015) *Gas Turbine Fundamentals and Axial Compressors* Lecture notes distributed in Gas Turbine Appreciation Short Course at Cranfield University on 2-6 March 2015,

Rodríguez, C. et al. (2013) 'Compressor Fouling: A Comparison of Different Fault Distributions Using a "Stage-Stacking" Technique', *ASME Turbo Expo 2013: Turbine Technical Conference and Exposition Volume 2: Aircraft Engine; Coal, Biomass and Alternative Fuels; Cycle Innovations San Antonio, Texas, USA, June 3–7, 2013*. San Antonio, Texas: ASME.

Scheffer, C. and Girdhar, P. (2004) *Practical Machinery Vibration Analysis and Predictive Maintenance*. Amsterdam: Elsevier.

Seddigh, F. and Saravanamuttoo, H.I.H. (1991) 'A Proposed Method for Assessing the Susceptibility of Axial Compressors to Fouling', *Journal of Engineering for Gas Turbines and Power*, 113(4) ASME, pp. 595–601.

Song, T.W. et al. (2003) 'An Improved Analytic Model to Predict Fouling Phenomena in the Axial Flow Compressor of Gas Turbine Engines', *Proceedings of the International Gas Turbine Congress, Tokyo, Nov. 2–7, IGTC2003 Paper No. TS-095*. Tokyo.

Spakovszky, Z.R. (2000a) ‘Analysis of Aerodynamically Induced Whirling Forces in Axial Flow Compressors’, *Journal of Turbomachinery*, 122, pp. 761–768.

Spakovszky, Z.S. (2000b) *Applications of Axial and Radial Compressor Dynamic System Modeling. PhD Thesis*. Massachusetts Institute of technology.

Stalder, J.-P. (2000) ‘Gas Turbine Compressor Washing State of the Art: Field Experiences’, *Journal of Engineering for Gas Turbines and Power*, 123(2) ASME, pp. 363–370.

Stamatis, A.G. (2013) ‘Engine Condition Monitoring and Diagnostics’, in Benini, E. (ed.) *Progress in Gas Turbine Performance*. INTECH, pp. 187–212.

Stroud, K.A. (2003) *Advanced Engineering Mathematics*. 4th edn. New York: Palgrave Macmillan.

Tarabrin, A.P. et al. (1998) ‘An Analysis of Axial Compressor Fouling and a Blade Cleaning Method’, *Journal of Turbomachinery*, 120(2) ASME, pp. 256–261.

Tryfonidis, M. et al. (1995) ‘Prestall Behavior of Several High-Speed Compressors’, *Journal of Turbomachinery*, 117(1), pp. 1–24.

Urban, L.A. (1973) ‘Gas Path Analysis Applied to Turbine Engine Condition Monitoring’, *Journal of Aircraft*, 10(7), pp. 400–406.

Vance, J.M. (1988) *Rotordynamics of Turbomachinery*. New York: John Wiley & Sons.

Visser, W.P.J. et al. (2004) *A generic approach for gas turbine adaptive modeling*. Netherland.

Voetec (2016) *WEATHER LOUVRE - horizontal*. Available at: http://veotecgroup.com/weather-louvre.html (Accessed: 21 November 2016).

Weigl, H. (1997) *Active Stabilization of Rotating Stall and Surge in a Transonic Single Stage Axial Compressor, PhD. Thesis*. Massachusetts Institute of Technology.

Wilcox, M. et al. (2010) *Guideline For Gas Turbine Inlet Air Filteration Systems*.

Yahyai, M. Al and Mba, D. (2015) ‘Investigation of the Synchronous Response in a Back-Back Centrifugal Compressor Due to Imbalance and Seal Distortion’, in Sinha, J. K. (ed.) *Vibration Engineering and Technology of Machinery: Proceedings of VETOMAC X 2014, held at the University of Manchester, UK, September 9-11, 2014*. Cham: Springer International Publishing, pp. 97–106.

Yang, H. and Xu, H. (2014) ‘The New Performance Calculation Method of Fouled Axial Flow Compressor’, *The Scientific World Journal*, 2014, pp. 1–10.

Yang, X. et al. (2014) ‘A Novel Gas Turbine Engine Health Status Estimation Method Using Quantum-Behaved Particle Swarm Optimization’, *Mathematical Problems in Engineering*, 2014, pp. 1–11.

Yoon, S.Y. et al. (2013) ‘Control of Surge in Centrifugal Compressors by Active Magnetic Bearings’, in *Advances in Industrial Control*. London: Springer-Verlag, pp. 1–275.

Young, W.C. and Budynas, R.G. (2011) *Roark’s Formulas for Stress and Strain*. 8th edn. New York: McGraw-Hill Companies.

Zachary, J. (2008) Advanced Gas Turbine Technology for Power Generation - Revolution or Evolution ?, *ISO Focus*,, pp. 26–29.

APPENDICES

Appendix A Steady State Solution of the General Equations of Disturbance in a Compressor

Governing equations of a general disturbance in a compression system,

$$\frac{d\mathrm{Q}}{d\xi} = \frac{S}{2l_c}[\bar{\psi}_c^c - P] \quad \text{A-1}$$

$$\frac{dP}{d\xi} = \frac{1}{2SB^2 l_c}[\mathrm{Q} - \mathrm{Q}_T] \quad \text{A-2}$$

$$\frac{d\mathrm{a}}{d\xi} = \frac{1}{(2+\mu)}\left[\frac{\mathrm{S}}{2}\bar{\psi}_c^{cc} - \lambda\mathrm{b}\right] \quad \text{A-3}$$

$$\frac{d\mathrm{b}}{d\xi} = \frac{1}{(2+\mu)}\left[\frac{\mathrm{S}}{2}\bar{\psi}_c^{cs} + \lambda\mathrm{a}\right] \quad \text{A-4}$$

Steady state solution of the general disturbance equations,

$$0 = \frac{S}{2l_c}[\bar{\psi}_c^c - P] \quad \text{A-5}$$

$$0 = \frac{1}{2SB^2 l_c}[\mathrm{Q} - \mathrm{Q}_T] \quad \text{A-6}$$

$$0 = \frac{1}{(2+\mu)}\left[\frac{\mathrm{S}}{2}\bar{\psi}_c^{cc} - \lambda\mathrm{b}\right] \quad \text{A-7}$$

$$0 = \frac{1}{(2+\mu)}\left[\frac{\mathrm{S}}{2}\bar{\psi}_c^{cs} + \lambda\mathrm{a}\right] \quad \text{A-8}$$

From Equations A-7 & A-8,

$$\frac{\mathrm{S}}{2}\bar{\psi}_c^{cc} - \lambda\mathrm{b} = 0 \quad \text{A-9}$$

$$\frac{\mathrm{S}}{2}\bar{\psi}_c^{cs} + \lambda\mathrm{a} = 0 \quad \text{A-10}$$

But,

$$\bar{\psi}_c^{cc} = -3\mathrm{a}[4Q(Q-1) + (a^2 + b^2)] - \psi_{cf}\left(\frac{\Delta MF}{2}\right)\cos\Gamma \quad \text{A-11}$$

$$\bar{\psi}_c^{cs} = -3\mathrm{b}[4Q(Q-1) + (a^2+b^2)] - \psi_{cf}\left(\frac{\Delta MF}{2}\right)\sin\Gamma \qquad \text{A-12}$$

Let,

$$R = 4Q(Q-1) \qquad \text{A-13}$$

$$A = a^2 + b^2;\ a = A\cos\eta;\ b = A\sin\eta\ ;\ \eta = \tan^{-1}\frac{b}{a} \qquad \text{A-14}$$

Equation A-9 becomes,

$$-\frac{\mathrm{S}}{2}\psi_{cf}\left(\frac{\Delta MF}{2}\right)\cos\Gamma = \left[\frac{3\mathrm{aS}}{2}(R+A^2) + \lambda\mathrm{b}\right] \qquad \text{A-15}$$

Equation A-10 becomes,

$$-\frac{\mathrm{S}}{2}\psi_{cf}\left(\frac{\Delta MF}{2}\right)\sin\Gamma = \left[\frac{3\mathrm{bS}}{2}(R+A^2) - \lambda\mathrm{a}\right] \qquad \text{A-16}$$

Squaring both sides of Equation A-15 and A-16 and adding both equations, thus,

$$\left[-\frac{\mathrm{S}}{2}\psi_{cf}\left(\frac{\Delta MF}{2}\right)\cos\Gamma\right]^2 + \left[-\frac{\mathrm{S}}{2}\psi_{cf}\left(\frac{\Delta MF}{2}\right)\sin\Gamma\right]^2 = \left[\frac{3\mathrm{aS}}{2}(R+A^2) + \lambda\mathrm{b}\right]^2 + \left[\frac{3\mathrm{bS}}{2}(R+A^2) - \lambda\mathrm{a}\right]^2 \qquad \text{A-17}$$

Simplifying,

$$\frac{\mathrm{S}^2}{4}\left(\frac{\psi_{cf}\Delta MF}{2}\right)^2 = \frac{9\mathrm{S}^2}{4}A^2(R+A^2)^2 + \lambda^2\mathrm{A}^2 \qquad \text{A-18}$$

$$A^2(R+A^2)^2 + \frac{4}{9}\frac{\lambda^2\mathrm{A}^2}{\mathrm{S}^2} = \frac{1}{9}\left(\frac{\psi_{cf}\Delta MF}{2}\right)^2 \qquad \text{A-19}$$

$$A^2(R+A^2)^2 + \left(\frac{2\lambda}{3S}\right)^2\mathrm{A}^2 - \left(\frac{\psi_{cf}\Delta MF}{6}\right)^2 = 0 \qquad \text{A-20}$$

$$A^6 + 2\mathrm{R}\mathrm{A}^4 + \left[R^2 + \left(\frac{2\lambda}{3S}\right)^2\right]\mathrm{A}^2 - \left(\frac{\psi_{cf}\Delta MF}{6}\right)^2 = 0 \qquad \text{A-21}$$

Substituting Equation A-13 into Equation A-21,

$$A^6 + [8\mathrm{Q}(Q-1)]\mathrm{A}^4 + \left[16\mathrm{Q}^2(Q-1)^2 + \left(\frac{2\lambda}{3S}\right)^2\right]\mathrm{A}^2 - \left(\frac{\psi_{cf}\Delta MF}{6}\right)^2 = 0 \qquad \text{A-22}$$

Determination of η

From Equation A-15 and A-16

$$-3\mathrm{aS}(R+A^2)-2\lambda\mathrm{b}=\mathrm{S}\psi_{cf}\left(\frac{\Delta MF}{2}\right)\cos\Gamma \qquad \text{A-23}$$

$$-3\mathrm{bS}(R+A^2)+2\lambda\mathrm{a}=\mathrm{S}\psi_{cf}\left(\frac{\Delta MF}{2}\right)\sin\Gamma \qquad \text{A-24}$$

Substitute for a and b from Equation A-14 into Equation A-23 & A-24; then multiply Equation A-23 by $\sin\eta$ and Equation A-24 by $\cos\eta$, therefore,

$$-3\mathrm{A}\cos\eta\sin\eta\,\mathrm{S}(R+A^2)-2\lambda\mathrm{A}\sin^2\eta=\mathrm{S}\psi_{cf}\left(\frac{\Delta MF}{2}\right)\sin\eta\cos\Gamma \qquad \text{A-25}$$

$$-3\mathrm{A}\cos\eta\sin\eta\,\mathrm{S}(R+A^2)+2\lambda\mathrm{A}\cos^2\eta=\mathrm{S}\psi_{cf}\left(\frac{\Delta MF}{2}\right)\cos\eta\sin\Gamma \qquad \text{A-26}$$

Subtract Equation A-26 from A-25,

$$-2\lambda\mathrm{A}(\sin^2\eta+\cos^2\eta)=\mathrm{S}\psi_{cf}\left(\frac{\Delta MF}{2}\right)(\sin\eta\cos\Gamma-\cos\eta\sin\Gamma) \qquad \text{A-27}$$

$$\sin\eta\cos\Gamma-\cos\eta\sin\Gamma=-\left(\frac{4\lambda\mathrm{A}}{\mathrm{S}\psi_{cf}\Delta MF}\right) \qquad \text{A-28}$$

From trigonometry,

$$\sin(A\pm B)=\sin A\cos B\pm\cos A\sin B$$

Thus, Equation A-28 becomes,

$$\sin(\eta-\Gamma)==-\left(\frac{4\lambda\mathrm{A}}{\mathrm{S}\psi_{cf}\Delta MF}\right) \qquad \text{A-29}$$

From trigonometry,

$$\sin(-\theta)=-\sin(\theta)$$

Thus,

$$\sin(\eta - \Gamma) = \left(\frac{4\lambda A}{S\psi_{cf}\Delta MF}\right) \quad \text{A-30}$$

Let $\eta^* = (\eta - \Gamma)$, therefore from Equation A-30,

$$\eta^* = \sin^{-1}\left(\frac{4A}{\psi_{cf}\Delta MF}\frac{\lambda}{S}\right) \quad \text{A-31}$$

Appendix B MIT 3-Stage Experimental Compressor Data

The geometric properties presented in the table below for the MIT 3-stage axial compressor test rig, represents the dimensions for the first blade row stage of the compressor.

Table B-1 MIT 3-stage axial compressor test rig data (Source: Al-Nahwi, 2000; Gamache, 1985)

S/N	Parameters	Values
1	Blade Chord (l)	0.0452 m
2	Blade Height (h)	0.0366 m
3	Mean Compressor Rotor Radius (R)	0.286 m
4	Blade Stagger Angle (γ)	43^o
5	Density of Air (ρ)	1.2 kg/m^3
6	Spin Speed of rotor (Ω)	251.33 rad/s
7	Number of stages (N)	3
8	Total Effective Length of Compressor (l_c)	5.53
9	Greitzer Parameter (B)	0.1
10	H,W	0.27, 0.25
11	S	1.08
12	λ, μ	0.68, 1.01
13	ψ_{co}	0.926
14	m	2
15	ψ_{CE}	14.82
16	Aerodynamic-Rotordynamic Coupling (χ)	7.83e-5
17	λ_{tu}	54.74
18	λ_{pr}	98.89
19	$\tau_{c0}, \tau_{c1}, \tau_{c2}, \tau_{c3}$	0.4472, -0.8254, 1.9392, -0.88774

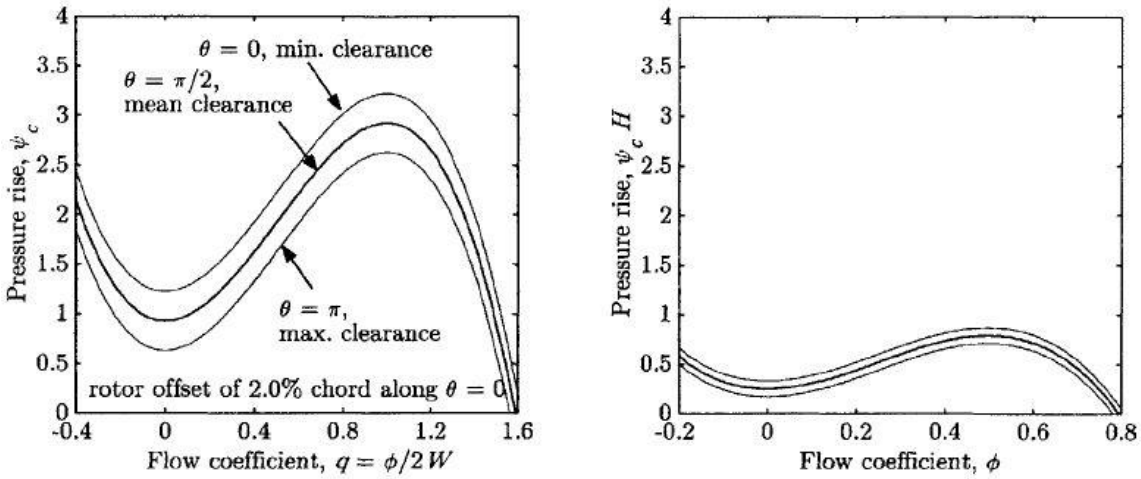

Figure 0-1 MIT 3-stage compressor rescaled pressure rise characteristics

(Source: Al-Nahwi, 2000)

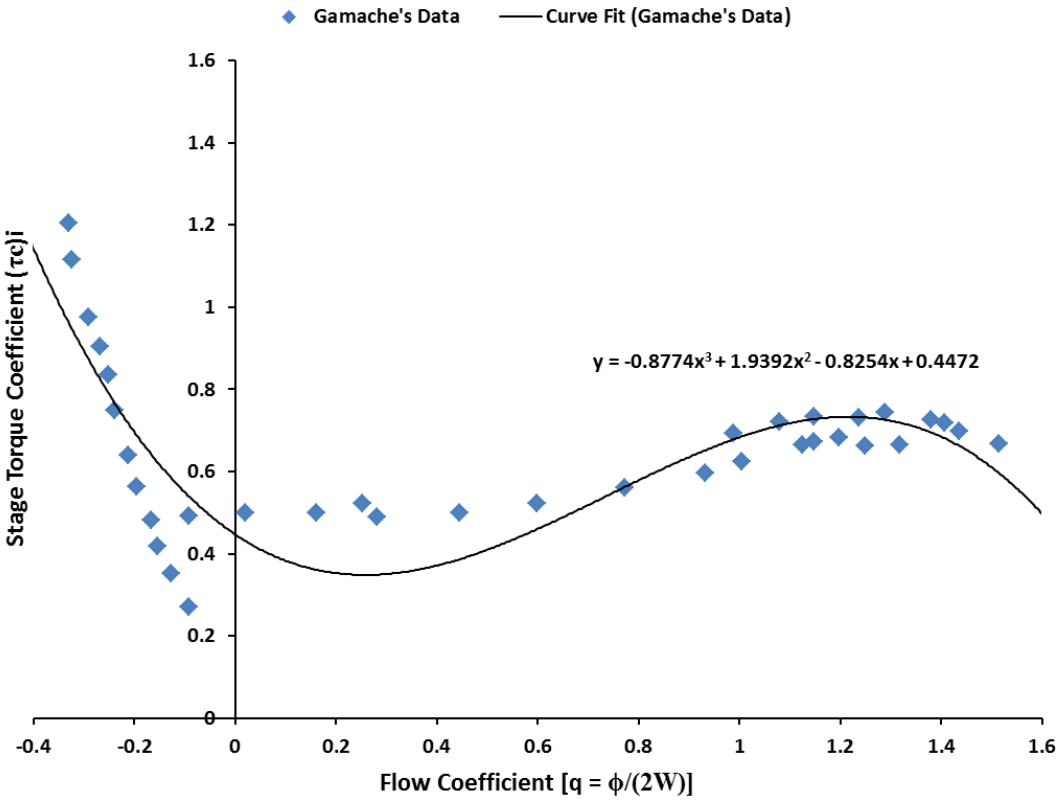

Figure 0-2 MIT 3-stage compressor stage torque characteristics (Source: Gamache, 1985)

Appendix C Compressor Specification for LM2500+

Table C-1 Compressor data for LM2500+

S/N	Parameters	Values
1	Blade Chord (l)	0.0452 m
2	Blade Height (h)	0.1775 m
3	Mean Compressor Rotor Radius (R)	0.372 m
4	Blade Stagger Angle (γ)	43^o
5	Density of Air (ρ)	1.2 kg/m^3
6	Spin Speed of rotor (Ω)	739.25 rad/s
7	Number of stages (N)	17
8	H,W	9.96, 0.0188
9	S	529.79
10	λ, μ	2.8243, 5.6486
11	ψ_{co}	9.811
12	m	2
13	Aerodynamic-Rotordynamic Coupling (χ)	4.9373e-5
14	λ_{tu}	92.6150
15	λ_{pr}	34.4968
16	$\tau_{c0}, \tau_{c1}, \tau_{c2}, \tau_{c3}$	0.4472, -0.8254, 1.9392, -0.88774

C.1 Preliminary Sizing of theLM2500+ Compressor First Stage

Table C-2 Preliminary specification for LM2500+ compressor

S/N	Parameters	Values
1	Overall Pressure	23.1
2	Polytrophic Efficiency	0.8932
3	Mass Flow (W)	84.1 Kg/s

4	Inlet Pressure (PT_1)	101325 N/m^2
5	Inlet Temperature (T_1)	288 ^{o}C
6	Ratio of Specific Heats	1.395
Initial Chosen Variables		
7	Number of Stages	17
8	Mean Blade Speed (U_m)	275 m/s
9	Mean Axial Velocity (V_a)	200 m/s
10	Absolute Air Angle at Inlet to Each Stage (α_0)	0
11	Inlet Hub/Tip Ratio $\left(\frac{D_{h1}}{D_{t1}}\right)$	0.615
12	Stage Temperature Rise Distribution	Constant
13	Annulus Configuration	Constant Outside Diameter

Compressor Inlet Geometry Sizing

Since $\alpha_0 = 0$, $V_{a(in)} = V_0 = 200$ and $V_0/\sqrt{T_1} = \frac{200}{\sqrt{288}} = 11.79$

From the tables for compressible flow of dry air (Ramsden, 2015),

$$Q_0 = 0.0343$$

But Q_0 is expressed as (Ramsden, 2015):

$$Q_0 = \frac{W\sqrt{T_1}}{K_B A_1 P_1} \qquad \text{C-1}$$

Let the blockage factor $K_B = 0.99$, from Ramsden(2015)

Substituting from Table C-2 into Equation C-2,

$$0.0343 = \frac{84.1\sqrt{288}}{0.99 \times A_1 \times 101325} \qquad \text{C-2}$$

$$\therefore Annulus\ Area, A_1 = 0.4148\ m^2$$

But annulus flow area is expressed as (Ramsden, 2015),

$$A_1 = \frac{\pi}{4} D_{t1}^2 \left(1 - \left[\frac{D_{h1}}{D_{t1}}\right]^2\right) \quad \text{C-3}$$

From Equation C-3, compressor tip diameter is (D_{t1}):

$$D_{t1} = 0.4148 \times \frac{4}{\pi} \times \frac{1}{(1 - 0.615^2)}$$

$$D_{t1} = 0.922 \text{ m}$$

Using the value of the hub-tip ratio of the compressor $\left(\frac{D_{h1}}{D_{t1}}\right)$, the hub diameter (D_{h1}) is determined by (Ramsden, 2015):

$$D_{h1} = \left(\frac{D_{h1}}{D_{t1}}\right) \times D_{t1} \quad \text{C-4}$$

$$D_{h1} = 0.615 \times 0.922 = 0.567 \text{ m}$$

The compressor mean diameter is (Ramsden, 2015):

$$D_{m1} = \frac{D_{t1} + D_{h1}}{2} \quad \text{C-5}$$

$$D_{m1} = \frac{0.922 + 0.567}{2} = 0.744\, m$$

The compressor first stage blade height (h) is (Ramsden, 2015):

$$h = \frac{D_{t1} - D_{h1}}{2} \quad \text{C-6}$$

$$h = \frac{0.922 - 0.567}{2} = 0.1775\, m$$

Appendix D RotorMatch - 2D Transfer Matrix Rotordynamic Analysis MATLAB Code

D.1 How to use the RotorMatch Code

The RotorMatch Code is made up of four components which are: Point.m, Field.m, Station.m and Rotor.m.

The entire four components must be present in other to create a rotor model to perform any rotordynamic analysis.

At present the RotorMatch code can perform only critical speed analysis and forced response analysis. The forced response analysis can be due to unbalance or aerodynamic force due to fouling.

For the aerodynamic force forced response, the Compressor.m needs to be present.

Examples using the RotorMatch Code

1. Creating a Field Matrix

```
f1 = Field();
f1.len = 0.75;
f1.dia = 10e-3;
f1.eMod = 2.1e11;
```

2. Creating a Point Matrix

```
p1 = Point();
p1.mass = 10;
p1.diaInertia = 0.02;
p1.polarInertia = 0.04;
```

3. Creating a Station (Standard TM element)

```
s1 = Station(f1,p1);
```

4. Creating a Rotor and adding a station

```
r = Rotor();
r.addStation(s1);
```

5. Adding a Boundary Condition

```
r.lBound = Rotor.PINNED_LEFT;
r.rBound = Rotor.PINNED_RIGHT;
```

6. Performing Critical Speed Analysis

```
critSpeed = r.getCriticalSpeed();
disp(critSpeed);
```

7. Performing a Forced Response Analysis

```
r.getForcedResponsePlot(2);
```

D.2 Point.m (RotorMatch Code)

```
classdef Point < handle
% this class represents a  matrix that describes the discontinuous
effects
% along the rotor
% Discontinuous effects: disc inertia forces, bearing stiffness &
damping,
% unbalance & gyroscopic moment
% author: Jombo Gbanaibolou

    properties
       mass = 0; % point mass in kg
       %-------------------------------------------------------
       %default bearing characteristics
       %-------------------------------------------------------
       kxx = 0,kyy = 0; % bearing stiffness in N/m
       kxy = 0,kyx = 0; % cross-coupled bearing stiffness in N/m
       cxx = 0,cyy = 0; % bearing damping in Ns/m
       cxy = 0,cyx = 0; % cross-coupled bearing damping in Ns/m
       %-------------------------------------------------------
       bearing = []; %default stiffness bearing
       %-------------------------------------------------------

       unbalx = 0; % x-axis unbalance mass in kg-m
       unbaly = 0; % y-axis unbalance mass in kg-m
       diaInertia = 0; %diametral mass moment of inertia in kgm^2
       polarInertia = 0; %polar mass moment of inertia in kgm^2

       %-------------------------------------------------------
       aerox = 0; % x-axis aerodynamic force in N
       aeroy = 0; % y-axis aerodynamic force in N
       %-------------------------------------------------------
       fx = 0; % x-axis constant force in N
       fy = 0; % y-axis constant force in N
       %-------------------------------------------------------
    end
```

```
    methods

        function obj = Point()
        % class constructor
        end

        function pc = getMatrix(obj, rotSpeed)
        % computes the complex point matrix
        % input: rotational speed in rad/s
        % output: pc -  9x9 complex point matrix

            m = obj.mass;
            shaftSpeed = rotSpeed/(2*pi); %rps
            if ~isempty(obj.bearing)
                obj.setBearing(shaftSpeed);
            end

            %bearing stiffness values
            sxx = obj.kxx;
            sxy = obj.kxy;

            syy = obj.kyy;
            syx = obj.kyx;

            %bearing damping values
            dxx = obj.cxx;
            dxy = obj.cxy;

            dyy = obj.cyy;
            dyx = obj.cyx;

            %mass moment of inertia values
            dm = obj.diaInertia;
            pm = obj.polarInertia;

            %component of the point matrix
            p1 = eye(4);
            p1(4,1) = (m*rotSpeed^2)- syy - 1i*rotSpeed*dyy;
            p1(3,2) = -(rotSpeed^2*dm);

            p2 = zeros(4);
            p2(4,1) = -syx - 1i*rotSpeed*dyx;
            p2(3,2) = 1i*(rotSpeed^2*pm);

            p3 = zeros(4);
            p3(4,1) = -sxy - 1i*rotSpeed*dxy;
            p3(3,2) = -1i*(rotSpeed^2*pm);

            p4 = eye(4);
            p4(4,1) = (m*rotSpeed^2)- sxx - 1i*rotSpeed*dxx;
            p4(3,2) = -(rotSpeed^2*dm);

            %unbalance, aerodynamic & other const. force component
matrix
            gy = zeros(4,1);
```

```
            gy(4) = -(rotSpeed)^2*obj.unbaly - (rotSpeed)^2*obj.aeroy
- obj.fy;

            gx = zeros(4,1);
            gx(4) = -(rotSpeed)^2*obj.unbalx - (rotSpeed)^2*obj.aerox
- obj.fx;

            %final complex point matrix (9x9)
            pc = [p1 p2 gy; p3 p4 gx; zeros(1,8) 1];
        end

        function setBearing(obj,shaftSpeed)
            % a function that sets the bearing stiffness & damping
coeff.
            % input: bearing - every bearing object should implement
the
            %        shaftSpeed - speed of shaft in rps or Hz
            % getStiffnessDamping(shaftSpeed) method, which outputs a
stiffness &
            % damping coefficient vector [kxx kyy cxx cyy kxy kyx cxy
cyx]

            kc = obj.bearing.getStiffnessDamping(shaftSpeed);

            obj.kxx = kc(1);
            obj.kyy = kc(2);
            obj.cxx = kc(3);
            obj.cyy = kc(4);
            obj.kxy = kc(5);
            obj.kyx = kc(6);
            obj.cxy = kc(7);
            obj.cyx = kc(8);
        end
    end
end
```

D.3 Field.m (RotorMatch Code)

```
classdef Field < handle
% this class represents a  matrix that describes the elastic behaviour
of a
% rotor shaft segment based on timoshenko beam theory
% It considers the effect of bending and shear deformation
% author: Jombo Gbanaibolou

    properties
        dia; % outside diameter of shaft segment  in metre
        len; % length of shaft segment in metre
        eMod = 2.1e11 ; % shaft segment modulus of elasticity N/m^2,
default steeel
    end
```

```
    methods

        function obj = Field()
        % class constructor
        end

        function fc = getMatrix(obj)
        % computes the field matrix
        % output: fc - 9x9 complex field matrix

            L = obj.len;
            E = obj.eMod;
            d = obj.dia;
            I = pi*d^4/64; %area moment of inertia for shaft segment
in m^4

            % component of the point matrix
            f1 = eye(4);
            f1(1,2) = L;
            f1(1,3) = L^2/(2*E*I);
            f1(1,4) = L^3/(6*E*I);
            f1(2,3) = L/(E*I);
            f1(2,4) = L^2/(2*E*I);
            f1(3,4) = L;

            f2 = zeros(4);

            %final complex point matrix (9x9)
            fc = [f1 f2 zeros(4,1); f2 f1 zeros(4,1); zeros(1,8) 1];

        end

    end
end
```

D.4 Station.m (RotorMatch Code)

```
classdef Station < handle
% this class represents a combination of a point and field matrix
object
% author: Jombo Gbanaibolou

    properties
        point;
        field;
    end

    methods

        function obj = Station(field,point)
            if(nargin > 0)
                obj.field = field;
```

```
                obj.point = point;
            end
        end

        function [sc, se] = getMatrix(obj,rotSpeed)
        % computes the complex(9x9) & extended(17x17)station transfer
matrix
        % input: rotational speed in rad/s
        % output: sc - complex (9x9) station matrix
        %         se - extended (17x17) station matrix

            p = obj.point.getMatrix(rotSpeed);
            f = obj.field.getMatrix();

            %complex station matrix (9x9)
            sc = p*f;

            %extended station transfer matrix (17x17)
            %real component
            sr_temp = real(sc);
            sr = sr_temp(1:end-1,1:end-1);
            gr = sr_temp(1:end-1,end);

            %imaginary component
            si_temp = imag(sc);
            si = si_temp(1:end-1,1:end-1);
            gi = si_temp(1:end-1,end);

            se = [sr -si gr; si sr gi; zeros(1,16) 1];

        end
    end

end
```

D.5 Rotor.m (RotorMatch Code)

```
classdef Rotor < handle
% this class represents a rotor model
% author: Jombo Gbanaibolou

    properties
       stationList = [];
       lBound; % left boundary conditions
       rBound; % right boundary conditions
    end

    properties(Constant)
    % constants that define the rotor boundary end condition state
vectors

       %left bc selects the column
```

```
    PINNED_LEFT = [2 4 6 8 10 12 14 16];
    FREE_LEFT = [1 2 5 6 9 10 13 14];
    FIXED_LEFT = [3 4 7 8 11 12 15 16];
    FLEXIBLE_LEFT = [1 2 5 6 9 10 13 14];

    %right bc selects the row
    PINNED_RIGHT = [1 3 5 7 9 11 13 15];
    FREE_RIGHT = [3 4 7 8 11 12 15 16];
    FIXED_RIGHT = [1 2 5 6 9 10 13 14];
    FLEXIBLE_RIGHT = [3 4 7 8 11 12 15 16];
end

methods
    function obj = Rotor()
      obj;
    end

    function addStation(obj, station)
    % builds the rotor model by adding stations
    % input: station objects

        if(isempty(obj.stationList))
            obj.stationList = station;
        else
            obj.stationList(end+1) = station;
        end

    end

    function [rc, re] = getMatrix(obj,rotSpeed)
    % computes the rotors overall transfer matrix
    % input: rotational speed in rad/sec
    % output: rc - complex (9x9) rotor matrix
    %         re - extended (17x17) rotor matrix

        %complex rotor matrix (9x9)
        rc = eye(9); %identity matrix
        for p = 1:numel(obj.stationList)
            [sc, se] = obj.stationList(p).getMatrix(rotSpeed);
            rc = sc*rc;
        end

        %extended rotor matrix (17x17)
        %real component
        rr_temp = real(rc);
        rr = rr_temp(1:end-1,1:end-1);
        gr = rr_temp(1:end-1,end);

        %imaginary component
        ri_temp = imag(rc);
        ri = ri_temp(1:end-1,1:end-1);
        gi = ri_temp(1:end-1,end);

        re = [rr -ri gr; ri rr gi; zeros(1,16) 1];
    end

    function [dm,freqMat] = applyBC(obj,rotSpeed)
```

```
        % applies the boundary end conditons of the rotor to the rotor
        % matrix
        % input: lBound left boundary condition,
        %        rBound right boundary conditon
        %        rotSpeed rotor rotational speed in rad/s
        % ouput: frequency matrix determinant and frequency matrix

            [rc, re] = obj.getMatrix(rotSpeed);
            rotorMatrix = re;

            % apply boundary conditions to determine freq. matrix
            %select rows
            freqMat= rotorMatrix(obj.rBound,:);
            %select columns
            freqMat = freqMat(:,obj.lBound); % frequency matrix

            dm = det(freqMat);
        end

        function cs = getCriticalSpeed(obj)
        % calculate the critical speed of the rotor-bearing system in
rad/s

            a = 1; %initial guess of the critical speed
            cs = fminsearch(@(x) obj.applyBC(x),a);

        end % end function getCriticalSpeed

        function svm = getForcedResponse(obj,rotSpeed)
        % this function performs a forced vibration analysis on the
rotor
        % input: rotational speed in rad/sec
        % Ouput: svm - state vector matrix

            % compute extended rotor mtrix
            [rc, re] = obj.getMatrix(rotSpeed);
            rotorMatrix = re;

            % apply boundary conditions to determine freq. matrix
            %select rows
            freqMat= rotorMatrix(obj.rBound,:);

            %select unbalance and aero component
            g = freqMat(:,end);
            g = -1*g;
            %select columns
            freqMat = freqMat(:,obj.lBound); % frequency matrix

            sv_0 = freqMat\g; %left boundary state vector values

            % Station vector matix initialization
            svm = zeros(17,length(obj.stationList)+1);

            % converting left boundary state vector values to a 17x1
vector
            index = obj.lBound;
```

```
            k = 1;
            while k <=length(sv_0)
               svm(index(k),1) =  sv_0(k);
               k = k + 1;
            end
            svm(end,1) = 1; % represents the unbalance state variable

            %compute other station vector values
            for p = 1:length(obj.stationList)
                [sc,se] = obj.stationList(p).getMatrix(rotSpeed);
                svm(:,p+1) = se * svm(:,p);
            end

        end

        function sv = stationVector(obj,svm,location)
           % a function that gives the station vector at a location
           % It selects the location station vector column from the
           % unbalanced forced response station vector matrix
           % first location

            sv = svm(:,location);
        end

        function getForcedResponsePlot(obj,location)
            % a function that plots the amplitude in m of the
vibration
            % response against the speed of rotation in cps
            % input: location - identifies the station of interest
from the
            %        left counting from 1

            k = 1;
            index = 1;
            y = [];
            x = [];
            sp = [];
            sp_limit = 100; %cps
            while k <= 2*pi*sp_limit
                svm = obj.getForcedResponse(k);
                sv = obj.stationVector(svm,location);
                y(index) = abs(sv(1));
                x(index) = abs(sv(5));
                sp(index) = k/(2*pi); %conversion from rad/s to cps

                k = k + 0.1;
                index = index + 1;
            end

            %y-axis=========================
            disp('V - values [y]');
            my = max(y); %max value
            my_i = y == my; %find index of max value
            cspy = sp(my_i); %critical speed, speed at maximum
response
            fprintf('max value of amplitude in m: %f \n',my);
```

```
            fprintf('speed of max value of amplitude in cps: %f
\n\n',cspy);

            figure(1);

            % Kikuchi rotor response plot scale
            %----------------------------------

%             plot(sp,y*1e6); %amplitude in micron
%             xlabel('Rotational speed in c/sec');
%             ylabel('y-axis Amplitude in micron');
%             hold on;
%             [pks,locs] = findpeaks(y);
%             plot(sp(locs),y(locs)*1e6,'--r');
%             hold off;
            %----------------------------------

            plot(sp,y); %amplitude in metre
            xlabel('Rotational speed in c/sec');
            ylabel('y-axis Amplitude in m');
            axis([0 10 0 2.5e-7]); % for Q = 1.2 plots
%             axis([0 10 0 2.5e-5]); % for Q = 1.0 plots

            %x-axis==========================
            disp('H - values [x]');
            mx = max(x); %max value
            mx_i = x == mx; %find index of max value
            cspx = sp(mx_i); %critical speed, speed at maximum
response
            fprintf('max value of amplitude in m: %f \n',mx);
            fprintf('speed of max value of amplitude in cps:: %f
\n',cspx);

            figure(2);

            % Kikuchi rotor response plot scale
            %----------------------------------
%             plot(sp,x*1e6); %amplitude in micron
%             xlabel('Rotational speed in c/sec');
%             ylabel('x-axis Amplitude in micron');
            %----------------------------------

            plot(sp,x); %amplitude in metre
            xlabel('Rotational speed in c/sec');
            ylabel('x-axis Amplitude in m');

        end
    end

end
```

D.6 JournalBearing.m

The journal bearing module represents a short bearing approximation solution. This module was used to validate the RotorMatch code against the Kikuchi(1970) rotor experimental data.

```
classdef JournalBearing < handle
    %JournalBearing this class represents a cylindrical journal
bearing
    %   Detailed explanation goes here

    properties
        viscosity; %dynamic viscosity of the lubricant Pa-s
        bearingLoad; %load on bearing in N
        journalDiameter; %diameter of journal in m
        bearingLength; %bearing length in m
        clearance; %bearing clearance in m
    end

    methods

        function obj = JournalBearing()
            obj;
        end

        function ld = getldratio(obj)
            % a function to calculate the L/D ratio of the bearing

            ld = obj.bearingLength/obj.journalDiameter;
        end

        function sn = getSommerfeld(obj,shaftSpeed)
           % a function to calculate the bearing sommerfeld number

           w = obj.bearingLoad;
           l = obj.bearingLength;
           d = obj.journalDiameter;
           r = d/2;

           p =  w/ (l*d); %average bearing pressure

           u = obj.viscosity;
           n = shaftSpeed;
           c = obj.clearance;

           sn = (u*n/p)*(r/c)^2;
        end

        function e = getEccentricity(obj,shaftSpeed)
            % determines the eccentricity ratio based on curve fitted
data
            % from "Theory of Hydrodynamic Lubrication" by Pinkus, O &
```

```
            % Sternlicht, B.

            s =  obj.getSommerfeld(shaftSpeed);
            ld = obj.getldratio();

            if (ld > 1)

                if (s <= 0.1)
                    e = -216.15*s^3 + 107.04*s^2 - 17.397*s + 1.1237;
                else
                    e = 0.032*s^(-0.875);
                end

            elseif (ld >= 0.5)
                ld1 = 0.5;
                e1 = -0.193*log(s) + 0.3588;

                ld2  = 1;
                if (s >= 0.5)
                    e2 = 0.0982*s^-0.990;
                elseif (s > 0.3)
                    ps1 = 0.3;
                    pe1 = -1329.8*ps1^5 + 1173.4*ps1^4 - 400.12*ps1^3
+ 69.731*ps1^2 - 7.8657*ps1 + 0.9008;

                    ps2 = 0.5;
                    pe2 = 0.0982*ps2^-0.990;

                    e2 = 1/(ps2-ps1)*(pe2*(s-ps1) + pe1*(ps2-s));
                else
                    e2 = -1329.8*s^5 + 1173.4*s^4 - 400.12*s^3 +
69.731*s^2 - 7.8657*s + 0.9008;
                end

                e = 1/(ld2-ld1)*(e2*(ld-ld1) + e1*(ld2-ld));

            elseif (ld >= 0.25)
                ld1 = 0.25;
                e1 = -0.18*log(s) + 0.5893;

                ld2  = 0.5;
                e2 = -0.193*log(s) + 0.3588;

                e = 1/(ld2-ld1)*(e2*(ld-ld1) + e1*(ld2-ld));

            elseif (ld >= 0.125)
                ld1 = 0.125;
                e1 = -0.176*log(s) + 0.8206;

                ld2  = 0.25;
                e2 = -0.18*log(s) + 0.5893;

                e = 1/(ld2-ld1)*(e2*(ld-ld1) + e1*(ld2-ld));
            end
        end
```

```
        function [kc,dkc] = getStiffnessDamping(obj,shaftSpeed)
            % a function that determines the stiffness & damping of a
full
            % journal bearing using the results from the short bearing
            % apporximation
            % expressions for stiffness and damping curve fitted from
data
            % from "Kirk, R. G. and Gunter, E. J. (1976).'Short
Bearing Analysis
            % Applied to Rotor Dynamics - Part 1: Theory', Journal of
Lubrication
            % Technology, Vol. 98, Issue 1, pp. 47-56.
            % output: kc (1x8) stiffness & damping coefficient vector
            %         [kxx kyy cxx cyy kxy kyx cxy cyx]
            %         dkc (1x8) dimenstiffness & damping coefficient
vector
            %         [dkxx dkyy dcxx dcyy dkxy dkyx dcxy dcyx]
            % all bearing classes should implement a
getStiffnessDamping
            % method

            e = obj.getEccentricity(shaftSpeed);

            %dimensional direct stiffness coefficients
            %=========================================
            %dkxx-------------------------------------
            if (e >= 0.965)
                dkxx = 123058*e - 117919;
            elseif (e >= 0.944)
                dkxx  = 23155*e - 21540;
            elseif (e >= 0.915)
                dkxx  = 6340.6*e - 5676.5;
            elseif (e >= 0.846)
                dkxx  = 1246.3*e - 1015.2;
            elseif (e >= 0.796)
                dkxx  = 7735.5*e^2 - 12376*e + 4972.8;
            else
                dkxx  = 2615*e^6 - 5464.4*e^5 + 4451.7*e^4 -
1734.8*e^3 + 329.94*e^2 - 22.716*e + 0.622;
            end

            %dkyy-------------------------------------
            if (e >= 0.931)
                dkyy = 102445.394*e - 93370.283;
            elseif (e >= 0.879)
                dkyy = 28607*e - 24618;
            elseif (e >= 0.800)
                dkyy = 5337.8*e - 4166.9;
            elseif (e >= 0.720)
                dkyy = 885.19*e - 602.66;
            elseif (e >= 0.574)
                dkyy = 3529.2*e^3 - 5692*e^2 + 3095.4*e - 560.77;
            elseif (e >= 0.481)
                dkyy = 43.951*e - 17.177;
            else
                dkyy = -7985.4*e^6 + 12476*e^5 - 7439.8*e^4 +
2196.6*e^3 - 333.52*e^2 + 27.858*e - 0.807;
            end
```

```
            %dimensional direct damping coefficients
            %=======================================
            %dcxx---------------------------------
            if (e >= 0.979)
                dcxx = 127919*e - 124850;
            elseif (e >= 0.937)
                dcxx = 7743.1*e - 7175.3;
            elseif (e >= 0.901)
                dcxx = 1035.5*e - 893.13;
            elseif (e >= 0.841)
                dcxx = 338.68*e - 265.35;
            elseif (e >= 0.381)
                dcxx = 3513.7*e^6 - 8783.9*e^5 + 8559.1*e^4 -
4028.7*e^3 + 924.35*e^2 - 85.606*e + 4.6476;
            else
                dcxx = 5.1921*e^2 + 0.336*e + 3.1029;
            end

            %dcyy---------------------------------
            if (e >= 0.902)
                dcyy = 30868*e - 27250;
            elseif (e >= 0.866)
                dcyy = 8467.9*e - 7052.8;
            elseif (e >= 0.801)
                dcyy = 2753.5*e - 2105.8;
            else
                dcyy = 10354*e^6 - 20488*e^5 + 15523*e^4 - 5467*e^3 +
907.62*e^2 - 57.583*e + 4.0761;
            end

            %dimensional coupled stiffness coefficients
            %=========================================
            %dkxy---------------------------------------

            dkxy = -37.728*e^5 + 28.727*e^4 - 9.7664*e^3 + 1.7095*e^2
- 0.0938*e + 1.603;

            %dkyx---------------------------------------
            if (e >= 0.976)
                dkyx = 219298*e - 210674;
            elseif (e >= 0.947)
                dkyx = 80917*e - 75619;
            elseif (e >= 0.918)
                dkyx = 21192*e - 19055;
            elseif (e >= 0.792)
                dkyx = 251098*e^3 - 616599*e^2 + 505518*e - 138296;
            else
                dkyx = 3412.7*e^6 - 6455.2*e^5 + 4780.6*e^4 -
1675.4*e^3 + 291.21*e^2 - 19.992*e + 2.0399;
            end

            dkyx = -dkyx;

            %dimensional coupled damping coefficients
            %=======================================
            %dcxy---------------------------------
```

```
            if (e >= 0.971)
                dcxy =  4e6*e^2 - 7e6*e + 3e6;
            elseif (e >= 0.938)
                dcxy = 12827*e - 11815;
            elseif (e >= 0.894)
                dcxy = 2817.2*e - 2428.9;
            elseif (e >= 0.848)
                dcxy = 1027*e - 828.1;
            elseif (e >= 0.793)
                dcxy = 372.04*e - 272.53;
            elseif (e >= 0.703)
                dcxy = 128.33*e - 79.383;
            else
                dcxy = -471.4*e^6 + 1226.6*e^5 - 1068.2*e^4 +
430.19*e^3 - 77.925*e^2 + 10.211*e - 0.1133;
            end

            dcxy = -dcxy;

            %dcyx-----------------------------------
            dcyx = dcxy;

            % dimensional stiffness and damping coefficients
            dkc = [dkxx dkyy dcxx dcyy dkxy dkyx dcxy dcyx];

            % stiffness and damping coefficients
            kxx = obj.stiffness(dkxx,shaftSpeed);
            kyy = obj.stiffness(dkyy,shaftSpeed);
            kxy = obj.stiffness(dkxy,shaftSpeed);
            kyx = obj.stiffness(dkyx,shaftSpeed);
            cxx = obj.damping(dcxx,shaftSpeed);
            cyy = obj.damping(dcyy,shaftSpeed);
            cxy = obj.damping(dcxy,shaftSpeed);
            cyx = obj.damping(dcyx,shaftSpeed);

            kc = [kxx kyy cxx cyy kxy kyx cxy cyx];
        end

    end

    methods (Access = private)

        function w = getW(obj,shaftSpeed)
            % a helper function

            mu = obj.viscosity;
            r = obj.journalDiameter/2;
            l = obj.bearingLength;
            spd = 2*pi*shaftSpeed;
            c = obj.clearance;

            w = (mu*r*l^3*spd)/(2*c^2);
        end

        function k = stiffness(obj,dk,shaftSpeed)
```

```
            % a function that dimensionalize the non dimen. stiffness
coeff.
            % input: dk - nondimensional stiffness coefficient
            % output: k - stiffness coefficient

            w = obj.getW(shaftSpeed);
            c = obj.clearance;
            k = dk*w/c;
        end

        function cp = damping(obj, dcp,shaftSpeed)
            % a function that dimensionalize the non dimen. damping
coeff.
            % input: dcp - nondimensional damping coefficient
            % output: cp - damping coefficient

            w = obj.getW(shaftSpeed);
            c = obj.clearance;
            spd = 2*pi*shaftSpeed;

            cp = (dcp*w)/(c*spd);
        end
    end

end
```

RotorMatch Validation Script

D.7 Kikuchi_1.m

This script represents the Kikuchi(1970) rotor model II-0.6-0.001 configuration.

Dependencies: need all of RotorMatch Code & JournalBearing.m to run

```
clear all;

tic;
%--------------------------
jb1 = JournalBearing();

jb1.viscosity = 28e-3;
jb1.bearingLoad = 254.079;
jb1.journalDiameter = 40.045e-3;
jb1.bearingLength = 24e-3;
jb1.clearance = 0.024e-3;

f0 = Field();
f0.len = 131e-3;%0
f0.dia = 40e-3;%1
f0.eMod = 2.1e11;%1

p0 = Point();
```

```
p0.mass = 0;
p0.bearing = jb1;

s0 = Station(f0,p0);
%--------------------------

f1 = Field();
f1.len =200e-3;
f1.dia = 40e-3;
f1.eMod = 2.1e11;

p1 = Point();
p1.mass = 13.47;
p1.polarInertia = 1.02e-1;
p1.diaInertia = 5.11e-2;

s1 = Station(f1,p1);

f2 = Field();
f2.len =200e-3;
f2.dia = 40e-3;
f2.eMod = 2.1e11;

p2 = Point();
p2.mass = 13.44;
p2.polarInertia = 1.02e-1;
p2.diaInertia = 5.11e-2;
p2.unbalx = 120e-6;
p2.unbaly = 120e-6;

s2 = Station(f2,p2);

f3 = Field();
f3.len =200e-3;
f3.dia = 40e-3;
f3.eMod = 2.1e11;

p3 = Point();
p3.mass = 13.47;
p3.polarInertia = 1.02e-1;
p3.diaInertia = 5.11e-2;

s3 = Station(f3,p3);

f4 = Field();
f4.len =200e-3;
f4.dia = 40e-3;
f4.eMod = 2.1e11;

p4 = Point();
p4.mass = 0;

%--------------------------
jb2 = JournalBearing();

jb2.viscosity = 26e-3;
```

```
jb2.bearingLoad = 254.079;
jb2.journalDiameter = 40.044e-3;
jb2.bearingLength = 24e-3;
jb2.clearance = 0.026e-3;
%---------------------------------
p4.bearing = jb2;

s4 = Station(f4,p4);

%---------------------------------
f5 = Field();
f5.len = 131e-3;
f5.dia = 40e-3;
f5.eMod = 2.1e11;

p5 = Point();
p5.mass = 0;

s5 = Station(f5,p5);
%---------------------------------
r = Rotor();
r.addStation(s0);
r.addStation(s1);
r.addStation(s2);
r.addStation(s3);
r.addStation(s4);
r.addStation(s5);
r.lBound = Rotor.FREE_LEFT; %Rotor.FLEXIBLE_LEFT
r.rBound = Rotor.FREE_RIGHT; %Rotor.FLEXIBLE_RIGHT

%forced response plot (Unbalance/Aerodynamic)
%====================================
r.getForcedResponsePlot(4);

%---------------------------------
toc;
```

D.8 kikuchi_2.m

This script represents the Kikuchi(1970) rotor model II-0.6-0.003 configuration.

Dependencies: need all of RotorMatch Code & JournalBearing.m to run

```
clear all;

tic;
%---------------------------
jb1 = JournalBearing();

jb1.viscosity = 29e-3;
jb1.bearingLoad = 254.079;
```

```
jb1.journalDiameter = 40.112e-3;
jb1.bearingLength = 24e-3;
jb1.clearance = 0.058e-3;

f0 = Field();
f0.len = 131e-3;%0
f0.dia = 40e-3;%1
f0.eMod = 2.1e11;%1

p0 = Point();
p0.mass = 0;
p0.bearing = jb1;

s0 = Station(f0,p0);
%---------------------------

f1 = Field();
f1.len =200e-3;
f1.dia = 40e-3;
f1.eMod = 2.1e11;

p1 = Point();
p1.mass = 13.47;
p1.polarInertia = 1.02e-1;
p1.diaInertia = 5.11e-2;

s1 = Station(f1,p1);

f2 = Field();
f2.len =200e-3;
f2.dia = 40e-3;
f2.eMod = 2.1e11;

p2 = Point();
p2.mass = 13.44;
p2.polarInertia = 1.02e-1;
p2.diaInertia = 5.11e-2;
p2.unbalx = 120e-6;
p2.unbaly = 120e-6;

s2 = Station(f2,p2);

f3 = Field();
f3.len =200e-3;
f3.dia = 40e-3;
f3.eMod = 2.1e11;

p3 = Point();
p3.mass = 13.47;
p3.polarInertia = 1.02e-1;
p3.diaInertia = 5.11e-2;

s3 = Station(f3,p3);

f4 = Field();
f4.len =200e-3;
```

```
f4.dia = 40e-3;
f4.eMod = 2.1e11;

p4 = Point();
p4.mass = 0;

%--------------------------
jb2 = JournalBearing();

jb2.viscosity = 28e-3;
jb2.bearingLoad = 254.079;
jb2.journalDiameter = 40.113e-3;
jb2.bearingLength = 24e-3;
jb2.clearance = 0.061e-3;
%---------------------------------
p4.bearing = jb2;

s4 = Station(f4,p4);

%---------------------------------
f5 = Field();
f5.len = 131e-3;
f5.dia = 40e-3;
f5.eMod = 2.1e11;

p5 = Point();
p5.mass = 0;

s5 = Station(f5,p5);
%---------------------------------
r = Rotor();
r.addStation(s0);
r.addStation(s1);
r.addStation(s2);
r.addStation(s3);
r.addStation(s4);
r.addStation(s5);
r.lBound = Rotor.FREE_LEFT; %Rotor.FLEXIBLE_LEFT
r.rBound = Rotor.FREE_RIGHT; %Rotor.FLEXIBLE_RIGHT

%Critical speed
%================================
% cs1 = r.getCriticalSpeed();
% disp(cs1); %rad/s
% cs2 = cs1 / (2*pi);
% disp(cs2); %rps

%forced response plot (Unbalance/Aerodynamic)
%===================================
r.getForcedResponsePlot(4);

%---------------------------------
toc;
```

D.9 kikuchi_3.m

This script represents the Kikuchi(1970) rotor model II-0.6-0.01 configuration.

Dependencies: need all of RotorMatch Code & JournalBearing.m to run

```
clear all;

tic;
%--------------------------
jb1 = JournalBearing();

jb1.viscosity = 42e-3;
jb1.bearingLoad = 254.079;
jb1.journalDiameter = 40.396e-3;
jb1.bearingLength = 24e-3;
jb1.clearance = 0.2e-3;

f0 = Field();
f0.len = 131e-3;%0
f0.dia = 40e-3;%1
f0.eMod = 2.1e11;%1

p0 = Point();
p0.mass = 0;
p0.bearing = jb1;

s0 = Station(f0,p0);
%--------------------------

f1 = Field();
f1.len =200e-3;
f1.dia = 40e-3;
f1.eMod = 2.1e11;

p1 = Point();
p1.mass = 13.47;
p1.polarInertia = 1.02e-1;
p1.diaInertia = 5.11e-2;

s1 = Station(f1,p1);

f2 = Field();
f2.len =200e-3;
f2.dia = 40e-3;
f2.eMod = 2.1e11;

p2 = Point();
p2.mass = 13.44;
p2.polarInertia = 1.02e-1;
p2.diaInertia = 5.11e-2;
p2.unbalx = 120e-6;
p2.unbaly = 120e-6;
```

```
s2 = Station(f2,p2);

f3 = Field();
f3.len =200e-3;
f3.dia = 40e-3;
f3.eMod = 2.1e11;

p3 = Point();
p3.mass = 13.47;
p3.polarInertia = 1.02e-1;
p3.diaInertia = 5.11e-2;

s3 = Station(f3,p3);

f4 = Field();
f4.len =200e-3;
f4.dia = 40e-3;
f4.eMod = 2.1e11;

p4 = Point();
p4.mass = 0;

%---------------------------
jb2 = JournalBearing();

jb2.viscosity = 47e-3;
jb2.bearingLoad = 254.079;
jb2.journalDiameter = 40.393e-3;
jb2.bearingLength = 24e-3;
jb2.clearance = 0.2e-3;
%---------------------------------
p4.bearing = jb2;

s4 = Station(f4,p4);

%---------------------------------
f5 = Field();
f5.len = 131e-3;
f5.dia = 40e-3;
f5.eMod = 2.1e11;

p5 = Point();
p5.mass = 0;

s5 = Station(f5,p5);
%---------------------------------
r = Rotor();
r.addStation(s0);
r.addStation(s1);
r.addStation(s2);
r.addStation(s3);
r.addStation(s4);
r.addStation(s5);
r.lBound = Rotor.FREE_LEFT; %Rotor.FLEXIBLE_LEFT
r.rBound = Rotor.FREE_RIGHT; %Rotor.FLEXIBLE_RIGHT
```

```
%Critical speed
%================================
% cs1 = r.getCriticalSpeed();
% disp(cs1); %rad/s
% cs2 = cs1 / (2*pi);
% disp(cs2); %rps

%forced response plot (Unbalance/Aerodynamic)
%====================================
r.getForcedResponsePlot(4);

%---------------------------------
toc;
```

Appendix E Aerodynamic Force and Moore-Greitzer Flowfield Model MATLAB Code

E.1 Compressor.m

The aim of the compressor module is to calculate the x-axis and y-axis total aerodynamic forces (i.e. summation of the turning force and pressure force) due to fouling

```
classdef Compressor < handle
    %Compressor class computes the Moore-Grietzer flowfield parameters
    %   Compressor class computes the Moore-Greitzer flowfield
parameters
    %   for an axial compressor and the aerodynamic forces due to
fouling

    properties

        %compulsory inputs
        %=================
        %compressor pressure rise characteristic definition
        h_parameter; %semi-height of compre. pressure rise charac.
        w_parameter; %semi-width of the compre. pressure rise charac.
        ave_rescaled_flow; %average rescaled flow coefficient
        fouling_parameter; % scaling of the compre. charac. due to
fouling

        %compressor geometry
        num_stages; %number of compressor stages
        blade_chord; %chord length of the compressor blade in metres
        mean_radius; %mean radius of the compressor in metres
        stagger; %stagger angle of the compressor blade in degrees
        blade_height; %height of blade

        %torque characteristics
        t0,t1,t2,t3,t4; %coefficients of compressor stage torque
characteristic

        %compressor rotordynamic parameter
        mass = 0; %compre. rotor mass in kg
        density = 1.2; %density of air in kg/m3

    end

    methods
        function obj = Compressor()
            obj;
```

```
        end

        function s = aspect_ratio(obj)
            %calculates the aspect ratio of the compressor pressure
rise
            %characteristics

            s = obj.h_parameter/obj.w_parameter;
        end

        function lm = inertia_parameter(obj)
            %calculates the inertia parameter for the rotor only

            lm =
(obj.num_stages*obj.blade_chord)/(obj.mean_radius*cosd(obj.stagger));
        end

        function [a,b,r] = nonuniformity(obj)
            %calculates the cartesian components [a along x-axis & b
along
            %y axis) of the flow non-uniformity

            s = obj.aspect_ratio();
            lm = obj.inertia_parameter();
            q = obj.ave_rescaled_flow;
            u = obj.fouling_parameter;

            %steady state solution of the Moore-Greitzer Compression
            %System governing equation

            p3 = 1;
            p2 = 8*q*(q-1);
            p1 = (16*q^2*(q-1)^2) +  ((2/3)*(lm/s))^2;
            p0 = -(u/6)^2;
            p = [p3 p2 p1 p0];
            temp_r = (roots(p)).^(1/2);
            r = temp_r(end);
            theta = asin((4*r*lm)/(u*s));
            a = r*cos(theta);
            b = r*sin(theta);

        end

        function t_sf = turning_force_scaling(obj)
            r = obj.mean_radius;
            s = obj.stagger;
            l = obj.blade_chord;
            lz = l*cosd(s);

            t_sf = (r/lz)^2*cosd(s);
        end

        function [fx, fy] = turning_force(obj)
            %calculates the turning force due to the circumferentially
            %varying velocity disturbance
```

```
            [a, b] = obj.nonuniformity();
            q = obj.ave_rescaled_flow;

            %coefficients of compressor stage torque characteristic
            t11 = obj.t1;
            t22 = obj.t2;
            t33 = obj.t3;

            fc = t11 + 2*t22*q + 3*t33*(q^2 + (a^2+b^2)/4);

            t_sf = obj.turning_force_scaling();
            %disp(t_sf);

            fx = (t_sf*b*fc)/4;
            fy = -(t_sf*a*fc)/4;

        end

        function p_sf = pressure_force_scaling(obj)
            r = obj.mean_radius;
            s = obj.stagger;
            l = obj.blade_chord;
            lz = l*cosd(s);
            h = obj.blade_height;

            p_sf = 2*(r/lz)^2*(l/h)*(cosd(s))^2;
        end

        function [fx, fy] = pressure_force(obj)
            %calculates the pressure force around the rotor due to the
flow
            %non-uniformity

            [a, b] = obj.nonuniformity();
            q = obj.ave_rescaled_flow;

            p_sf = obj.pressure_force_scaling();
            %disp(p_sf);
            w = obj.w_parameter;

            fx = p_sf*w^2*q*a;
            fy = p_sf*w^2*q*b;
        end

        function [fx, fy] = aero_force(obj)
            %calculates the non-dimensional total aerodynamic force
around
            %the rotor due to the flow non-uniformity

            %turning force
            [tx, ty] = obj.turning_force();

            %pressure force
            [px, py] = obj.pressure_force();

            %total aerodynamic force
```

```
            fx = tx + px;
            fy = ty + py;
        end

        function cp = aero_rotor_coupling(obj)
            % represents the aerodynamic-rotordynamic coupling
parameter

           n_st = obj.num_stages;
           den = obj.density;
           r = obj.mean_radius;
           h = obj.blade_height;
           lz = obj.blade_chord*cosd(obj.stagger);
           m = obj.mass;


           cp = (n_st*den*2*pi*r*h*lz)/m;
        end

        function [fx, fy] = dim_aero_force(obj)
            %calculates the partial dimensional total aerodynamic
force
            %around the rotor due to the flow non-uniformity
            %its partial dimen, due to the absence of the rotational
speed
            %term. this form is suitable for the rotordynamic model

            %non-dimensional total aero. force
            [fx, fy] = obj.aero_force();

            %aero-rotordynamic coupling
            cp = obj.aero_rotor_coupling();

            %partial dimensional total aerodynamic force
            fx = cp*fx*obj.mass*obj.blade_chord;
            fy = cp*fy*obj.mass*obj.blade_chord;
        end

        function [fx, fy] = dim_aero_force_sp(obj, rot_speed)
            %calculates the full dimensional total aerodynamic force
around
            %the rotor due to the flow non-uniformity

            %non-dimensional total aero. force
            [fx, fy] = obj.aero_force();

            %aero-rotordynamic coupling
            cp = obj.aero_rotor_coupling();

            %full dimensional total aerodynamic force
            fx = cp*fx*obj.mass*obj.blade_chord*rot_speed^2;
            fy = cp*fy*obj.mass*obj.blade_chord*rot_speed^2;
        end
    end

end
```

E.2 LM2500.m (Forced Response Analysis Script)

In this script, the rotordynamic model (RotorMatch Code) and aerodynamic model (Compressor.m) has been integrated to determine the response of a fictional LM2500+ engine.

Dependencies: needs all RotorMatch Code and Compressor.m to run

```
clear all;

tic;
% AERODYNAMICS
%=============
%INPUT
%=========================
%compressor characteristic
h = 9.96;
w = 0.0188;

%compressor geometry
num_stages = 17;
blade_chord = 0.0452;
mean_radius = 0.372;
stagger = 43;
blade_height = 0.1775;

%stage torque characteristic
t0 = 0.4472;
t1 = -0.8254;
t2 = 1.9392;
t3 = -0.8774;

%fouling parameters
f1 = 0.0299;
f2 = 0.0597;
f3 = 0.0896;
f4 = 0.1194;
f5 = 0.1493;

%compressor rotordyn. parameters
mass = 566.67; % compre rotor mass in kg

%-------------------------
comp1 = Compressor();

comp1.h_parameter = h;
comp1.w_parameter = w;

comp1.num_stages = num_stages;
```

```
comp1.blade_chord = blade_chord;
comp1.mean_radius = mean_radius;
comp1.stagger = stagger;
comp1.blade_height = blade_height;

comp1.t0 = t0;
comp1.t1 = t1;
comp1.t2 = t2;
comp1.t3 = t3;

comp1.mass = mass;
comp1.fouling_parameter = f5;
comp1.ave_rescaled_flow = 1.0; % variable Q = 1 - 1.6

%=========================

% ROTORDYNAMICS
%==============

f1 = Field();
f1.len = 0;
f1.dia = 1;
f1.eMod = 1;

p1 = Point();
p1.mass = 0;
p1.kxx = 0.2316e8; % bearing stiffness in N/m
p1.kyy = 0.2316e8;
p1.cxx = 0.0089e8; % bearing damping in Ns/m
p1.cyy = 0.0089e8;

s1 = Station(f1,p1);

f2 = Field();
f2.len = 1.3118;
f2.dia = 0.045;
f2.eMod = 2.1e11;

p2 = Point();
p2.mass = mass;
p2.diaInertia = 19.61;
p2.polarInertia = 39.21;
[p2.aerox, p2.aeroy]  = comp1.dim_aero_force();

s2 = Station(f2,p2);

f3 = Field();
f3.len = 1.3118;
f3.dia = 0.045;
f3.eMod = 2.1e11;

p3 = Point();
p3.mass = 0;
p3.kxx = 0.2316e8; % bearing stiffness in N/m
p3.kyy = 0.2316e8;
p3.cxx = 0.0089e8; % bearing damping in Ns/m
```

```
p3.cyy = 0.0089e8;

s3 = Station(f3,p3);

r = Rotor();
r.addStation(s1);
r.addStation(s2);
r.addStation(s3);
r.lBound = Rotor.FLEXIBLE_LEFT;
r.rBound = Rotor.FLEXIBLE_RIGHT;

critSpeed = r.getCriticalSpeed();
fprintf('The critical speed in rad/s: %f \n',critSpeed);
fprintf('The critical speed in rps: %f \n\n',critSpeed/(2*pi));

%forced response plot (Unbalance/Aerodynamic)
%====================================
r.getForcedResponsePlot(4);

%---------------------------------
toc;
```

Other Analysis (Aerodynamic Flow Field & Force Simulation Scripts)

Flow Field Scripts

E.3 Resultant Amplitude 'A' of Disturbed Flow Coefficient (AeroSim_nonuniformity_r_all.m)

Dependencies: needs Compressor.m to run

```
clear all;

%INPUT
%=========================
%compressor characteristic
h = 9.96;
w = 0.0188;

%compressor geometry
num_stages = 17;
blade_chord = 0.0452;
mean_radius = 0.372;
stagger = 43;

%fouling parameters
f1 = 0.0299;
f2 = 0.0597;
f3 = 0.0896;
f4 = 0.1194;
f5 = 0.1493;
```

```
%=========================

comp1 = Compressor();

comp1.h_parameter = h;
comp1.w_parameter = w;

comp1.num_stages = num_stages;
comp1.blade_chord = blade_chord;
comp1.mean_radius = mean_radius;
comp1.stagger = stagger;

comp1.fouling_parameter = f1;

q = 1:0.005:1.6;
r1 = zeros(1,length(q));
for k = 1:length(q)
    comp1.ave_rescaled_flow = q(k);
    [a,b,r] = comp1.nonuniformity();
    r1(k) = r;
end

hold on;
plot(q,r1,'k');

comp2 = Compressor();

comp2.h_parameter = h;
comp2.w_parameter = w;

comp2.num_stages = num_stages;
comp2.blade_chord = blade_chord;
comp2.mean_radius = mean_radius;
comp2.stagger = stagger;

comp2.fouling_parameter = f2;

r2 = zeros(1,length(q));
for k = 1:length(q)
    comp2.ave_rescaled_flow = q(k);
    [a,b,r] = comp2.nonuniformity();
    r2(k) = r;
end

plot(q,r2,'g');

comp3 = Compressor();

comp3.h_parameter = h;
comp3.w_parameter = w;

comp3.num_stages = num_stages;
comp3.blade_chord = blade_chord;
comp3.mean_radius = mean_radius;
comp3.stagger = stagger;
```

```
comp3.fouling_parameter = f3;

r3 = zeros(1,length(q));
for k = 1:length(q)
    comp3.ave_rescaled_flow = q(k);
    [a,b,r] = comp3.nonuniformity();
    r3(k) = r;
end

plot(q,r3,'b');


comp4 = Compressor();

comp4.h_parameter = h;
comp4.w_parameter = w;

comp4.num_stages = num_stages;
comp4.blade_chord = blade_chord;
comp4.mean_radius = mean_radius;
comp4.stagger = stagger;

comp4.fouling_parameter = f4;

r4 = zeros(1,length(q));
for k = 1:length(q)
    comp4.ave_rescaled_flow = q(k);
    [a,b,r] = comp4.nonuniformity();
    r4(k) = r;
end

plot(q,r4,'c');


comp5 = Compressor();

comp5.h_parameter = h;
comp5.w_parameter = w;

comp5.num_stages = num_stages;
comp5.blade_chord = blade_chord;
comp5.mean_radius = mean_radius;
comp5.stagger = stagger;

comp5.fouling_parameter = f5;

r5 = zeros(1,length(q));
for k = 1:length(q)
    comp5.ave_rescaled_flow = q(k);
    [a,b,r] = comp5.nonuniformity();
    r5(k) = r;
end

plot(q,r5,'m');
axis([0.99 1.6 0 0.35]);
xlabel('\bf Q :\rm rescaled flow coefficient');
```

```
ylabel('\bf A :\rm resultant amplitude of disturbed flow
coefficient');
legend('Case 1','Case 2','Case 3','Case 4','Case 5');
```

E.4 'a' Amplitude of Disturbed Flow Coefficient (AeroSim_nonuniformity_a_all.m)

Dependencies: needs Compressor.m to run

```
clear all;

%INPUT
%=========================
%compressor characteristic
h = 9.96;
w = 0.0188;

%compressor geometry
num_stages = 17;
blade_chord = 0.0452;
mean_radius = 0.372;
stagger = 43;

%fouling parameters
f1 = 0.0299;
f2 = 0.0597;
f3 = 0.0896;
f4 = 0.1194;
f5 = 0.1493;

%=========================

comp1 = Compressor();

comp1.h_parameter = h;
comp1.w_parameter = w;

comp1.num_stages = num_stages;
comp1.blade_chord = blade_chord;
comp1.mean_radius = mean_radius;
comp1.stagger = stagger;

comp1.fouling_parameter = f1;

q = 1:0.0005:1.6;
a1 = zeros(1,length(q));


for k = 1:length(q)
    comp1.ave_rescaled_flow = q(k);
    [a,b,r] = comp1.nonuniformity();
    a1(k) = a;
end
```

```
hold on;
plot(q,a1,'k');

comp2 = Compressor();

comp2.h_parameter = h;
comp2.w_parameter = w;

comp2.num_stages = num_stages;
comp2.blade_chord = blade_chord;
comp2.mean_radius = mean_radius;
comp2.stagger = stagger;

comp2.fouling_parameter = f2;

a2 = zeros(1,length(q));
for k = 1:length(q)
    comp2.ave_rescaled_flow = q(k);
    [a,b,r] = comp2.nonuniformity();
    a2(k) = a;
end

plot(q,a2,'g');

comp3 = Compressor();

comp3.h_parameter = h;
comp3.w_parameter = w;

comp3.num_stages = num_stages;
comp3.blade_chord = blade_chord;
comp3.mean_radius = mean_radius;
comp3.stagger = stagger;

comp3.fouling_parameter = f3;

a3 = zeros(1,length(q));
for k = 1:length(q)
    comp3.ave_rescaled_flow = q(k);
    [a,b,r] = comp3.nonuniformity();
    a3(k) = a;
end

plot(q,a3,'b');


comp4 = Compressor();

comp4.h_parameter = h;
comp4.w_parameter = w;

comp4.num_stages = num_stages;
comp4.blade_chord = blade_chord;
comp4.mean_radius = mean_radius;
comp4.stagger = stagger;
```

```
comp4.fouling_parameter = f4;

a4 = zeros(1,length(q));
for k = 1:length(q)
    comp4.ave_rescaled_flow = q(k);
    [a,b,r] = comp4.nonuniformity();
    a4(k) = a;
end

plot(q,a4,'c');


comp5 = Compressor();

comp5.h_parameter = h;
comp5.w_parameter = w;

comp5.num_stages = num_stages;
comp5.blade_chord = blade_chord;
comp5.mean_radius = mean_radius;
comp5.stagger = stagger;

comp5.fouling_parameter = f5;

a5 = zeros(1,length(q));
for k = 1:length(q)
    comp5.ave_rescaled_flow = q(k);
    [a,b,r] = comp5.nonuniformity();
    a5(k) = a;
end

plot(q,a5,'m');
axis([0.99 1.6 0 0.35]);
xlabel('\bf Q :\rm rescaled flow coefficient');
ylabel('\bf a\rm - amplitude of disturbed flow coefficient');
legend('Case 1','Case 2','Case 3','Case 4','Case 5');
```

E.5 'b' Amplitude of Disturbed Flow Coefficient (AeroSim_nonuniformity_b_all.m)

Dependencies: needs Compressor.m to run

```
clear all;

%INPUT
%=========================
%compressor characteristic
h = 9.96;
w = 0.0188;
```

```
%compressor geometry
num_stages = 17;
blade_chord = 0.0452;
mean_radius = 0.372;
stagger = 43;

%fouling parameters
f1 = 0.0299;
f2 = 0.0597;
f3 = 0.0896;
f4 = 0.1194;
f5 = 0.1493;

%=========================

comp1 = Compressor();

comp1.h_parameter = h;
comp1.w_parameter = w;

comp1.num_stages = num_stages;
comp1.blade_chord = blade_chord;
comp1.mean_radius = mean_radius;
comp1.stagger = stagger;

comp1.fouling_parameter = f1;

q = 1:0.0005:1.6;
b1 = zeros(1,length(q));


for k = 1:length(q)
    comp1.ave_rescaled_flow = q(k);
    [a,b,r] = comp1.nonuniformity();
    b1(k) = b;
end

hold on;
plot(q,b1,'k');

comp2 = Compressor();

comp2.h_parameter = h;
comp2.w_parameter = w;

comp2.num_stages = num_stages;
comp2.blade_chord = blade_chord;
comp2.mean_radius = mean_radius;
comp2.stagger = stagger;

comp2.fouling_parameter = f2;

b2 = zeros(1,length(q));
for k = 1:length(q)
    comp2.ave_rescaled_flow = q(k);
```

```
    [a,b,r] = comp2.nonuniformity();
    b2(k) = b;
end

plot(q,b2,'g');

comp3 = Compressor();

comp3.h_parameter = h;
comp3.w_parameter = w;

comp3.num_stages = num_stages;
comp3.blade_chord = blade_chord;
comp3.mean_radius = mean_radius;
comp3.stagger = stagger;

comp3.fouling_parameter = f3;

b3 = zeros(1,length(q));
for k = 1:length(q)
    comp3.ave_rescaled_flow = q(k);
    [a,b,r] = comp3.nonuniformity();
    b3(k) = b;
end

plot(q,b3,'b');


comp4 = Compressor();

comp4.h_parameter = h;
comp4.w_parameter = w;

comp4.num_stages = num_stages;
comp4.blade_chord = blade_chord;
comp4.mean_radius = mean_radius;
comp4.stagger = stagger;

comp4.fouling_parameter = f4;

b4 = zeros(1,length(q));
for k = 1:length(q)
    comp4.ave_rescaled_flow = q(k);
    [a,b,r] = comp4.nonuniformity();
    b4(k) = b;
end

plot(q,b4,'c');


comp5 = Compressor();

comp5.h_parameter = h;
comp5.w_parameter = w;
```

```
comp5.num_stages = num_stages;
comp5.blade_chord = blade_chord;
comp5.mean_radius = mean_radius;
comp5.stagger = stagger;

comp5.fouling_parameter = f5;

b5 = zeros(1,length(q));
for k = 1:length(q)
    comp5.ave_rescaled_flow = q(k);
    [a,b,r] = comp5.nonuniformity();
    b5(k) = b;
end

plot(q,b5,'m');
axis([0.99 1.6 0 0.022]);
xlabel('\bf Q :\rm rescaled flow coefficient');
ylabel('\bf b\rm - amplitude of disturbed flow coefficient');
legend('Case 1','Case 2','Case 3','Case 4','Case 5');
```

Aerodynamic Force Scripts

Turning and pressure aerodynamic force prediction script for the LM2500+ engine due to the different cases of fouling considered in this research.

E.6 Aero_turning_force.m

Dependencies: needs Compressor.m to run

```
clear all;

%INPUT
%=========================
%compressor characteristic
h = 9.96;
w = 0.0188;

%compressor geometry
num_stages = 17;
blade_chord = 0.0452;
mean_radius = 0.372;
stagger = 43;
blade_height = 0.1775;

%stage torque characteristic
t0 = 0.4472;
t1 = -0.8254;
t2 = 1.9392;
t3 = -0.8774;
```

```
%fouling parameters
f1 = 0.0299;
f2 = 0.0597;
f3 = 0.0896;
f4 = 0.1194;
f5 = 0.1493;

%=========================

comp1 = Compressor();

comp1.h_parameter = h;
comp1.w_parameter = w;

comp1.num_stages = num_stages;
comp1.blade_chord = blade_chord;
comp1.mean_radius = mean_radius;
comp1.stagger = stagger;
comp1.blade_height = blade_height;

comp1.t0 = t0;
comp1.t1 = t1;
comp1.t2 = t2;
comp1.t3 = t3;

comp1.fouling_parameter = f1;


q = 1:0.0005:1.6;
px1 = zeros(1,length(q));
py1 = zeros(1,length(q));
for k = 1:length(q)
    comp1.ave_rescaled_flow = q(k);
    [fx,fy] = comp1.turning_force();
    px1(k) = fx;
    py1(k) = fy;
end

%-------------------------------------

comp2 = Compressor();

comp2.h_parameter = h;
comp2.w_parameter = w;

comp2.num_stages = num_stages;
comp2.blade_chord = blade_chord;
comp2.mean_radius = mean_radius;
comp2.stagger = stagger;
comp2.blade_height = blade_height;

comp2.t0 = t0;
comp2.t1 = t1;
comp2.t2 = t2;
comp2.t3 = t3;
```

```
comp2.fouling_parameter = f2;

px2 = zeros(1,length(q));
py2 = zeros(1,length(q));
for k = 1:length(q)
    comp2.ave_rescaled_flow = q(k);
    [fx,fy] = comp2.turning_force();
    px2(k) = fx;
    py2(k) = fy;
end


%-------------------------------------

comp3 = Compressor();

comp3.h_parameter = h;
comp3.w_parameter = w;

comp3.num_stages = num_stages;
comp3.blade_chord = blade_chord;
comp3.mean_radius = mean_radius;
comp3.stagger = stagger;
comp3.blade_height = blade_height;

comp3.t0 = t0;
comp3.t1 = t1;
comp3.t2 = t2;
comp3.t3 = t3;

comp3.fouling_parameter = f3;

px3 = zeros(1,length(q));
py3 = zeros(1,length(q));
for k = 1:length(q)
    comp3.ave_rescaled_flow = q(k);
    [fx,fy] = comp3.turning_force();
    px3(k) = fx;
    py3(k) = fy;
end

%-------------------------------------

comp4 = Compressor();

comp4.h_parameter = h;
comp4.w_parameter = w;

comp4.num_stages = num_stages;
comp4.blade_chord = blade_chord;
comp4.mean_radius = mean_radius;
comp4.stagger = stagger;
comp4.blade_height = blade_height;

comp4.t0 = t0;
comp4.t1 = t1;
```

```
comp4.t2 = t2;
comp4.t3 = t3;

comp4.fouling_parameter = f4;

px4 = zeros(1,length(q));
py4 = zeros(1,length(q));
for k = 1:length(q)
    comp4.ave_rescaled_flow = q(k);
    [fx,fy] = comp4.turning_force();
    px4(k) = fx;
    py4(k) = fy;
end

%-------------------------------------

comp5 = Compressor();

comp5.h_parameter = h;
comp5.w_parameter = w;

comp5.num_stages = num_stages;
comp5.blade_chord = blade_chord;
comp5.mean_radius = mean_radius;
comp5.stagger = stagger;
comp5.blade_height = blade_height;

comp5.t0 = t0;
comp5.t1 = t1;
comp5.t2 = t2;
comp5.t3 = t3;

comp5.fouling_parameter = f5;

px5 = zeros(1,length(q));
py5 = zeros(1,length(q));
for k = 1:length(q)
    comp5.ave_rescaled_flow = q(k);
    [fx,fy] = comp5.turning_force();
    px5(k) = fx;
    py5(k) = fy;
end

%-------------------------------------

figure(1);
plot(q,px1,'k',q,px2,'g',q,px3,'b',q,px4,'c',q,px5,'m');
% axis([0.4 1.6 0 0.25]);
xlabel('\bf Q :\rm rescaled flow coefficient');
ylabel('\bf Ftx :\rm Non-dimensional turning force along x-axis');
legend('Case 1','Case 2','Case 3','Case 4','Case 5');

figure(2);
plot(q,py1,'k',q,py2,'g',q,py3,'b',q,py4,'c',q,py5,'m');
% axis([0.4 1.6 0 0.25]);
xlabel('\bf Q :\rm rescaled flow coefficient');
```

```
ylabel('\bf Fty :\rm Non-dimensional turning force along y-axis');
legend('Case 1','Case 2','Case 3','Case 4','Case 5');
```

E.7 Aero_pre_force.m

Dependencies: needs Compressor.m to run

```
clear all;

%INPUT
%=========================
%compressor characteristic
h = 9.96;
w = 0.0188;

%compressor geometry
num_stages = 17;
blade_chord = 0.0452;
mean_radius = 0.372;
stagger = 43;
blade_height = 0.1775;

%fouling parameters
f1 = 0.0299;
f2 = 0.0597;
f3 = 0.0896;
f4 = 0.1194;
f5 = 0.1493;

%=========================

comp1 = Compressor();

comp1.h_parameter = h;
comp1.w_parameter = w;

comp1.num_stages = num_stages;
comp1.blade_chord = blade_chord;
comp1.mean_radius = mean_radius;
comp1.stagger = stagger;
comp1.blade_height = blade_height;

comp1.fouling_parameter = f1;


q = 1:0.0005:1.6;
px1 = zeros(1,length(q));
py1 = zeros(1,length(q));
for k = 1:length(q)
    comp1.ave_rescaled_flow = q(k);
```

```
    [fx,fy] = comp1.pressure_force();
    px1(k) = fx;
    py1(k) = fy;
end

%-------------------------------------

comp2 = Compressor();

comp2.h_parameter = h;
comp2.w_parameter = w;

comp2.num_stages = num_stages;
comp2.blade_chord = blade_chord;
comp2.mean_radius = mean_radius;
comp2.stagger = stagger;
comp2.blade_height = blade_height;

comp2.fouling_parameter = f2;

px2 = zeros(1,length(q));
py2 = zeros(1,length(q));
for k = 1:length(q)
    comp2.ave_rescaled_flow = q(k);
    [fx,fy] = comp2.pressure_force();
    px2(k) = fx;
    py2(k) = fy;
end


%-------------------------------------

comp3 = Compressor();

comp3.h_parameter = h;
comp3.w_parameter = w;

comp3.num_stages = num_stages;
comp3.blade_chord = blade_chord;
comp3.mean_radius = mean_radius;
comp3.stagger = stagger;
comp3.blade_height = blade_height;

comp3.fouling_parameter = f3;

px3 = zeros(1,length(q));
py3 = zeros(1,length(q));
for k = 1:length(q)
    comp3.ave_rescaled_flow = q(k);
    [fx,fy] = comp3.pressure_force();
    px3(k) = fx;
    py3(k) = fy;
end

%-------------------------------------
```

```
comp4 = Compressor();

comp4.h_parameter = h;
comp4.w_parameter = w;

comp4.num_stages = num_stages;
comp4.blade_chord = blade_chord;
comp4.mean_radius = mean_radius;
comp4.stagger = stagger;
comp4.blade_height = blade_height;

comp4.fouling_parameter = f4;

px4 = zeros(1,length(q));
py4 = zeros(1,length(q));
for k = 1:length(q)
    comp4.ave_rescaled_flow = q(k);
    [fx,fy] = comp4.pressure_force();
    px4(k) = fx;
    py4(k) = fy;
end

%-------------------------------------

comp5 = Compressor();

comp5.h_parameter = h;
comp5.w_parameter = w;

comp5.num_stages = num_stages;
comp5.blade_chord = blade_chord;
comp5.mean_radius = mean_radius;
comp5.stagger = stagger;
comp5.blade_height = blade_height;

comp5.fouling_parameter = f5;

px5 = zeros(1,length(q));
py5 = zeros(1,length(q));
for k = 1:length(q)
    comp5.ave_rescaled_flow = q(k);
    [fx,fy] = comp5.pressure_force();
    px5(k) = fx;
    py5(k) = fy;
end

%-------------------------------------

figure(1);
plot(q,px1,'k',q,px2,'g',q,px3,'b',q,px4,'c',q,px5,'m');
axis([0.99 1.6 0 0.004]);
xlabel('\bf Q :\rm rescaled flow coefficient');
ylabel('\bf Fpx :\rm Non-dimensional pressure force along the x-
axis');
legend('Case 1','Case 2','Case 3','Case 4','Case 5');
```

```
figure(2);
plot(q,py1,'k',q,py2,'g',q,py3,'b',q,py4,'c',q,py5,'m');
xlabel('\bf Q :\rm rescaled flow coefficient');
ylabel('\bf Fpy :\rm Non-dimensional pressure force along the y-
axis');
legend('Case 1','Case 2','Case 3','Case 4','Case 5');
```

E.8 Al-Nahwi Compressor (Compressor.m)

```
classdef Compressor < handle
    %Compressor class computes the Moore-Grietzer flowfield
parameters.
    %   Compressor class computes the Moore-Greitzer flowfield
parameters
    %   for an axial compressor

    properties

        %compulsory inputs
        %=================
        %compressor pressure rise characteristic definition
        h_parameter; %semi-height of compre. pressure rise charac.
        w_parameter; %semi-width of the compre. pressure rise charac.
        ave_rescaled_flow; %average rescaled flow coefficient
        fouling_parameter; % scaling of the compre. charac. due to
fouling

        %compressor geometry
        num_stages; %number of compressor stages
        blade_chord; %chord length of the compressor blade in metres
        mean_radius; %mean radius of the compressor in metres
        stagger; %stagger angle of the compressor blade in degrees
        blade_height; %height of blade

        %torque characteristics
        t0,t1,t2,t3,t4; %coefficients of compressor stage torque
characteristic
    end

    methods
        function obj = Compressor()
            obj;
        end

        function s = aspect_ratio(obj)
            %calculates the aspect ratio of the compressor pressure
rise
            %characteristics

            s = obj.h_parameter/obj.w_parameter;
        end

        function lm = inertia_parameter(obj)
            %calculates the inertia parameter for the rotor only
```

```
            lm =
(obj.num_stages*obj.blade_chord)/(obj.mean_radius*cosd(obj.stagger));
        end

        function [a,b,r] = nonuniformity(obj)
            %calculates the cartesian components [a along x-axis & b
along
            %y axis) of the flow non-uniformity

            s = obj.aspect_ratio();
            lm = obj.inertia_parameter();
            q = obj.ave_rescaled_flow;
            u = obj.fouling_parameter;

            %steady state solution of the Moore-Greitzer Compression
            %System governing equation

            p3 = 1;
            p2 = 8*q*(q-1);
            p1 = (16*q^2*(q-1)^2) +  ((2/3)*(lm/s))^2;
            p0 = -(u/3)^2;
            p = [p3 p2 p1 p0];
            temp_r = (roots(p)).^(1/2);
            r = temp_r(end);
            theta = asin((2*r*lm)/(u*s));
            a = r*cos(theta);
            b = r*sin(theta);

        end

        function c_tf = turning_force_coupling(obj)
            r = obj.mean_radius;
            s = obj.stagger;
            l = obj.blade_chord;
            lz = l*cosd(s);

            c_tf = (r/lz)^2*cosd(s);
        end

        function [fx, fy] = turning_force(obj)
            %calculates the turning force due to the circumferentially
            %varying velocity disturbance

            [a, b] = obj.nonuniformity();
            q = obj.ave_rescaled_flow;

            %coefficients of compressor stage torque characteristic
            t11 = obj.t1;
            t22 = obj.t2;
            t33 = obj.t3;

            fc = t11 + 2*t22*q + 3*t33*(q^2 + (a^2+b^2)/4);

            c_tf = obj.turning_force_coupling(); %aero-rotor. coupling
turning scale factor
```

```
            %disp(c_tf);

            fx = (c_tf*b*fc)/4;
            fy = -(c_tf*a*fc)/4;

        end

        function c_pf = pressure_force_coupling(obj)
            r = obj.mean_radius;
            s = obj.stagger;
            l = obj.blade_chord;
            lz = l*cosd(s);
            h = obj.blade_height;

            c_pf = 2*(r/lz)^2*(l/h)*(cosd(s))^2;
        end

        function [fx, fy] = pressure_force(obj)
            %calculates the pressure force around the rotor due to the
flow
            %non-uniformity

            [a, b] = obj.nonuniformity();
            q = obj.ave_rescaled_flow;

            c_pf = obj.pressure_force_coupling(); %aero-rotor.
coupling pressure scale factor
            %disp(c_pf);
            w = obj.w_parameter;

            fx = c_pf*w^2*q*a;
            fy = c_pf*w^2*q*b;
        end
    end

end
```

E.9 Al-Nahwi Aerodynamic Force Plot (AeroSim_force_all.m)

```
clear all;

%INPUT
%=========================
%compressor characteristic
h = 0.27;
w = 0.25;

%compressor geometry
num_stages = 3;
```

```
blade_chord = 0.0452;
mean_radius = 0.286;
stagger = 43;
blade_height = 0.0366;

%stage torque characteristic
t0 = 0.4472;
t1 = -0.8254;
t2 = 1.9392;
t3 = -0.8774;

%fouling parameters
f1 = 0.1482; %14.82 x 0.01
%=========================

comp1 = Compressor();

comp1.h_parameter = h;
comp1.w_parameter = w;

comp1.num_stages = num_stages;
comp1.blade_chord = blade_chord;
comp1.mean_radius = mean_radius;
comp1.stagger = stagger;
comp1.blade_height = blade_height;

comp1.t0 = t0;
comp1.t1 = t1;
comp1.t2 = t2;
comp1.t3 = t3;

comp1.fouling_parameter = f1;


q = -0.4:0.001:1.6;

%x-component aero. force
px = zeros(1,length(q));
ptx = zeros(1,length(q));
ppx = zeros(1,length(q));

%y-component aero. force
py = zeros(1,length(q));
pty = zeros(1,length(q));
ppy = zeros(1,length(q));

%total aero. force
p = zeros(1,length(q));
pt = zeros(1,length(q));
pp = zeros(1,length(q));

for k = 1:length(q)
    comp1.ave_rescaled_flow = q(k);
    [tfx,tfy] = comp1.turning_force();
    [pfx,pfy] = comp1.pressure_force();
```

```
    %x-component aero. force
    ptx(k) = tfx;
    ppx(k) = pfx;
    px(k) = tfx + pfx;

    %y-component aero. force
    pty(k) = tfy;
    ppy(k) = pfy;
    py(k) = tfy + pfy;

    %total aero. force
    pt(k) = (tfx^2 + tfy^2)^0.5;
    pp(k) = (pfx^2 + pfy^2)^0.5;
    p(k) = pt(k) + pp(k);
end

%-------------------------------------

%total aerodynamic force
figure(1);
plot(q,pt,'r',q,pp,'b',q,p,'k');
axis([-0.4 1.6 -2 4]);
xlabel('\bf Q :\rm rescaled flow coefficient');
ylabel('Force amplitudes, (F)_i');
legend('turning','pressure','sum');

%x-component aerodynamic force
figure(2);
plot(q,ptx,'r',q,ppx,'b',q,px,'k');
axis([-0.4 1.6 -2 4]);
xlabel('\bf Q :\rm rescaled flow coefficient');
ylabel('X force components, (Fx)_j');
legend('turning','pressure','sum');

%y-component aerodynamic force
figure(3);
plot(q,pty,'r',q,ppy,'b',q,py,'k');
axis([-0.4 1.6 -2 4]);
xlabel('\bf Q :\rm rescaled flow coefficient');
ylabel('Y force components, (Fy)_j');
legend('turning','pressure','sum');
```

Appendix F TurboMatch LM2500+ Input Files

F.1 Design Point Input File

```
TITLE: Design Point Performance Simulation For LM2500 PLUS
       TURBOMATCH Input File

AUTHOR:Jombo Gbanaibolou
==================================================
////

DP SI GM VA FP
-1
-1
INTAKE  S1,2       D1-6              R200
COMPRE  S2,3       D7-18             R205     V7 V8
PREMAS  S3,10,4    D19-22
BURNER  S4,5       D23-30            R215
MIXEES  S5,10,6
TURBIN  S6,7       D31-45                     V32
TURBIN  S7,8       D46-60                     V46 V47
NOZCON  S8,9,1     D61-62             R220
PLOTBD             D50,57
PERFOR  S1,0,0     D46,64-66,220,200,215,0,0,0,0
CODEND

DATA ITEMS ////
1 0.0              ! INTAKE: Altitude [m]
2 0.0              ! Deviation from ISA temperature [K]
3 0.0              ! Mach number
4 0.995            ! Pressure recovery, according to USAF
5 0.0              ! Deviation from ISA pressure [atm]
6 60.0             ! Relative humidity [%]

7 -1.0             ! COMPRESSOR I: Z = (R-R[choke])/(R[surge]-
R[choke])
8 1.0              ! Relative rotational speed PCN
9 23.1             ! DP Pressure ratio
10 0.84            ! DP ETA
11 0.0             ! Error selection
12 3.0             ! Compressor map number
13 1.0             ! Shaft number
14 1.0             ! PR degradation scaling factor
15 1.0             ! NDMF degradation scaling factor
16 1.0             ! ETA degradation scaling factor
17 0.0            ! Effective component volume [m^3] (only for
transient)
18 0.0             ! Stator angle (VSV) relative to DP

19 0.01            ! PREMAS: LAMDA W Cooling bypass (Wout1/Win)
```

```
20 0.0              ! DELTA W
21 1.0              ! LAMBDA P
22 0.0              ! DELTA P

23 0.05             ! COMBUSTOR: Pressure loss (=DP/P inlet
total)
24 0.998            ! Combustion efficiency
25 -1.0             ! Fuel flow (if -1.0, TET must be defined)
26 0.0              ! (>0) Water flow [kg s-1 or lb s-1] or (<0)
WAR
27 288              ! Temperature of water stream [K]
28 0.0              ! Phase of water (0=liquid, 1=vapour)
29 1.0              ! ETA degradation scaling factor
30 -1.0             ! Effective component volume [m^3] (only for
transient)

31 0.0              ! COMPRESSOR TURBINE: Auxiliary or power
output [W]
32 0.80             ! Relative to max enthalpy drop to
temperature ratio:ZT
33 0.6              ! Relative non-dim speed CN
34 0.87             ! DP ETA
35 -1.0             ! Relative non-dim PCN (= -1 for compressor
turbine)
36 1.0              ! Shaft Number (for power turbine, the value
0 is used)
37 4.0              ! Turbine map number
38 -1.0             ! Power law index "n" (POWER = PCN^n)
39 1.0              ! TF degradation scaling factor
40 1.0              ! DH degradation scaling factor
41 1.0              ! ETA degradation scaling factor
42 0.0              ! Rotor rotational speed [RPS] (only for
transient)
43 0.0              ! Rotor moment of inertia [kg.m^2] (only for
transient)
44 0.0              ! Effective component volume [m^3] (only for
transient)
45 0.0              ! NGV angle, relative to D.P.

46 29500000.00      ! FPT TURBINE: Auxiliary or power output [W]
47 0.8              ! Relative to max enthalpy drop to
temperature ratio:ZT
48 0.6              ! Relative non-dim speed CN
49 0.87             ! DP ETA
50 1.0              ! Relative non-dim PCN (= -1 for compressor
turbine)
51 0.0              ! Shaft Number (for power turbine, the value
0 is used)
52 4.0              ! Turbine map number
53 -1.0             ! Power law index "n" (POWER = PCN^n)
54 1.0              ! TF degradation scaling factor
55 1.0              ! DH degradation scaling factor
56 1.0              ! ETA degradation scaling factor
```

```
57 0.0              ! Rotor rotational speed [RPS] (only for
transient)
58 0.0              ! Rotor moment of inertia [kg.m^2] (only for
transient)
59 -1.0              ! Effective component volume [m^3] (only for
transient)
60 0.0              ! NGV angle, relative to D.P.

61 -1.0             ! CONVERGENT NOZZLE: = "-1" exit area is
fixed
62 1.0              ! Scaling factor

63 1.0              ! ENGINE RESULTS: Power output - Power or
Power turbine
64 0.0              ! Propeller efficiency (= -1 for
turbojet/turbofan)
65 0.0              ! Scaling index ("1" = scaling needed, "0" =
no scaling)
66 0.0              ! Required DP shaft power (no scaling is
needed)

-1
1 2 84.10           ! item 2 at station 1 = Mass flow(kg/s)
5 6 1500.0          ! item 6 at station 5 = Total temperature (K)
-1                  ! End of DP data
-3
```

F.2 Off-Design Input File (comparison with LM2500+ datasheet)

```
TITLE: OFF-Design Performance Simulation For LM2500 PLUS
       TURBOMATCH Input File

AUTHOR:Jombo Gbanaibolou
====================================================
////

OD SI GM VA FP
-1
-1
INTAKE  S1,2       D1-6              R200
COMPRE  S2,3       D7-18             R205     V7 V8
PREMAS  S3,10,4    D19-22
BURNER  S4,5       D23-30            R215
MIXEES  S5,10,6
TURBIN  S6,7       D31-45                     V32
TURBIN  S7,8       D46-60                     V46 V47
NOZCON  S8,9,1     D61-62             R220
PLOTBD             D50,57
PERFOR  S1,0,0     D46,64-66,220,200,215,0,0,0,0
```

```
CODEND

DATA ITEMS ////
1 0.0              ! INTAKE: Altitude [m]
2 0.0              ! Deviation from ISA temperature [K]
3 0.0              ! Mach number
4 0.995            ! Pressure recovery, according to USAF
5 0.0              ! Deviation from ISA pressure [atm]
6 60.0             ! Relative humidity [%]

7 -1.0             ! COMPRESSOR I: Z = (R-R[choke])/(R[surge]-
R[choke])
8 1.0              ! Relative rotational speed PCN
9 23.1             ! DP Pressure ratio
10 0.84            ! DP ETA
11 0.0             ! Error selection
12 3.0             ! Compressor map number
13 1.0             ! Shaft number
14 1.0             ! PR degradation scaling factor
15 1.0             ! NDMF degradation scaling factor
16 1.0             ! ETA degradation scaling factor
17 0.0            ! Effective component volume [m^3] (only for
transient)
18 0.0             ! Stator angle (VSV) relative to DP

19 0.01            ! PREMAS: LAMDA W Cooling bypass (Wout1/Win)
20 0.0             ! DELTA W
21 1.0             ! LAMBDA P
22 0.0             ! DELTA P

23 0.05            ! COMBUSTOR: Pressure loss (=DP/P inlet
total)
24 0.998           ! Combustion efficiency
25 -1.0            ! Fuel flow (if -1.0, TET must be defined)
26 0.0             ! (>0) Water flow [kg s-1 or lb s-1] or (<0)
WAR
27 288             ! Temperature of water stream [K]
28 0.0             ! Phase of water (0=liquid, 1=vapour)
29 1.0             ! ETA degradation scaling factor
30 -1.0            ! Effective component volume [m^3] (only for
transient)

31 0.0             ! COMPRESSOR TURBINE: Auxiliary or power
output [W]
32 0.80            ! Relative to max enthalpy drop to
temperature ratio:ZT
33 0.6           ! Relative non-dim speed CN
34 0.87            ! DP ETA
35 -1.0            ! Relative non-dim PCN (= -1 for compressor
turbine)
36 1.0             ! Shaft Number (for power turbine, the value
0 is used)
37 4.0             ! Turbine map number
```

```
38 -1.0            ! Power law index "n" (POWER = PCN^n)
39 1.0             ! TF degradation scaling factor
40 1.0             ! DH degradation scaling factor
41 1.0             ! ETA degradation scaling factor
42 0.0             ! Rotor rotational speed [RPS] (only for
transient)
43 0.0             ! Rotor moment of inertia [kg.m^2] (only for
transient)
44 0.0             ! Effective component volume [m^3] (only for
transient)
45 0.0             ! NGV angle, relative to D.P.

46 29500000.00     ! FPT TURBINE: Auxiliary or power output [W]
47 0.8             ! Relative to max enthalpy drop to
temperature ratio:ZT
48 0.6             ! Relative non-dim speed CN
49 0.87            ! DP ETA
50 1.0             ! Relative non-dim PCN (= -1 for compressor
turbine)
51 0.0             ! Shaft Number (for power turbine, the value
0 is used)
52 4.0             ! Turbine map number
53 -1.0            ! Power law index "n" (POWER = PCN^n)
54 1.0             ! TF degradation scaling factor
55 1.0             ! DH degradation scaling factor
56 1.0             ! ETA degradation scaling factor
57 0.0             ! Rotor rotational speed [RPS] (only for
transient)
58 0.0             ! Rotor moment of inertia [kg.m^2] (only for
transient)
59 -1.0             ! Effective component volume [m^3] (only for
transient)
60 0.0             ! NGV angle, relative to D.P.

61 -1.0            ! CONVERGENT NOZZLE: = "-1" exit area is
fixed
62 1.0             ! Scaling factor

63 1.0             ! ENGINE RESULTS: Power output - Power or
Power turbine
64 0.0             ! Propeller efficiency (= -1 for
turbojet/turbofan)
65 0.0             ! Scaling index ("1" = scaling needed, "0" =
no scaling)
66 0.0             ! Required DP shaft power (no scaling is
needed)

-1
1 2 84.10          ! item 2 at station 1 = Mass flow(kg/s)
5 6 1500.0         ! item 6 at station 5 = Total temperature (K)
-1                 ! End of DP data
2 -30
-1
```

```
-1
2 -20
-1
-1
2 -10
-1
-1
2 0
-1
-1
2 10
-1
-1
2 20
-1
-1

-3
```

Appendix G TJ100 Compression System

G.1 Determination of Compression System Geometry

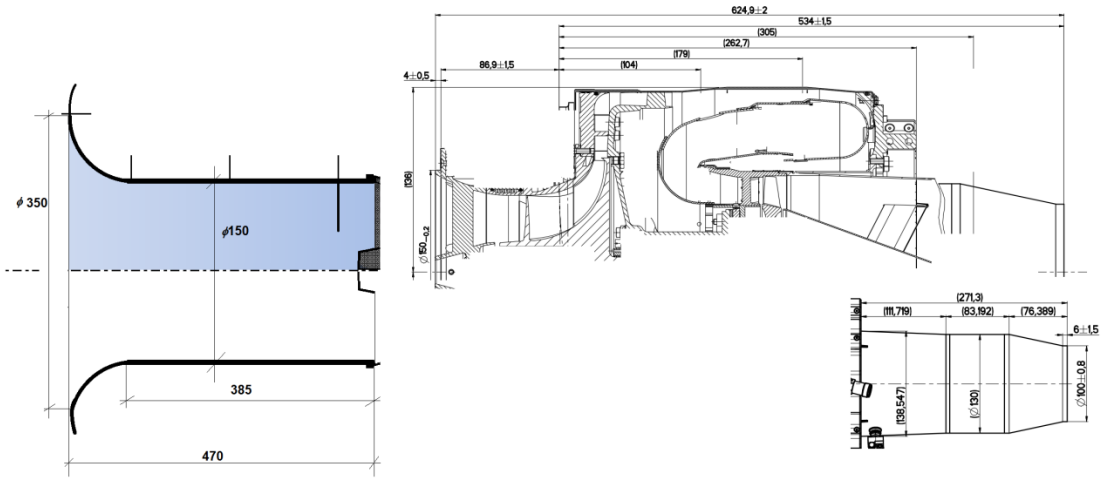

Figure 0-3 Geometric dimensions for TJ00 engine

Centrifugal Compressor Geometry Parameters

1. Impeller inlet tip radius(r_t)

$$\mathrm{r}_t \approx 56.88\ \mathrm{mm} = 0.05688\ \mathrm{m} \qquad \text{G-1}$$

2. Impeller inlet hub radius (r_h)

$$\mathrm{r}_h \approx 22.75\ \mathrm{mm} = 0.02275\ \mathrm{m} \qquad \text{G-2}$$

3. Compressor inlet flow area (A_c)

$$\mathrm{A}_c = \pi(r_t^2 - r_h^2) \qquad \text{G-3}$$

$$\mathrm{A}_c = 3.142 \times (0.05688^2 - 0.02275^2) = 0.008539\, m^2 \qquad \text{G-4}$$

4. Effective length of the compressor and ducts [inlet & outlet duct] (L_c)

$$\mathrm{L}_c = \text{length of inlet duct} + \text{length of compressor} + \text{length of outlet duct}$$

$$\mathrm{L}_c = (470 + 86.9 + 104)\ \text{mm} = 660.9\ \text{mm} \approx 0.66\, m \qquad \text{G-5}$$

5. Impeller Tip Speed

$$\mathrm{U} = \left(\frac{\pi N}{30}\right)\mathrm{r}_t = \left(\frac{3.142 \times 57500}{30}\right) \times 0.05688 \approx 342.54\ m/s \qquad \text{G-6}$$

where N is the rotor speed in revolution per minute and r_t is the impeller tip radius.

Plenum Geometry Parameters

6. Length of Plenum

$$\mathrm{L}_P = 262.7\text{mm} = 0.2627\ \text{m} \qquad \text{G-7}$$

7. Volume of Plenum (V_p)

$$\mathrm{V}_p = \pi \mathrm{L}_p (r_2^2 - r_1^2)$$
$$= 3.142 \times 262.7 \times (136^2 - 75^2) \approx 1.0624e^7\ mm^3 \approx 0.0106\, m^3 \qquad \text{G-8}$$

where L_p is the length of the plenum, r_2 & r_1 are the outer and inner radius of the combustor when approximated as a cylindrical annulus.

8. Helmholtz Frequency (ω_h)

$$\omega_h = \mathrm{a}\sqrt{\frac{A_c}{V_p L_c}} \qquad \text{G-9}$$

where a is the speed of sound, A_c is the compressor flow through area, V_p is the plenum volume and L_c is the effective compressor length

$$\omega_h = 340.27\sqrt{\frac{0.008539}{0.0106 \times 0.66}} \approx 375.926\ rad/s\ \approx 59.82\ Hz \quad \text{G-10}$$

Throttle Geometry Parameters

9. Throttle outlet flow area A_T

$$\mathrm{A}_T = \frac{\pi d^2}{4} \quad \text{G-11}$$

Where d is diameter of the nozzle outlet flow area.

$$\mathrm{A}_T = \frac{3.142 \times 130^2}{4} mm^2 = 13274.95\ mm^2 \approx 0.0133\ m^2 \quad \text{G-12}$$

10. Length of the throttle duct (L_T)

$$\mathrm{L}_T = 370\ \mathrm{mm} = 0.37\ \mathrm{m} \quad \text{G-13}$$

G.2 TJ100 Generalized Compressor Pressure Rise Characteristic (Baseline and Fouled)

1. Baseline Engine

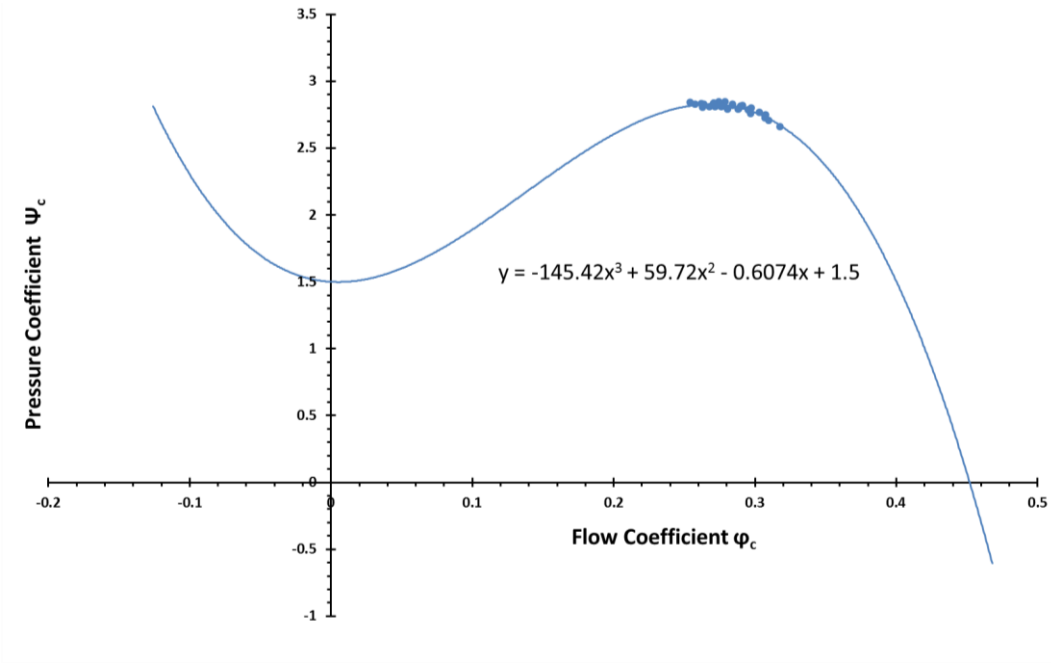

Figure 0-4 Baseline compressor pressure rise characteristic

2. Fouled Engine

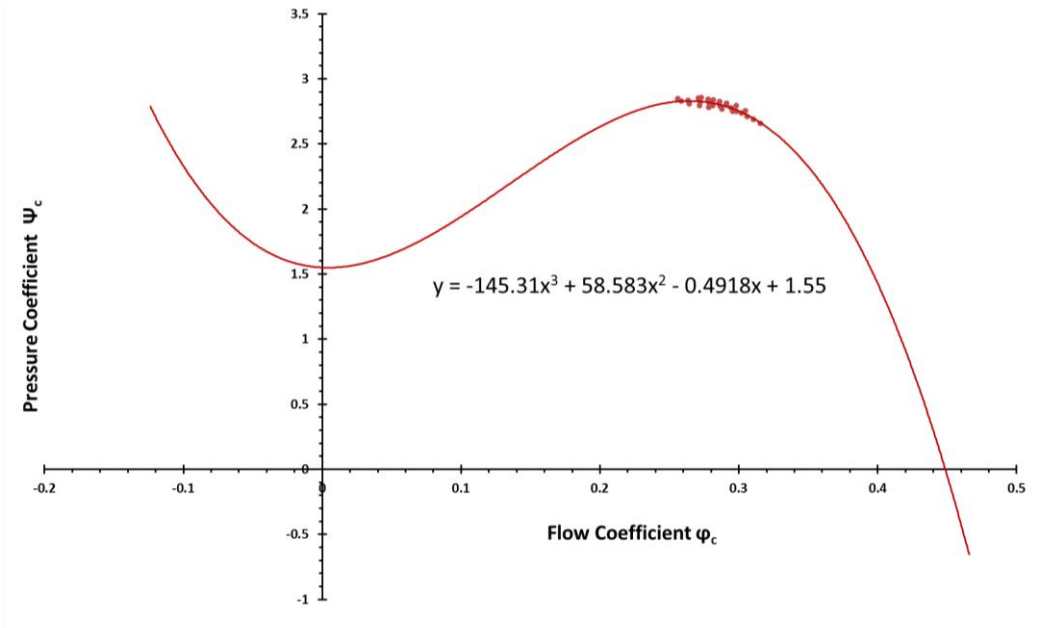

Figure 0-5 Fouled compressor pressure rise characteristic

G.3 Experimental Data & Analysis for Plenum Pressure Coefficient Disturbance

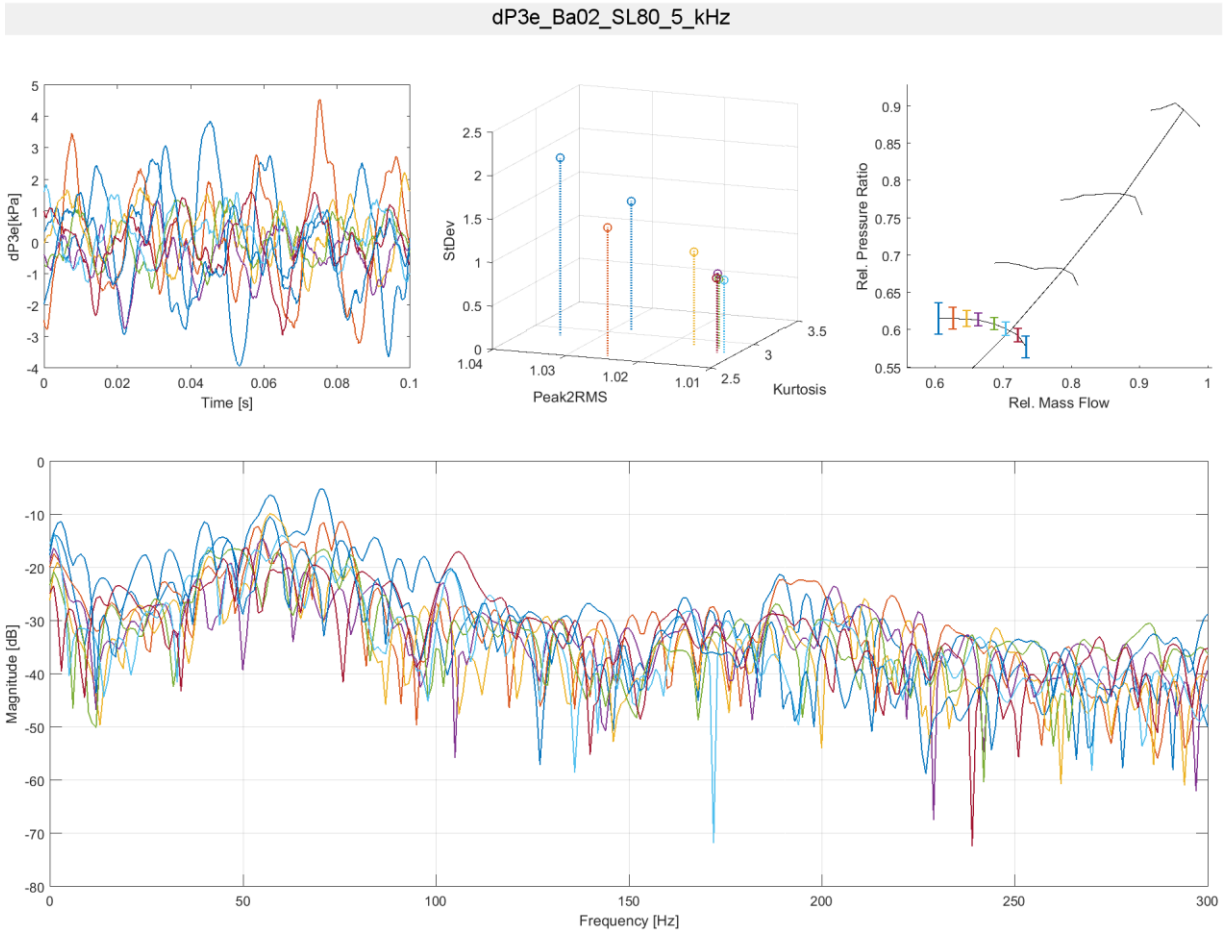

Figure 0-6 Baseline: plenum pressure coefficient disturbance data & analysis for PCN 0.80 (Source: Jiri, 2016b)

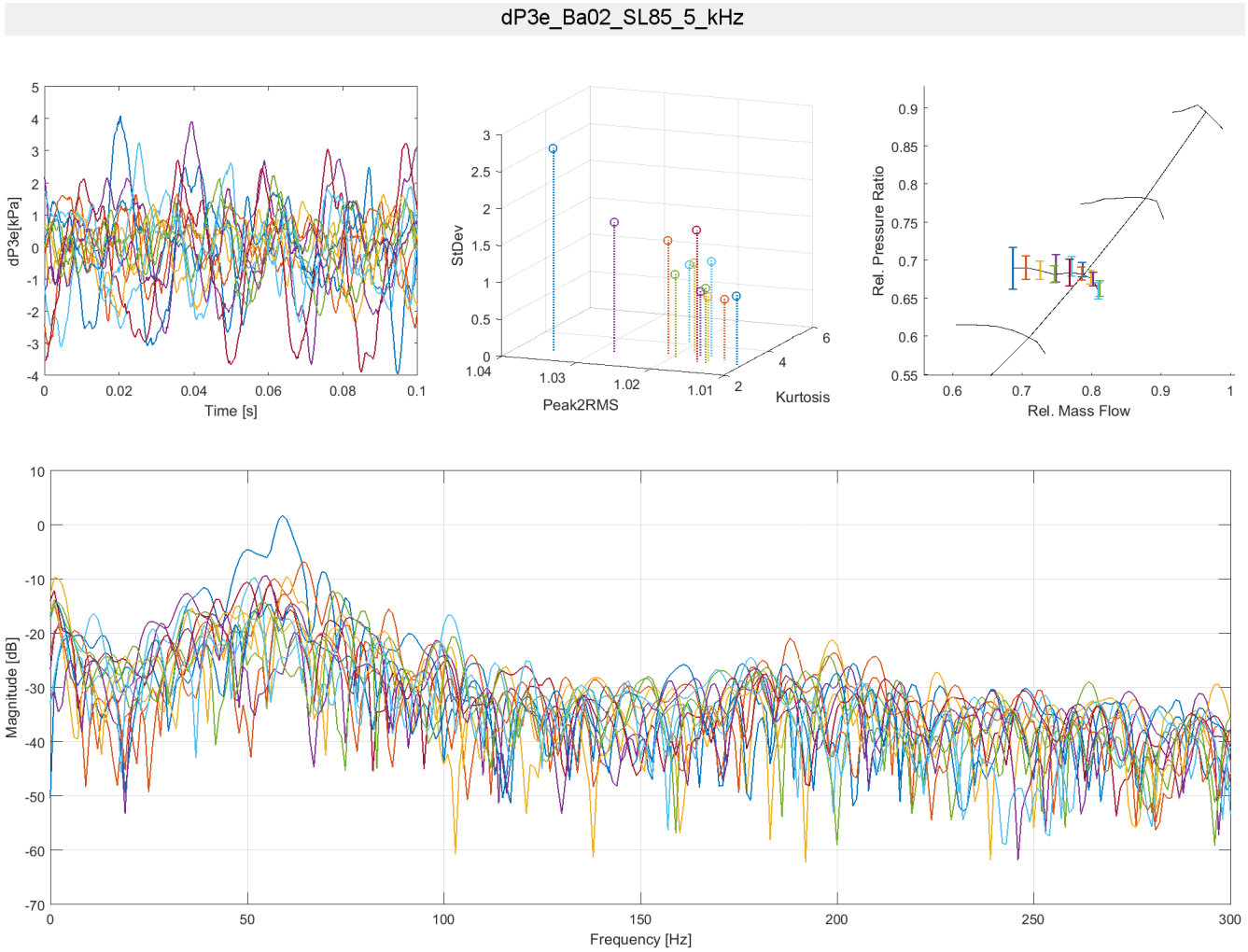

Figure 0-7 Baseline: plenum pressure coefficient disturbance data & analysis for PCN 0.85 (Source: Jiri, 2016b)

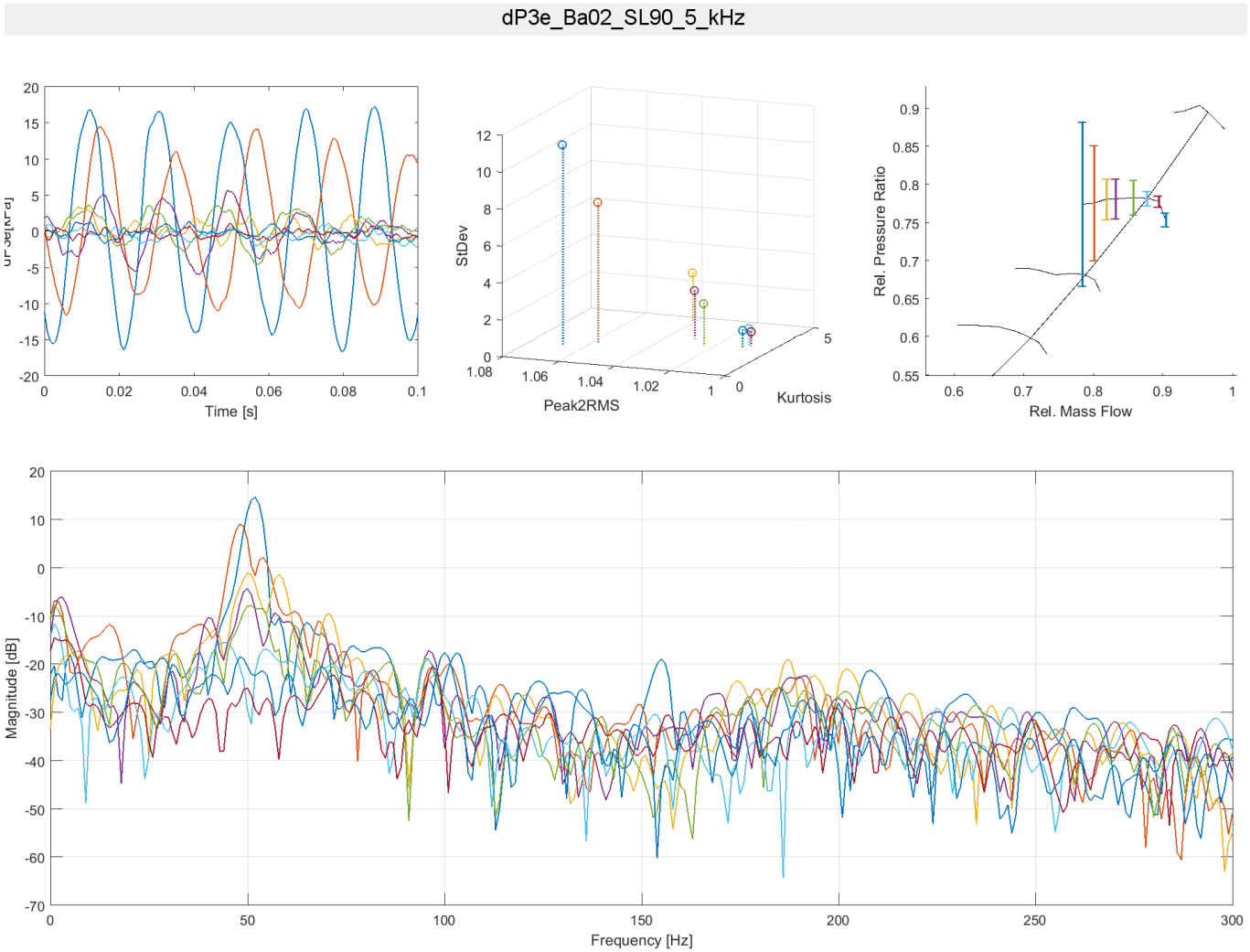

Figure 0-8 Baseline: plenum pressure coefficient disturbance data & analysis for PCN 0.90 (Source: Jiri, 2016b)

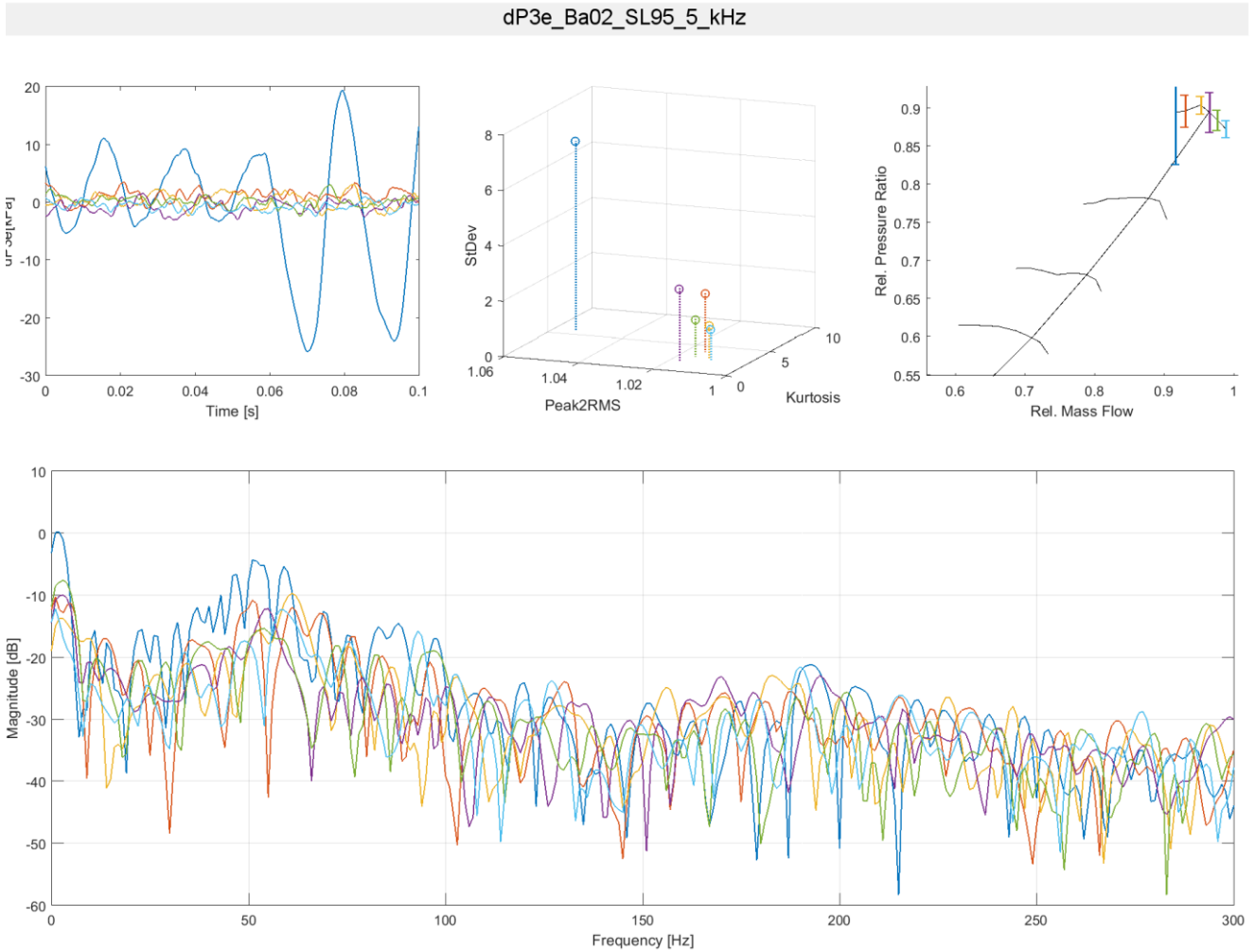

Figure 0-9 Baseline: plenum pressure coefficient disturbance data & analysis for PCN 0.95 (Source: Jiri, 2016b)

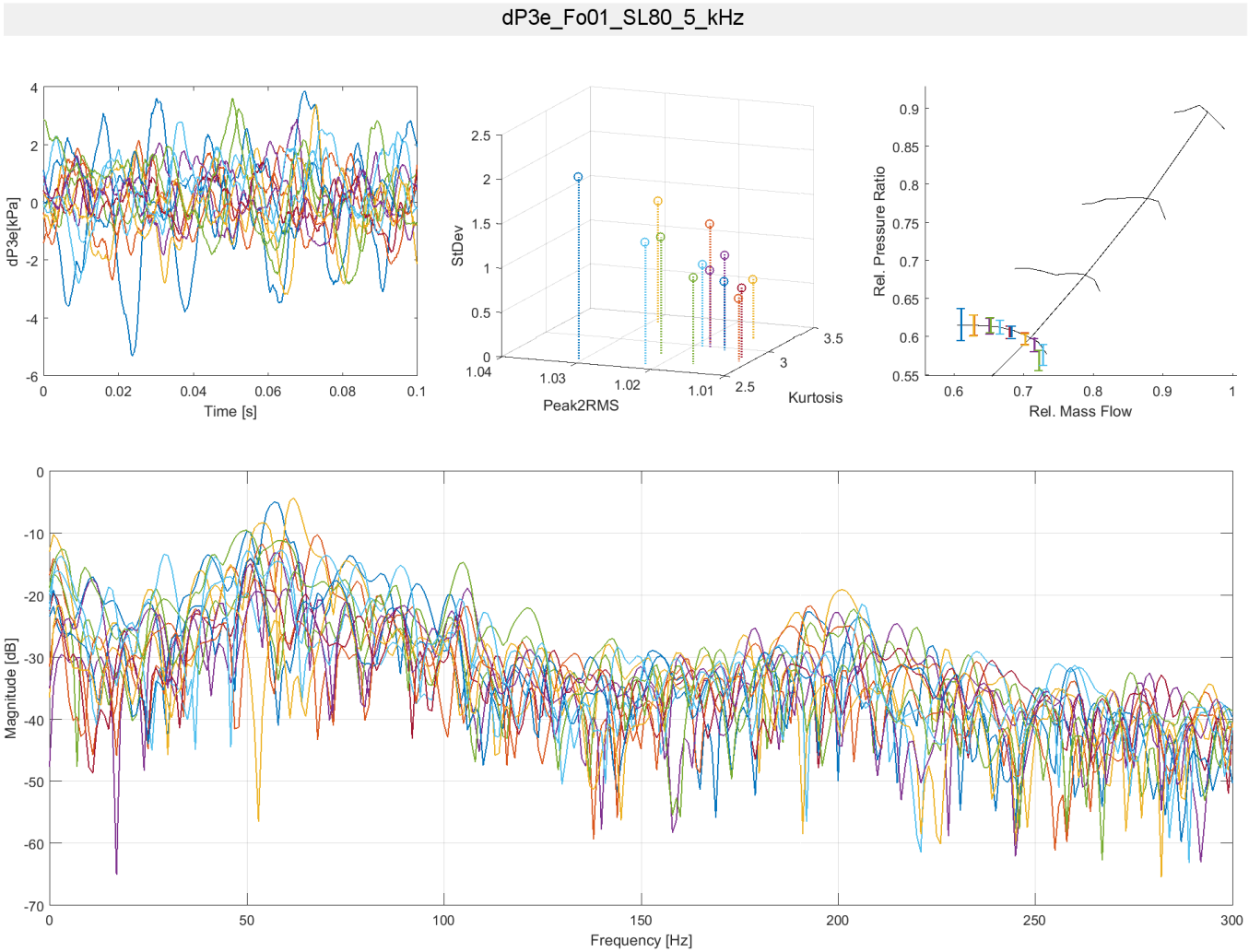

Figure 0-10 Fouled: plenum pressure coefficient disturbance data & analysis for PCN 0.80 (Source: Jiri, 2016b)

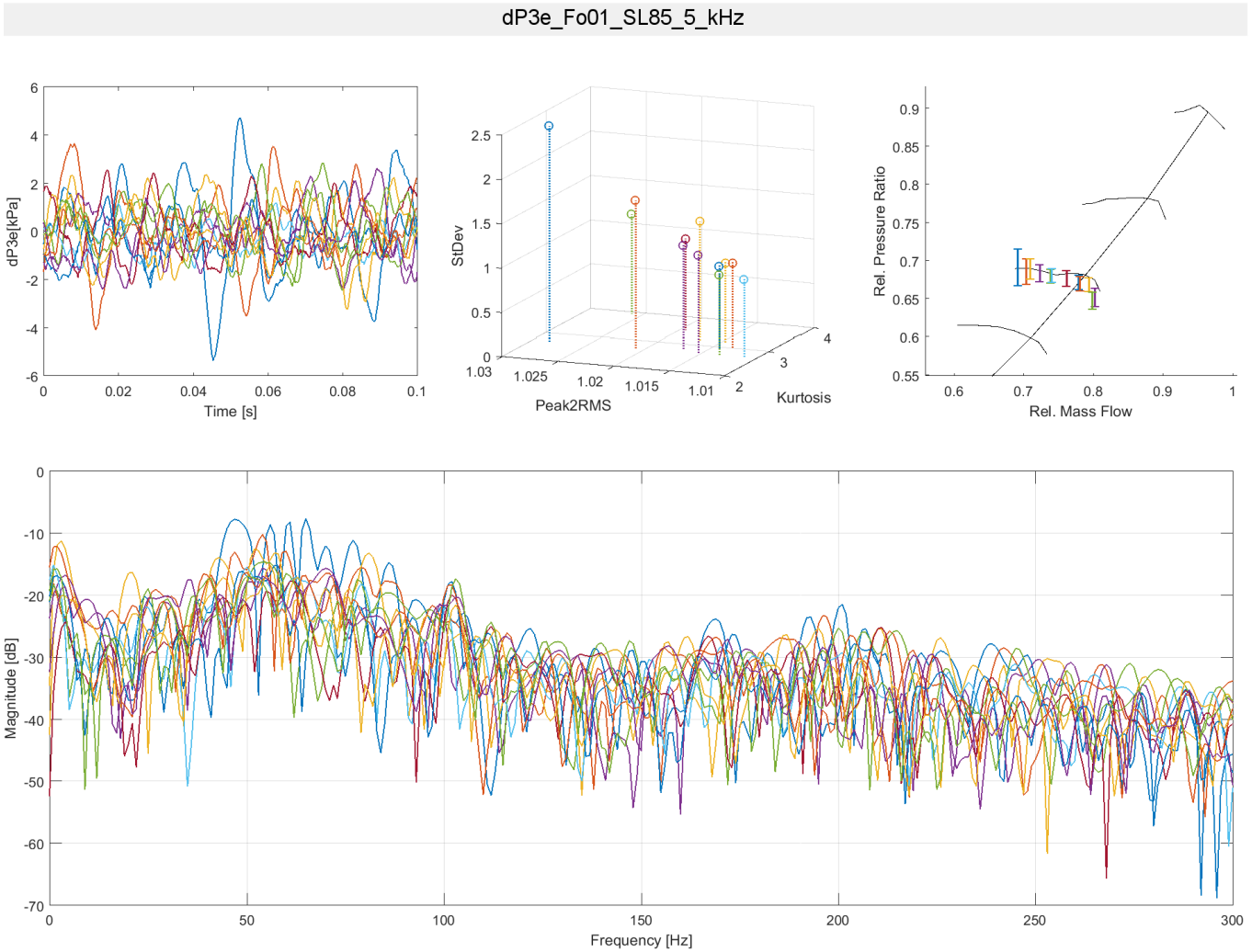

Figure 0-11 Fouled: plenum pressure coefficient disturbance data & analysis for PCN 0.85 (Source: Jiri, 2016b)

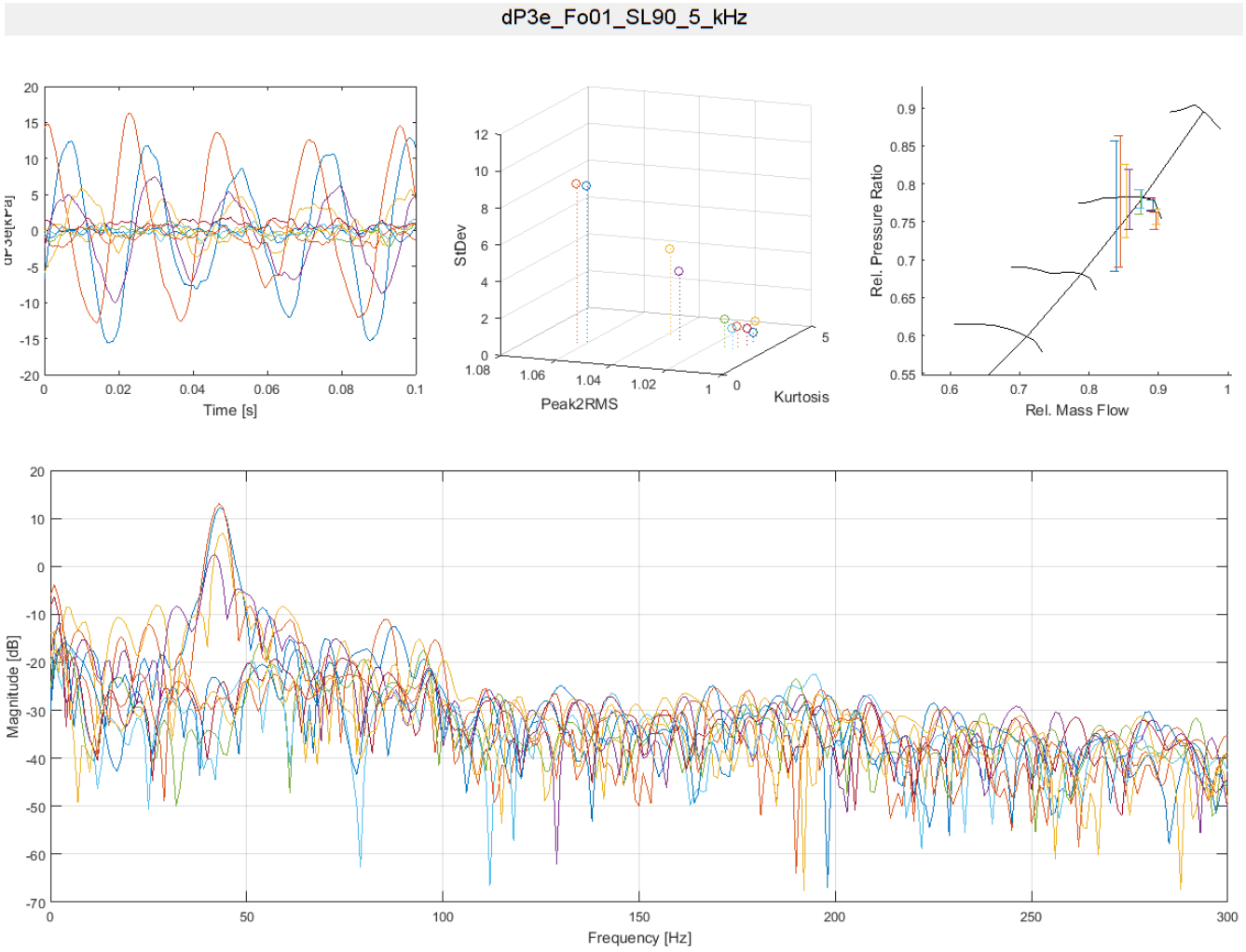

Figure 0-12 Fouled: plenum pressure coefficient disturbance data & analysis for PCN 0.90 (Source: Jiri, 2016b)

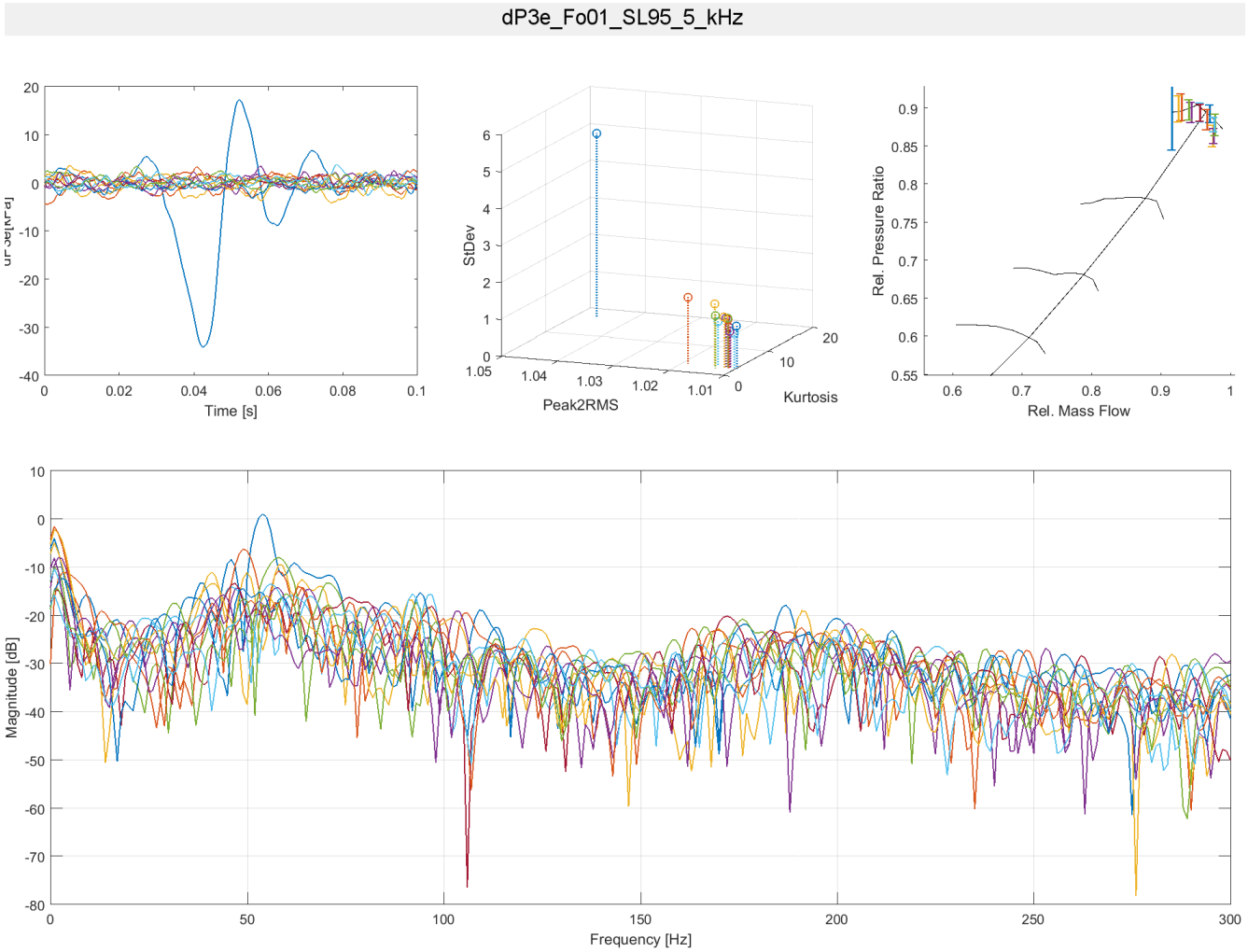

Figure 0-13 Fouled: plenum pressure coefficient disturbance data & analysis for PCN 0.95 (Source: Jiri, 2016b)

G.4 MATLAB Code Implementation of the Greitzer Compression System Model

1. greitzer.m

```
function dydt = greitzer(t,y)

    %Input Data
    %==========
    %Compressor
    %----------
    r = 0.05688;%impeller tip radius in m
    lc = 0.66; %effective length of compressor duct in m
    ac = 0.008539; %flow area of compressor in m^2
    w = 0.95*57500; %rotational speed in rpm


    %Plenum
    %------
    vp = 0.0106; %plenum volume in m^3

    %Throttle
    %--------
    lt = 0.37; %length of throttle duct in m
    at = 0.013; %area of throttle duct in m^2
%     s = 39.5; %baseline throttle parameter b80 = 39.8, b85 = 39.7,
b90 = 40, b95 = 39.5
    s = 40.6; %fouled throttle parameter f80 = 41.2, f85 = 41.9, f90 =
41.8, f95 = 40.6

    %Greitzer B parameter
    a = 340.27; %speed of sound in air in m/s @ ISA
    u = (pi*w*r)/30; %impeller tip speed in m/s^2
    b = (u/(2*a))*(vp/(ac*lc))^0.5;

    %g parameter
    g = (lt/at)/(lc/ac);

    %Governing equations
    %===================
    dydt = zeros(4,1);
    dydt(1) = (y(4)-y(3))*b;
    dydt(2) = (y(3)-s*y(2)^2)*(b/g);
    dydt(3) = (y(1)-y(2))/b;

    if (y(1)<= 0)
        n = 2;
%         n = 0.5;
    elseif (y(1)<=0.34)
        n = 0.5;
    else
        n = 0.5;
    end
```

```
    %baseline (excludes the 0.5 speed line)
%     css = -145.42*y(1)^3 + 59.72*y(1)^2 - 0.6074*y(1) + 1.5;

    %fouled (excludes the 0.5 speed line)
    css = -145.31*y(1)^3 + 58.583*y(1)^2 - 0.4918*y(1) + 1.55;

    %tu parameter
    tu = (pi*r*n)/(lc*b);
    dydt(4) = (css-y(4))/tu;

end
```

2. main.m

```
clear all;

%initialization
tspan = [0 200];
y0 = [0; 0.1; 0.71; 0.71];

[t,y] = ode45(@greitzer, tspan, y0);

sig= y(:,3);

%helmholtz frequency
a = 340.27; %speed of sound in air in m/s @ ISA
lc = 0.66; %effective length of compressor duct in m
ac = 0.008539; %flow area of compressor in m^2
vp = 0.0106; %plenum volume in m^3

wh = a*(ac/(lc*vp))^0.5; %helmholtz freq in rad/s

figure(1);
plot(t/wh,sig);
title('Plenum Pressure rise Time Series')
xlabel('time (s)');
ylabel('Amplitude');
% xlim([0 1]);
% ylim([2.7 2.9]);%[2.7 2.95] [2.6 3]

figure(2);
plot(t/wh,y(:,1));
title('Compressor Flow Coeff. Time Series')
xlabel('time (s)');
ylabel('Amplitude')

%mean disturbance flow coefficient
fprintf('\nMean Flow Coefficient: %f \n\n',(mean(y(1000:end,1))));


figure(3);
x = fft(sig);
L = length(sig);
```

```
P2 = abs(x/L);
P1 = P2(1:L/2+1);
P1(2:end-1) = 2*P1(2:end-1);
Fs = L/(t(end)/wh);
f = Fs*(0:(L/2))/L;

%finding the peak frequencies
%----------------------------
[pks,locs] = findpeaks(P1);
pfreq = f(locs); %peak frequency
num = 10; % number of peak frequencies to select
for k = 1:num
    fprintf('%d : freq(Hz): %f Amp.: %f  \n',k,pfreq(k),pks(k));
end
%----------------------------

plot(f,P1,pfreq,pks,'or');
title('FFT of Plenum Pressure rise Time Series');
xlabel('f (Hz)');
ylabel('Amplitude');


figure(4);
plot(f,P1,pfreq,pks,'or');
title('FFT of Plenum Pressure rise Time Series');
xlabel('f (Hz)');
ylabel('Amplitude');
xlim([5 100]);
```